The *Chandra* Proposers' Observatory Guide

Prepared by:
Chandra X-ray Center
Chandra Project Science, MSFC
Chandra IPI Teams

Version 15.0
December 2012

Contents

List of Figures

List of Tables

What's New for Cycle 15?

Please see the Call for Proposals
(http://cxc.harvard.edu/proposer/CfP/html/CfP_chapter1.html)
list of "What's New" items for Cycle 15.

Chapter 1

Mission Overview

The *Chandra* X-Ray Observatory (*CXO*), combines an efficient high-resolution ($\leq 1/2$ arcsecond) X-ray telescope with a suite of advanced imaging and spectroscopic instruments. The Observatory was successfully launched by *NASA*'s Space Shuttle Columbia on July 23, 1999, with Col. Eileen Collins commanding. Subsequently an Inertial Upper Stage and *Chandra*'s Internal Propulsion System placed the Observatory in a high elliptical orbit. *Chandra* is the X-Ray component of *NASA*'s four Great Observatories. The other components are the Hubble Space Telescope, the late Compton Gamma-Ray Observatory and the Spitzer Space Telescope.

1.1 Program Organization

The *Chandra* Project is managed by *NASA*'s Marshall Space Flight Center. The Project Scientist is Martin C. Weisskopf. Day-to-day responsibility for *Chandra* science operations lies with the Chandra X-ray Center (*CXC*), Harvey Tananbaum, Director. The *CXC* is located at the Cambridge Massachusetts facilities of the Smithsonian Astrophysical Observatory (*SAO*) and the Massachusetts Institute of Technology (*MIT*). The *Chandra* Operations Control Center (*OCC*) is also located in Cambridge. The *CXC* uses the *OCC* to operate the Observatory for *NASA*.

1.2 Unique Capabilities

Chandra was designed to provide order-of-magnitude advances over previous X-ray astronomy missions with regards to spatial and spectral resolution. The High Resolution Mirror Assembly (HRMA) produces images with a half-power diameter (HPD) of the point spread function (PSF) of < 0.5 arcsec. Both grating systems – the Low Energy Transmission Grating (LETG) and the High Energy Transmission Grating (HETG) – offer resolving powers well in excess of 500 over much of their bandwidth which, together, cover the range from $\leq$ 0.1 to 10 keV.

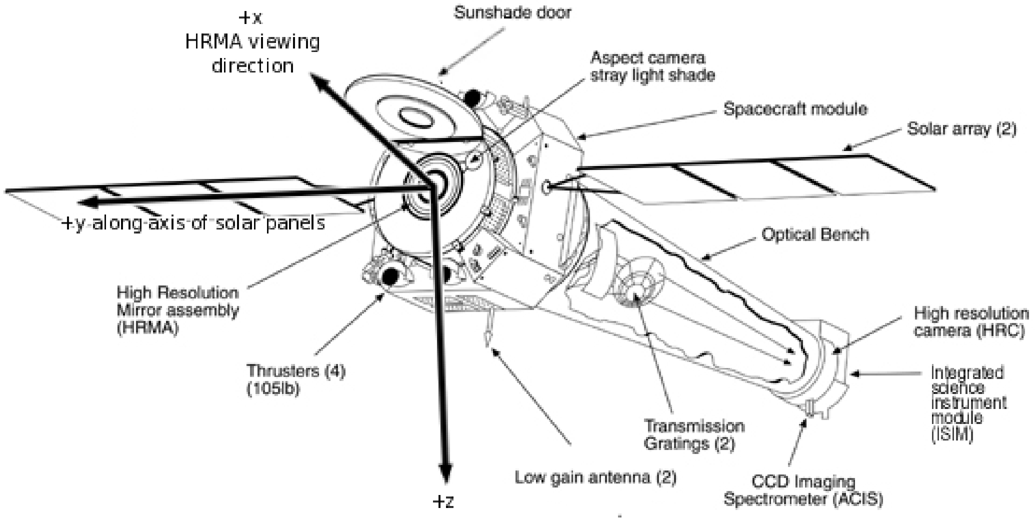

Figure 1.1: The *Chandra* Observatory with certain subsystems labeled.

1.3 Observatory Overview

An outline drawing of the *Chandra* X-ray Observatory is shown in Figure 1.1. *Chandra* consists of a spacecraft and a telescope/science-instrument payload. The spacecraft provides power, communications, command, data management, and pointing control and aspect determination. The principal elements of the observatory that will be discussed in this document are:

- The High Resolution Mirror Assembly (HRMA)(Chapter 4)
- The Aspect System (Chapter 5)
- The Focal-plane Science Instruments (SIs):
  - The Advanced CCD Imaging Spectrometer (ACIS)(Chapter 6)
  - The High Resolution Camera (HRC)(Chapter 7)
- The Objective Transmission Gratings:
  - High Energy Transmission Grating (HETG)(Chapter 8)
  - Low Energy Transmission Grating (LETG)(Chapter 9)

These and related elements of the *Chandra* Project are introduced briefly in the remainder of this chapter.

1.4 Pointing Control and Aspect Determination (PCAD)

The PCAD system controls the pointing and dithering of the observatory and provides the data from which both the relative and absolute aspect are determined. Dithering is imposed in order to spread the instantaneous image over many different pixels of the focal plane detector to smooth out pixel-to-pixel variations. The dither pattern is a Lissajous figure (and can be seen quite clearly in the un-aspect corrected data from bright point sources). The amplitude, phase, and velocity depend on which instrument (ACIS or HRC) is in the focal plane.

Key elements of the PCAD system are the set of redundant gyroscopes, momentum wheels, and an aspect system consisting of a four inch optical telescope with (redundant) CCD detector. The aspect camera simultaneously images a fiducial light pattern produced by light emitting diodes placed around the focal-plane instruments along with the flux from up to five bright stars that may be in the aspect camera's field-of-view. An interesting consequence is that the user may request that one of the targets of the aspect camera be at the location of the X-ray target. For bright optical counterparts, this option allows real-time optical monitoring albeit at the price of a reduced-accuracy aspect solution – see Chapter 5 for further details.

1.5 HRMA

The HRMA consists of a nested set of four paraboloid-hyperboloid (Wolter-1) grazing-incidence X-ray mirror pairs, with the largest having a diameter of 1.2 m (twice that of the *Einstein* Observatory). The focal length is 10 m.

The mirror glass was obtained from Schott Glasswerke; grinding and polishing was performed at Hughes Danbury Optical Systems; coating at Optical Coating Laboratory; and the mirror alignment and mounting at Eastman-Kodak Co. The mirrors weigh about 1000kg. Details of the HRMA and its performance are presented in Chapter 4.

The *Chandra* Telescope Scientist was the late Leon Van Speybroeck, of the Smithsonian Astrophysical Observatory.

1.6 Science Instrument Module (SIM)

The Science Instrument Module consists of the special hardware that provides mechanical and thermal interfaces to the focal-plane scientific instruments (SIs). The most critical functions from an observer's viewpoint are the capability to adjust the telescope focal length and the ability to move the instruments along an axis orthogonal to the optical axis.

The SIM houses the two focal instruments - the ACIS and the HRC. Each of these have two principal components - HRC-I and -S and ACIS-I and -S. The focal plane instrument layout is shown in Figure 1.2. The SIM moves in both the X-axis (focus) and the Z-axis

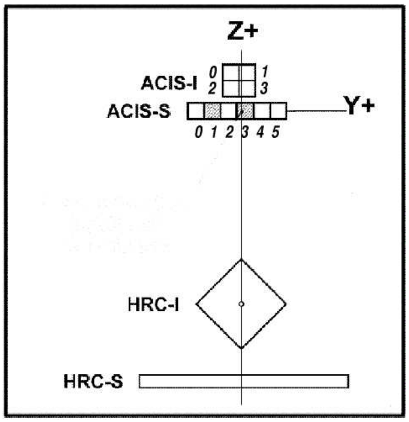

Figure 1.2: Arrangement of the ACIS and the HRC in the focal plane. The view is along the axis of the telescope from the direction of the mirrors. For reference, the two back-illuminated ACIS-S chips are shaded. Numbers indicate positions of chips I0-I3 and S0-S5. SIM motion can be used to place the aimpoint at any point on the vertical solid line.

(instrument and aimpoint (1.6.1) selection). Note that the Y-Axis parallels the dispersion direction of the gratings.

1.6.1 Aimpoints

Aimpoints are the nominal positions on the detector where the flux from a point source is placed. Note there is a slight (less than 20") distinction between the aimpoint and the on-axis position, which for most practical purposes can be ignored. The aimpoints are discussed in detail in the chapters about each instrument and in Chapter 3.

1.7 Ground System

The ground system consists of the *Chandra* X-ray Center (*CXC*) and the Operations Control Center (*OCC*) in Cambridge, MA, the Engineering Support Center (ESC) at *MSFC*, and various *NASA* communications systems including the Deep Space Network operated for *NASA* by the Jet Propulsion Laboratory. See Section 2.6.2 for details.

1.8 Orbit

The Chandra orbit is highly elliptical and varies with time. As of December 2012 the apogee height was $\sim 145,000$ km and the perigee height was $\sim 4,000$ km. During 2013 the orbital eccentricity, having passed its maximum of 0.88 during 2012, will decrease, reaching 0.84 by the end of 2013, at which point the apogee height will be $\sim 142,000$ km and the perigee height will be $\sim 7,000$ km. Over the following ~ 4 years the apogee and perigee will draw closer together, reaching a minimum eccentricity of ~ 0.68 in early 2018. The orbit allows for reasonably high observing efficiency as the satellite spends most of the time well above the radiation belts ($\sim 80\%$) and long continuous observations (currently ~ 180 ksec) are made possible by the orbital period of 63.5h (but see Section 3.3 for limitations due to spacecraft thermal considerations).

1.9 Particle Detector

There is a particle detector mounted near the telescope, called the Electron, Proton, Helium INstrument (EPHIN) (see Section 2.5). This detector is used to monitor the local charged particle environment as part of the scheme to protect the focal-plane instruments from particle radiation damage. Data taken during an observation are available to the observer. The performance of EPHIN has degraded at higher temperatues in recent years. Pitch angle restrictions are in place to keep EPHIN at an acceptible operating temperature (see Section 3.3.2).

The Co-Principal Investigators of the EPHIN instrument are Drs. Reinhold Muller-Mellin and Hoarst Kunow of the University of Kiel, Germany.

1.10 ACIS

ACIS is comprised of two CCD arrays, a 4-chip array, ACIS-I; and a 6-chip array, ACIS-S. The CCDs are flat, but the chips in each array are positioned (tilted) to approximate the relevant focal surface: that of the HRMA for ACIS-I and that of the HETG Rowland circle for ACIS-S. ACIS-I was designed for CCD imaging and spectrometry; ACIS-S can be used both for CCD imaging spectrometry and also for high-resolution spectroscopy in conjunction with the HETG grating.

There are two types of CCD chips. ACIS-I is comprised of front-illuminated (FI) CCDs. ACIS-S is comprised of 4 FI and 2 back-illuminated (BI) CCDs, one of which is at the best focus position. The efficiency of the ACIS instrument has been discovered to be slowly changing with time, most likely as a result of molecular contamination build-up on the optical blocking filter. The BI CCDs response extends to lower energies than the FI CCDs and the energy resolution is mostly independent of position. The low-energy response of the BI CCDs is partially compromised by the contaminant build-up. The FI CCD response is more efficient at higher energies but the energy resolution varies with position due to radiation damage caused by protons reflecting through the telescope during radiation-zone passages in the early part of the mission. Details in Chapter 6.

The Principal Investigator is Prof. Gordon Garmire of the Pennsylvania State University.

1.11 HRC

The HRC is comprised of two microchannel plate (MCP) imaging detectors: the HRC-I designed for wide-field imaging; and, HRC-S designed to serve as a readout for the LETG. The HRC-I is placed at right angles to the optical axis, tangent to the focal surface. The HRC-S is made of three flat elements, the outer two of which are tilted to approximate the LETG Rowland circle. The HRC detectors have the highest spatial resolution on *Chandra*, matching the HRMA point spread function most closely. Under certain circumstances, the HRC-S detector also offers the fastest time resolution (16μs). Details concerning the HRC are in Chapter 7.

The Instrument Principal Investigator is Dr. Stephen Murray of the Smithsonian Astrophysical Observatory.

1.12 HETG

The HETG, when operated with the ACIS-S, forms the High-Energy Transmission Grating Spectrometer (HETGS) for high resolution spectroscopy. The HETGS achieves resolving power ($E/\Delta E$) up to 1000 in the band between 0.4 keV and 10.0 keV. The HETG is comprised of two grating assemblies – the High Energy Grating (HEG) and the Medium Energy Grating (MEG) – on a single structure that can, by command, be placed in the optical path just behind the HRMA. The HEG intercepts X-rays from only the two inner mirror shells and the MEG intercepts X-rays from only the two outer mirror shells. The HEG and MEG dispersion directions are offset by 10 degrees so the two patterns can be easily distinguished. Details are presented in Chapter 8.

The Instrument Principal Investigator for the HETG is Prof. Claude Canizares, of the *MIT* Center for Space Research.

1.13 LETG

The LETG when operated with the HRC-S, forms the Low Energy Transmission Grating Spectrometer (LETGS). The LETGS provides the highest spectral resolution on *Chandra* at low (0.08 - 0.2 keV) energies. The LETG is comprised of a single grating assembly that, on command, can be placed in the optical path behind the HRMA. The LETG grating facets intercept and disperse the flux from all of the HRMA mirror shells. Details are given in Chapter 9.

The LETG was developed at the Laboratory for Space Research in Utrecht, the Netherlands, in collaboration with the Max-Planck-Institut für Extraterrestrische Physik in Garching, Germany. The Instrument Principal Investigator is Dr. Jelle Kaastra of the Laboratory for Space Research.

1.14 Effective Area Comparisons

The effective areas of the imaging instruments are shown in Figure 1.3. The ACIS curves allow for the expected degradation of the ACIS efficiency caused by molecular contamination predicted for the middle of Cycle 14. A comparison of the effective areas of the grating spectrometers are shown in Figure 1.4. Note that the data from the HEG and MEG are obtained simultaneously. The comparisons shown here are based on the most recent calibration at the time of issuance of this document and are subject to revision. The proposer is urged to read the detailed material in the appropriate chapters and examine the *CXC* web site (see Section 1.16) for updates.

1.15 Allocation of observing time

Observing time is awarded through the *NASA* proposal and peer review process. The prospective user must submit a proposal in which the observation is described and justified in terms of the expected results. The proposer must also show that the observation is well suited to *Chandra* and that it is technically feasible. Refer to the Call for Proposals (*CfP*, http://cxc.harvard.edu/proposer/CfP/) for more information.

1.16 How to get information and help

The *CXC* web page (http://cxc.harvard.edu) provides access to documents, proposal preparation tools, and proposal submission software. The *Proposers' Observatory Guide* and *CfP* are also available in printed form by request through the *CXC* HelpDesk or by writing to *Chandra* Director's Office, Mail stop 4, 60 Garden St., Cambridge, MA 02138.

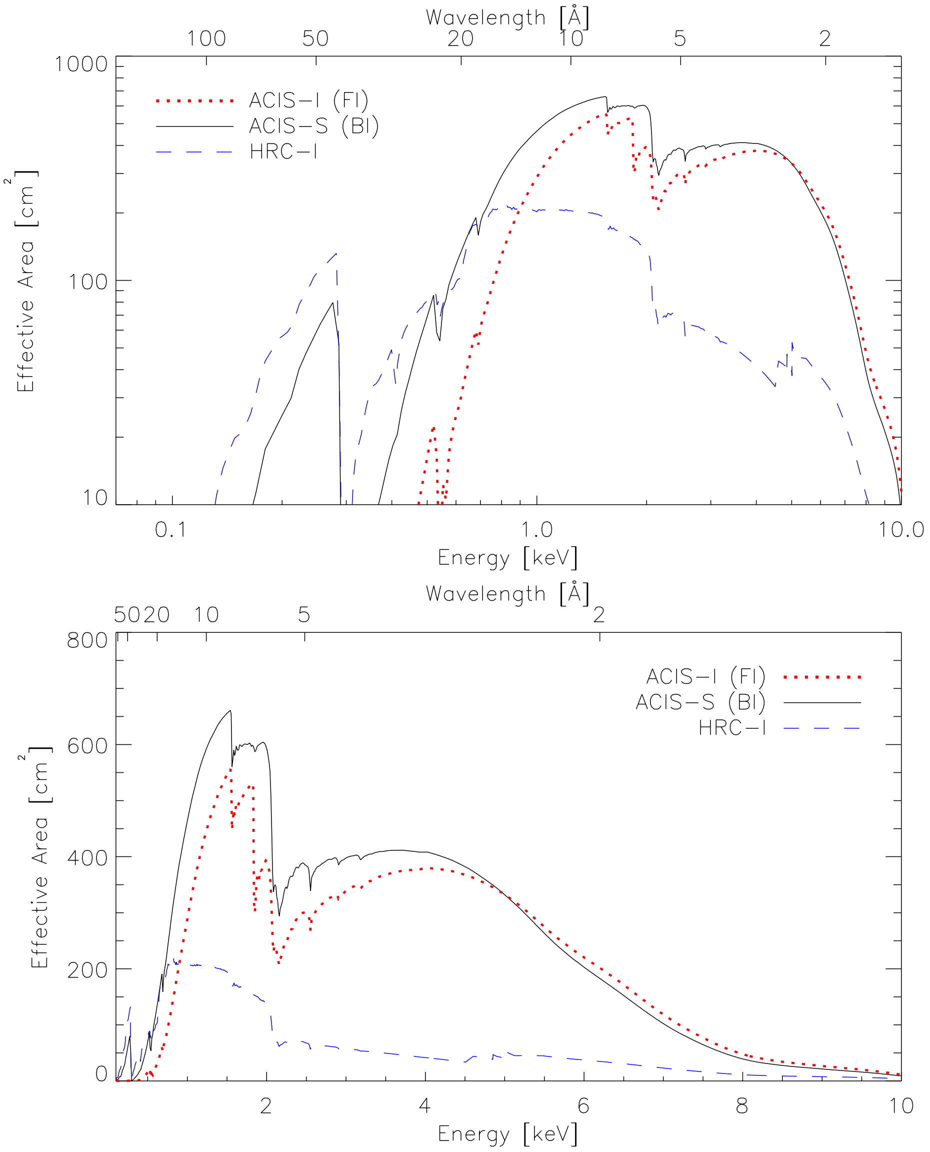

Figure 1.3: Comparison of the on-axis effective areas for observing a point source (integrated over the PSF) of the HRMA/HRC-I, the HRMA/ACIS(FI), and the HRMA/ACIS(BI) combinations. The ACIS curves show the predicted values for the middle of Cycle 14.

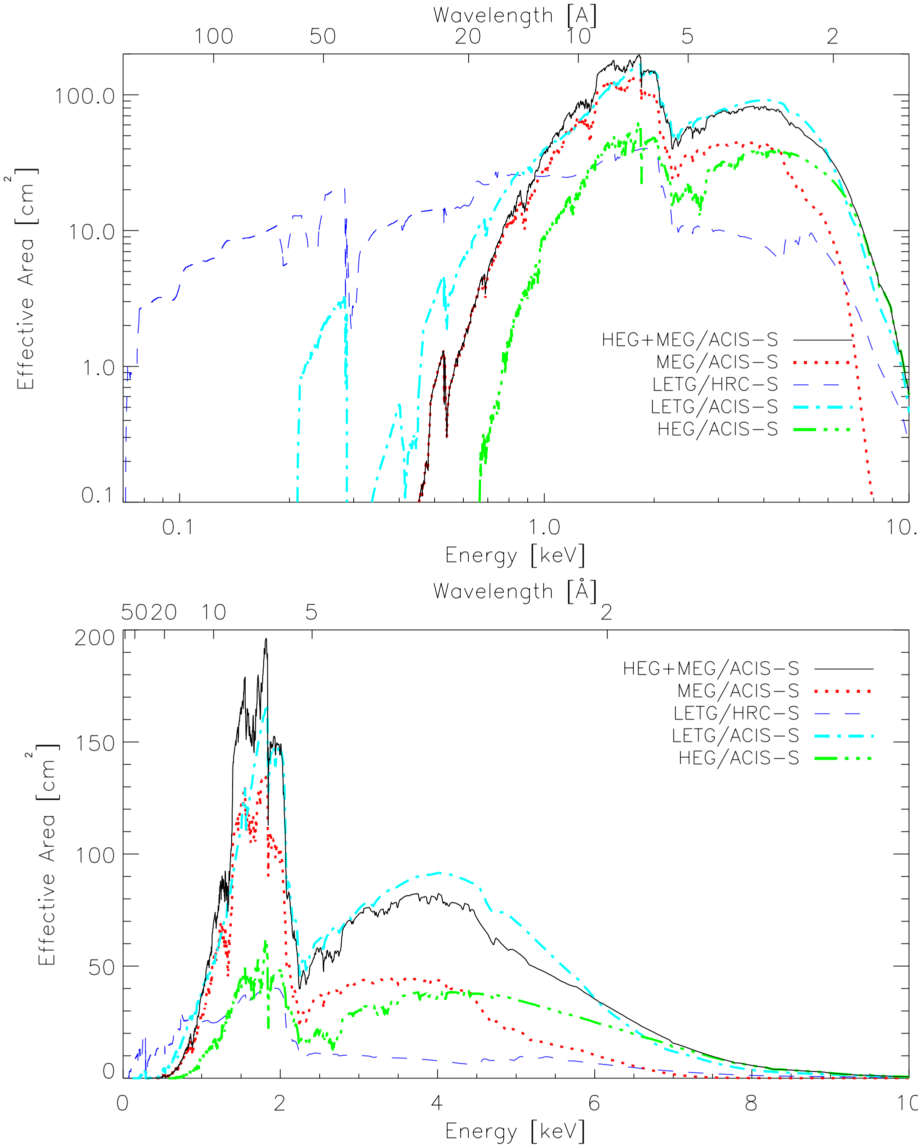

Figure 1.4: Comparison of the total first-order (positive and negative orders combined) effective areas of the LETG and HETG (HEG and MEG are shown separately and summed) spectrometers. HEG and MEG spectra are obtained simultaneously and can sometimes be usefully combined. For a given energy in the range of overlap the resolving power of the HEG is approximately twice that of the MEG, which in turn is approximately twice that of the LETG. The LETG extends to much lower energies than reached by the HETG+ACIS-S combination, especially when used with the HRC-S detector. For full details on spectrometer performance and observation planning see Chapters 8 (HETG) and 9 (LETG).

Chapter 2

Spacecraft, Telescope, Operations, & Mission Planning

2.1 Introduction

In this chapter we provide a brief overview of the spacecraft, the telescope system including the Science Instrument Module (SIM), operations, and mission planning.

A number of observatory parameters are given in Table 2.1.

2.2 Spacecraft

An outline drawing of the Observatory was shown in Figure 1.1. The spacecraft equipment panels are mounted to, and supported by, a central cylindrical structure. The rear of the spacecraft attaches to the telescope system.

The spacecraft includes six subsystems:

1. **Structures and Mechanical** Subsystem. This subsystem includes all spacecraft structures, mechanisms (both mechanical and electro-mechanical), and structural interfaces with the Space Shuttle. Mechanisms, such as those required for the sunshade door, are also part of this subsystem.

2. **Thermal Control** Subsystem. Thermal control is primarily passive, using thermal coatings and multi-layer insulation blankets. On-board-computer-controlled electrical heaters augment these passive elements to maintain sensitive items such as the HRMA at nearly constant temperature.

3. **Electrical and Power** Subsystem. This subsystem includes all hardware necessary to generate, condition, and store electrical energy. Power is generated by solar cells mounted on two solar array wings (three panels each), sized to provide a 15% end-of-life power margin. Electrical power is stored in three, NiH_2, 30-Ampere-hour

Table 2.1: Spacecraft Parameters

Chandra “dry” weight (incl. reserve)		4790 kg
Loaded Propellant		40 kg
Electrical Power		3 $\mathrm{NiH_2}$ Amp-hr batteries
		Two 3-panel solar arrays
Nominal Operating Power		800-120 W
Optical bench length		$\sim$ 10 meters
SIM focus adjustment range		$\pm$0.4 inches
SIM focus adjustment accuracy		$\pm$0.0005 inches
SIM Z-position adjustment repeatability		$\pm$0.005 inches
Solid-state recorder capacity		1.8 Gb $\times$ 2
On-board command storage		5400 command words
Nominal command storage period		72 hours
Observatory telemetry data-rate		32 kbps
Telemetry playback downlink rates		1024, 512 and 256 kbps
Nominal ground contact periods		45 to 75 minutes per 8 hours
SI telemetry rate		24 kbps
Telemetry format	1 major frame	= 32.8 seconds
		= 128 minor frames
Clock error		$< 100\mu$s
Clock stability		1:10^9 per day
Clock frequency		1.024 MHz

batteries. These batteries provide spacecraft power during times when either the Earth or Moon partially or completely blocks the Sun. Even so, the battery capacity requires that certain non-critical items, including science instruments, be powered down during eclipses. These eclipses occur infrequently due to the particular nature of the *Chandra* orbit.

4. **Communication, Command, and Data Management** (CCDM) Subsystem. This subsystem includes all the equipment necessary to provide ranging, modulation, and demodulation of radio frequency transmission of commands and data to and from the Deep Space Network *NASA* Communication System. The CCDM includes two low gain antennas, providing omni-directional communications, an on-board computer (OBC), a serial digital data bus for communication with other spacecraft components, the spacecraft clock, and a telemetry formatter which provides several different formats.

5. **Pointing Control and Aspect Determination** (PCAD) Subsystem. This subsystem includes the hardware and control algorithms for attitude determination and for attitude and solar array control. The solar arrays can be rotated about one axis. The PCAD subsystem also includes hardware for safing the observatory. Specific details of the PCAD subsystem especially relevant to scientific performance are discussed in Chapter 5.

6. **Propulsion Subsystem** . This subsystem consists of the Integral Propulsion Subsystem (IPS) and the Momentum Unloading Propulsion Subsystem (MUPS). The IPS contains the thrusters and fuel for control of the orbit and spacecraft orientation during orbit transfer. This subsystem was disabled once the final orbit was achieved for observatory safety reasons. The MUPS provides momentum unloading during normal on-orbit operations. Given the current performance there is sufficient MUPS fuel to support ∼20 additional years of operation.

2.3 Telescope System

The principal element of the telescope system is the High Resolution Mirror Assembly (HRMA, Chapter 4). The HRMA, comprised of four concentric grazing incidence X-ray telescopes, focuses X-rays on the selected detector located in the Science Instrument Module (SIM, Section 2.4).

The telescope system also includes:

1. Optical Bench Assembly
2. Spacecraft Support Structure Assembly
3. Fiducial Transfer Optical Components
4. Spacecraft to Telescope Support Struts

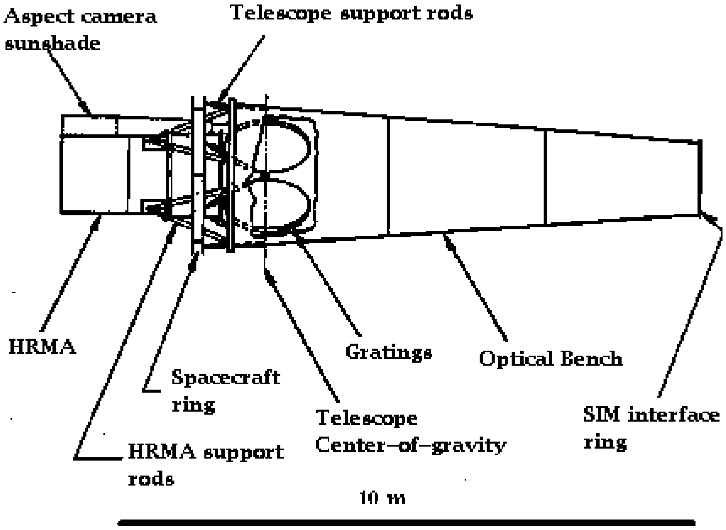

Figure 2.1: Major components of the telescope system. The grating assemblies are also shown.

5. Forward and Aft HRMA Contamination Covers
6. Magnetic Baffle Assembly
7. Stovepipe Baffle

The Optical Bench Assembly is primarily the long composite structure separating the HRMA from the SIM. The Spacecraft Support Structure Assembly includes the ring to which the spacecraft is mounted. The Fiducial Transfer Assembly Optical Components are discussed in Chapter 5. The Spacecraft to Telescope Support Struts are self-explanatory and are shown in Figure 2.1. The forward and aft contamination covers were opened on-orbit and cannot be closed. The forward contamination cover also serves as the sun-shade.

The Magnetic Baffle Assembly was designed to prevent low energy (up to about ~ 100 keV) electrons (reflecting through the x-ray optics) from reaching the focal plane. More details about these baffles may be found at http://wwwastro.msfc.nasa.gov/xray/spectops.

The stovepipe baffle, located inside the optical bench and at the entrance to the SIM, includes tantalum coated plates to prevent x-rays, other than those passing through the telescope, from reaching the focal plane. There are several such baffles inside the optical bench. Details of the baffles may be found at the WWW address above.

2.4 Science Instrument Module (SIM)

The SIM, shown schematically in Figure 2.2, is a movable bench on which the focal-plane x-ray detectors are mounted. Kinematic mounts (flexures) and thermal isolation

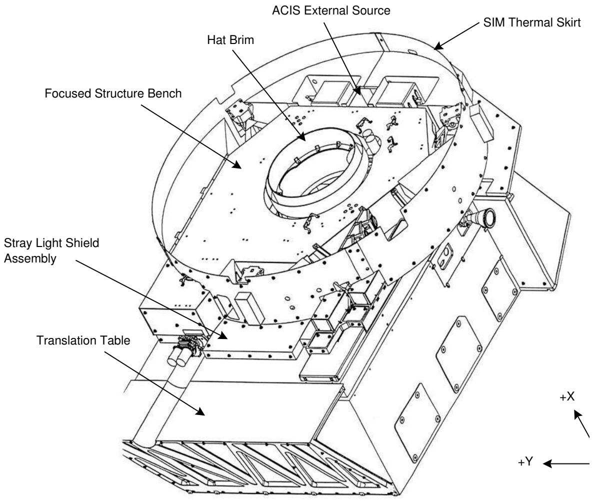

Figure 2.2: A schematic of the Science Instrument Module.

are provided between the SIM and the telescope optical bench. A graphite epoxy support structure houses the translation stage.

2.4.1 SIM Motions

The focal plane instruments are positioned by the SIM Z-axis translation stage with a repeatability to ±0.005 inches over a translation range of 20 inches. The SIM X-axis motion sets the focus to an accuracy of ±0.0005 inches over a range of 0.8 inches. The fine-focus adjustment step is 0.00005 inches.

2.5 Electron Proton Helium Instrument (EPHIN)

The local particle radiation environment is monitored by the EPHIN detector. EPHIN consists of an array of 5 silicon detectors with anti-coincidence shielding. The instrument is sensitive to electrons in the energy range 150 keV - 5 MeV, and protons/helium isotopes in the energy range 5 - 49 MeV/nucleon. The field of view is 83 degrees and the instrument is mounted on the sun side of the spacecraft near the HRMA. EPHIN data rates are monitored by the OBC, which activates commands to safe the ACIS and HRC during periods of high radiation such as a solar flare.

The forerunner of the *Chandra*-EPHIN was flown on the SOHO satellite. Information is available at http://www.ieap.uni-kiel.de/et/ag-heber/costep/ephin.php. The EPHIN instrument was built by the Institut fur Experimentelle und Angewandte Physik at the University of Kiel, Germany. Drs. Reinhold Muller-Mellin and Hoarst Kunow are the Co-Principal Investigators.

2.6 Operations

2.6.1 Launch and On-orbit Verification

Chandra was launched on board the Space Shuttle Columbia from the Kennedy Space Center in Florida on July 23, 1999 at 12:31:00:04 a.m. EDT. The Observatory was deployed from the Space Shuttle a few hours later at 8:45 a.m. EDT. Two burns of the IUS (Inertial Upper Stage) took place an hour after *Chandra* was released. A series of five burns of the Integral Propulsion System (IPS) over the period July 24 - August 7 took *Chandra* to its final orbit.

Once in final orbit, the Orbital Activation and Checkout (OAC) phase started. During this time, all systems were brought on-line and numerous calibrations were performed. After the contamination covers on the HRMA were opened, and after a few passages through the radiation belts under this condition, the front-illuminated ACIS CCDs showed signs of decreased, and spatially-dependent, energy resolution together with increased charge transfer inefficiency (CTI), consistent with radiation damage. Steps were successfully taken to prevent further damage (see Chapter 6). Due to this situation, and because of uncertainties of the long term stability of the FI chips at that time, additional ACIS calibrations were performed and emphasis was placed on observations requiring the use of the FI CCDs. Note that the back-illuminated CCDs were unaffected, and the situation is now stable in that further degradation has been slowed to match pre-launch expectations. See Chapter 6 for further details. Normal operations started in November 1999.

2.6.2 The Ground System

The *Chandra* "Ground System" is comprised of facilities required to operate the spacecraft, receive and analyze the spacecraft telemetry and provide scientific support to the user community. The ground system includes the following elements:

Deep Space Network (DSN). The DSN is used for communicating commands to the spacecraft and receiving telemetry.

***NASA* Communications** (NASCOM). NASCOM provides communications links between the DSN and the *OCC* and between the *OCC* and other ground facilities.

Operations and Control Center (*OCC*) is responsible for operating the observatory. This includes activities such as preparing command loads, processing telemetry, attitude determination, monitoring health and safety, etc. *OCC* personnel utilize two major software environments, the Online System (ONLS) and the Offline System (OFLS). The ONLS deals primarily with real-time operations such as receiving telemetry and sending commands through the DSN. The OFLS deals with functions such as mission planning and supporting engineering analysis. The Software Maintenance Facility (SMF) which maintains the flight software is operated by NGST and is located at the *OCC*.

***Chandra* Science Center** (*CXC*). The *CXC* is the focal point for service to the scientific community. The *CXC* is contracted to issue the *CfP* and organize peer reviews. The *CXC* assists prospective observers in developing proposals, generates an observing plan from the proposals that are selected, and supplies data products to observers. The *CXC* performs on-orbit calibration and maintains the calibration data-base, produces response functions, etc. The *CXC* is responsible for providing limited assistance to observers, including software, for analyzing data. The *CXC* is also responsible for archiving *Chandra* data.

2.6.3 Commanding

All normal *Chandra* operations are preplanned. The OFLS divides the weekly mission schedule into approximately one day segments and generates spacecraft and instrument commands to be executed that day. Once a day, this command load is uplinked to the spacecraft and stored. Three consecutive daily segments are loaded to assure autonomous operation for 72 hours. Stored command loads can be interrupted if necessary, and updated either because of an emergency or to accommodate Targets of Opportunity. The interruption process may require up to 24 hours to complete depending on numerous factors including the availability of ground contact. In a true emergency, ground contact can always be scheduled.

2.6.4 Telemetry

The telemetry is formatted into major frames and minor frames - a major frame lasts 32.8 seconds and includes 128 minor frames. Each minor frame contains 1019 bytes of science and engineering data plus a 6 byte header (yes - 1025, not 1024, total bytes!) that includes a 3-byte minor frame counter – the Virtual Channel Data Unit (VCDU) counter – which rolls over every 49.8 days.

During normal science operations, telemetry data is generated on the Observatory at a rate of 32 kbps, of which 24 kbps are devoted to the “science stream” data from one of the focal plane instruments and the remainder allocated to other systems, including 0.5 kbs to the “next-in-line” instrument. The data is recorded on one of two solid state recorders for subsequent transmission. Each solid state recorder has a capacity of 1.8 Gbits equivalent to 16 hours of operation.

The recorded data are transmitted through one of the low gain antennas to the ground at 1024 kbps, (or 512 kbps, or 256 kbps) during scheduled Deep Space Network contacts every eight hours. Contacts last 45-75 minutes. The ground stations, in turn, transmit the data to JPL which then transmits the data to the *OCC*.

2.6.5 SI Science Data

There are individual telemetry formats for HRC and ACIS data. The 24 kbps data is collected by the CCDM subsystem from each instrument as a sequence of 8-bit serial-digital words through a Remote Command and Telemetry Unit (RCTU). An additional small amount of housekeeping telemetry is always collected from each instrument independent of the selected format.

2.6.6 Event Timing and the Spacecraft Clock

The CCDM subsystem provides prime and redundant 1.024 MHz clocks, and the ($1/1.024\mu$s) pulses are utilized by the two focal plane instruments for timing. Each instrument has electronics that counts the elapsed time since the beginning of the current telemetry major frame. The time of events recorded on *Chandra* are given in Terrestrial Time (TT) which differs from UTC by about a minute. (See http://tycho.usno.navy.mil/systime.html for a discussion.) The accuracy of the time relationship is 100 microseconds. The spacecraft clock is stable to better than one part in 10^9 per day.

2.7 Mission Planning

2.7.1 The Long-Term Schedule

The *Chandra* scheduling process seeks to maximize the fraction of time on-target while minimizing risk to the spacecraft. Once the list of approved target observations for a new cycle has been finalized and targets have been reviewed in detail by the Observer/PI via USINT (http://cxc.harvard.edu/cdo/observation_scheduling.html#usp), they are scheduled by the Science Mission Planners into a Long Term Schedule (LTS). LTS observations, scheduled into weekly bins, generally do not fully occupy the time available for science scheduling; a reserve of unconstrained observations are kept in a pool and used to fill in weekly short-term schedules.

Once a new LTS is populated at the start of a Cycle, Mission Planners begin the process of weekly scheduling. As the Cycle goes on, the remaining LTS is amended weekly and posted on-line at http://cxc.harvard.edu/target_lists/longsched.html. Observers should note that the predictive fidelity of the LTS generally decreases farther into the future. The placement of the unconstrained pool targets can change at any time. Each week as the LTS is revised, non-pool targets may also be reassigned for a variety of reasons including multi-telescope coordination. Observations may be bumped or not completed because of high radiation or targets-of-opportunity (TOOs).

Both the LTS and the STS (Short Term Schedule) web pages show sequence numbers for every observation that are hyper-linked to descriptive target pages. The STS is available on-line at http://cxc.harvard.edu/target_lists/stscheds/index.html. Each target page further contains a link to a plot that displays the roll, pitch, and visibility for the target for the duration of the Cycle. The target page also contains links to images of the appropriate Chandra instrument superposed at the correct roll on 2 deg images of the sky available from *NASA* SkyView. Any time an observation is reassigned to a new weekly bin or scheduled precisely within a week in a short-term schedule, a revised set of images is posted.

The LTS takes into account the intrinsic target visibility (based primarily on minimum Sun, Earth and Moon angles; see Section 3.3.2), additional target constraints approved by the Peer Review, and thermal limitations of the spacecraft. These additional constraints are described in Chapter 3. While user-imposed constraints can significantly enhance the science return of an observation, proposers should be aware that limitations are imposed on the number of constrained observations that may be accepted at Peer Review (see the *CfP*). Additionally, all constraints effectively translate into time constraints that may affect the number of weekly bins available for scheduling the observation. Weekly schedules are interrupted unpredictably by the space radiation environment or TOO observations. This inevitably means that the next opportunity to meet all the observing constraints can be significantly delayed if those constraints are stringent.

2.7.2 Selecting Candidates for Short-Term Scheduling

Each week, the Mission Planning and Flight Operations Teams construct an Observation Request (OR) list. The list is composed of a combination of LTS and pool targets chosen to meet both the science requirements of the observations and the constraints of the observatory. The OR is a "short list" of targets that *can* be scheduled: not all of them will be scheduled. Well before construction of the OR list, all observing parameters must be finalized. An overview of the process follows.

- the observer is contacted before the cycle begins to confirm that observation parameters most critical to mission planning (such as coordinates and constraints) are correct.
- the target is placed in the LTS or in the pool list
- the observer verifies correctness of all observing parameters after a second contact from the *CXC*.
- the target is made available for scheduling
- the target appears in an OR list as a candidate for short-term scheduling

- the target is either scheduled for a specific time that week, returned to be placed in a later week during the revision of the LTS or returned to the list of pool targets.
- the target is observed in the scheduled week or bumped to a later week

Some targets may be assigned to several OR lists before they are finally scheduled. Observers are contacted by *CXC* personnel if their targets appear in an approved schedule and then subsequently not observed, due, for example, to a radiation shutdown or a TOO.

2.7.3 The Short Term Scheduling Process

Mission Planning assigns priorities in the OR list to emphasize constrained observations; otherwise they would rarely be scheduled for observation since they tend to have a negative impact on the observing efficiency. Whenever possible the ORs span a range of angles about the satellite-Sun line to prevent excess accumulation of momentum. In consultation with the Science Mission Planning Team, the Flight Operations Team (FOT) constructs detailed short-term schedules and command loads for the spacecraft that combine science observations with engineering activities. Along with observing efficiency, thermal, power, momentum, and pointing constraints are all factored in, as well as minimization of maneuver error and optimal guide star acquisition. Several iterations of optimization and safety checks are not uncommon for each weekly schedule before its approval by all teams concerned (FOT and Mission Planning, Mechanisms, Command Management, ACIS, HRC, Pointing Control and Aspect, Flight Director). Once a final schedule is approved, the *CXC* updates the LTS pool list and *ObsCat* accordingly.

The *CXC* currently starts to prepare short-term schedules 3 weeks in advance. Thus at any given time there are 3 weekly schedules in various stages of preparation. Changes in any of these require a rebuild which is very labor intensive. Fast-response TOOs are currently the only allowed changes. Even small changes to a schedule typically require 24-48 hour turnaround. During nominal Mission Planning, the final STS is approved and ready for upload by the Wednesday or Thursday before the STS commands begin executing Sunday night or Monday morning (GMT). Hence, given the nominal planning cycle, fast ($<$ 1 week) turn-around TOOs can most efficiently be incorporated into the short term schedule if they are submitted to the *CXC* by mid-week. Such submission/notification will reduce the amount of disruption, allow time to meet constraints and preferences for other targets, and optimize the chances that all the observing requirements for the TOO can be met.

Chapter 3

Offset Pointing, Visibility, and other Constraints

3.1 Introduction

This chapter gathers together several topics pertaining to observation planning, irrespective of focal-plane instrument and grating configuration, to serve as additional guidelines for preparing proposals. Most of these topics are automatically addressed by the target visibility interface webtool (*ProVis*) or the observation visualizer software (*ObsVis*) available as part of CIAO. The intention here is to familiarize the user with the considerations.

3.2 Offset Pointing

The offset pointing convention for *Chandra* is that a negative offset of a coordinate moves the image to more positive values of the coordinate and vice-versa. Examples of offset pointings of the ACIS instrument are shown in Figure 3.1. Examples using the HRC are shown in Figure 3.2.

3.3 Visibility

There are a number of factors that limit when observations can be performed. These are discussed in the following subsections.

3.3.1 Radiation Belt Passages

High particle-radiation levels are encountered as the Observatory approaches perigee. Data acquisition ceases whenever certain particle-radiation thresholds are exceeded. A working number for the altitude at which this takes place is about 60,000 km. Cessation of observations and protection of the instruments in regions of high radiation results in approximately 20% of the 63.5 hour *Chandra* orbit being unusable.

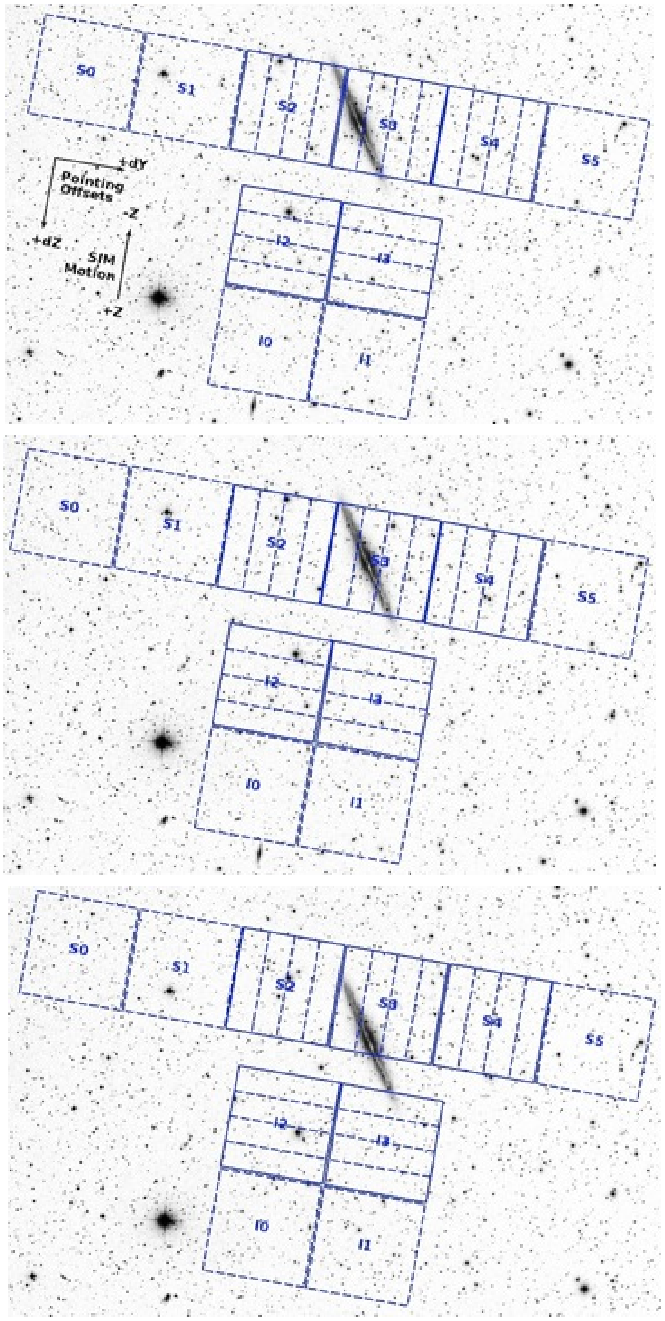

Figure 3.1: Image created with ObsVis shows the ACIS field of view overlaid on the optical image field of the galaxy NGC 891. North is up and East is to the left. Roll is measured positive, West of North. The roll angle shown is 10°. Five chips are turned on (solid outlines, with dashed node boundaries shown) and five off (dashed chip outlines). Top Panel: Target is centered at the nominal ACIS-S aimpoint. Offset (Y,Z) coordinate system is also shown, refer to Figure 6.1 Middle Panel: The target has been offset 90 arcsec in the negative Y direction: (Y,Z) offset of (-1.5, 0) in arcmin. In the Bottom Panel the offset is (-1.5, -3) in arcmin

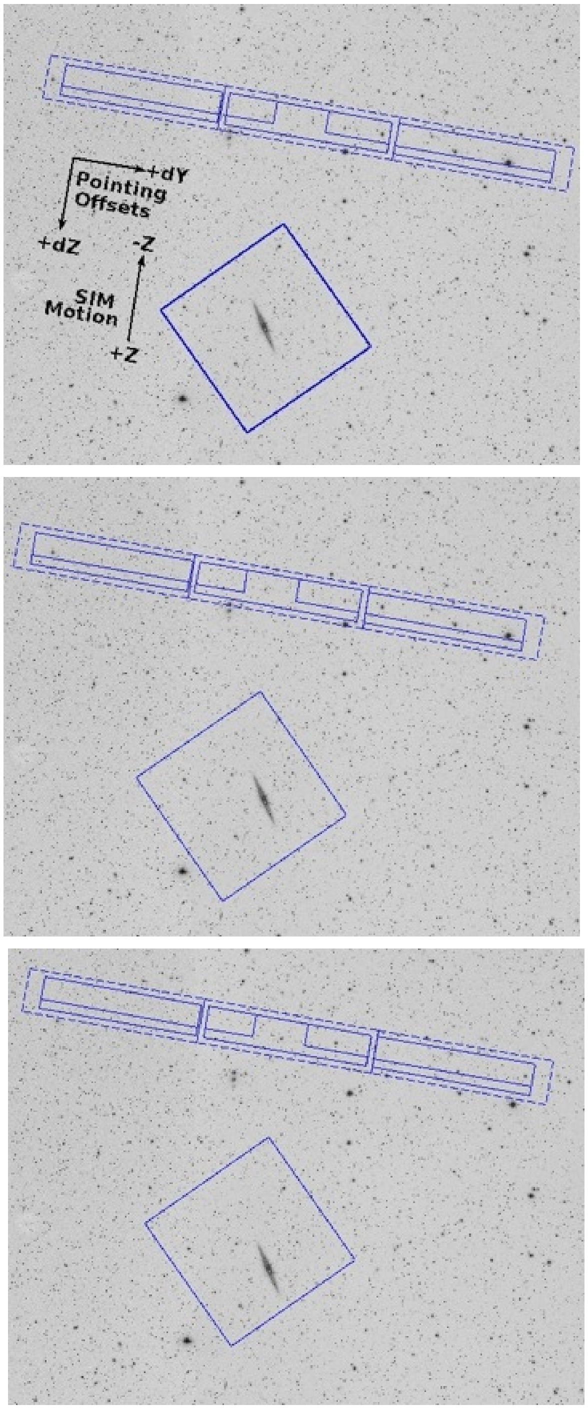

Figure 3.2: Example of offset pointing with HRC, overlaid on a DSS-I R-band optical image. North is up and East is to the left. Roll is measured positive, West of North. The roll angle shown is 10°. Top Panel: The target, the edge-on galaxy NGC 891, is at the nominal HRC-I aimpoint. Offset (Y,Z) coordinate system is also shown, refer to Figure 6.1. Center Panel: The target is offset with (Y,Z) offset of (-5,0) arcmin. Bottom Panel: The offset is (-5,-5). Note the small dot at the location of the HRC-I aimpoint.

3.3.2 Avoidances

The following constraints are necessary to ensure the health and safety of the spacecraft and science instruments. Proposals which violate these constraints may be rejected.

1. Sun avoidance – cannot be overridden – viewing is restricted to angles larger than 46 degrees from the limb of the Sun. This restriction makes about 15% of the sky inaccessible on any given date, but no part of the sky is ever inaccessible for more than 3 months.

2. Moon avoidance – viewing is restricted to angles larger than 6 degrees from the limb of the Moon. This restriction makes less than 1% of the sky inaccessible at any time. This avoidance can be waived, but at the price of a reduced-accuracy aspect solution (see Chapter 5).

3. Bright Earth avoidance – viewing is restricted to angles larger than 10 degrees from the limb of the bright Earth. This restriction makes less than 5% of the sky inaccessible at any time, but there are certain regions which can only be viewed, continuously, for up to about 30 ks. The avoidance can be waived, but at the price of a reduced-accuracy aspect solution (see Chapter 5). Figure 3.3 illustrates the point that the Earth avoidance region is nearly stationary. This is a consequence of the combination of high elliptical orbit and radiation belt passages. This partially blocked region moves several degrees per year, reflecting the evolution of the orbital elements.

   The greatest amount of observing time is available in the vicinity of apogee, when the satellite moves most slowly and the Earth and its avoidance zone occupy an approximately stationary location on the sky, visible in Figure 3.3 as the extension to the south of the sun avoidance band.

4. Roll angles – the spacecraft and instruments were designed to take advantage of the Observatory having a hot and a cold side. Thus, the spacecraft is preferentially oriented with the Sun on the $-Z$ side of the $X - Y$ plane, where $+X$ is in the viewing direction, the Y-axis is parallel to the solar panel axes, and $+Z$ is in the direction of the ACIS radiator (see Figure 1.1). In this orientation there is only one "roll angle" (rotation about the viewing- or X-axis - positive West of North) for which the solar panels can be rotated so that they are directly viewing the sun - the nominal roll angle. Small deviations ($\sim$degrees) from the nominal roll angle may be allowed depending on the viewing geometry. The roll-angle constraint imposes further visibility restrictions. These can also be evaluated with the *ProVis* tool.

3.3.3 Pitch Angle Constraints

Gradual changes in the thermal properties of the spacecraft with time require us to impose restrictions in the durations of observations at various solar pitch angles (i.e., angles

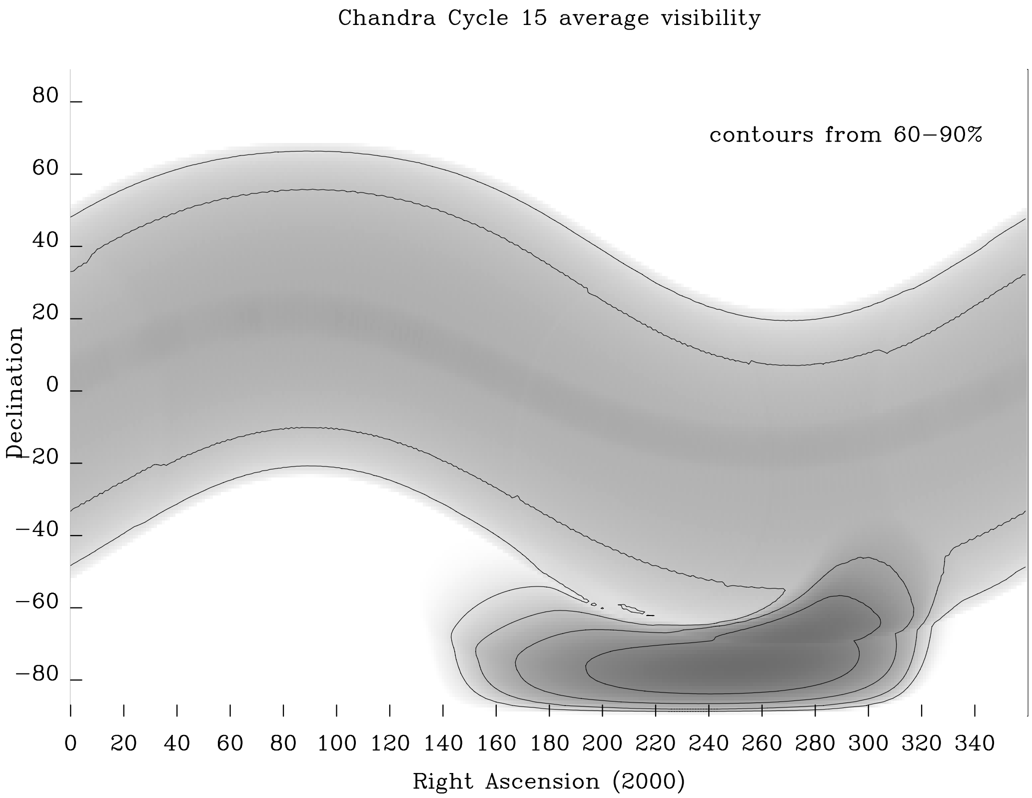

Figure 3.3: The *Chandra* visibility showing contours of fractional visibility averaged over the 12-month interval of Cycle 15. The darker the shade of gray, the lower the visibility. The five contour levels correspond to 50%, 60%, 70%, 80%, and 90% average visibility.

between viewing directions and the direction to the Sun). These restrictions are evolving with time; observers are urged to consult Announcements on the CXC Proposers webpages for updates (http://cxc.harvard.edu/proposer/). The principal pitch restrictions are of several kinds:

1. The Electron Proton Helium Instrument (EPHIN, Section 2.5) detector, used in safing the science instruments from high levels of particle radiation, suffers degraded performance at elevated temperatures. During extended observations at pitch angles of between approximately 65 and 135 degrees the EPHIN, which also acts as a proxy for the temperatures of other spacecraft components affected by -Z side solar heating, can reach temperatures that may result in anomalous performance. Exact performance depends on the near term thermal history. The *CXC* has developed a model to predict EPHIN temperature as a function of time and pitch angle to aid in Mission Planning.

2. Solar pitch angles greater than 170 degrees are not accessible. This is necessary to prevent excessive cooling of the propellant lines, which might then rupture. We urge that you carefully consider how to configure your observation so that it does not require a pitch angle greater than 170 degrees. This may be done, for example, by imposing no constraints on the observation, or by using the *Chandra* Pitch Roll and Visibility tool (*ProVis*) at http://cxc.harvard.edu/soft/provis/ to see if your time or roll constraint can be achieved within the allowable pitch angles, i.e. between 46 and 170 degrees. (Even this must be tempered by consideration of other pitch-angle constraints discussed in this section.) It is possible that a peer-review accepted proposal may, in fact, not be accomplished because of these safety constraints. To avoid this possibility, observers are urged to plan their observations carefully using all the proposal preparation tools and contacting the CXC HelpDesk if necessary.

3. There are observing restrictions in the pitch angle range 156-170 degrees imposed by the need to prevent propellant lines from dipping to low temperatures before line heaters switch on.

4. Owing to the changing thermal environment, the ACIS Power Supply and Mechanism Controller (PSMC) Detector Electronics Assembly (DEA) has been warming and is expected to continue doing so. The temperature is affected by both the solar pitch angle and by the number of ACIS chips in use. As a result, allowable durations for 6-chip ACIS observations at solar pitch angles of less than about 60 degrees will be limited. ACIS observers are being asked to specify optional chips and the priority order in which these may be turned off; this information will be used as needed during the mission planning process to control ACIS temperatures (see Section 6.20.1). Observers are encouraged to avoid specifying ACIS observations that require 5 or 6 chips and that must also be executed at solar pitch angle below about 60 degrees.

5. The Integral Propulsion System (see Section 2.2) tank pressure and temperature approach potentially unsafe levels as a result of accumulated dwell in bi-modal pitch

regions (45-70 degrees and to a lesser extent 110-130 degrees). The time constants are long, and the associated restrictions affect principally the development of the long-term schedule (see Section 2.7.1).

6. The ACIS electronics can heat to unsafe temperatures during long dwells at high solar pitch angles, resulting in limitations on observations at 130-170 degrees. These limitations depend to some extent on the number of ACIS chips in use.

These spacecraft constraints have several implications for proposers:

- Observations can be performed over the full range of accessible solar pitch angles (46 to 170 deg), but if they are too long for the particular observing conditions they will be broken into shorter durations, which may be separated by a day or more. The maximum continuous duration depends on the target pitch and thermal history of the spacecraft. It can be estimated from the figure given on the MAXEXPO web page (http://cxc.harvard.edu/proposer/maxexpo.html). Observations with roll constraints must either be of appropriately limited duration or the roll constraints must be generous enough to allow multiple segments at their different, time-dependent, roll angles. Constraining roll angles to be constant for multiple segments may cause planning difficulties, as achieving off-nominal roll angles can only be done for a limited range of off-nominal roll angles around the nominal value (accessible from ProVis).
- Simultaneous longer-duration observations with telescopes that have a limited range of accessible pitch angles (such as XMM: approximately 70-110 degrees) may be very difficult, or even impossible, to schedule.
- Targets near the ecliptic poles (such as the Magellanic Clouds) are especially affected by these considerations since their pitch angles are always close to 90 degrees.

3.4 Other Constraints and Considerations

The instrument constraints are discussed in the chapters devoted specifically to the instruments. User-imposed constraints are discussed in the instructions for completing the *Chandra* Remote Proposal Submission (RPS) form. We summarize these here.

3.4.1 Instrument Constraints and Considerations

For details on the following limitations, please refer to Chapters 6 (for ACIS) and 7 (for HRC).

- The HRC has a brightness limit which limits the flux per microchannel plate pore.
- The HRC has a telemetry limit. Exceeding this limit, amongst other consequences, reduces observing efficiency.

- The HRC has linearity limits. Exceeding these limits voids the effective area calibrations.
- The ACIS has a telemetry limit. Exceeding this limit, amongst other consequences, reduces observing efficiency.
- The ACIS is subject to the effects of pulse pileup. Dealing with this effect requires careful planning of the observation.
- The ACIS has a limit for the total amount of allowed flux in a pixel during an observation. The limit only impacts a small number of potential observations, primarily those of very bright sources that request the dither to be turned off. Please see Section 6.18.

3.4.2 User-Imposed Constraints

Chandra users may need to specify a number of observing constraints particular to their observations. In general, the specification of a user-imposed constraint decreases the efficiency of the observatory and therefore should be well justified in the proposal. Note that only a limited number of constrained observations can be accommodated (see the *CfP* for details). User imposed constraints are summarized here.

Time Constraints:

Time Windows – specific time intervals in which an observation must be scheduled. Such constraints are primarily for use in coordinated observing campaigns or for arranging an observation to coincide with some time-critical aspect of the target.

Monitoring Intervals – for observing a target repeatedly, with intervals and durations specified.

Phase Interval – specific phase intervals for observing sources with long, regular periods.

Coordinated Observations – targets specified to be observed by Chandra and another observatory within a given time period.

Continuity of observation – specifying that an observation be performed in a single (or the fewest possible) segment(s).

Group Observation – a target which needs to be observed within a particular time range with other targets in the program.

Roll Constraints: – specifying a particular roll angle and tolerance.

Chapter 4

High Resolution Mirror Assembly (HRMA)

4.1 Introduction

The *Chandra* X-ray telescope consists of 4 pairs of concentric thin-walled, grazing-incidence Wolter Type-I mirrors called the High Resolution Mirror Assembly (HRMA) [X-ray optics are reviewed by B. Aschenbach (1985)]. The front mirror of each pair is a paraboloid (P_n) and the back a hyperboloid (H_n). The eight mirrors were fabricated from Zerodur glass, polished, and coated with iridium on a binding layer of chromium.

4.1.1 Description and Physical Configuration

The HRMA, shown schematically in Figure 4.1, contains the nested mirrors, center, forward and aft aperture plates, baffles, inner and outer cylinders, mounts, pre- and post-collimators, fiducial light transfer components, mirror support sleeves, forward and aft contamination covers, flux contamination monitors, and thermal control hardware. The outer mirror pair is number 1, and, progressing inwards, 3, 4, and 6. The original design had six mirror pairs; numbers 2 and 5 were eliminated. The pair diameters range from about 0.65 to 1.23 meters. The distance from the center of the Central Aperture Plate (CAP) separating the paraboloid and hyperboloid mirrors to the HRMA focus is 10.0548 meters, with each mirror pair varying slightly about this value. Note that this distance is close to, but not exactly, the focal length. An annular on-axis beam enters each mirror pair, is reflected from paraboloids and hyperboloids and exits to converge to a focus. The angle θ between the direction of the reflected ray and the optical axis lies between two cone angles θ_c and θ_d. These and other important HRMA characteristics are listed in Table 4.1.

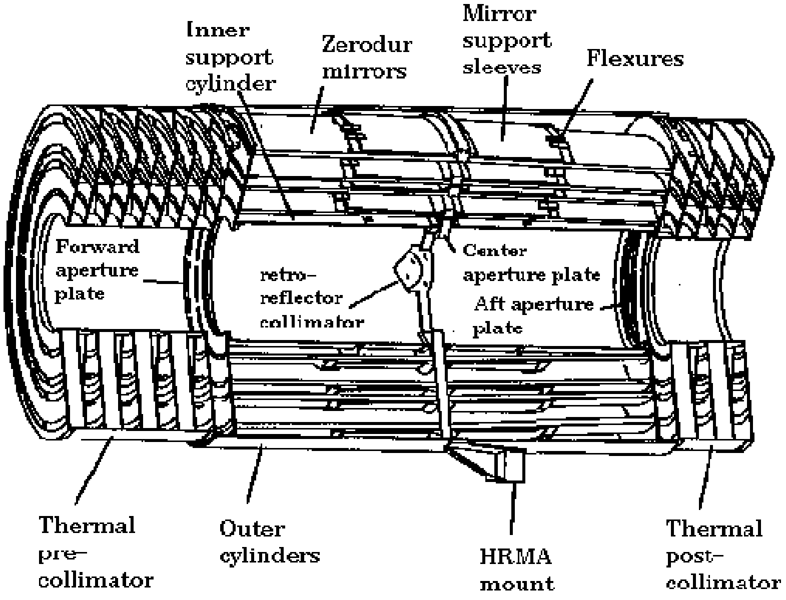

Figure 4.1: The four nested HRMA mirror pairs and associated structures.

Table 4.1: *Chandra* HRMA Characteristics

Optics	Wolter Type-I
Mirror coating	Iridium (330 Å, nominal)
Mirror outer diameters (1, 3, 4, 6)	1.23, 0.99, 0.87, 0.65 m
Mirror lengths (P_n or H_n)	84 cm
Total length (pre- to post-collimator)	276 cm
Unobscured clear aperture	1145 cm^2
Mass	1484 kg
Focal length	10.070 ± 0.003 m
Plate scale	$48.82 \pm 0.02\,\mu$m arcsec^{-1}
Exit cone angles from each hyperboloid:	
θ_c (1, 3, 4, 6)	3.42°, 2.75°, 2.42°, 1.80°
θ_d (1, 3, 4, 6)	3.50°, 2.82°, 2.49°, 1.90°
f-ratios (1, 3, 4, 6)	8.4, 10.4, 11.8, 15.7
PSF FWHM (with detector)	$< 0.5''$
Effective area:	@ 0.25 keV 800 cm^2
	@ 5.0 keV 400 cm^2
	@ 8.0 keV 100 cm^2
Ghost-free field of view	$30'$ diameter

4.1.2 Sub-assembly Calibration

Extensive measurements of the mirror shapes and of the surface characteristics were made at Hughes-Danbury Optical Systems (HDOS) during fabrication of the mirror segments and during assembly at Eastman-Kodak Co. HRMA throughput depends critically on the coating of the individual mirror elements carried out at Optical Coating Laboratory, Santa Rosa, California. Mirror flats were present in the coating chamber and coated with iridium at the same time as the HRMA mirror elements. Reflectivity of X-rays from these witness flats was measured with the X-ray beam from the synchrotron at the Brookhaven National Laboratory [Graessle, D. E., et al., 1998, 2004].

4.1.3 Operating Environment

Insulation and heaters maintain the HRMA temperature at 70°F (21°C) on-orbit to minimize changes from the assembly, alignment environments, and to minimize molecular contamination.

4.1.4 Heritage

The *Chandra* mirrors represent a logical progression from those of the *Einstein* (HEAO-2) [Giacconi et al. 1979] and *Rosat* [Trümper 1983; Aschenbach 1991] missions. Each of these previous X-ray observatories utilized nested Wolter Type-I optics with about 4 arcsec angular resolution. The *Einstein* mirror assembly had considerably less geometric area than *Chandra*, while *Rosat* had comparable area ($1100\,\mathrm{cm}^2$) at low energies ($< 1\,\mathrm{keV}$).

To verify the technology required for the spatial resolution of *Chandra*, a Validation Engineering Test Article-I (VETA-I) was constructed and tested in 1991. VETA-I contained the P_1H_1 proto-flight mirror shells constructed to final tolerances, but uncoated and with ends uncut. The VETA-I tests included the image full-width-half-maximum, encircled energy, effective area, and ring focus properties (for azimuthal and low spatial-frequency figure). Many of the results of these tests appear in SPIE Proceedings 1742. A good overview of the VETA tests is given by Zhao et al. 1994, in SPIE Proceedings 2011.

4.2 Calibration and Performance

4.2.1 Calibration and Model

Before launch, the HRMA underwent extensive ground calibration tests at the X-Ray Calibration Facility (XRCF) at Marshall Space Flight Center (MSFC), Huntsville, AL, from September 1996 through May 1997. The full HRMA XRCF Calibration Report is accessible at http://cxc.harvard.edu/cal/Hrma/XRCFReport.html. During these tests, the mirror assembly was mounted horizontally in a vacuum chamber and irradiated with X-rays from various electron-impact sources located at a distance of 524.7 meters. The data taken at the XRCF include the effective area and image distributions as a function of incident energy and angle. The mirror performance during these tests differs from that expected in space because of gravity distortions and the finite source size and distance; consequently, the calibration data cannot be directly compared to flight observations. The approach taken was to develop a model based upon surface and assembly measurements taken before the X-ray calibration activity. The X-ray calibration data then were used to validate this model and to make minor adjustments in model parameters to achieve satisfactory agreement with the observations. Further minor modifications were made as a result of flight experience. A series of papers in SPIE Proceedings 3113 report the results of the HRMA ground calibration.

The HRMA characteristics illustrated in this chapter were generated by a ray trace program using this model. Note that this chapter typically gives characteristics of the HRMA only; unless otherwise indicated, blurring caused by the detector and the aspect solution is *not* included. These effects are *very* important for on-axis sources, and are included in the instrument chapters (Chapters 6 and 7). See also Section 4.4.

4.2.2 HRMA Effective Area

The unobscured geometric aperture of the HRMA is 1145 cm^2. The obstruction of the HRMA aperture by supporting struts is less than 10%. Since reflectivity of the mirror optics depends on photon energy as well as grazing angle, the HRMA throughput varies with X-ray energy.

The HRMA effective area is derived from the the predictions of the ray trace code discussed above along with empirical corrections based on the XRCF ground-based calibration data. The initial XRCF correction (i.e., the correction used to calculate the HRMA effective area prior to CALDB 4.1.1) was derived assuming that there was no molecular contamination on the mirrors. Subsequent in-flight gratings observations of blazars showed a discontinuity in the spectrum near the Ir-M edges when reduced with the contaminant free model; this suggests that there may be molecular contamination on the mirrors on-orbit (see Figure 4.2). Using these data and ray trace simulations, it was estimated that a 22Å layer of hydrocarbon could be present on the mirror optics. An updated HRMA effective area was released in CALDB 3.2.1 on Dec. 15, 2005 based on the predictions of the ray trace code with a uniform 22Å layer of hydrocarbon molecular contamination on all 8 pieces of optics on-orbit.

Subsequently, inconsistencies in the measure of cluster temperatures derived by two different methods (line and continuum measures) led to a re-analysis of the data taken at the XRCF. This reanalysis provided evidence that molecular contamination was already present on the mirrors at XRCF. Thus, since the initial, ad-hoc, empirical correction of the HRMA model had already corrected for most of the effects of the molecular contamination, the addition of another 22Å of contamination in the ray trace model post-launch (CALDB 3.2.1) was an over-correction.

During XRCF testing, a system of shutters was placed behind the HRMA so that the effective area of the 4 shells could be measured independently. These tests were essential since the gratings intercept X-rays from different shells. Two focal plane instruments were

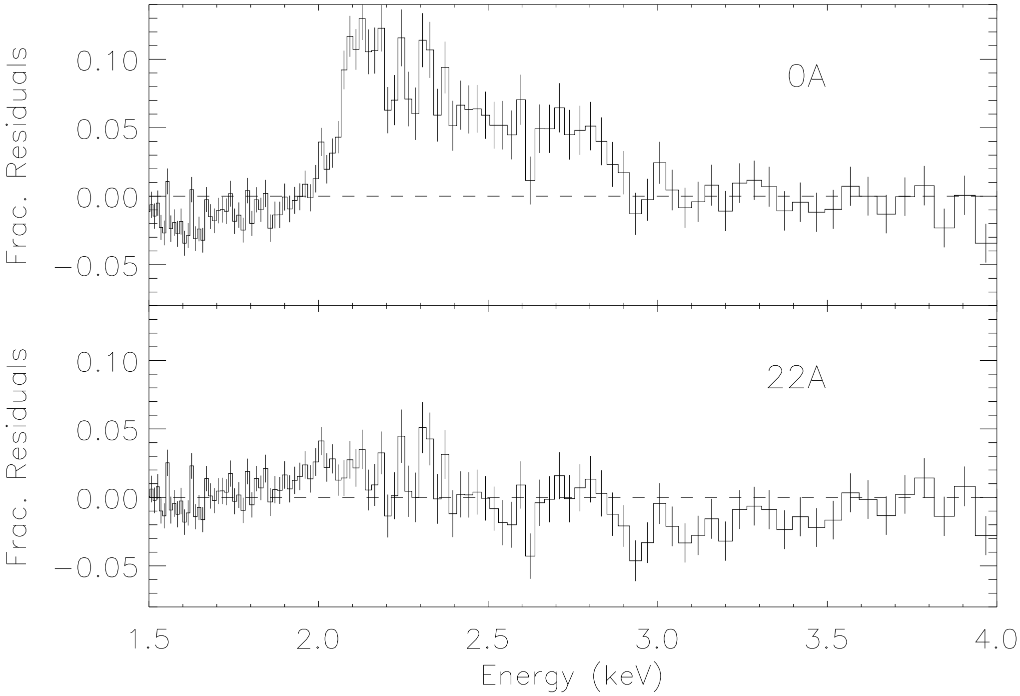

Figure 4.2: Combined residuals from power-law fits to 18 blazar observations (Marshall, H.L., 2005). The residuals in the upper panel are based upon models of contaminant free optics, while those in the lower are based upon a model of the mirror surfaces which includes a thin (22Å) hydrocarbon layer.

used during XRCF: 1) a flow proportional counter (FPC) and 2) a solid state detector (SSD). Both of these instruments were non-imaging detectors and were used in conjunction with a number of different pin hole apertures. Using the data obtained from each mirror pair, the thicknesses of the contaminant on shells 1, 3, 4 and 6 were determined to be 28, 18, 20 and 27Å respectively. Thus a new version of the HRMA effective area (CALDB 4.1.1) was released in January 2009, based on the predictions of the ray trace code with the, as-measured, contamination depths on each shell. In addition, an energy independent correction is applied to the predictions of the ray trace code for each shell to determine the absolute effective area. The correction factor for each shell is calculated by averaging the averaged FPC line data to ray trace ratio and the averaged SSD continuum data to ray trace ratio. Note that, while a gray (i.e. energy-independent) correction is applied to each shell, the overall empirical correction for the full HRMA absolute effective area is not energy-independent, since different shells contribute a different fraction of the total effective area at different energies (see Figure 4.3). This figure reflects an even more refined analysis of the XRCF data than what was used in calculating the HRMA effective area in the CALDB 4.1.1 release. The new analysis results in a slightly lower effective area but is still consistent with the CALDB 4.1.1 data within errors.

Several HRMA effective area models have been generated with different methods for calculating the gray corrections for each shell (e.g., no gray correction or gray corrections with unequal weighting between the FPC and SSD data) to determine the systematic effect of the gray corrections on the gas temperatures derived from ACIS observations of clusters of galaxies. For cool clusters (kT < 4 keV), the derived gas temperatures are essentially independent of the method used to calculate the gray correction. For hotter clusters, the derived temperatures vary by $\pm$ 2% depending on the algorithm used.

The combined HRMA/ACIS and HRMA/HRC effective areas released in CALDB 4.1.1 are shown in Figure 4.4 and the effect of off-axis vignetting on the HRMA effective area is shown in Figure 4.5 at several different photon energies. Note that this change in the effective area also serves to bring Chandra and XMM-Newton continuum measurements of cluster temperatures into closer agreement.

4.2.3 Point-Spread-Function and Encircled Energy Fraction

The *Chandra* HRMA point-spread function (PSF) has been simulated with numerical ray trace calculations based upon the mirror model previously discussed. A most useful parameter is the encircled energy fraction (the two-dimensional integral of the PSF) as a function of radius from the image center. The PSF and the encircled energy fraction for a given radius depend upon off-axis angle and energy. The HRMA optical axis is defined for practical purposes, and calibrated in flight, as the direction of the sharpest PSF. The PSF broadens, and the encircled energy fraction decreases, as (1) the off-axis angle increases because of mirror aberrations; and (2) the X-ray energy increases because of increased X-ray scattering.

On-axis PSF

Figure 4.6 shows the encircled energy fraction as a function of image radius for an on-axis point source and for different energies. The resulting increase in image size with energy is apparent. Figure 4.7 shows the radii of selected encircled energy fractions as functions of energy for an on-axis point source. Table 4.2 lists the encircled energy fraction contained within one and ten arc seconds diameters for an on-axis point source at different energies.

Pre-flight measurements and images taken at the XRCF show that there is a slight ($\approx 500\mu$m) offset between the optical axes of the paraboloids and hyperboloids, and that pair 6 is slightly tilted with respect to the other three. Consequently, the image from mirror pair 6 is not as symmetrical as the images produced by the other shells. The effect of this asymmetry on images depends on energy because of the different relative contribution of mirror pair 6.

Figure 4.8 shows simulated HRMA/HRC-I images at several energies. The effect of the mirror pair 6 alignment errors can be seen in the higher energy images as then mirror pair 6 becomes the dominant contributor to the total effective area. Note the movement of position of the core as well as the asymmetric flaring. The $\sim 0.2''$ core motion is comparable

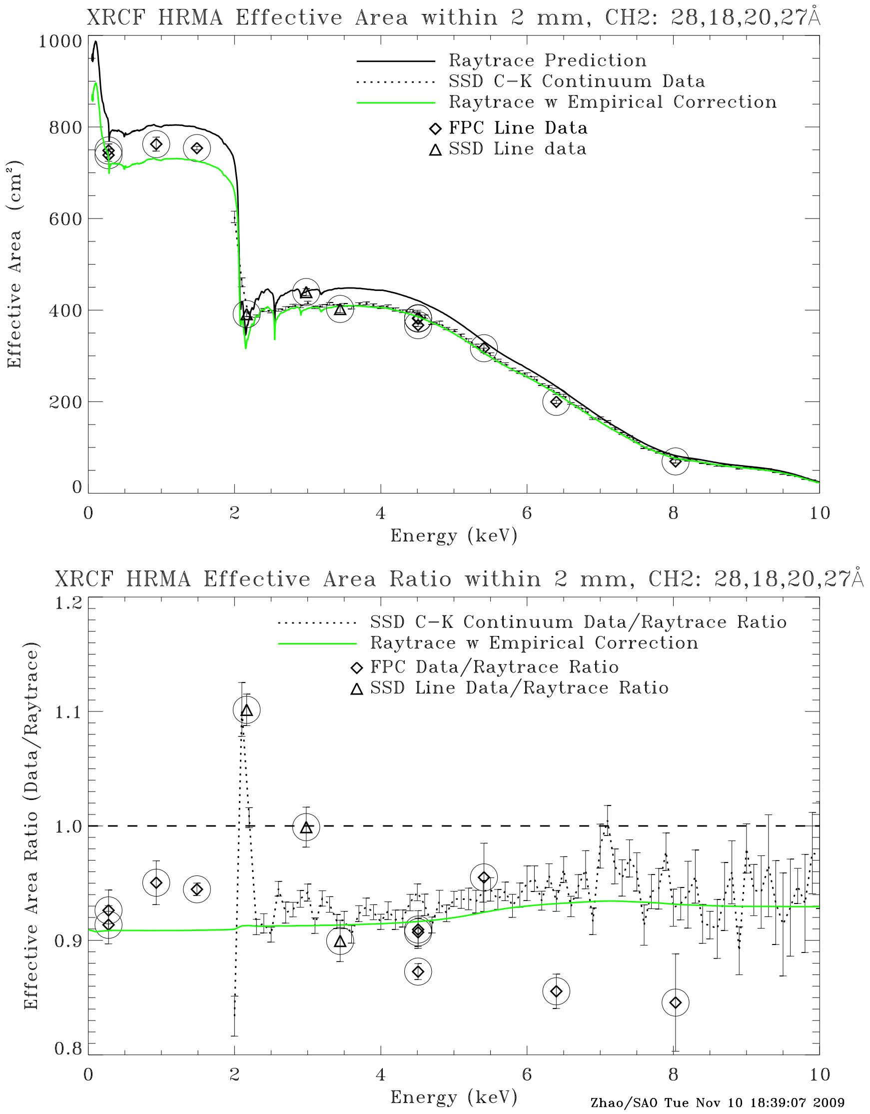

Figure 4.3: The HRMA Effective area: The top panel shows the ray trace prediction and the XRCF measurement data of the HRMA effective area as a function of energy. The bottom panel shows the ratio of the XRCF data to the ray trace. The ray trace includes the effects of molecular (CH2) contamination with variable thickness on the mirrors. The dotted line with error bars are the C-K continuum data, taken simultaneously with a solid state detector (SSD). Data obtained from spectral line sources with a flow proportional counter (FPC) are shown as diamonds; those obtained with a solid state detector (SSD) are shown as triangles. All the line measurements are circled for clarity. The solid (green) line in the bottom panel shows the XRCF empirical correction to the ray trace based on the XRCF data. The solid (green) line in the upper panel shows the absolute HRMA effective area with the XRCF empirical correction. [Note that the color is viewable only in the electronic version.]

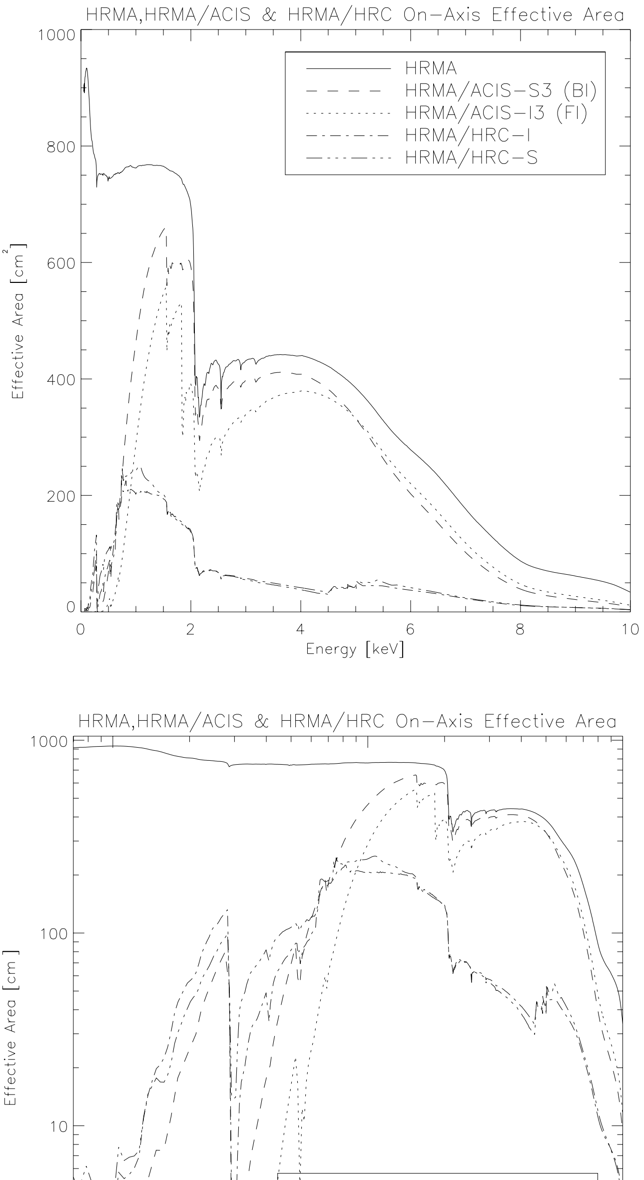

Figure 4.4: The HRMA/ACIS and HRMA/HRC effective areas versus X-ray energy in linear-linear (top) and log-log (bottom) scales. The structure near 2 keV is due to the iridium M-edge. The HRMA effective area is calculated by the ray trace simulation based on the HRMA model and scaled by the XRCF calibration data. The HRMA/ACIS effective area is the product of the HRMA effective area and the Quantum Efficiency (QE) of ACIS-I3 (front illuminated) or ACIS-S3 (back illuminated). The HRMA/HRC effective area is the product of HRMA effective area and the QE of HRC-I or HRC-S at their aimpoints, including the effect of UV/Ion Shields (UVIS). [Note: the colored lines are viewable in the electronic version]

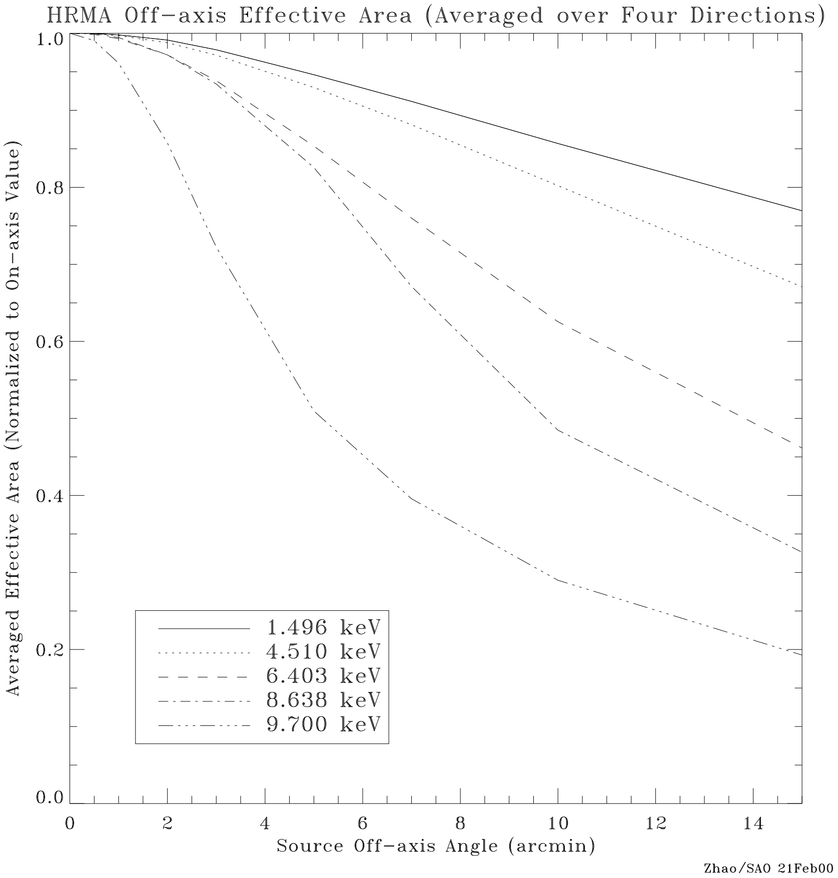

Figure 4.5: The HRMA effective area versus off-axis angle, averaged over four azimuthal directions, for selected energies, normalized to the on-axis area for that energy.

to other factors of image degradation encountered in flight, such as uncertainties in the aspect solution.

The HRMA PSF has a faint halo extending to large angles, resulting from X-rays scattering from micro-roughness on the mirror surfaces. This scattering is energy dependent; the spectrum of the scattered X-rays hardens significantly with increasing angle from the source. An empirical model was generated based on the ground calibration measurements; a number of systematic effects remain to be accounted for, and the uncertainties in the flux in the wings are probably at least 30-50%. This model is described more fully in http://cxc.harvard.edu/cal/Hrma/XRCF-Wings.html. A deep calibration observation of Her X-1 (obsid 3662) was obtained in order to improve the understanding of the PSF wings. The SIM was shifted to move the optical axis to $\sim 1'$ from the edge of the S3 detector furthest from the frame store; a Y-offset moved the image $\sim 1'$ into node 0 of the detector. The resulting pointing is $\sim 45''$ off-axis, effectively on-axis with regard to the mirror scattering properties. The analysis is discussed in more detail in

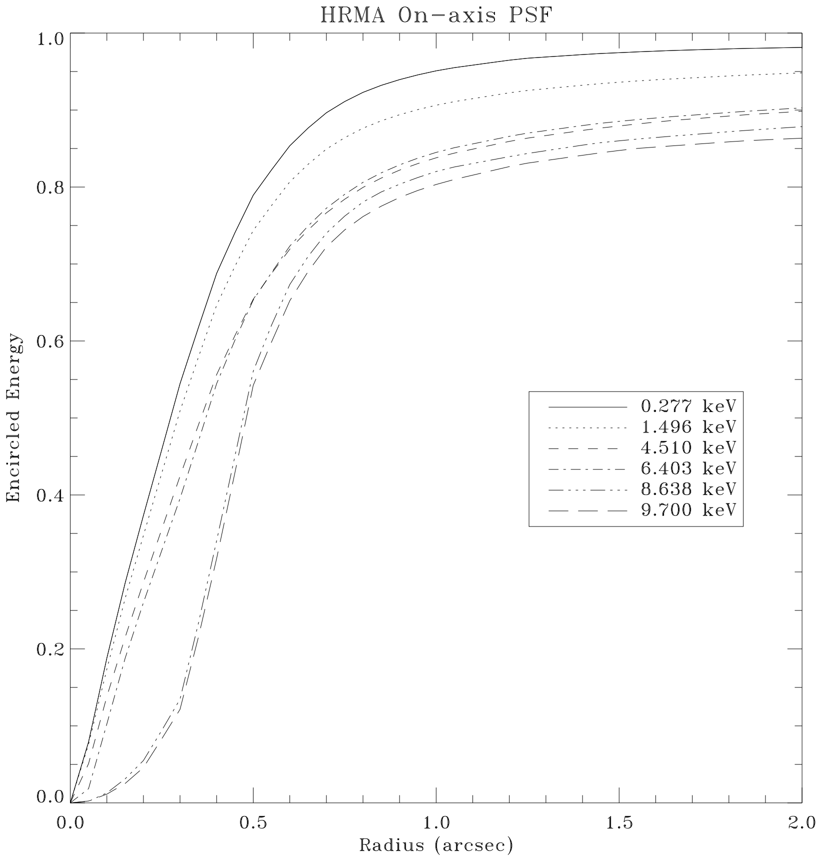

Figure 4.6: The Fractional encircled energy as a function of angular radius, calculated for an on-axis point source, at selected X-ray energies. The curves are the combined response and centered at the common focus of the full HRMA, i.e. four nested mirror pairs. For higher energies (8.638 keV and 9.700 keV), the curves are broadened at small radii. This is because the focus of higher energies does not coincide with the the HRMA common focus, but is offset by about $0.2''$, due to a slight tilt of the HRMA mirror pair 6.

http://cxc.harvard.edu/cal/Hrma/rsrc/Publish/Optics/PSFWings/wing_analysis_rev1b.pdf; see also http://cxc.harvard.edu/cal/Hrma/UsersGuide.html.

Radial profiles of the Her X-1 scattering wings are plotted for energy bands 1.0-2.0 keV and 3.0-4.0 keV in Fig. 4.9. These are surface brightness profiles normalized by the source count rate estimated from the transfer streak spectrum. The units of the normalized profiles are in arcsec^{-2}. A fit (power-law plus exponential cutoff) is overplotted, and the fit applies for $\theta > 15''$. Inside $15''$, the profiles are increasingly depressed because of the effects of pileup in this very bright source. The shape of the wing profile is well represented (beyond $15''$), but the overall normalization may be off up to a factor of two.

Because the mirror scattering is in part diffractive, the diffuse mirror scattering halo is energy dependent. Spectra extracted from the diffuse mirror scattering wings of the PSF

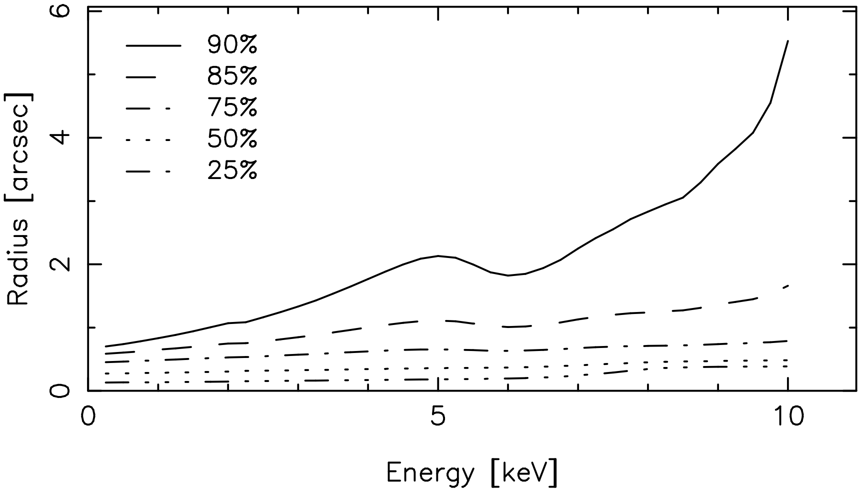

Figure 4.7: The radii of selected encircled energy fractions as functions of X-ray energy for an on-axis point source, calculated from the mirror model derived from ground-based calibration data.

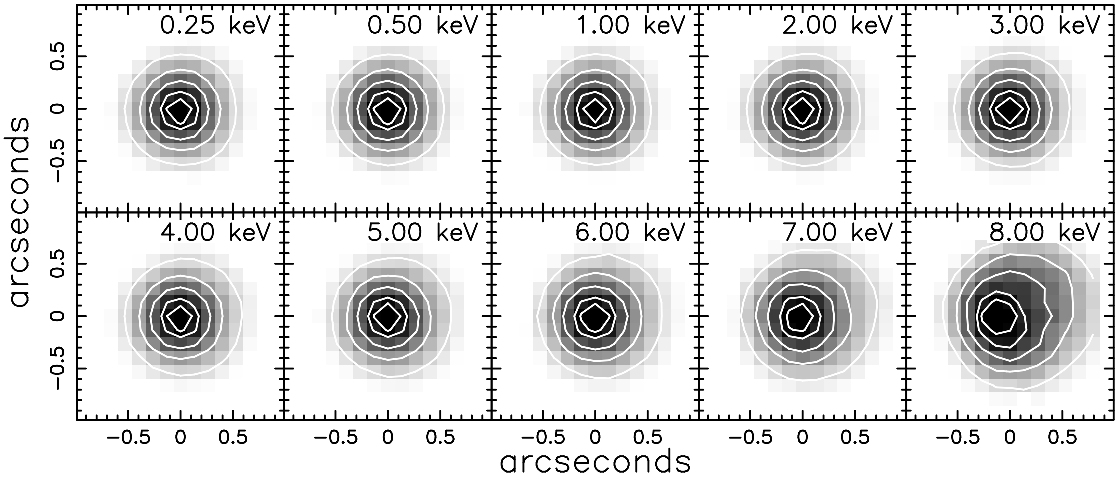

Figure 4.8: Simulated on-axis HRMA/HRC-I images of on-axis mono-energetic point sources with aspect blurring. The grayscale is a linear stretch; surface brightness contours are at 90%, 80%, 60%, 40%, and 20% of the peak brightness. The 8 keV image core is asymmetric and off-center due to the shell 6 misalignment.

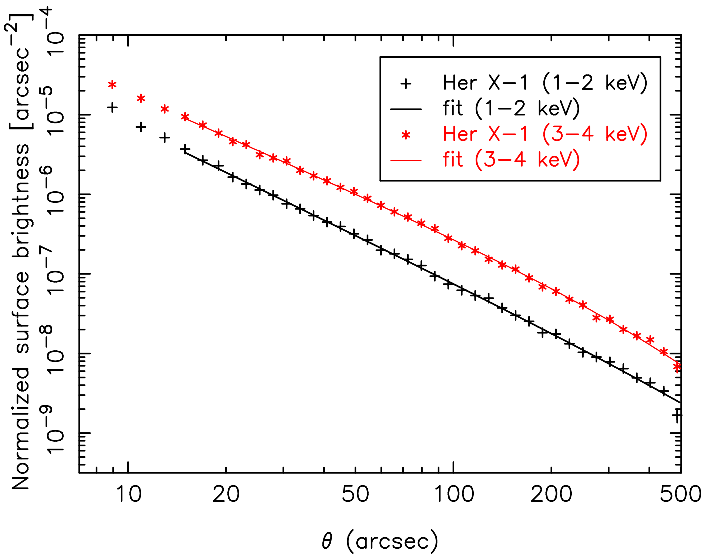

Figure 4.9: Normalized radial profiles (units arcsec^{-2}) of the Her X-1 scattering wings. The shapes are well determined beyond 15″, but the overall normalization may be uncertain by a factor of 2. The lower curve shows the 1.0-2.0 keV profile and the upper curve shows the 3.0-4.0 keV profile. In each case, the heavy solid line is a power-law plus exponential cutoff fit to the Her X-1 data. The overall normalizations are uncertain by up to a factor of two.

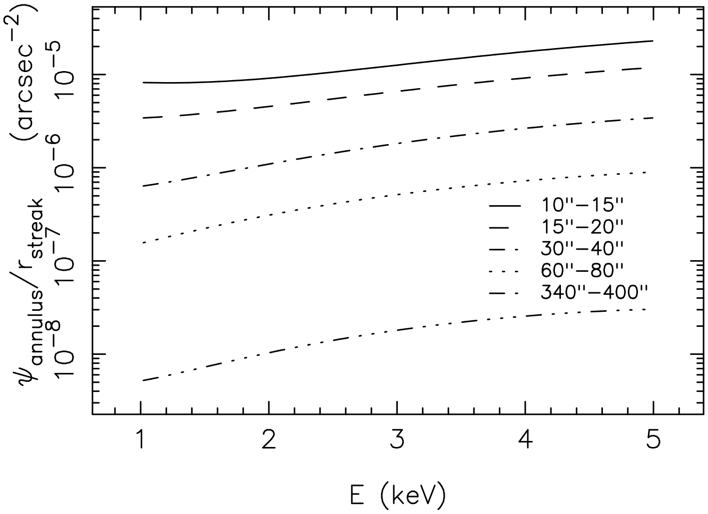

Figure 4.10: Hardening of the diffuse mirror scattering halo with distance from the direct image. The spectra for a number of annuli were normalized by the area of the extraction regions (taking into account chip edges) giving $\psi_{annulus}$ counts s^{-1} keV^{-1} arcsec^{-2}. These were each divided by a spectrum evaluated using the transfer streak events for the direct image, r_{streak} counts s^{-1} keV^{-1}. The legend indicates annular radii in arcsec.

Table 4.2: HRMA Encircled Energy Performance

X-ray:		Encircled Energy Fraction	
E	λ	Diameter	
keV	Å	$1''$	$10''$
0.1085	114.2712	0.7954	0.9979
0.1833	67.6401	0.7937	0.9955
0.2770	44.7597	0.7906	0.9929
0.5230	23.7064	0.7817	0.9871
0.9297	13.3359	0.7650	0.9780
1.4967	8.2838	0.7436	0.9739
2.0424	6.0706	0.7261	0.9674
2.9843	4.1545	0.6960	0.9560
3.4440	3.6000	0.6808	0.9479
4.5108	2.7486	0.6510	0.9319
5.4147	2.2898	0.6426	0.9300
6.4038	1.9361	0.6365	0.9344
8.0478	1.5406	0.5457	0.9185
8.6389	1.4352	0.5256	0.9151
10.0000	1.2398	0.4971	0.8954

are significantly modified from the spectrum of the incident source X-rays. Generally, the scattering halo spectrum becomes harder with increasing angle from the source. Fig. 4.10 shows the ratio of diffuse spectra extracted from annuli centered on the specular image of Her X-1 (normalized by extraction region area) to the corresponding spectrum extracted from the ACIS transfer streak for the source; the transfer streak spectrum is thought to be ∼4% piled up.

Off-axis PSF

The PSF broadens for off-axis sources, and there is considerable distortion in the image even if the HRMA were perfect. This distortion is due to the aberrations of Wolter type I optics and to the different focal surfaces (Figure 4.11) for the four mirror pairs. The increase in image size with off-axis angle is greatest for the inner shell, and hence is larger for higher X-ray energies.

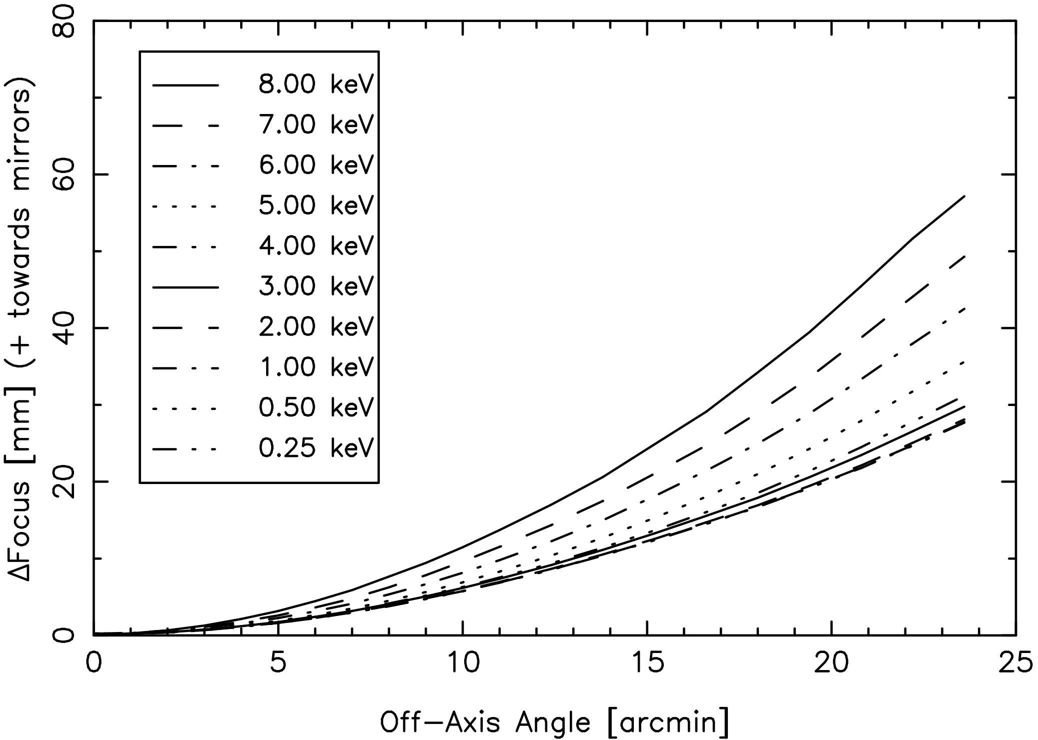

Figure 4.11: The HRMA focal surface (from simulations), indicating its dependence on energy and off-axis source position.

Figure 4.12 shows the dependence of encircled energy radii on off-axis angle on the HRC-I with the HRMA focus at the HRC-I aimpoint. Because the HRC-I is axially symmetric with respect to the HRMA optical axis, the off-axis encircled energy radii are almost azimuthally symmetric, except some small asymmetry due to the imperfect HRMA as mentioned above. The figure gives the averaged radii for 1.49 keV and 6.40 keV at 50% and 90% encircled energy. The blurs due to the HRC-I spatial resolution and the aspect solution, estimated to be FWHM: $0.22''$, are included.

The ACIS-I surface is not axially symmetric with respect to the HRMA optical axis, because the HRMA aimpoint is located near the inner corner of one of the four ACIS-I chips – I3. Thus the off-axis encircled energy radii are not azimuthally symmetric. Figure 4.13 shows the dependence of encircled energy radii on off-axis angle on the four ACIS-I chips. The figure gives the encircled energy radii for 1.49 keV and 6.40 keV at 50% and 90% encircled energy in four azimuthal directions – from the aimpoint to the outer corners of the four ACIS-I chips. The blurs due to the ACIS-I spatial resolution and the *Chandra* aspect error are included.

Figures 4.14 and 4.15 illustrate the effect of aberrations on images of off-axis point sources at 1.49 keV and 6.4 keV. The images are simulations of the HRMA alone, projected to the HRC-I detector plane. The degradation in image quality is primarily due to the separation between the detector plane and the effective focal plane, which is a strong function of both energy and off-axis angle (see Figure 4.11). Cusps in the HRMA images are due to a slight misalignment of the parabolic and hyperbolic mirrors. The signal in these figures is much higher than what might be expected in an actual observation. Figure 4.16 shows how the morphology of an off-axis image varies with the number of counts in the image. It is very easy to mistakenly conclude that an off-axis source is extended or has several components, even with a large number of counts.

4.3 Ghost Images

Baffles prevent non-reflected or singly reflected photons from impinging on the focal plane within the central $30'$ diameter region of the field of view. Outside of this region, however, singly reflected photons from strong off-axis sources may appear. The spray of singly reflected photons is faint relative to the direct image, but can be quite complex. Each individual paraboloidal or hyperboloidal mirror can generate its own single-reflection ghosts. These form loops sweeping in toward the center of the focal plane as the source off-axis angle increases. The ghost loops from the smallest mirrors are the first to approach the central regions as source off-axis angle increases. With increasing source off-axis angle, the large mirrors come into play. As a loop approaches the central $30'$ diameter region of the field of view, the inner parts of the loop fade and break up.

These single-reflection ghosts can impinge on the detector even if the source itself does not fall within the detector field of view. These ghosts mainly affect the outermost portions of those detectors which extend to large off-axis angles: HRC-I, and the spectroscopy arrays, HRC-S and ACIS-S. Figure 4.17 shows simulated ghost images on the ACIS-S

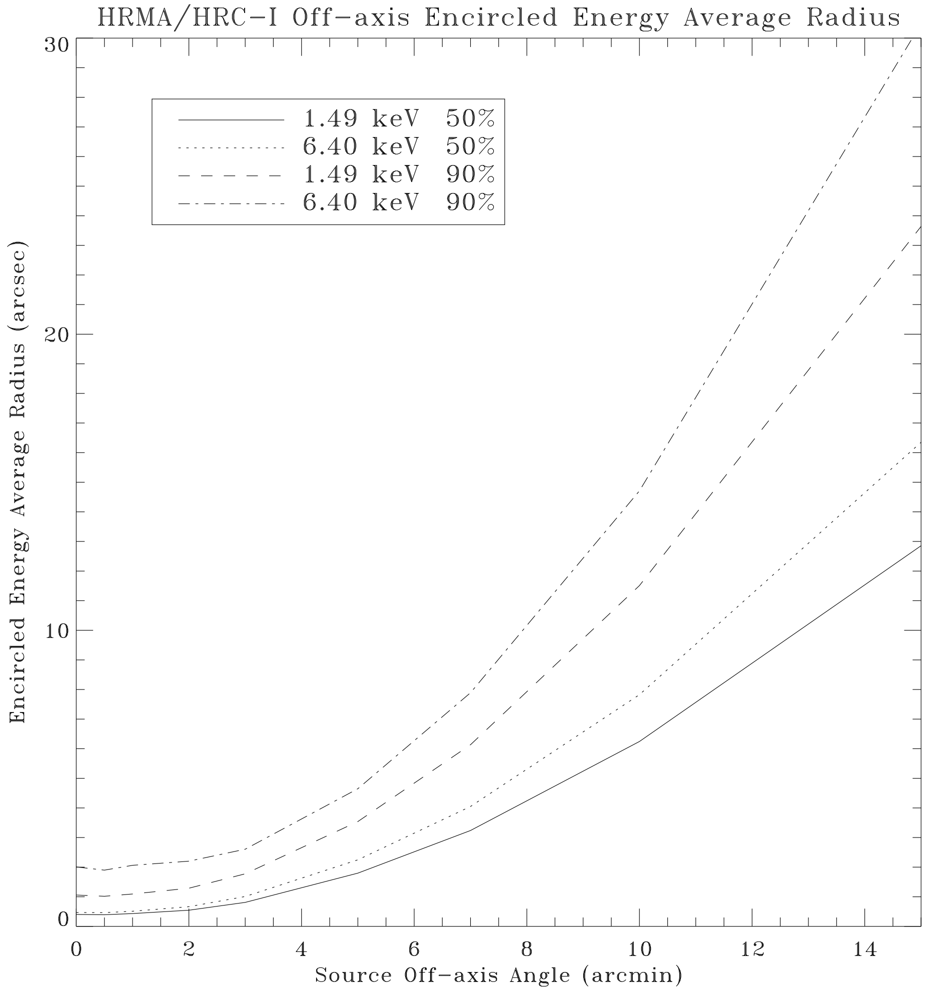

Figure 4.12: The HRMA/HRC-I encircled energy average radii for circles enclosing 50% and 90% of the power at 1.49 and 6.40 keV as a function of off-axis angle. The HRC-I surface is a flat plane perpendicular to the optical axis, which does not follow the curved *Chandra* focal plane. These curves include the blurs due to the HRC-I spatial resolution and the *Chandra* aspect error.

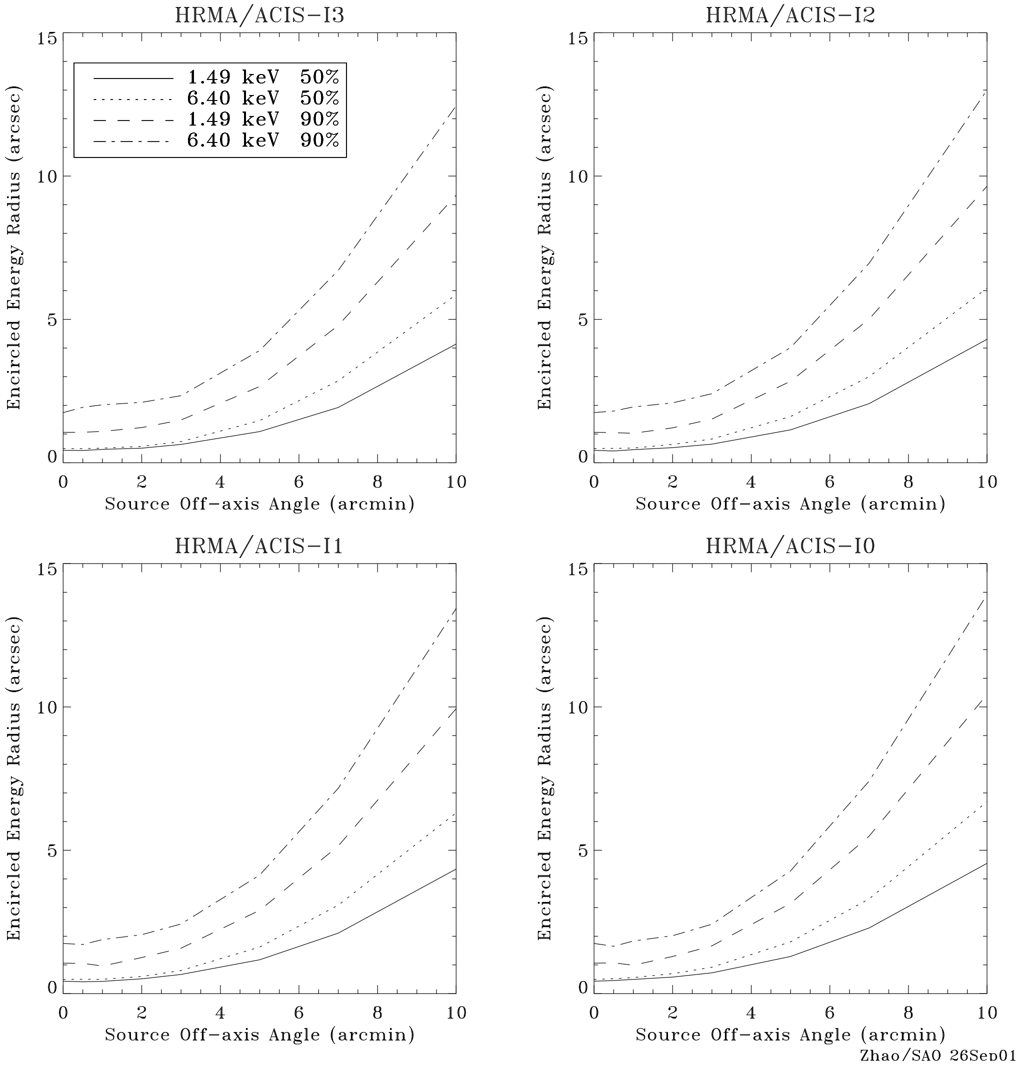

Figure 4.13: The HRMA/ACIS-I encircled energy radii for circles enclosing 50% and 90% of the power at 1.49 and 6.40 keV as a function of off-axis angle. The ACIS-I surface is composed by four tilted flat chips which approximate the curved *Chandra* focal plane. The HRMA optical axis passes near the aimpoint which is located near the inner corner of chip I3. Thus the off-axis encircled energy radii are not azimuthally symmetric. The four panels show these radii's radial dependence in four azimuthal directions – from the aimpoint to the outer corners of the four ACIS-I chips. These curves include the blurs due to the ACIS-I spatial resolution and the *Chandra* aspect error.

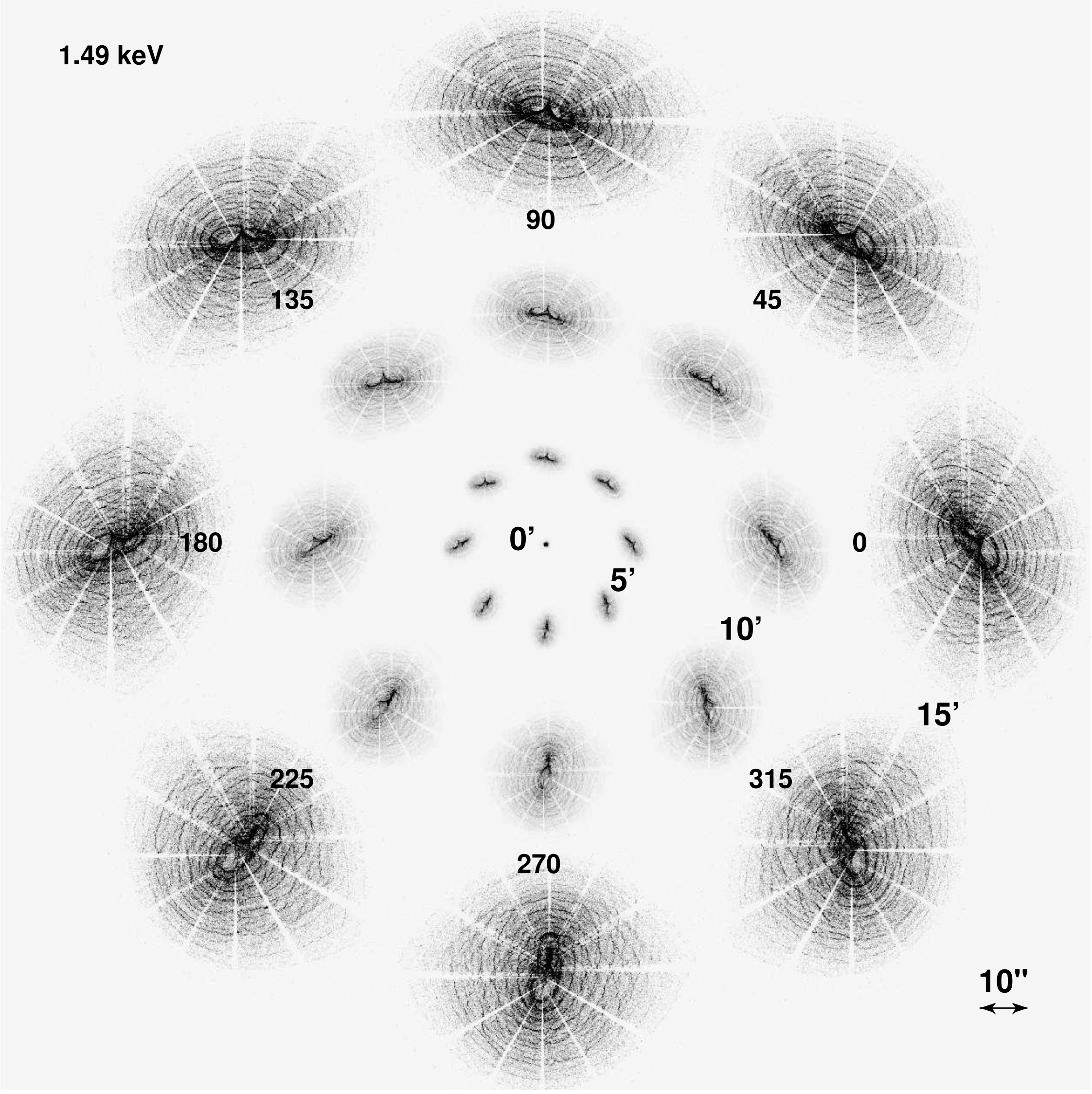

Figure 4.14: Simulated 1.49 keV images, for the HRMA only. Images are shown with a linear stretch, as they would appear on the sky, at three off-axis angles ($5'$, $10'$, and $15'$) and various azimuths. The images are all to the same scale, illustrated by the scale bar. The spacing between images is arbitrary. The surface brightness of the images at $10'$ and $15'$ has been enhanced to show structure. Spokes in the images are due to shadowing by mirror support struts. Cusps are due to a slight misalignment of the parabolic and hyperbolic mirrors. These simulations are at an effective roll of zero – observations should be "de-rolled" before comparison to these images.

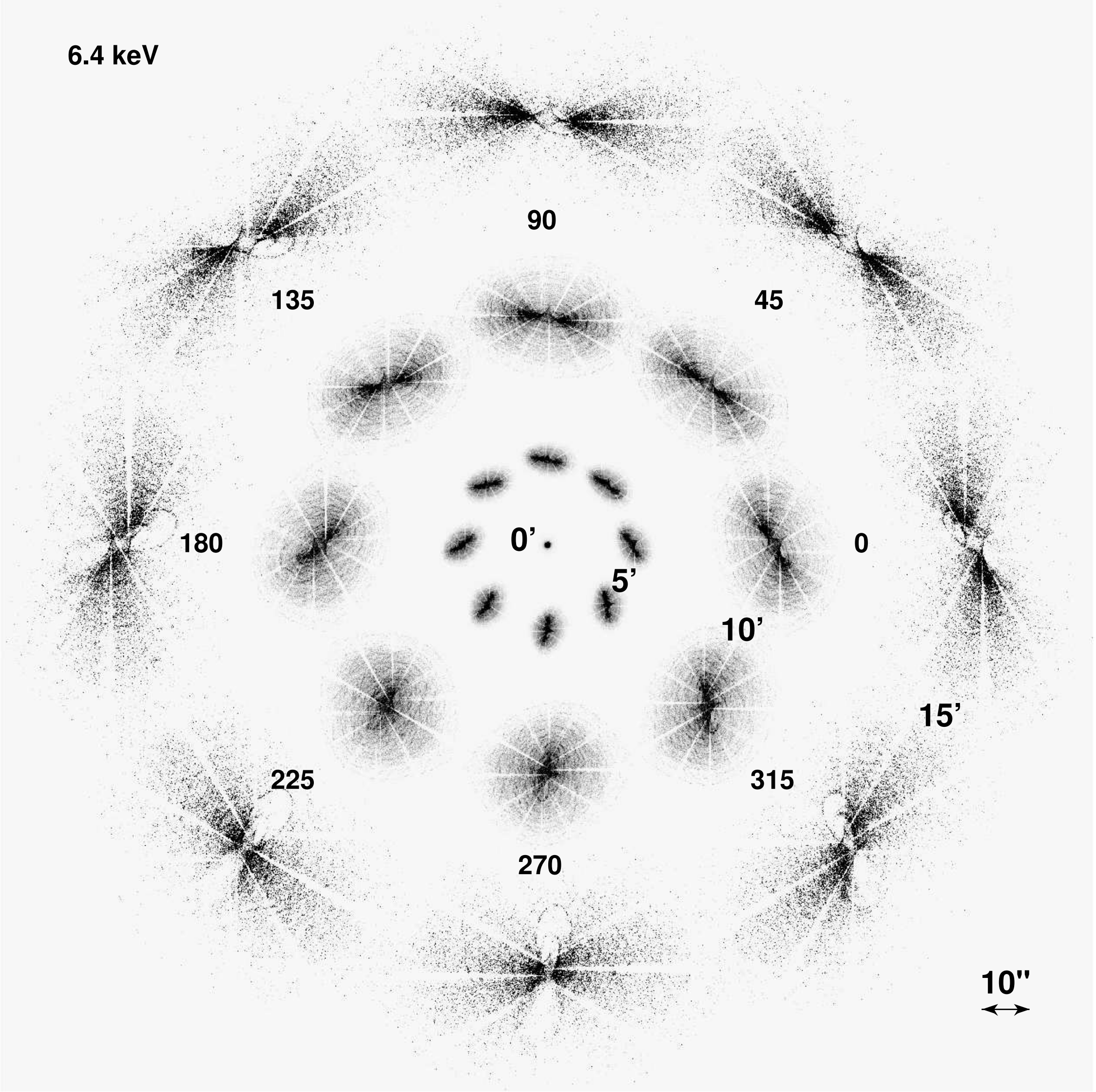

Figure 4.15: Simulated 6.4 keV images, for the HRMA only. Images are shown with a linear stretch, as they would appear on the sky, at three off-axis angles (5′, 10′, and 15′) and various azimuths. The images are all to the same scale, illustrated by the scale bar. The spacing between images is arbitrary. The surface brightness of the images at 10′ and 15′ has been enhanced to show structure. Spokes in the images are due to shadowing by mirror support struts. Cusps are due to a slight misalignment of the parabolic and hyperbolic mirrors. These simulations are at an effective roll of zero – observations should be "de-rolled" before comparison to these images.

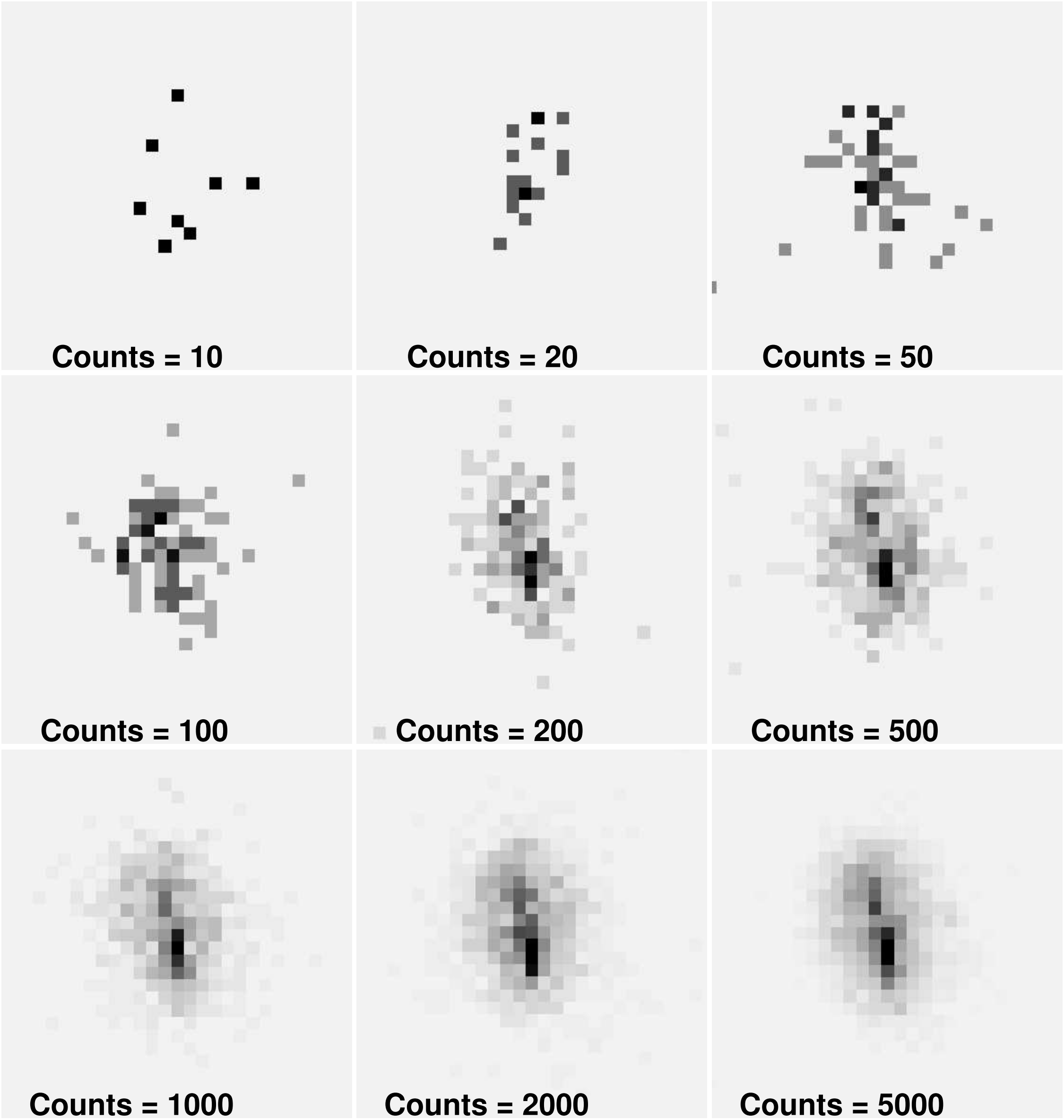

Figure 4.16: A simulated 1.49 keV point source at an off-axis angle of $5'$, binned to ACIS pixels. The panels show what the source would look like with a varying number of counts. Note how the apparent morphology is a strong function of the number of counts, and how even with a large number of counts one might mistake it for an extended source or even for multiple sources.

array. Point sources were simulated at a range of off-axis angle θ and at a fixed off-axis azimuth ($\phi = 5°$). The effects discussed above (e.g. fading of the loops as they approach the central field) can be seen in comparing the ghosts in the $30'$–$32.5'$–$35'$ sequence, or in the $50'$–$52.5'$ sequence.

Imaging observations with HRC-I or spectroscopy observations with HRC-S or ACIS-S which are near very bright sources can be checked using ChaRT/Marx ray traces to determine whether single-reflection ghost images are likely to be a problem.

4.4 Effects of Aspect and Instrument Uncertainties

The HRMA performance discussed in the previous sections will be slightly degraded by uncertainties in the aspect solution and the details of the imaging detector spatial response function. The ground software system also deliberately adds a small random position error to reduce image artifacts which result from instrument and data system integer location values. The randomization may be turned off in data processing if desired. These effects are illustrated for the HRC-I and HRC-S instruments in Figures 4.18 and 4.19 respectively. These figures also show the fractional encircled energy as a function of radius actually observed in flight compared to model calculations at 0.277, 1.496 and 6.403 keV. An aspect error of $0.22''$ (FWHM) was included in the model calculations. The observed encircled energy curve most resembles that calculated for a monoenergetic source at 1.5 keV because this is typically the energy of the average detected photon.

Similar calculations have been performed for the ACIS-S(S3) over a wider range of energies; the results are shown in Figure 4.20. The simulation accounted for the typical spacecraft jitter, so the location of the instrument pixel boundaries has little effect. There is, however, a small effect of the location of the source compared to the data system pixel boundaries. These particular calculations were performed for a point source centered on the boundary between two data system pixels. The ACIS-I instrument response is similar.

Figures 4.18, 4.19, and 4.20 may be compared with Figure 4.6 to estimate the image performance degradation due to non-HRMA effects.

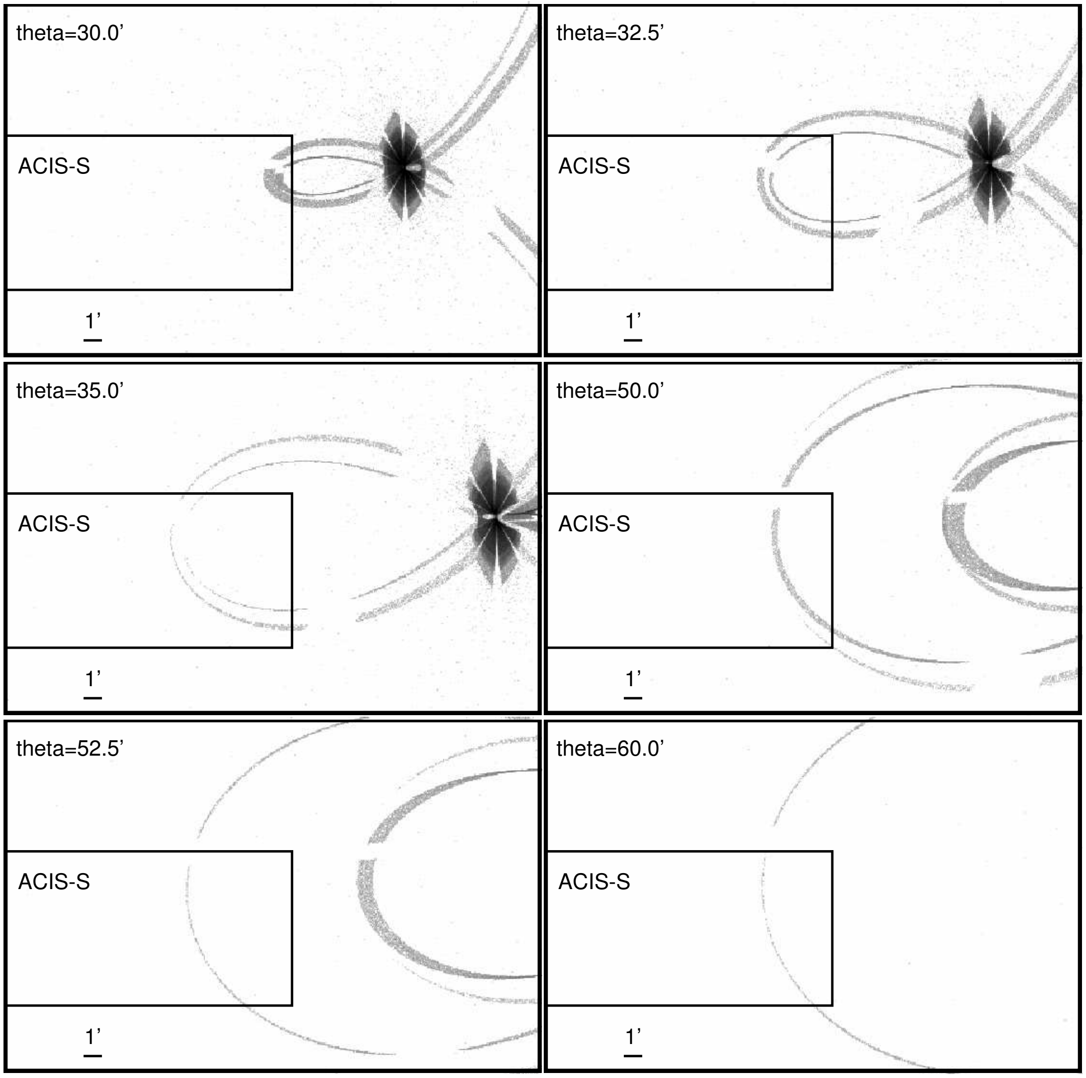

Figure 4.17: Simulated images of off-axis sources. The off-axis angle, theta (θ, in arcmin), is indicated, and all simulations were performed for the same value of ϕ (5°). The rectangle indicates the footprint for one end of the ACIS-S detector. These simulations illustrate how singly reflected photons can hit the detector even when the specular image is well outside the field of view. The surface brightness of these ghosts is low relative to the brightness of the X-ray sources, but could be relevant in planning observations near extremely bright X-ray sources.

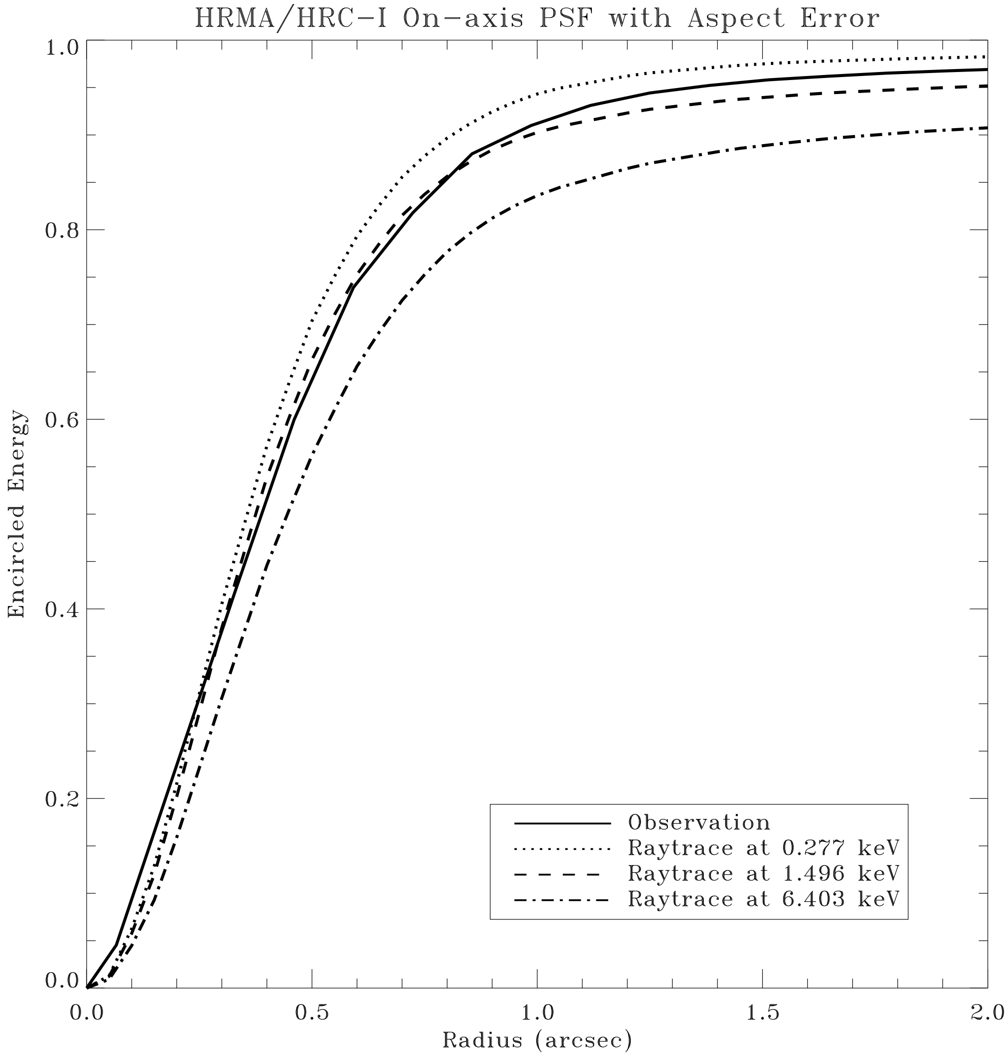

Figure 4.18: The HRMA/HRC-I on-axis fractional encircled energy as a function of angular radius from a point source (Ar Lac) observed in flight compared to ray trace simulations for an on-axis point-source at selected X-ray energies, including the aspect uncertainties and the HRC-I pixelization effects.

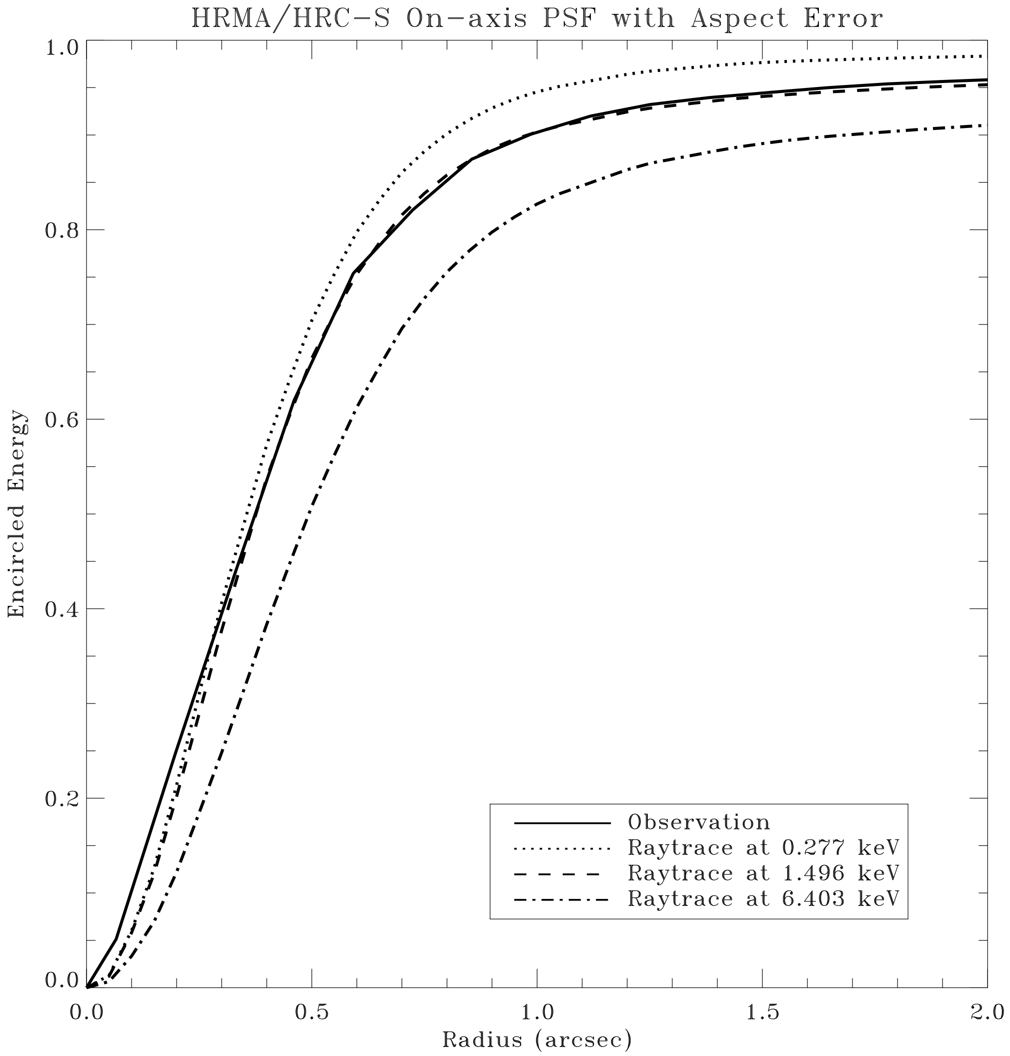

Figure 4.19: The HRMA/HRC-S on-axis fractional encircled energy as a function of angular radius from a point source (LMC X-1) observed in flight compared to ray trace simulations for an on-axis point-source at selected X-ray energies, including the aspect uncertainties and the HRC-S pixelization effects.

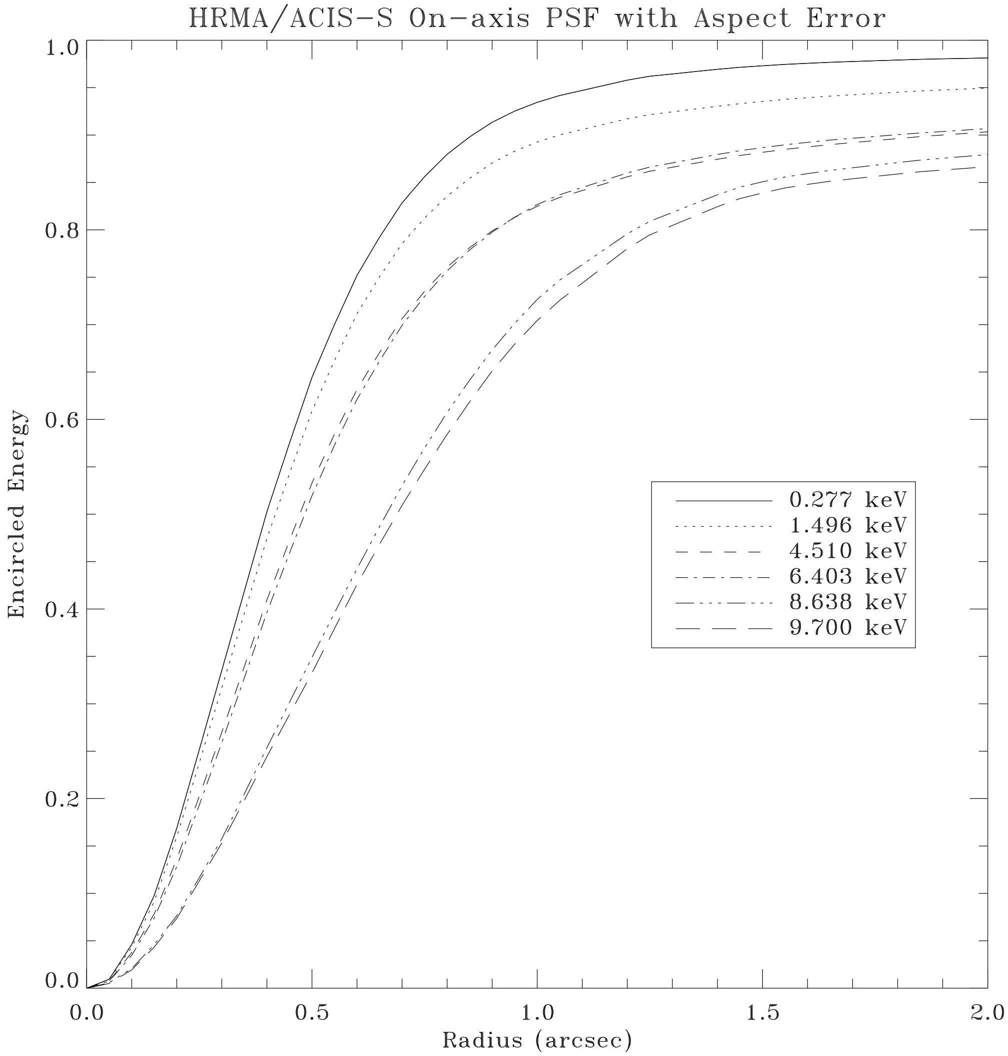

Figure 4.20: The fractional encircled energy as a function of angular radius expected for in flight ACIS-S(S3) measurements for an on-axis point-source at selected X-ray energies. The curves are the combined response of the four nested mirror pairs, typical aspect uncertainties, and the ACIS response function.

4.5 References

Aschenbach, B. 1985, Rep. Prog. Phys. 48, 579
Aschenbach, B. 1991, Rev. Mod. Astron. 4, 173
Boese, F.G. 2000, Astron. Ap. Suppl. 507, 141
Edgar, R.J., et al. 1997, SPIE Proceedings, 3113, 124
Elsner, R.F., et al. 1998, SPIE Proceedings, 3444, 177
Gaetz, T.J., et al. 1997, SPIE Proceedings, 3113, 77
Gaetz, T.J., et al. 2000, SPIE Proceedings, 4012, 41
Gaetz, T.J., 2004,
http://cxc.cfa.harvard.edu/cal/Hrma/rsrc/Publish/Optics/PSFWings/wing_analysis_rev1b.pdf
Gaetz, T.J. and Jerius, D. 2005, http://cxc.harvard.edu/cal/Hrma/UsersGuide.html
Gaetz, T.J., et al. 2004, SPIE Proceedings, 5165, 411
Giacconi, R., et al. 1979, ApJ, 230, 540
Graessle, D.E., et al. 1998, SPIE Proceedings, 3444, 140
Graessle, D.E., et al. 2004, SPIE Proceedings, 5165, 469
Henke, B.L., et al. 1993, Atomic Data and Nuclear Data Tables, 54, 181
Hughes, J.P., et al. 1993, SPIE Proceedings, 1742, 152
Jerius, D., et al. 2000, SPIE Proceedings, 4012, 17
Jerius, D., et al. 2004, SPIE Proceedings, 5165, 402
Jerius, D., et al. 2004, SPIE Proceedings, 5165, 433
Kolodziejczak, J.J., et al. 1997, SPIE Proceedings, 3113, 65
Marshall, H.L., 2005, http://space.mit.edu/ASC/calib/heg_meg/meg_heg_report.pdf
Marshall, H.L., 2005a, private communications
O'Dell, S.L. and Weisskopf, M.C. 1998, SPIE Proceedings, 3444, 2
Olds, C.R. and Reese, R.P. 1998, SPIE Proceedings, 3356, 910
Schwartz, D.A., et al. 2000, SPIE Proceedings, 4012, 28
Trümper, J., 1983, Adv. Space Res. 2(4), 241.
Van Speybroeck, L.P., et al. 1997, SPIE Proceedings, 3113, 89
Weisskopf, M.C. and O'Dell, S.L. 1997, SPIE Proceedings, 3113, 2
Weisskopf, M.C., et al. 2000, SPIE Proceedings, 4012, 2
Zhao, P., et al. 1993, SPIE Proceedings, 1742, 26
Zhao, P., et al. 1993, SPIE Proceedings, 1742, 75
Zhao, P., et al. 1994, SPIE Proceedings, 2011, 59
Zhao, P. and Van Speybroeck, L.P. 1995, SPIE Proceedings, 2515, 391
Zhao, P., et al. 1997, SPIE Proceedings, 3113, 106
Zhao, P., et al. 1998, SPIE Proceedings, 3444, 234
Zhao, P. and Van Speybroeck, L.P. 2003, SPIE Proceedings, 4851, 124
Zhao, P., et al. 2004, SPIE Proceedings, 5165, 482

Postscript copies of various aspects of the HRMA calibration can be obtained from the *CXC* Optics Calibration Group at http://cxc.harvard.edu/cal/Hrma/XRCFReport.html

A detailed guide to using and understanding the HRMA is available at http://cxc.harvard.edu/cal/Hrma/UsersGuide.html

Further information can be obtained from the MSFC *Chandra* calibration page at http://wwwastro.msfc.nasa.gov/xray/xraycal/

Chapter 5

Pointing Control and Aspect Determination System

5.1 Introduction

The system of sensors and control hardware that is used to point the observatory, maintain the stability, and provide data for determining where the observatory has been pointing is called the Pointing Control and Aspect Determination (PCAD) system. As *Chandra* detectors are essentially single-photon counters, an accurate post-facto history of the spacecraft pointing direction is sufficient to reconstruct an X-ray image.

In this chapter we briefly discuss the hardware that comprises the PCAD system, how it is used, and its flight performance. Further information can be found on the Aspect Information web page within the main *CXC* Science web site (http://cxc.harvard.edu/cal/ASPECT).

5.2 Physical configuration

The main components of the PCAD system are:

Aspect camera assembly (ACA) – 11.2 cm optical telescope, stray light shade, two CCD detectors (primary and redundant), and two sets of electronics

Inertial reference units (IRU) – Two IRUs, each containing two 2-axis gyroscopes.

Fiducial light assemblies (FLA) – LEDs mounted near each science instrument (SI) detector which are imaged in the ACA via the FTS

Fiducial transfer system (FTS) – The FTS directs light from the fid lights to the ACA, via the retroreflector collimator (RRC) mounted at the HRMA center, and a periscope

Coarse sun sensor (CSS) – Sun position sensor, all-sky coverage

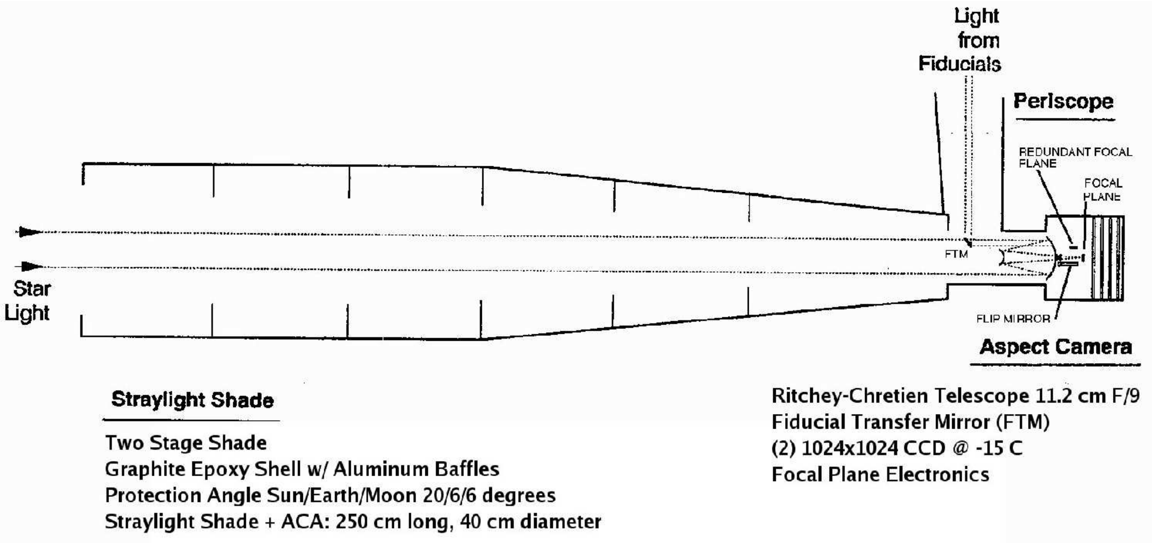

Figure 5.1: Aspect camera assembly

Fine sun sensor (FSS) – Sun position sensor, 50 degree FOV and 0.02 degree accuracy

Earth sensor assembly (ESA) – Conical scanning sensor, used during the orbital insertion phase of the mission

Reaction wheel assembly (RWA) – 6 momentum wheels which change spacecraft attitude

Momentum unloading propulsion system (MUPS) – Liquid fuel thrusters which allow RWA momentum unloading

Reaction control system (RCS) – Thrusters which change spacecraft attitude

Since data from the CSS, FSS, and ESA are not normally used in the processing of science observations these are not discussed. However, in the unlikely event of a complete failure of the ACA, we would attempt to use CSS and FSS data.

5.2.1 ACA

The aspect camera assembly (Figure 5.1) includes a sunshade ($\sim$2.5 m long, $\sim$55 cm in diameter), a 11.2 cm, F/9 Ritchey-Chretien optical telescope, and light-sensitive CCD detector(s). This assembly and its related components are mounted on the side of the HRMA. The camera's field of view is 1.4×1.4 deg and the sun-shade is designed to protect the instrument from the light from the Sun, Earth, and Moon, with protection angles of 47, 20 and 6 deg, respectively.

The aspect camera focal plane detector is a 1024×1024 Tektronix CCD chip operating between -16°C and -19.7°C, with 24×24 micron ($5'' \times 5''$) pixels, covering the spectral band

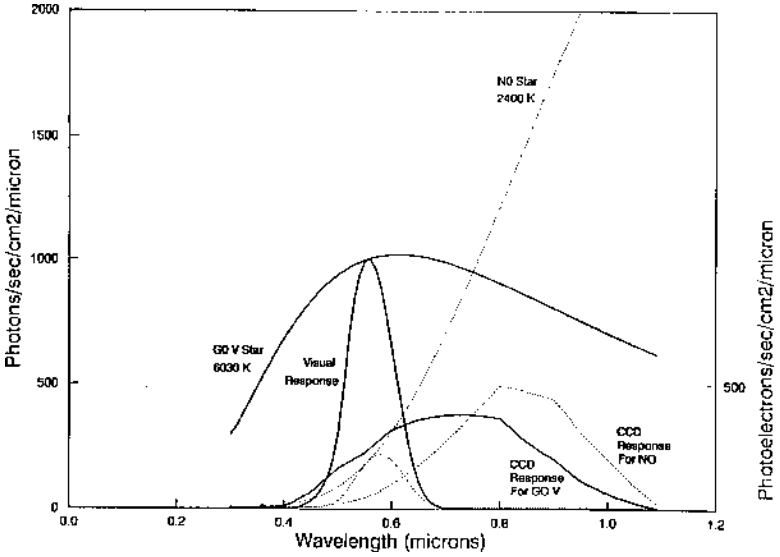

Figure 5.2: Spectral response of the ACA CCD. The same signal-to-noise is achieved for a V=11.7 magnitude N0 star as for a V=10 magnitude G0V star. Also shown are the spectra and the standard visual response for the two stars.

between 4000 and 9000 Å. The optics of the camera are defocused (point source FWHM = 9 arcsec) to spread the star images over several CCD pixels in order to increase accuracy of the centering algorithm, and to reduce variation in the point response function over the field of view. There is a spare identical CCD chip, which can be illuminated by inserting a rotatable mirror.

The ACA electronics track a small pixel region (either $4 \times 4, 6 \times 6$, or 8×8 pixels) around each fiducial light and star image. There are a total of eight such image slots available for tracking. Typically five guide stars and three fiducial lights (section 5.2.2) are tracked. The average background level is subtracted on-board, and image centroids are calculated by a weighted-mean algorithm. The image centroids and magnitudes are used on-board by the PCAD, and are also telemetered to the ground along with the raw pixel data.

The spectral response of the CCD detector (Figure 5.2) is such that faint cool stars (e.g. type N0), with visual magnitudes much fainter than selected guide stars (i.e., 10.5 mag) can produce large numbers of counts. These so-called “spoiler stars” are effectively avoided in the mission planning stage.

5.2.2 Fiducial lights and Fiducial Transfer System

Surrounding each of the SI detectors is a set of light emitting diodes, or “fiducial lights”, which serve to register the SI focal plane laterally with respect to the ACA boresight.

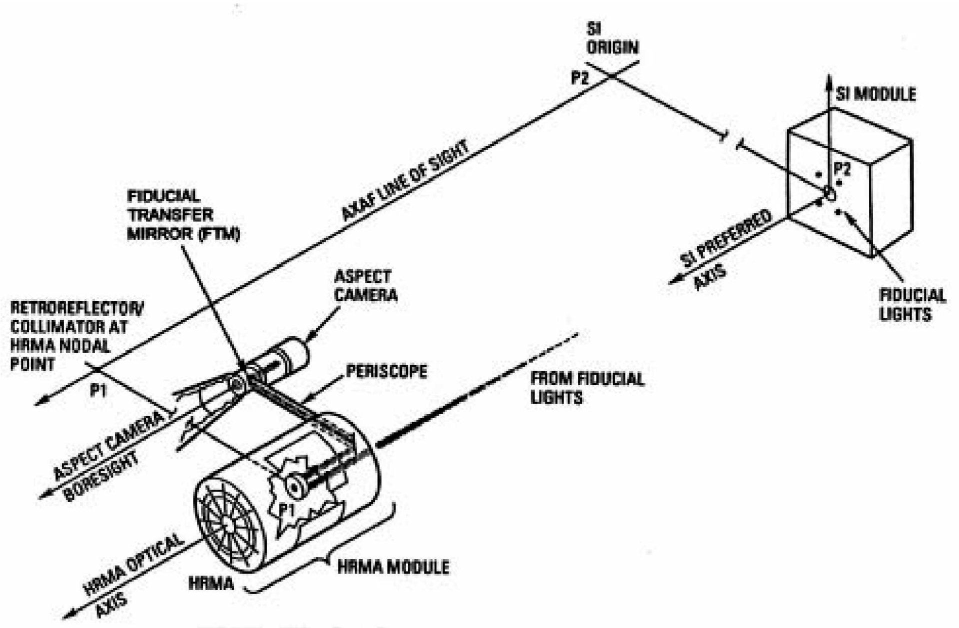

Figure 5.3: Fiducial Transfer System

Each fiducial light produces a collimated beam at 635 nm which is imaged onto the ACA CCD via the RRC, the periscope, and the fiducial transfer mirror (Figure 5.3).

5.2.3 IRU

Two Inertial Reference Units (IRU) are located in the front of the observatory on the side of the HRMA. Each IRU contains two gyros, each of which measures an angular rate about 2 gyro axes. This gives a total of eight gyro channels. Data from four of the eight channels can be read out at one time. The gyros are arranged within the IRUs and the IRUs are oriented such that all 8 axes are in different directions and no three axes lie in the same plane. The gyros' output pulses represent incremental rotation angles. In high-rate mode, each pulse nominally represents $0.75''$, while in low-rate mode (used during all normal spacecraft operations) each pulse represents nominally $0.02''$.

5.2.4 Momentum control – RWA and MUPS

Control of the spacecraft momentum is required both for maneuvers and to maintain stable attitude during science observations. Momentum control is primarily accomplished using 6 Teldix RDR-68 reaction wheel units mounted in a pyramidal configuration. During observing, with the spacecraft attitude constant apart from dither, external torques on the spacecraft (e.g. gravity gradient, magnetic) will cause a buildup of momentum in the

RWA. Momentum is then unloaded by firing the MUPS and simultaneously spinning down the reaction wheels.

5.3 Operating principles

The *Chandra* aspect system serves two primary purposes: on-board spacecraft pointing control and aspect determination and post-facto ground aspect determination, used in X-ray image reconstruction and celestial location.

The PCAD system has 9 operational modes (6 normal and 3 safe modes) which use different combinations of sensor inputs and control mechanisms to control the spacecraft and ensure its safety. These modes are described in Section 5.7.1. In the normal science pointing mode, the PCAD system uses sensor data from the ACA and IRUs, and control torques from the RWAs, to keep the target attitude within ∼30” of the telescope boresight. This is done using a Kalman filter which optimally combines ACA star centroids (typically 5) and angular displacement data from two 2-axis gyroscopes. On short time scales (∼seconds) the spacecraft motion solution is dominated by the gyroscope data, while on longer timescales it is the star centroids that determine the solution.

Post-facto aspect determination is done on the ground and uses more sophisticated processing and better calibration data to produce a more accurate aspect solution. The suite of *CXC* tools to perform this processing is called the aspect pipeline. The key improvements over PCAD aspect come from better image centroiding and using Kalman smoothing (which uses all available data over the observation period – as opposed to historical data). In addition, the aspect pipeline folds in the position of the focal-plane instrument as determined by the fiducial light data.

5.4 Performance

5.4.1 Post-Facto and On-Orbit Aspect Determination

The important PCAD system performance parameters and a comparison to the original requirements are shown in Table 5.1. In each case the actual performance far exceeds the requirements. Celestial location accuracy measures the absolute accuracy of Chandra X-ray source locations. Based on observations of 587 point sources detected within $2'$ of the boresight and having accurately known coordinates, the 90% source location error circle has a radius of less than $0.6''$ overall, and less than $0.7''$ for each SI (Figure 5.4). Approximately 1.6% of sources are outside a $1''$ radius. The difference in astrometric accuracy for different SIs is a function of two factors: number of available data points for boresight calibration and accuracy of the fiducial light SIM-Z placement[1]. The plotted level of accuracy applies for observations that have been processed or reprocessed after

---

[1] These values apply for sources within 3 arcmin of the aimpoint and with the SIM-Z at the nominal detector value. Observations on ACIS or HRC-S at large off-nominal SIM-Z can suffer additional residual aspect offsets of up to 0.5 arcsec and for HRC-I this can be up to 3 arcsec.

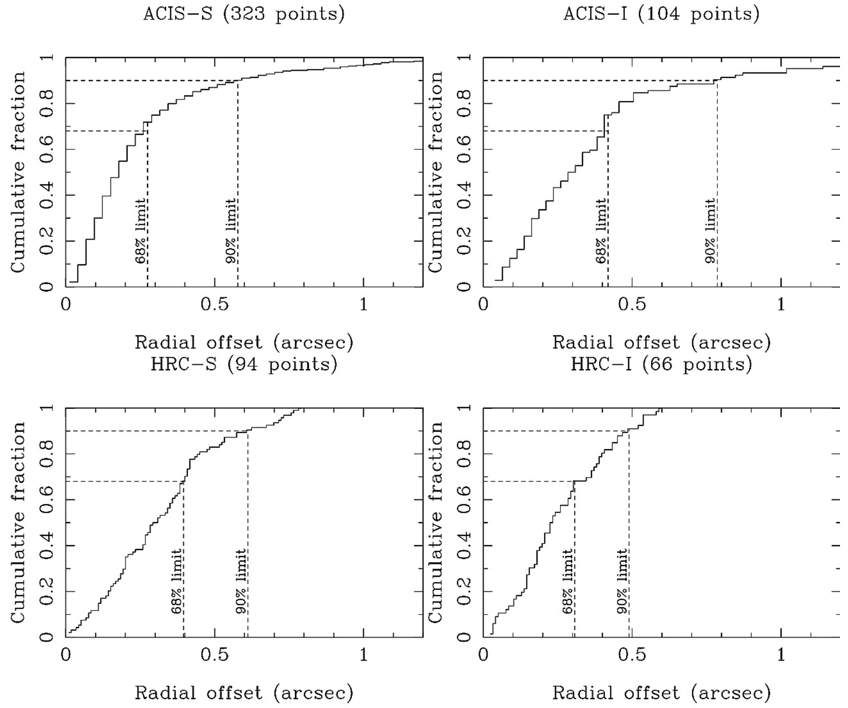

Figure 5.4: Cumulative histogram of celestial accuracy for *Chandra* X-ray source locations for each SI. Radial offset is the distance in arcsec between the optical coordinate, typically from the Tycho-2 catalog, and the *Chandra* position.

Dec. 31, 2003. This condition applies to all Chandra observations currently in the archive. For pre-2004 observations it is recommended that users download the latest version of the observation from the archive.

The image reconstruction performance measures the effective blurring of the X-ray PSF due to aspect reconstruction. A direct measure of this parameter can be made by determining the time-dependent jitter in the centroid coordinates of a fixed celestial source. Any error in the aspect solution will be manifested as an apparent wobble in the source location. Unfortunately this method has limitations. ACIS data are count-rate limited and we find only an upper limit: aspect reconstruction effectively convolves the HRMA PSF with a Gaussian having FWHM of less than $0.25''$. HRC observations can produce acceptably high count rates, but the HRC photon positions (at the chip level) have systematic errors due to uncertainties in the HRC de-gap calibration[2]. These errors exactly mimic the expected dither-dependent signature of aspect reconstruction errors, so no such analysis with HRC data has been done. An indirect method of estimating aspect reconstruction blurring is to use the aspect solution to de-dither the ACA star images and

---

[2] See "Position modeling, de-gap corrections, and event screening" in the References section of Chapter 7

Table 5.1: Aspect System Requirements and Performance

Description	**Requirement**	**Actual**
Celestial location	$1.0''$ (RMS radius)	$0.5''$
Image reconstruction	$0.5''$ (RMS diameter)	$0.3''$
Absolute celestial pointing	$30.0''$ (99.0%, radial)	$6.0''$
PCAD 10 sec pointing stability	$0.12''$ (95% RMS)	$0.06''$ (pitch) $0.07''$ (yaw)

measure the residual jitter. We have done this for 350 observations and find that 99% of the time the effective blurring is less than $0.20''$ (FWHM).

Absolute celestial pointing refers to the accuracy with which an X-ray source can be positioned at a specified location on the detector, and is about $6''$ in radius. This is based on the spread of apparent fiducial light locations for observations through 2012. Because of the excellent celestial location accuracy, the fiducial light locations are a very accurate and convenient predictor of where an on-axis X-ray source would fall on the detector. It should be noted that the $6''$ value represents the repeatability of absolute pointing on timescales of less than approximately one year. During the first 4 years of the mission, there was an exponentially decaying drift in the nominal aimpoint of about $10''$, probably due to a long-term relaxation in the spacecraft structural alignment. Since that time the drift rate has been less than about $1''$/year in the spacecraft Y and Z directions apart from large jumps associated with the cooling the ACA CCD in Jul-2003 and Dec-2006 and the safemode in Jul-2011. The continued drift at this time is believed to be directly related to the increasing temperatures of the ACA housing and the ACA telescope mount. These drifts have been a driving factor in updates to the ACIS default aimpoint offsets.

The PCAD 10-second pointing stability performance is measured by calculating the RMS attitude control error (1-axis) within successive 10 second intervals. The attitude control error is simply the difference between the ideal (commanded) dither pattern and the actual measured attitude. Flight data show that 95% of the RMS error measurements are less than $0.06''$ (pitch) and $0.07''$ (yaw). Systematic offsets are not included in this term.

In addition to the four key performance requirements listed in Table 5.1 we also measure the relative astrometric accuracy which is achieved with Chandra data. This refers to the residual astrometric offsets assuming that the X-ray coordinates have been registered using well-characterized counterparts of several X-ray sources in the field. The most comprehensive dataset for measuring relative astrometry is based on the 900 ksec ACIS-I observation of the Orion Nebula. The members of COUP (Chandra Orion Ultradeep Project) have kindly provided us with a data file for over 1300 X-ray sources listing the offset from a 2MASS counterpart and the off-axis angle[3]. The left plot of Figure 5.5 shows a scatter plot of offset (arcsec) versus off-axis angle (arcmin). The right side of the

---

[3] Full details available in Getman et al. 2005, ApJS, 160, 319. In our analysis we include only the 1152 sources with more than 50 counts.

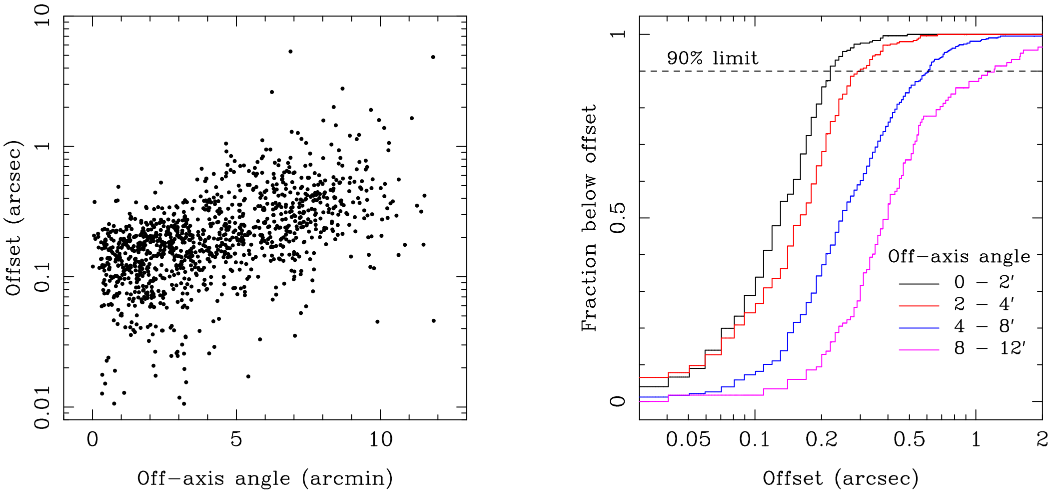

Figure 5.5: Left: scatter plot of offset (arcsec) versus off-axis angle (arcmin) for sources in the ultra-deep ACIS-I Orion observation. Right: cumulative histograms of the fraction of sources with relative offset below the specified value.

figure shows cumulative histograms of the fraction of sources with relative offset below the specified value. This is broken into bins of off-axis angle as listed in the plot. In the "on-axis" (0 - 2′) bin, 90% of sources have offsets less than 0.22″. After, accounting for the ~ 0.08″ RMS uncertainty in 2MASS coordinates, this implies the intrinsic 90% limit is 0.15″. See http://www.ipac.caltech.edu/2mass/releases/allsky/doc/.

5.4.2 On-Board Acquisition and Tracking

As described in Section 5.8, in normal operations, the ACA is used to acquire and track stars and fiducial lights. Occasional failures in acquisition and difficulties in tracking are expected due to uncertainties in star position and magnitude, the presence of spoiler stars, CCD dark current noise (see Section 5.6.3), and other factors.

Table 5.2 summarizes success statistics for star acquisition and tracking[4].

Table 5.2: Star Acquisition and Tracking Success

Catalog Star Magnitude	**Acquisition Success**	**Tracking Success**
All stars	97%	99%
10.3 - 10.6 mag stars	83%	94%
10.6 - 10.9 mag stars	68%	85%

---

[4] A star is "successfully" tracked if it spends less than 5% of the observation in the loss of track state.

5.5 Heritage

The *Chandra* aspect camera design is based on the Ball CT-601 star tracker, which was also used for the RXTE mission. The *Chandra* IRUs are nearly identical to the SKIRU V IRUs, some 70 of which have been built by the manufacturer - Kearfott. These IRUs are similar to those used on CGRO.

5.6 Calibration

5.6.1 Pre-launch calibration

IRU component testing at Kearfott provided calibration data necessary for accurate maneuvers and for deriving the aspect solution. The key parameters are the scale factor (arcsec/gyro pulse) and the drift rate stability parameters. The stability parameters specify how quickly the gyro readout random-walks away from the true angular displacement. These terms limit the aspect solution accuracy during gyro hold observations (Section 5.8.2).

ACA component testing at Ball provided calibration data necessary for on-orbit pointing control and for post-facto ground processing. On-orbit, the ACA uses CCD gain factors, the plate scale factor, and temperature dependent field distortion coefficients to provide the control system with star positions and brightnesses. In ground processing, the *CXC* aspect pipeline makes use of those calibration data as well as CCD read noise, flat-field maps, dark current maps, and the camera PSF in order to accurately determine star positions.

5.6.2 Orbital activation and checkout calibration

Orbital activation and checkout of the PCAD occurred during the first 30 or so days of the *Chandra* mission. During the first phase of OAC, before the HRMA sunshade door was opened, it was possible to use the ACA to observe the fiducial lights (period 1). After the sunshade door was opened it was possible to fully check the aspect camera using star light (period 2).

Chandra activation produced the following aspect system calibration data:

- Bias, alignment, scale factor of the CSS and FSS (period 1)
- Coarse gyro bias (period 1)
- ACA CCD dark current map (period 1)
- Fiducial light intensity, image, and centroid at nominal voltage (periods 1 and 2)
- IRU bias, alignment, scale factor (period 2)
- ACA alignment and field distortion coefficients (period 2)

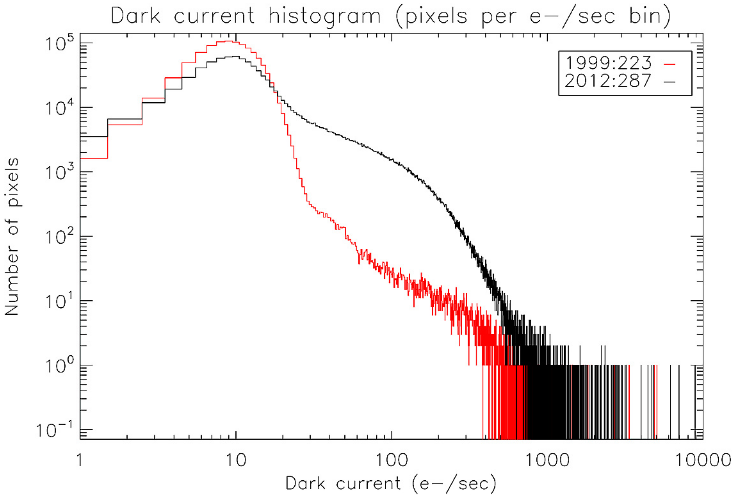

Figure 5.6: Differential histogram of dark current distribution for the ACA CCD in 1999-Aug and 2012-Oct

5.6.3 On-orbit calibrations

During the *Chandra* science mission, aspect system components require on-orbit calibration to compensate for alignment or scale factor drifts, and to evaluate ACA CCD degradation due to cosmic radiation. The IRU-1 calibration coefficients were updated once (Jul-2002) based on analysis of PCAD data for 3105 maneuvers during the course of the mission. Following the swap to IRU-2 in Jul-2003, new coefficients have been updated as needed (6 times between 2003 and 2012).

The following ACA calibrations are performed, as-needed, based on the trending analyses of aspect solution data.

Dark current

Cosmic radiation damage will produce an increase in both the mean CCD dark current and the non-Gaussian tail of "warm" (damaged) pixels in the ACA CCD. This is illustrated in Figure 5.6, which shows the distribution of dark current shortly after launch and in 2012-Oct. The background non-uniformity caused by warm pixels (dark current > 100 e^-/sec) is the main contributor to star centroiding error, though the effect is substantially reduced by code within the aspect pipeline which detects and removes most warm pixels.

Currently the fraction of warm CCD pixels is 7% and is increasing linearly at 0.4% per year. The impact of this continued radiation damage has been analyzed within a study of ACA lifetime issues. The analysis shows that we expect no significant degradation of X-ray image quality (due to aspect) even in the worst case scenario out to 20 years after launch. One key issue is the loss of power margin in the ACA thermoelectric cooler which maintains the CCD at -19 C. It is expected that the CCD temperature at 20 years will be somewhere between -15 C to -18 C, thus increasing the fraction of warm pixels by up to a factor of 65% beyond the simple linear extrapolation. Current data and analysis indicate that this increase in the fraction of warm pixels will cause negligible degredation of post-facto image reconstruction and no significant reduction in on-board control margin.

Dark current calibrations are performed approximately three times per year. Because the ACA has no shutter, a dark current calibration must be done with *Chandra* pointing at a star field which is as free from optical sources as possible. Five full-frame CCD maps are collected, each with slight pointing offsets in order to allow removal of field stars. The entire calibration procedure takes approximately 3 hours.

Flickering pixels

The dark current of radiation damaged pixels is observed to fluctuate by factors of up to 25% on time scales of 1 to 50 ksec. This behavior was studied using a series of ACA monitor windows commanded during perigee passes in 2002. In 2008 and 2009, similar monitor window data was acquired and analysed and the flickering pixel behavior was seen to be qualitatively unchanged from that seen in 2002. An important consequence of the flickering pixel phenomenon is that the dark current pixel values obtained during the dark current calibration may not be directly subtracted from observation pixel data in post-facto processing. Instead, users of monitor window data should use a warm pixel detection algorithm such as the one implemented in ground processing[5].

Charge transfer inefficiency (CTI)

Radiation damage degrades the efficiency with which charge is transferred in the CCD by introducing dislocations in the semiconductor which trap electrons and prevent their transfer. The most important consequence is a "streaking" or "trailing" of star images along the readout column(s), which can introduce systematic centroid shifts. These shifts depend primarily on CCD transfer distance to the readout and star magnitude.

The procedure for calibrating the mean CTI is to dither a faint star across the CCD quadrant boundary and observe the discontinuity in centroid (the CCD is divided electrically into four quadrants). In 2004, a total of 20 calibration observations were performed during perigee, each with a guide star dithering over a quadrant boundary. Despite significant concerns prior to launch, as well as notable CTI degradation in the ACIS front-illuminated chips, there is no evidence of increased CTI in the ACA CCD.

---

[5] Cresitello-Dittmar, M., Aldcroft, T. L., & Morris, D. 2001. On the Fly Bad Pixel Detection for the Chandra X-ray Observatory's Aspect Camera. ADASS X ASP Conf. Ser., Vol. 238, 439 http://www.adass.org/adass/proceedings/adass00/P1-22/

Field distortion

The precise mapping from ACA CCD pixel position to angle relative to the ACA boresight is done with the “ACA field distortion polynomial”. This includes plate scale factors up to third order as well as temperature-dependent terms. In order to verify that no mechanical shift in the ACA had occurred during launch, a field distortion calibration was performed during the orbital activation and checkout phase. The on-orbit calibration revealed no mechanical shift. Such a shift would have caused degraded celestial location accuracy.

The calibration was done by observing a dense field of stars with the spacecraft in normal pointing mode. Two reference stars were observed continuously, while sets of 4 stars each were observed for 100 seconds. The calibration was completed after observing 64 stars over the ACA field of view, taking roughly 60 minutes. There are currently no plans to repeat this on-orbit calibration. Instead, the field distortion coefficients are monitored by long-term trending of observed star positions relative to their expected positions.

Responsivity

Contamination buildup on the CCD surface was predicted in pre-launch estimates to result in a mean throughput loss of 9% after 5 years on-orbit, though the calculation of this number has significant uncertainties. The buildup of contaminants is tracked by a trending analysis of magnitudes for stars which have been observed repeatedly throughout the mission (e.g. in the AR LAC field). To date, these trending analyses show no indication of contamination build-up. In the unlikely event that future contamination occurs and causes significant operational impact, we will consider “baking-out” the CCD on-orbit. In this procedure the current to the CCD thermo-electric cooler is reversed so as to *heat* the device to approximately 30 C for a period of several hours. After bake-out the CCD would be returned to its nominal operating temperature of -19 C.

5.7 Operations

5.7.1 PCAD modes

The PCAD system has 9 operational modes (6 normal and 3 safe) which use different combinations of sensor inputs and control mechanisms to control the spacecraft and ensure its safety. These modes are listed in Table 5.3. Normal science observations are carried out in Normal Pointing Mode (NPM), while slews between targets are done in Normal Maneuver Mode (NMM).

5.7.2 Operational constraints

The ACA will meet performance requirements when the ACA line of sight is separated from: the Sun by 45 degrees or more; the limb of the bright Earth by 10 degrees or more; and the dark Earth or Moon by 6 degrees or more. If these restrictions are violated, the

Table 5.3: PCAD modes

Mode	Sensors	Control	Description
Standby	—	—	OBC commands to RWA, RCS, and SADA disabled, for initial deployment, subsystem checkout, etc.
Normal Pointing	IRU, ACA	RWA	Point at science target, with optional dither
Normal Maneuver	IRU	RWA	Slew between targets at peak rate of 2° per minute
Normal Sun	IRU, CSS, FSS	RWA	Acquire sun and hold spacecraft -Z axis and solar arrays to the sun
Safe Sun	IRU, CSS, FSS	RWA	Safe mode: acquire sun and hold spacecraft -Z axis and solar arrays to the sun
Derived Rate Safe Sun	IRU, CSS, FSS	RWA	Similar to Safe Sun Mode, but using only one gyro (two axes) plus sun sensor data
Transfer orbit only - now disabled			
Powered Flight	IRU	RCS	Control *Chandra* during Liquid Apogee Engine burns
RCS Maneuver	IRU	RCS	Control *Chandra* using the RCS
RCS Safe Sun	IRU, CSS, FSS	RCS	Same as Safe Sun Mode, but using RCS instead of RWA for control

star images may be swamped by scattered background light, with the result that added noise on the star position will exceed the the $0.360''$ requirement (1-σ,1-axis).

5.7.3 Output data

The important output data from the ACA are the scaled raw pixel intensities in regions (4×4, 6×6, or 8×8 pixel) centered on each of the star and fiducial light images. These data are placed in the engineering portion of the telemetry stream, which is normally allocated $8\,\mathrm{kbit\,s^{-1}}$. During an ACA dark current calibration (Section 5.6.3), *Chandra* utilizes a $512\,\mathrm{kbit\,s^{-1}}$ telemetry mode in real-time contact to enable read-out of the entire CCD (1024×1024 pixels). The key data words in telemetry from the IRU are the 4 accumulated gyro counts (32 bits every 0.256 sec).

5.8 Performing an Observation

5.8.1 Star acquisition

After maneuvering at a rate of up to 2°/minute to a new celestial location using gyroscope data and the reaction wheels, *Chandra* begins the star acquisition sequence, a process which typically takes from 1 to 4 minutes. First the OBC commands the ACA to search for up to 8 acquisition stars, which are selected to be as isolated from nearby stars as possible. The search region size is based on the expected uncertainty in attitude, which is a function of the angular size of the slew. If two or more acquisition stars are found, an attitude update is performed using the best (brightest) pair of stars. This provides pointing knowledge to $3''$ ($3\,\sigma$ per axis). Next the guide star search begins. Depending on the particular star field configuration, the star selection algorithm may choose guide stars which are the same as the acquisition stars. In this case the guide star acquisition time is somewhat reduced. When at least two guide stars have been acquired and pointing control errors converge, the on-board Kalman filtering is activated and the transition to Normal Point Mode is made, at which point sensing of the fiducial lights begins.

5.8.2 Science pointing scenarios

The on-board PCAD system is flexible and allows several different *Chandra* science pointing scenarios, described in the following sections.

Normal Pointing Mode Dither

The large majority of observations are performed using Normal Point Mode, with dither selected. In this case the *Chandra* line-of-sight will be commanded through a Lissajous pattern. Dithering distributes photons over many detector elements (microchannel pores or CCD pixels) and serves several purposes: reduces uncertainty due to pixel to pixel variation in quantum efficiency (QE); allows sub-sampling of the image; and, in the case of the HRC, distributes the total exposure over many microchannel pores - useful since the QE of a pore degrades slowly with exposure to photons. The dither pattern parameters are amplitude, phase, and period for two axes. Each of the six parameters is separately commandable and differ for the two different instruments (See Chapters 6 and 7). The default values for these parameters are given in Table 5.4. Dither can be disabled for ACIS observations, while the minimum dither rate required to maintain the health of the HRC is $0.02''$/sec. The maximum dither rate, determined by PCAD stability requirements, is $0.22''$/sec.

Table 5.4: Default dither parameters

Parameter	**HRC**	**ACIS**
Phase (pitch)	0.0 rad	0.0 rad
Phase (yaw)	0.0 rad	0.0 rad
Amplitude (pitch)	20.0 arcsec	8.0 arcsec
Amplitude (yaw)	20.0 arcsec	8.0 arcsec
Period (pitch)	768.6 sec	707.1 sec
Period (yaw)	1087.0 sec	1000.0 sec

Normal Pointing Mode Steady

This mode is identical to NPM dither, but without the dither.

Pointing at solar system objects

Observations of moving solar system objects are done using a sequence of pointed observations, with the object moving through the field of view during each dwell period. Except in special circumstances, each pointing is selected so that the object remains within $5'$ of the *Chandra* line-of-sight. Most solar system objects move slowly enough that a single pointed observation will suffice.

Raster scan

Survey scans of regions larger than the instrument field of view are specified simply with a grid, i.e., a list of target coordinates giving the field centers. The fields can optionally overlap, depending on the science requirements of the survey.

Offset and gyro hold

In special circumstances it will be necessary to perform observations without tracking guide stars. It may occur that a field has no suitable acquisition and guide stars, although this situation has not been encountered to date. A more likely situation is that a very bright object, such as the Earth or Moon, saturates the ACA CCD and precludes tracking stars. In this case *Chandra* will first be maneuvered to a nearby pointing which has guide stars to establish fine attitude and a gyro bias estimate. A dwell time of approximately 25 minutes is needed to calibrate the bias estimate, which is the dominant term in the drift equation below. *Chandra* will then be maneuvered to the target. The default automatic transition to NPM will be disabled, and the spacecraft will hold on the target attitude in NMM.

While holding on gyros only, the spacecraft attitude will drift due to noise in the gyros, which results in an aspect solution error. The variance of the angle drift for each gyro axis, in time t, is given by

$$\sigma^2 = \sigma_b^2 t^2 + \sigma_v^2 t + \sigma_u^2 t^3/3$$

Ground test data for gyro noise parameters indicate worst case values of $\sigma_u = 1.5 \times 10^{-5}$ arcsec sec$^{-3/2}$ and $\sigma_v = 0.026$ arcsec sec$^{-1/2}$. Analysis of the residual Kalman filter bias estimate gives $\sigma_b = 0.002$ arcsec sec^{-1}. This results in 1-σ angle drift errors of: 0.3$''$ for 0.1 ksec; 2.2$''$ for 1 ksec; 11$''$ for 5 ksec; and 22$''$ for 10 ksec. After a maximum of 7.2 ksec, *Chandra* will be maneuvered back to the nearby field with guide stars in order to re-establish fine attitude and update the gyro drift rate.

5.8.3 PCAD capabilities (advanced)

Monitor star photometry

The ACA has the capability to devote one or more of the eight image slots to "monitor" particular sky locations. This allows simultaneous optical photometry of one or more targets in the ACA field of view. These optical sources can be slightly fainter than the ACA guide star limit of $m_{ACA} = 10.2$ mag. The bright-end limit for monitor star photometry is $m_{ACA} = 6.2$ mag. However, since there are a fixed number of image slots, devoting a slot to photometry instead of tracking a guide star results in a degradation of the image reconstruction and celestial location accuracy (Section 5.4). Using one monitor slot represents a 15 - 25% increase in the aspect image reconstruction RMS diameter, depending on the particular guide star configuration. Two monitor slots would increase the diameter by about 50 - 60%, but this configuration is not operationally allowed under normal circumstances. The photometric accuracy which can be achieved depends primarily on the star magnitude, integration time, CCD dark current, CCD read noise, sky background, and the CCD dark current uncertainty.

Dark current uncertainty ultimately limits the photometric accuracy at the faint end, and results from uncalibrated pixel-to-pixel changes in dark current due to radiation damage. This includes both changing background pixels as Chandra dithers, as well as intrinsic flickering in the radiation-damaged CCD pixels. This flickering, which occurs on time scales from less than 1 ksec to more than 10 ksec, poses fundamental problems for accurate photometry since the background dark current is a strong random function of time. With straightforward data processing, the noise introduced by the dark current variations (both spatial and temporal) is approximately 300 e-/sec. A star with an ACA magnitude of 12.0 produces about 1100 e-/sec, giving a S/N of 3.7. This represents the practical faint limit for ACA monitor star photometry. Somewhat improved S/N could be obtained with a more sophisticated analysis which tracks the time-dependent dark current of each pixel. Users interested in processing ACA monitor window data are advised to contact the CXC HelpDesk for assistance.

The zero instrument magnitude is defined as the Aspect Camera response to a zero magnitude star of spectral class G0V. The conversion from V and B magnitude to ACA instrument magnitude, based on flight data, is given approximately by

$$m_{ACA} = V + 0.426 - 1.06(B-V) + 0.617(B-V)^2 - 0.307(B-V)^3$$

5.9 Ground Processing

For each science observation, the aspect system data described in Section 5.7.3 are telemetered to the ground to allow post-facto aspect determination by the *CXC* aspect pipeline, as part of the standard *CXC* data processing pipeline. The important components of the pipeline are:

Gyro process: Filter gyro data, gap-fill, and calculate raw spacecraft angular rate

ACA process: Filter bad pixels, make CCD-level corrections (e.g. dark current), find spoiler stars, centroid, make camera-level corrections, convert to angle

Kalman filter and smooth: Optimally combine ACA and gyro data to determine ACA celestial location and image motion

Combine ACA and fids: Derive fid light solution and combine with ACA solution to generate image motion and celestial location at the focal plane science instrument.

5.9.1 Data products

The data products which are produced by the aspect solution pipeline are listed in Table 5.5. Key data elements include: IRU accumulated counts; raw pixel data for 8 images; observed magnitudes, pixel positions of the aspect stars and fiducial lights versus time; and aspect solution versus time. The star data are used to determine the RA, Dec, and roll (and corresponding uncertainties) of the HRMA axis as a function of time. The fid light images are used to track any drift of the SIM away from the nominal position. One cause of such drift is thermal warping of the optical bench assembly. The Kalman filtering routines also calculate an optimal estimate of the gyro bias rate as a function of time.

5.9.2 Star catalog

The Aspect system uses the *AGASC* (AXAF Guide and Aspect Star Catalog) version 1.6. Further information about the *AGASC*, as well as access to catalog data, can be found on the *CXC AGASC* web page http://cxc.harvard.edu/agasc). The *AGASC* was

Table 5.5: Aspect pipeline data products

Product	Description
ASPSOL	Final aspect solution with errors
ASPQUAL	Aspect solution quality indicators
AIPROPS	Aspect Intervals
ACACAL	ACA calibration data from ODB and CALDB
GSPROPS	Guide star properties, both from the AXAF Guide and Acquisition Star Catalog, and as actually observed with the ACA
FIDPROPS	Fiducial light properties, as commanded and as observed
ACADATA	Aspect camera telemetry (including ACA housekeeping), and images after CCD -level correction
ACACENT	Image centroids and associated fit statistics
GYROCAL	Gyro calibration data from ODB and CALDB
GYRODATA	Gyro raw and gap-filled, filtered data
KALMAN	Intermediate and final data in Kalman filter and smoother

prepared by the *CXC* Mission Planning and Operations & Science Support groups, and is a compilation of the Hubble Guide Star Catalog, the Positions and Proper Motion Catalog and the Tycho Output Catalog.

Chapter 6

ACIS: Advanced CCD Imaging Spectrometer

6.1 Introduction & Layout

The Advanced CCD Imaging Spectrometer (ACIS) offers the capability to simultaneously acquire high-resolution images and moderate resolution spectra. The instrument can also be used in conjunction with the High Energy Transmission Grating (HETG) or Low Energy Transmission Grating (LETG) to obtain higher resolution spectra (see Chapters 8 and 9). ACIS contains 10 planar, 1024 x 1024 pixel CCDs (Figure 6.1); four arranged in a 2x2 array (ACIS-I) used for imaging, and six arranged in a 1x6 array (ACIS-S) used either for imaging or as a grating readout. Currently any combination of up to 6 CCDs may be operated simultaneously. However, see the discussion in Section 6.20.1 where we encourage users, where possible, to specify as many as 5 chips as optional. Prior popular combinations include an extended ACIS-I imaging mode, using chips I0-I3 plus S2 and S3; and an ACIS-S imaging mode, using chips S1-S4 plus I2 and I3. Operating six chips enhances the chance of serendipitous science, but at the price of increased total background counting rate and therefore a somewhat enhanced probability of saturating telemetry. Another penalty for 6 operating CCDs is an increased power load (Section 6.20.1). Two CCDs are back-illuminated (BI) and eight are front-illuminated (FI). The response of the BI devices extends to energies below that accessible to the FI chips. The chip-average energy resolution of the BI devices is better than that of the FI devices.

The original Instrument Principal Investigator for ACIS is Prof. Gordon Garmire (Pennsylvania State University). ACIS was developed by a collaboration between Penn State, the *MIT* Kavli Institute for Astrophysics and Space Research and the Jet Propulsion Laboratory, and was built by Lockheed Martin and *MIT*. The *MIT* effort was led by Dr. George Ricker. The CCDs were developed by *MIT*'s Lincoln Laboratory.

ACIS is a complex instrument having many different characteristics and operating modes. Radiation damage suffered by the FI chips has had a negative impact on their energy resolution – the BI devices were not impacted – thus impacting the basic con-

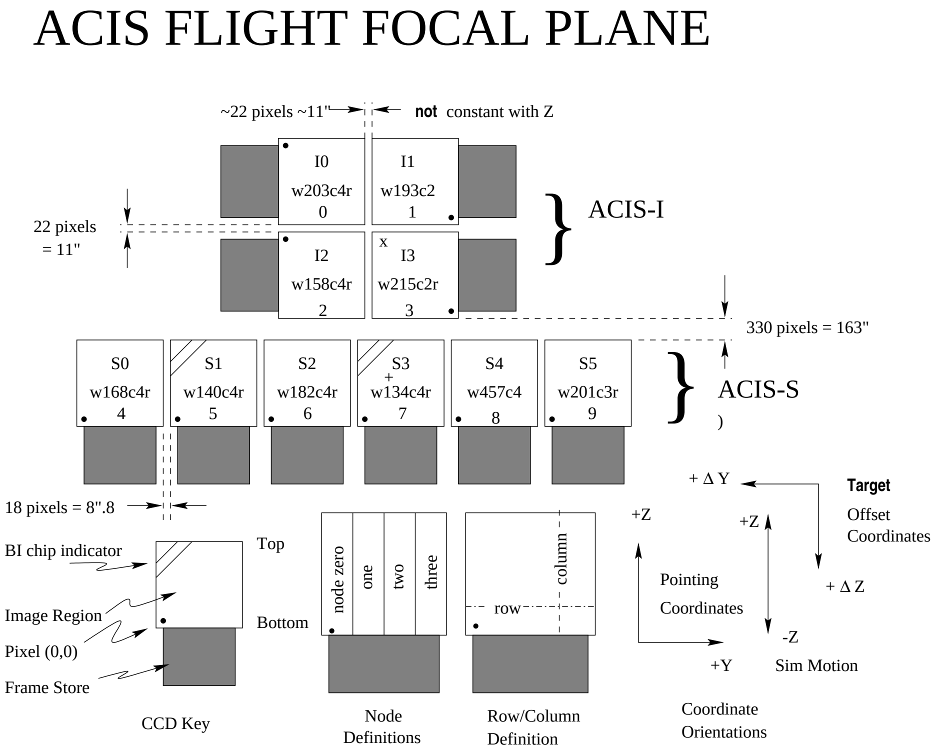

Figure 6.1: A schematic drawing of the ACIS focal plane; insight to the terminology is given in the lower left. Note the nominal aimpoints: on S3 (the '+') and on I3 (the 'x'). It is standard practice to add an offset to all observations on S3 to move the source away from the node 0-1 boundary (see Section 6.10). Note the differences in the orientation of the I and S chips, important when using subarrays (Section 6.12.1). Note also the (Y, Z) coordinate system and the target offset convention (see Chapter 3) as well as the SIM motion (+/-Z). The view is along the optical axis, from the source toward the detectors, (-X). The numerous ways to refer to a particular CCD are indicated: chip letter+number, chip serial number, and ACIS chip number. The node numbering scheme is illustrated lower center.

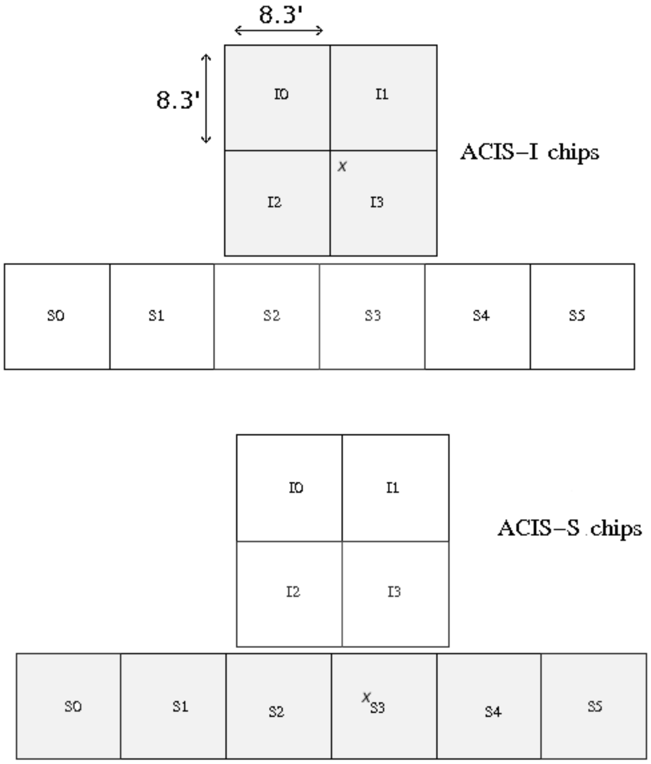

Figure 6.2: A schematic drawing of the ACIS focal plane, not to scale. The ACIS-I array consists of chips I0-I3. Chips S2 and S3 are often turned on in addition to I0-I3 when ACIS-I is used in imaging mode as indicated in the top figure. ACIS-S consists of chips S0-S5. When operated in imaging mode chips S1-S4 plus I2 and I3 are often turned on (bottom figure). When operated in spectroscopy mode S0-S5 are usually turned on. See 6.20.1 for more details on chip choices.

siderations as to how to make best use of the instrument. We discuss the trade-offs in this chapter. Software methods for improving the energy resolution of the FI CCDs are discussed in Section 6.7.1. The low energy response of ACIS has also been affected by the build-up of a contaminant on the optical blocking filters and this is discussed in Section 6.5.1.

Many of the characteristics of the ACIS instrument are summarized in Table 6.1.

6.2 Basic Principles

A CCD is a solid-state electronic device composed primarily of silicon. A "gate" structure on one surface defines the pixel boundaries by alternating voltages on three electrodes spanning a pixel. The silicon in the active (depletion) region (the region below the gates wherein most of the absorption takes place) has an applied electric field so that charge moves quickly to the gate surface. The gates allow confined charge to be passed down a "bucket brigade" (the buried channel) of pixels in parallel to a serial readout at one edge by appropriately varying ("clocking") the voltages in the gates.

The ACIS front-illuminated CCDs have the gate structures facing the incident X-ray beam. Two of the chips on the ACIS-S array (S1 and S3) have had treatments applied to the back sides of the chips, removing insensitive, undepleted bulk silicon material and leaving the photo-sensitive depletion region exposed. These are the BI chips and are deployed with the back side facing the HRMA.

Photoelectric absorption of an X-ray in silicon results in the liberation of a proportional number of electrons: an average of one electron-hole pair for each 3.7 eV of energy absorbed. Immediately after the photoelectric interaction, the charge is confined by electric fields to a small volume near the interaction site. Charge in a FI device can also be liberated below the depletion region, in an inactive substrate, from where it diffuses into the depletion region. This charge may easily appear in two or more pixels.

Good spectral resolution depends upon an accurate determination of the total charge deposited by a single photon. This in turn depends upon the fraction of charge collected, the fraction of charge lost in transfer from pixel to pixel during read-out, and the ability of the readout amplifiers to measure the charge. Spectral resolution also depends on read noise and the off-chip analog processing electronics. The ACIS CCDs have readout noise less than 2 electrons RMS. Total system noise for the 40 ACIS signal chains (4 nodes/CCD) ranges from 2 to 3 electrons (rms) and is dominated by the off-chip analog processing electronics.

The CCDs have an "active" or imaging section (see Figure 6.1) which is exposed to the incident radiation and a shielded "frame store" region. A typical mode of the ACIS CCD operation is: (1) the active region is exposed for a fixed amount of time (full frame ~ 3.2 s); (2) at the end of the exposure, the charge in the active region is quickly (~ 41 ms) transferred in parallel into the frame store; (3) the next exposure begins; (4) simultaneously, the data in the frame store region is transferred serially to a local processor

Focal plane arrays:	
I-array	4 CCDs placed to lie tangent to the focal surface
S-array	6 CCDs in a linear array tangent to the grating Rowland circle
CCD format	1024 by 1024 pixels
Pixel size	23.985 microns (0.4920±0.0001 arcsec)
Array size	16.9 by 16.9 arcmin ACIS-I
	8.3 by 50.6 arcmin ACIS-S
On-axis effective Area	110 cm^2 @ 0.5 keV (FI)
(integrated over the PSF	600 cm^2 @ 1.5 keV (FI)
to >99% encircled energy)	40 cm^2 @ 8.0 keV (FI)
Quantum efficiency	$> 80\%$ between 3.0 and 6.5 keV
(frontside illumination)	$> 30\%$ between 0.7 and 11.0 keV
Quantum efficiency	$> 80\%$ between 0.8 and 5.5 keV
(backside illumination)	$> 30\%$ between 0.4 and 10.0 keV
(QEs do not include contaminant layer transmission)	
Charge transfer inefficiency(parallel)	FI: $\sim 2\times10^{-4}$; BI: $\sim 2\times10^{-5}$
Charge transfer inefficiency(serial)	S3(BI): $\sim 7\times10^{-5}$; S1(BI): $\sim 1.5\times10^{-4}$; FI: $< 2\times10^{-5}$
System noise	$<\sim$ 2 electrons (rms) per pixel
Max readout-rate per channel	$\sim$ 100 kpix/sec
Number of parallel signal channels	4 nodes per CCD
Pulse-height encoding	12 bits/pixel
Event threshold	FI: 38 ADU ($\sim$150–350 eV)
	BI: 20 ADU ($\sim$150–220 eV)
Split threshold	13 ADU
Max internal data-rate	6.4 Mbs (100 kbs $\times 4 \times 16$)
Output data-rate	24 kb per sec
Minimum row readout time	2.8 ms
Nominal frame time	3.2 sec (full frame)
Allowable frame times	0.2 to 10.0 s
Frame transfer time	40 μsec (per row)
Point-source sensitivity	4×10^{-15} ergs cm^{-2} s^{-1} in 10^4 s (0.4-6.0 keV)
Detector operating temperature	-90 to -120°C

Table 6.1: ACIS Characteristics

Table 6.2: Nominal Optical Blocking Filter Composition and Thicknesses

ACIS-I	Al/Polyimide/Al	1200Å 2000Å 400Å
ACIS-S	Al/Polyimide/Al	1000Å 2000Å 300Å

which, after removing bias (see Section 6.13), identifies the position and amplitude of any "events" according to a number of criteria depending on the precise operating mode. These criteria always require a local maximum in the charge distribution above the event threshold (see Table 6.1). The position and the amount of charge collected, together with similar data for a limited region containing and surrounding the pixel are classified ("graded") and then passed into the telemetry stream.

6.3 Optical Blocking Filter & Optical Contamination

Since the CCDs are sensitive to optical as well as X-ray photons, optical blocking filters (OBFs) are placed just over the CCDs between the chips and the HRMA. The filters are composed of polyimide (a polycarbonate plastic) sandwiched between two thin layers of aluminum. The nominal thicknesses of the these components for the two arrays are given in Table 6.2. Details of the calibration of these filters may be found in the ACIS calibration report at http://www.astro.psu.edu/xray/docs/cal_report/node188.html. These calibrations do not include the more recent effects of molecular contamination. This is discussed in Section 6.5.1.

The threshold for optical contamination (a 1 ADU (3.4 eV) shift in the bias level) is based on on-orbit calibrations of a number of stars with different optical spectra. The threshold for detectable visible light contamination varies according to source color and is lowest for red stars observed on ACIS-S The detection threshold for an M star on the ACIS-S array is V∼8.1 for the nominal 3.2 second exposure or V∼6.3 using a 0.4s frame time and a 1/8 chip subarray. The thresholds are about 5 visual magnitudes brighter for the ACIS-I array. While the impact of the OBF molecular contamination has not been studied in detail, a preliminary estimate (using typical optical constants for organic materials) suggests little change in the broadband optical transmission. See Section 6.19 for a discussion of the observation of optically bright targets such as solar system objects.

6.4 Calibration

Measurements of ACIS include laboratory calibrations, a system-level ground calibration of the HRMA and ACIS at the X-Ray Calibration Facility (XRCF) at MSFC, and on-orbit calibration using celestial and on-board radioactive X-ray sources. The ACIS external calibration source (ECS) consists of an Fe-55 source and a target made of aluminum and titanium. The source emits five strong lines (Al K–α at 1.49 keV, Ti K–α and β, at 4.51

and 4.93 keV, and Mn K–α and β at 5.90 and 6.49 keV. A number of weaker lines are also present.

The on-orbit calibration of ACIS is a continuing activity. All calibration data are, or will be, described in detail, at http://cxc.harvard.edu/cal/. The user is urged to consult the WWW site and its links for the latest information.

6.5 Quantum Efficiency and Effective Area

The quantum efficiencies near the readout for the ACIS CCDs for the standard grade set, including optical blocking filters and molecular contamination, are shown in Figure 6.3. Note that the quantum efficiency for the FI chips varies somewhat with row number (not shown), and decreases by 5–15% farthest from the readout at energies above about 4 keV. This is due to the migration of good grades to bad grades produced by charge transfer inefficiency (CTI), which varies with row number. The quantum efficiency (QE) variation with position for the BI chips is much smaller.

Cosmic rays tend to cause large blooms on FI chips, and much smaller ones on BI chips. This results in a 2–4% decrement of the QE for FI chips and $\sim 0.5\%$ for BI chips.

The combined HRMA/ACIS on-axis effective areas are shown in Figure 6.4 (log energy scale) and 6.5 (linear energy scale). The effective areas are for an on-axis point source and a 20-arcsecond-diameter detection cell. The ACIS effective areas include a correction that accounts for the build-up of molecular contamination on the ACIS filters (see the discussion in Section 6.5.1). Figures 6.4 and 6.5 show the predicted ACIS effective areas for the middle of Cycle 14 based on the current time-dependent ACIS contamination models.

There is a count rate dependent effect, currently under investigation, that may impact a subset of observers. The problem is that the effective area calibration at the Si K edge (1.842 keV; 6.74 Å) appears to be somewhat incorrect, but only at very high count rates. At high rates, the edge will appear somewhat higher than it should be. Here high count rate is: 1.9×10^{10} erg cm^{-2} s^{-1} (ACIS) and 1.1×10^{-9} erg cm^{-2} s^{-1} (HETG/ACIS). Of course at these counting rates pileup will likely dominate ACIS observations, but not necessarily HETG/ACIS observations. In very extreme cases, the effective discrepancy between the fluxes determined by the nominal effective area and observation may be as large as 10%. The effect manifests itself in strong residuals around the edge region for sources with moderate absorption columns ($< 3 \times 10^{21}$ cm^{-2}), an underestimate of the actual source column at higher absorption columns, and a change in effective area at higher energies.

Figure 6.6 shows the vignetting (defined as the ratio of off-axis to on-axis effective area) as a function of energy at several off-axis angles. These data are from a calibration observation of G21.5, a bright supernova remnant. The detector was appropriately offset for each off-axis angle so that the data were obtained at the same focal position, minimizing the effects of any spatially-dependent variations in the CCD response.

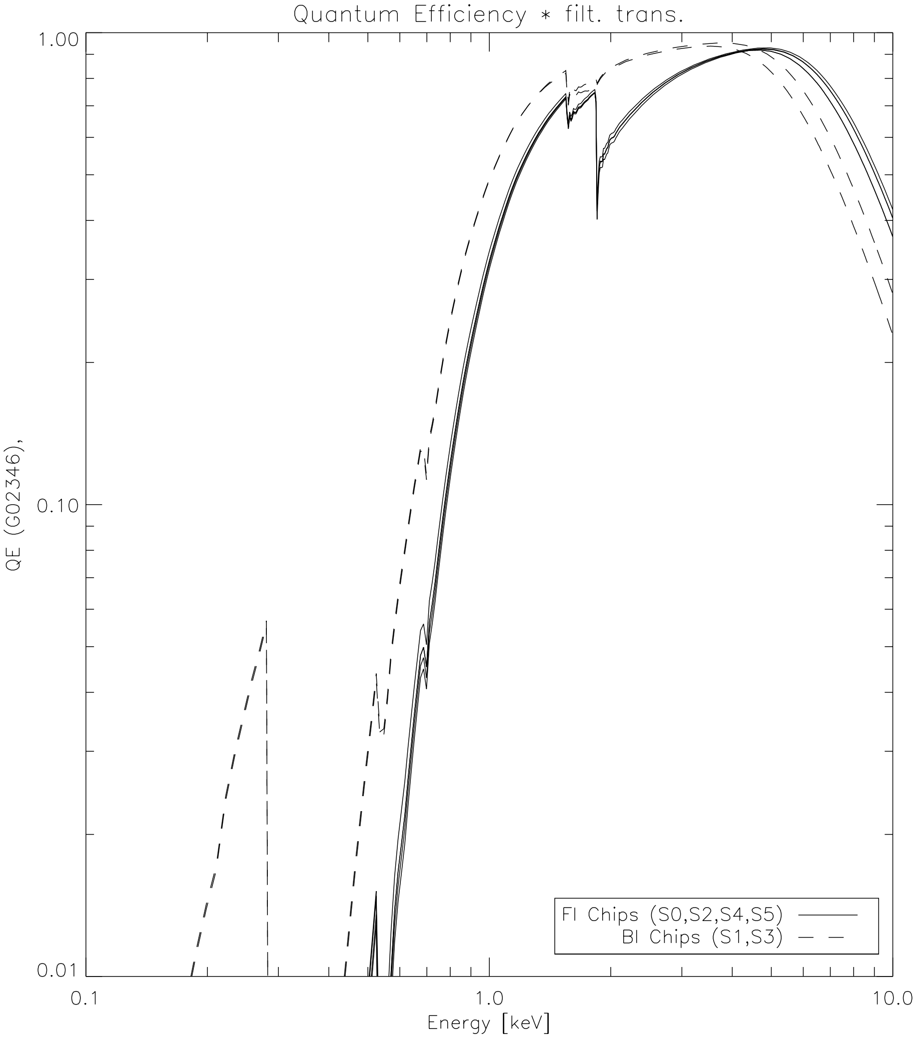

Figure 6.3: The quantum efficiency, convolved with the transmission of the appropriate optical blocking filter, of the FI CCDs (from a row nearest the readout) and the two BI CCDs as a function of energy. S3 is somewhat thicker, hence more efficient, than S1. These curves include the effects of molecular contamination, as discussed in the text.

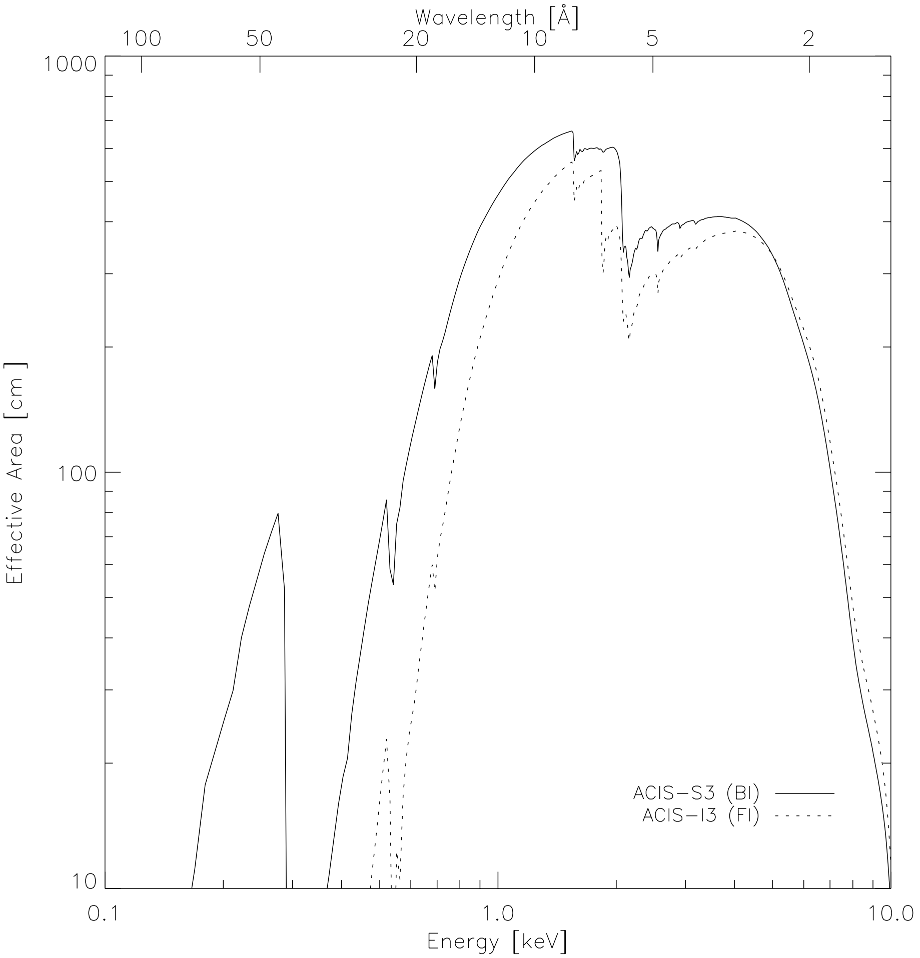

Figure 6.4: The HRMA/ACIS predicted effective area versus the energy on a log scale. The dashed line is for the FI CCD I3, and the solid line is for the BI CCD S3. These curves include the effects of molecular contamination, as discussed in the text.

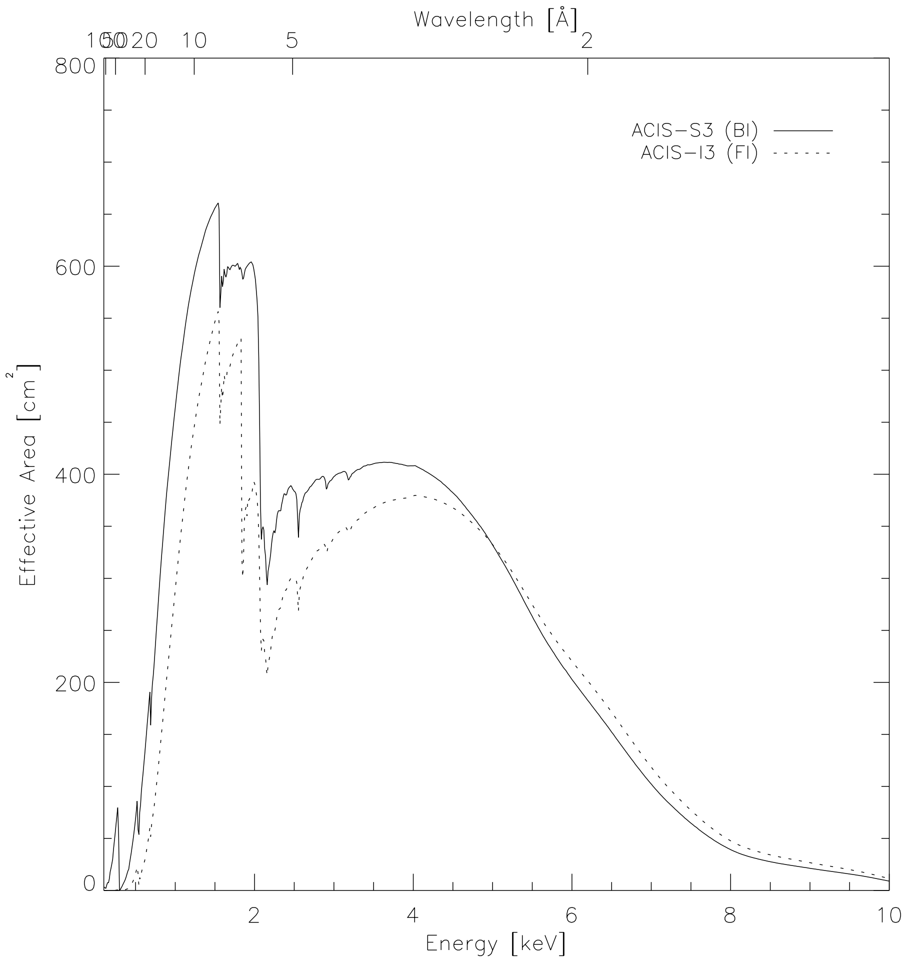

Figure 6.5: The HRMA/ACIS predicted effective area versus the energy on a linear scale. The dashed line is for the FI CCD I3, and the solid line is for the BI CCD S3. These curves include the effects of molecular contamination, as discussed in the text.

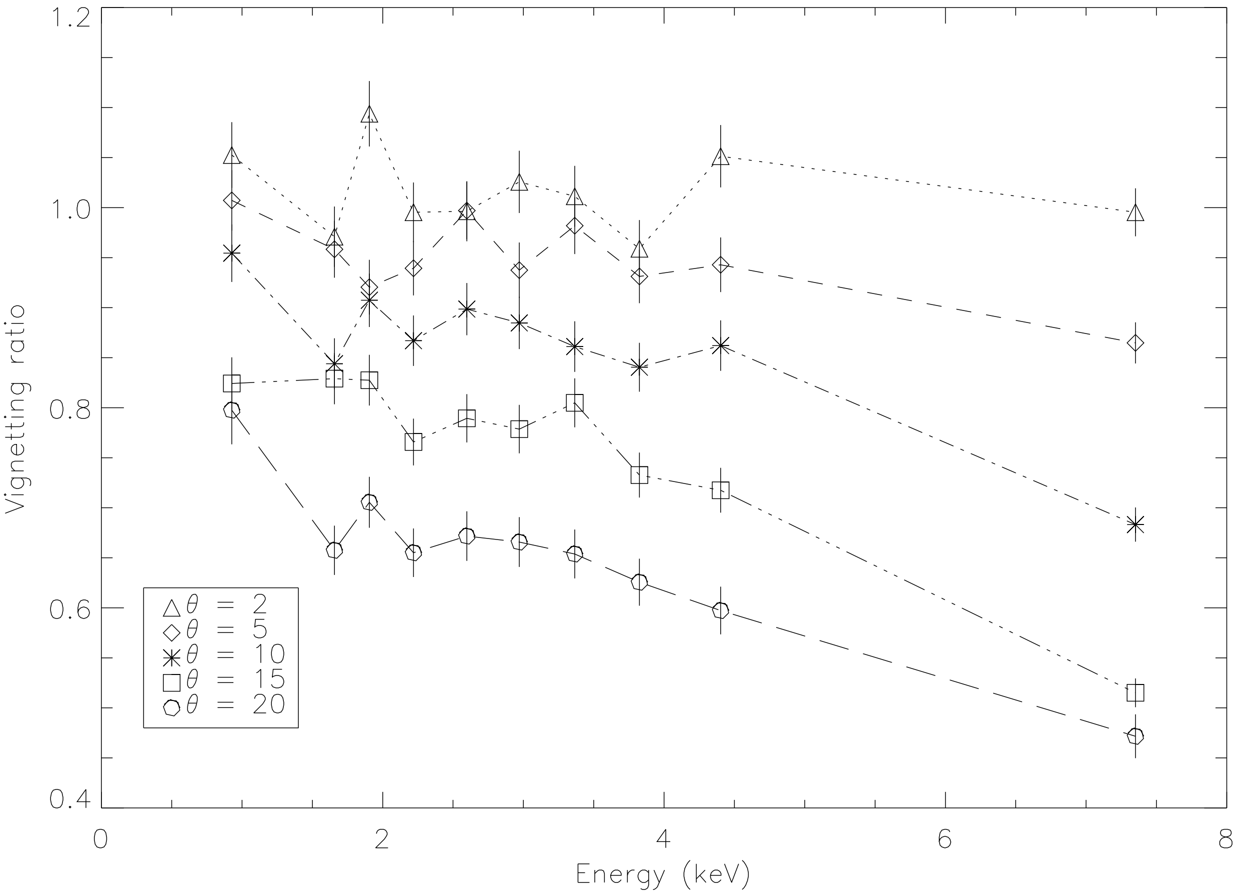

Figure 6.6: Vignetting (the ratio of off-axis to on-axis effective area) as a function of energy for several off axis angles in arcminutes.

6.5.1 Molecular Contamination of the OBFs

Astronomical observations and data acquired from the on-board ACIS external calibration source (ECS) show that there has been a slow and continuous degradation in the ACIS effective area at low energies. Our best explanation is that this is due to the build-up of out-gassed material condensing on the cold ACIS filters. The HRC operates at a warmer temperature and shows no sign of contamination build-up. The degradation in effective area is most severe at low energies. The build-up of contamination has been monitored by ECS observations before and after each perigee passage and by periodic observations with the gratings. The grating observations have shown that the contaminant is dominated by carbon, with smaller amounts of oxygen and fluorine. The ECS is used to monitor the degradation in effective area at energies above the C-K edge. The depth of the contaminant increases from the center of the detectors toward the edges where the filters are cooler.

Over the past few years we have performed annual raster scans of the rich cluster Abell 1795 to monitor the build-up of contamination on the ACIS filters. Analysis of the ECS and Abell 1795 produce consistent results for the optical depth of the contaminant at 700 eV. Since the ECS continues to fade due to the 2.7 year half-life of ^{55}Fe, we will be relying more heavily on these Abell 1795 observations to normalize the optical depth of the contaminant in the future.

An initial model of the contamination on the ACIS filter was developed for use in CIAO and other data reduction packages and released in CALDB v3.0.0 (Dec. 2004). Beginning in 2006, there were some systematic differences in the actual build-up rate of the contaminant on the ACIS filters compared with the predictions of the 2004 model. These differences were initially noticed from discrepancies in the optical depth of the contaminant as measured from ECS data and gratings observations of AGN. As a result, updated versions of the ACIS-I and ACIS-S contamination models were released in CALDB 4.2 (Dec. 2009). A further update to the ACIS-I contamination model was released in CALDB 4.4.1 (Dec. 2010). Analysis of calibration (both imaging and gratings) and ECS observations taken over the last few years show that the condensation rate of the molecular contamination onto the ACIS filters has increased. The inflection point in the growth curve of the ACIS contamination is consistent with the date when one of the ACIS detector housing heaters was turned off in April 2008 to help stabilize the ACIS focal plane temperature and detector gain. Also, since 2008, the difference between the optical depth at the edges and centers of the detectors has been increasing at a greater rate. As a result of these changes in the behavior of the ACIS contamination, an updated ACIS contamination model was released in CALDB 4.4.10 on May 30, 2012. This new model accounts for the greater condensation rate and spatial dependence of the molecular contaminant onto the ACIS filters.

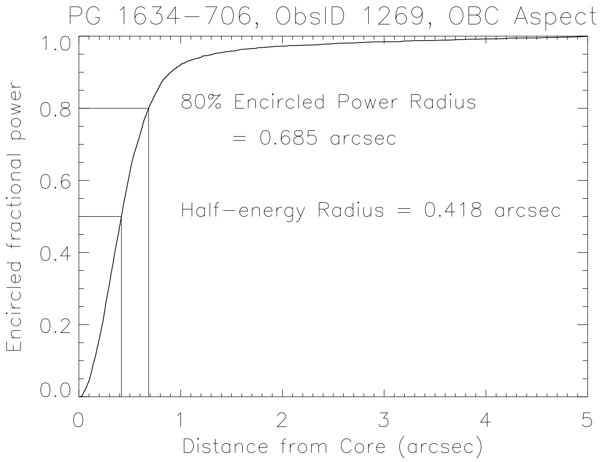

Figure 6.7: The on-orbit encircled broad-band energy versus radius for an ACIS observation of point source PG1634-706 (ObsID 1269). The curve is normalized to unity at a radius of 5 arcseconds. We estimate that the statistical uncertainty is 3%, and the systematic uncertainty due to power beyond 5″ is 2%. The effective energy is 1 keV.

6.6 Spatial Resolution & Encircled Energy

The spatial resolution for on-axis imaging with HRMA/ACIS is limited by the physical size of the CCD pixels (24.0 μm square ∼0.492 arcsec) and not the HRMA. This limitation applies regardless of whether the aimpoint is selected to be the nominal point on I3 or S3 (Figure 6.1). Approximately 90% of the encircled energy lies within 4 pixels (2 arcsec) of the center pixel at 1.49 keV and within 5 pixels (2.5 arcsec) at 6.4 keV. Figure 6.7 shows an in-flight calibration. There is no evidence for any differences in data taken with either S3 or I3 at the nominal focus. The ACIS encircled energy as a function of off-axis angle is discussed in Chapter 4 (see Section 4.2.2 and Figure 4.13).

Off-axis, the departure of the CCD layout from the ideal focal surface and the increase of the HRMA PSF with off-axis angle become dominating factors. Since the ideal focal surface depends on energy, observers for whom such considerations may be important are urged to make use of the MARX simulator to study the impact on their observation.

6.7 Energy Resolution

The ACIS FI CCDs originally approached the theoretical limit for the energy resolution at almost all energies, while the BI CCDs exhibited poorer resolution. The pre-launch energy resolution as a function of energy is shown in Figure 6.8. Subsequent to launch and orbital activation, *the energy resolution of the FI CCDs has become a function of the row number*, being near pre-launch values close to the frame store region and substantially degraded in

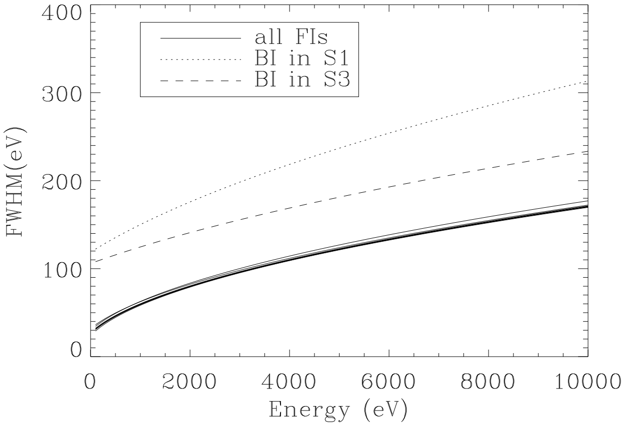

Figure 6.8: The ACIS pre-launch energy resolution as a function of energy.

the farthest row. An illustration of the dependence on row is shown in Figure 6.9.

The loss of energy resolution is due to increased charge transfer inefficiency (CTI) caused by low energy protons encountered during radiation belt passages and Rutherford scattering through the X-ray telescope onto the focal plane. Subsequent to the discovery of the degradation, operational procedures were changed: ACIS is not left at the focal position during radiation belt passages. Since this procedure was initiated, no further degradation in performance has been encountered beyond that predicted from pre–launch models. The BI CCDs were not impacted, which is consistent with the proton-damage scenario – it is far more difficult for low-energy protons from the direction of the HRMA to deposit their energy in the buried channels of the BI devices, since the channels are near the gates and the gates face in the direction opposite to the HRMA. Thus the energy resolution for the two BI devices remains nearly at pre-launch values. The position-dependent energy resolution of the FI chips depends significantly on the ACIS operating temperature. Since activation, the ACIS operating temperature has been lowered in steps and is now set at the lowest temperature thought safely and consistently achievable ($\sim -120°$C).

6.7.1 Correcting the Energy Resolution of the CCDs

The ACIS instrument team has developed a correction algorithm that recovers much of the lost energy resolution the FI CCDs. The correction recovers a significant fraction of the CTI-induced loss of spectral resolution of the FI CCDs at all energies. The algorithm has been incorporated in the *CIAO* tool acis_process_events as of *CIAO* 2.3. Figure 6.9 illustrates the improvement that the tool provides. As of December 2006, data for the two BI chips can also be corrected in the same way, including a correction for serial CTI for the BI chips, though the effects are more subtle. The resulting response is very nearly uniform across the BI chips once this correction is made. An alternative corrector may be

Table 6.3: Spectral Resolution at default aimpoints

ccd	chipx	chipy	1.49 keV	5.9 keV
I3, no offset	941	988	155.757	284.542
I3, w offset	972	964	131.488	256.309
S3, no offset	224	490	95.3451	147.033
S3, w offset	206	521	96.7391	151.302

found at the *Chandra* contributed SW exchange web site and also at the Penn State ACIS page (http://www.astro.psu.edu/users/townsley/cti/install.html).

The energy resolution (here taken to mean the full width at half maximum [FWHM] of a narrow spectral line) of ACIS varies roughly as the square root of the energy, and increases with distance from the readout. On FI chips (the I array and all the S array chips but S1 and S3), the increase with CHIPY (row number) is dramatic, as can be seen in Figure 6.9. The spatial dependence on BI chips (S1 and S3) is much weaker, but depends on both coordinates. To illustrate, we have measured the resolution at the default aimpoints (see Table 6.3), using the aluminum (1.49 keV) and manganese (5.9 keV) K-alpha lines in the external calibration source. Data were summed over three months in the summer of 2009, and over an area of 32 × 32 pixels.

6.8 Hot Pixels and Columns

Hot pixels and columns are defined to be those which produce a high spurious or saturated pulse-height for a large number of consecutive frames of data. These depend on operating conditions such as temperature. One should always refer to the *CXC* web site for the most recent list. To date, S1 is the device with the largest number of such pixels and columns.

6.9 Cosmic Ray Afterglows

Cosmic ray hits sometimes deposit so much charge that it appears in a number of successive frames in the same pixels. These cosmic ray afterglows are essentially temporary hot pixels, and are removed by the hot pixel logic if they contain more than approximately 8 events.

6.10 Aimpoints

Aimpoints are the nominal positions on the ACIS where the flux from a point source with no target offsets is placed. There are two nominal aimpoints, indicated in Figure 6.1 - one on the corner of I3 on the ACIS-I array (the ACIS-I aimpoint), and one near the boundary between nodes 0 and 1 on S3 of the ACIS-S array (the ACIS-S aimpoint). Their exact positions are given in Table 6.4. Note that the aimpoint is not the same as the optical

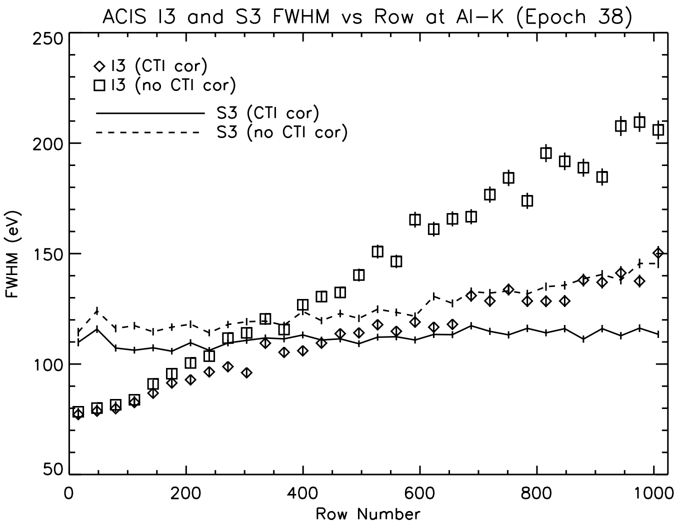

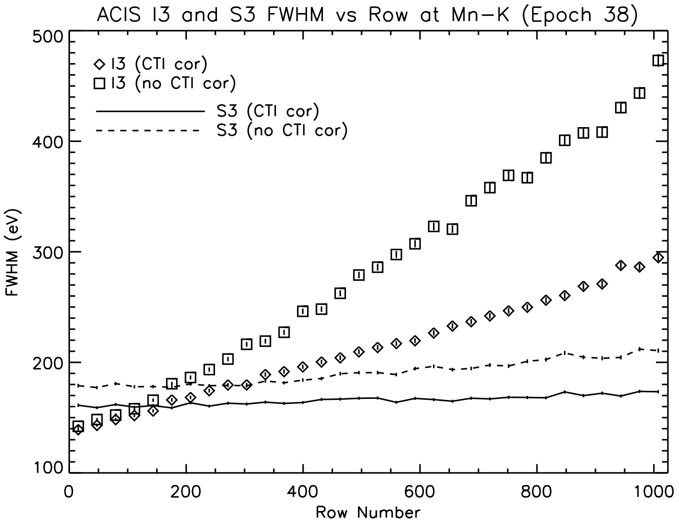

Figure 6.9: We plot energy resolution (FWHM in eV) vs row number (CHIPY) for several cases. At the top, we show Aluminum K-alpha (1.49 keV), while the bottom plot is for Manganese K-alpha (5.9 keV). In each panel, the data points represent the response of the I3 chip (upper curve, without CTI correction; lower curve, with CTI correction), while the lines represent the response of S3. Data were taken from May through July of 2009, on I3 node 3, and S3 node 0 (where the aimpoints are). Nominal aim points are given in chip coordinates in tables 6.4 and 6.5.

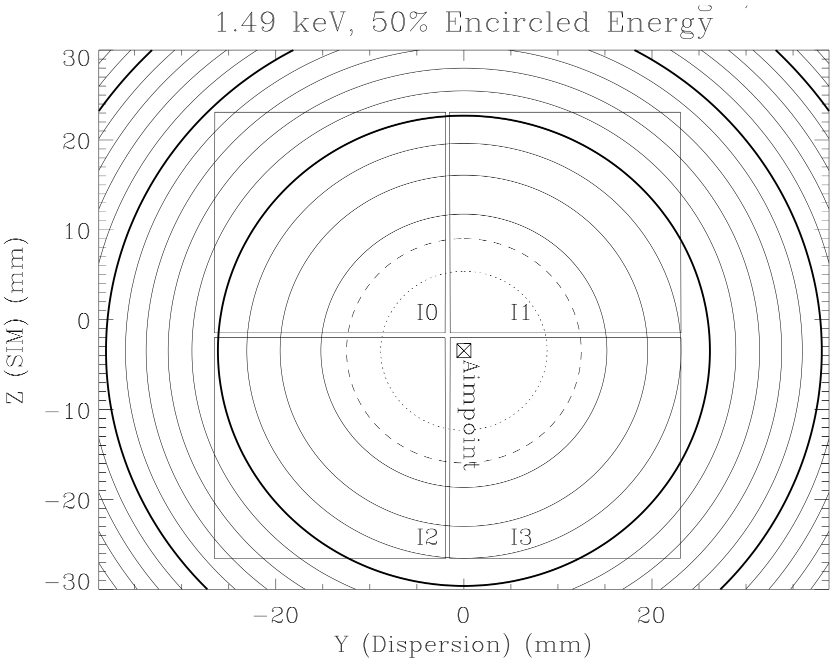

Figure 6.10: Approximate contours of constant 50% encircled energy at 1.49 keV when the ACIS-I default aimpoint is selected. The dotted line is 1 arcsec, the dashed line is 1.5 arcsec. The remainder are at 1 arcsec intervals. The thicker solid lines highlight the 5, 10, and 15 arcsec contours.

axis, which is defined as the position of the narrowest PSF and found approximately 10" from the aimpoints. Because of thermal relaxation of spacecraft structures, the chip coordinates of the optical axis have changed over the mission lifetime. For zero SIM-Z offsets, the aimpoint on ACIS-I is at the I3 chip coordinates (941,988) and on ACIS-S, at the S3 chip coordinates (224,490). Approximate contours of constant encircled energy for ACIS-I and ACIS-S observations for the default aimpoints are shown in Figures 6.10 and 6.11. If required, other aimpoints may be selected along the Z-axis.

In late 2006, a $10''$ shift in the alignment of the aspect camera occurred when its primary focal plane temperature was cooled from −15C to −19C. In 2011 July, *Chandra* entered a safemode, and since that time the aimpoint has drifted back to near the 2007 position. However, its short term instability has increased in the past two years or so, especially after the safemode. In combination with the long-term alignment drift, the ACIS aimpoints using the previous default Y and Z offsets have shifted. In order to place the aimpoint so that targets are at the optimal positions with respect to CHIP geometry and telescope focus, we have updated the default offsets for ACIS-S to $\Delta Y = +9''$ and $\Delta Z = -15''$, to avoid dithering across the node boundary on the S3 chip. For ACIS-I the default offsets of $\Delta Y = -12''$ and $\Delta Z = -15''$ are unchanged. For grating observations an

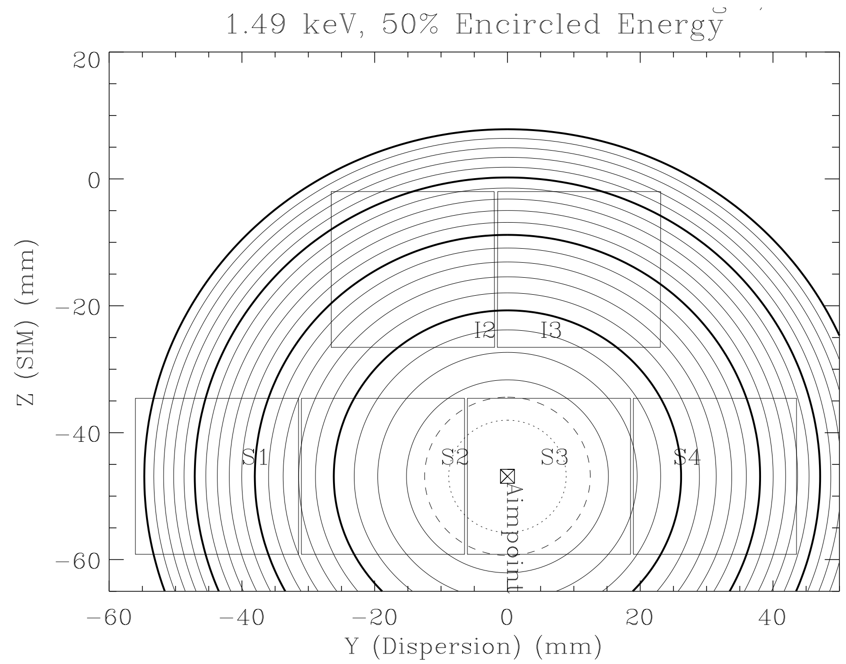

Figure 6.11: Approximate contours of constant 50% encircled energy at 1.49 keV when the ACIS-S default aimpoint is selected. The dotted line is 1 arcsec, the dashed line is 1.5 arcsec. The remainder are at 1 arcsec intervals. The thicker solid lines highlight the 5, 10, 15 and 20 arcsec contours.

Table 6.4: Aimpoint positions summarized in pixels (chip-x, chip-y)

ACIS-I :	(941, 988) in I3	no offsets
ACIS-I :	(972, 964) in I3	with offsets of $\Delta Y = -12''$, $\Delta Z = -15''$
ACIS-S :	(224, 490) in S3	no offsets
ACIS-S :	(206, 521) in S3	with default offsets $\Delta Y = +9''$, $\Delta Z = -15''$

Table 6.5: Recommended SIM-Z offsets

Observation Mode	SIM-Z Offset	Source Position (w/Offsets $\Delta Y = +9''$, $\Delta Z = -15''$)
ACIS-S w/ HETG TE mode:	-3mm = -1.02417′	(206, 396)
ACIS-S w/ HETG CC mode:	-4mm = -1.36556′	(206, 354)
ACIS-S w/ LETG TE mode:	-8mm = -2.73112′	(206, 187)
ACIS-S w/ LETG CC mode:	-8mm = -2.73112′	(206, 187)

offset toward the readout on the ACIS-S array is often recommended (i.e. in the negative Z direction – see Table 6.5). Note that standard ACIS subarrays (Section 6.12.1) will not center zeroth order if the recommended aimpoints are selected for a grating observation. In this case, a custom subarray is necessary (e.g. see Section 8.5)

Further information can be found in the memos linked from this page: http://cxc.harvard.edu/cal/Hrma/OpticalAxisAndAimpoint.html. Fig 6.12 shows the detailed drift of the aimpoint on ACIS-S3 over the life of the mission.

Lastly, it should be kept in mind that the observatory is typically dithered about the aimpoint with an 8″ half-amplitude (see Section 6.11, and 6.5 for recommended offsets).

6.11 Dither

Unless specially requested, the spacecraft is dithered during all observations. The dither pattern is a Lissajous figure. For observations with ACIS, the dither pattern spans 16 arcsec peak to peak. The dither serves two purposes: (1) to provide some exposure in the gaps between the CCDs, and (2) to smooth out pixel-to-pixel variations in the response. The dither is removed during high-level ground processing of the data. The exposure time in the gaps between chips (and at the outside edges) will be less than that for the remainder of the field. Default dither parameters are listed in Table 5.4.

6.11.1 Gaps Between the CCDs

The approximate sizes of the various gaps between chips are shown in Figure 6.1. Note that the Y-gaps in the ACIS-I array vary with Z due to the way the CCDs are tilted.

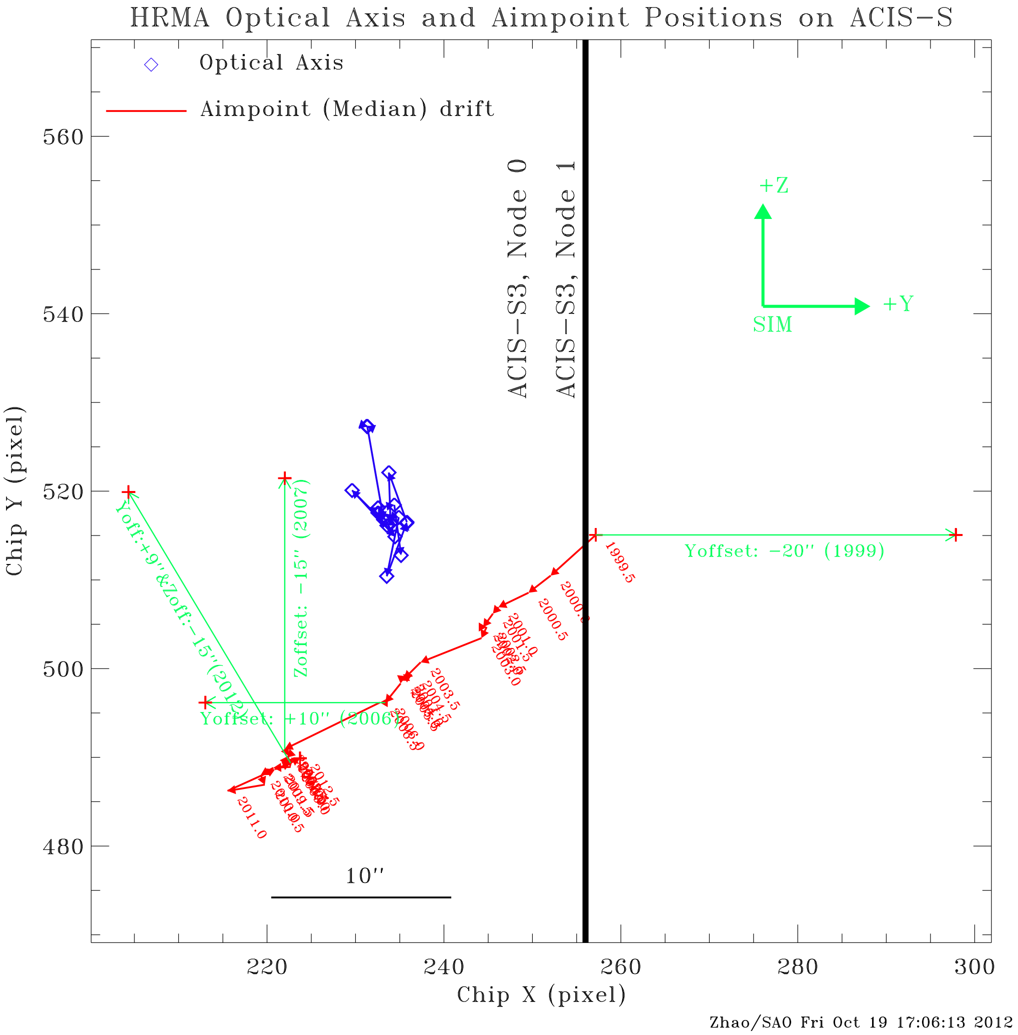

Figure 6.12: Position of the optical axis on the S3 CCD at various times in the mission. Since 1999, the aimpoint (position of optimal focus) has drifted (dark lines), and default pointing offsets (lighter lines) have been changed several times to move the image away from the node boundary. Dates are given in format YYYY-MM (year, followed by month).

6.12 Operating Modes

Here we describe the ACIS operating modes. There are only two such modes. One is Timed Exposure (TE) and the other is Continuous Clocking (CC). One must select one or the other for an observation as it is not possible to simultaneously operate individual CCDs in different modes during a single observation.

6.12.1 Timed Exposure (TE) Mode

A timed exposure refers to the mode of operation wherein a CCD collects data (integrates) for a preselected amount of time - the Frame Time. Once this time interval has passed, the charge from the 1024 x 1024 active region is quickly ($\sim$ 41 ms) transferred to the framestore region and subsequently read out through (nominally) 1024 serial registers.

Frame Times - Full Frames Frame times are selectable within a range of values spanning the time interval from 0.2 to 10.0 seconds. If the data from the entire CCD are utilized (full frame) then *the nominal (and optimal!) frame time is 3.2 s*, T_{opt}. Selecting a frame time *shorter* than the nominal value (e.g. to decrease the probability of pileup - Section 6.15) has the consequence that there will be a time during which *no* data are taken, "deadtime", as 3.2 s are required for the frame store readout process regardless of the frame time. The fraction of time during which data are taken is simply the ratio of the selected frame time to the sum of the nominal frame time and the 41 msec transfer time – *e.g.* for a new frame time of t (<3.2) secs, the fraction of time during which data are taken is $t/(T_{opt} + 0.041)$. We note, strictly speaking, the full-frame time depends on how many CCD s are on – see the equation below – but the differences are very small. Finally, we note that selecting a frame time *longer* than the most efficient value increases the probability of pileup occurring and is not recommended.

Frame Times & Subarrays It is also possible for one to select a *subarray* - a restricted region of the CCD in which data will be taken. A subarray is fully determined by specifying the number of rows separating the subarray from the framestore region (q) and the number of rows in the subarray (n). Examples of subarrays are shown in Figure 6.13. The nominal frame time for a subarray depends on (q), (n), and the total number of CCDs that are activated (m) – see Table 6.6. The nominal frame time is given by:

$$T(msec) = 41.12 \times \mathrm{m} + 0.040 \times (\mathrm{m} \times \mathrm{q}) + 2.85 \times \mathrm{n} - 32.99.$$

As with full frames, selecting a frame time less than the most efficient value results in loss of observing efficiency. Frame times are rounded up to the nearest 0.1 sec, and can range from 0.2 to 10.0 sec

When operating with only one chip, subarrays as small as 100 rows are allowed (this permits 0.3 sec frame times which pay no penalty in dead time). For multichip observations, the smallest allowed number of rows is 128.

Table 6.6: CCD Frame Time (seconds) for Standard Subarrays

Subarray	ACIS-I (no. of chips)		ACIS-S (no. of chips)	
	1	6	1	6
1	3.0	3.2	3.0	3.2
1/2	1.5	1.8	1.5	1.8
1/4	0.8	1.2	0.8	1.1
1/8	0.5	0.8	0.4	0.7

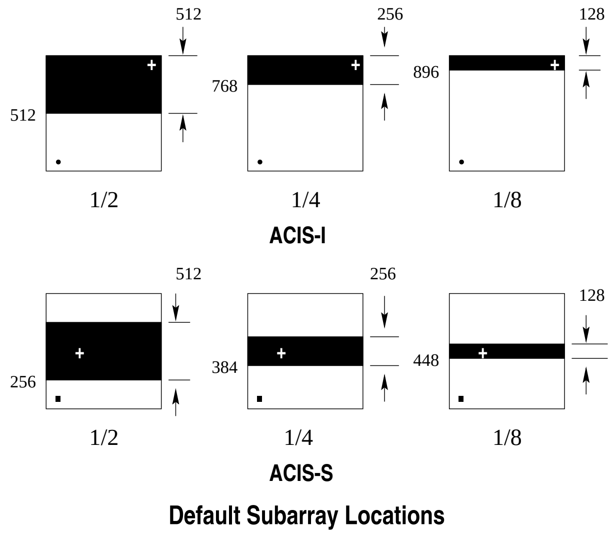

Figure 6.13: Examples of various subarrays. The heavy dot in the lower left indicates the origin

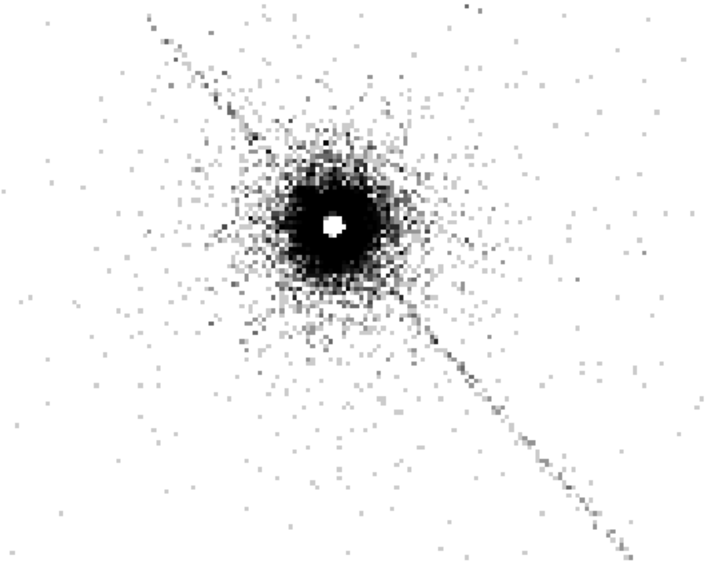

Figure 6.14: Trailed image of a strong X-ray source. The core of the image is faint due to pileup. Most events here are rejected because of bad grades. The readout direction is parallel to the trail.

Trailed Images It takes 40 μsec to transfer the charge from one row to another during the process of moving the charge from the active region to the framestore region. This has the interesting consequence that each CCD pixel is exposed, not only to the region of the sky at which the observatory was pointing during the long (frame time) integration, but also, for 40 μsec each, to every other region in the sky along the column in which the pixel in question resides. Figure 6.14 is an example where there are bright features present, so intense, that the tiny contribution of the flux due to trailing is stronger than the direct exposure - hence the trailed image is clearly visible. Trailed images are also referred to as "read out artifact" and "out-of-time images". The user needs to be aware of this phenomenon as it has implications for the data analysis - e.g. estimates of the background. In some cases, the trailed image can be used to obtain an unpiled spectrum and can also be used to perform 40 microsecond timing analysis (of extremely bright sources).

6.12.2 Alternating Exposures

In some instances, it is desirable to have both long and short frame times. If the exposure time is made very short, pile-up may be reduced, but the efficiency of the observation is greatly reduced by the need to wait for the full 3.2 seconds (if six chips are clocked) for the framestore array processing.

With alternating exposure times, all CCDs are clocked in unison, but have two exposure times. One (typically short) primary exposure of length $0.2 < t_p < 10.0$ sec is followed by k

standard exposures t_s (for example, 3.2 seconds if six chips are clocked). Permissible values of k range from zero (the standard single exposure mode) to 15. The short exposures are used to reduce photon pileup, and the long exposures are useful for studying the fainter objects in the field of view. For example, a typical choice of long and short exposure times might be 3.2 and 0.3 seconds. If $k = 3$, ACIS would perform one 0.3 second exposure, followed by three exposures of 3.2 seconds, repeating until the total observing time expires.

If the duty cycle of long exposures is $1 : k$ (short:long), the observing efficiency η is then

$$\eta = 1 - \frac{t_s - t_p}{t_s(k+1)}$$

for $t_p < 3.2$ sec and $t_s \geq 3.2$ sec.

6.12.3 Continuous Clocking (CC) Mode

The continuous clocking mode is provided to allow 3 msec timing at the expense of one dimension of spatial resolution. In this mode, one obtains 1 pixel x 1024 pixel images, each with an integration time of 2.85 msec. Details as to the spatial distribution in the columns are lost - other than that the event originated in the sky along the line determined by the length of the column.

In the continuous clocking mode, data is continuously clocked through the CCD and framestore. The instrument software accumulates data into a buffer until a virtual detector of size 1024 columns by 512 rows is filled. The event finding algorithm is applied to the data in this virtual detector and 3 x 3 event islands are located and recorded to telemetry in the usual manner (Section 6.14.1). This procedure has the advantage that the event islands are functionally equivalent to data accumulated in TE mode, hence differences in the calibration are minimal. The row coordinate (called CHIPY in the FITS file) maps into time in that a new row is read from the framestore to the buffer every 2.85 msec. This does have some minor impacts on the data. For example, since the event-finding algorithm is looking for a local maximum, it cannot find events on the edges of the virtual detector. Hence CHIPX cannot be 1 or 1024 (as in TE mode). Moreover, CHIPY cannot be 1 or 512. In other words, events cannot occur at certain times separated by 512*2.85 msec or 1.4592 sec. Likewise, it is impossible for two events to occur in the same column in adjacent time bins.

The TIMEs in continuous-clocking mode Level 1 event data files are the read-out times, not the times of arrival. The differences between the read-out times and the times of arrival are in the range 2.9 to 5.8 s. The differences depend on the nominal location of the source on the CCD and the dither of the telescope. Code to compute the times of arrival at the spacecraft from the read-out times has been developed and was released as part of the tool acis_process_events in *CIAO* 3.0. Data processed with this version of acis_process_events will have Level 2 files with corrected times.

6.13 Bias Maps

In general, the CCD bias, the amplitude of the charge in each pixel in the absence of external radiation, is determined at various times - every change of instrumental parameters or setup when ACIS is in place at the focus of the telescope. These bias maps have proven to be remarkably stable and are automatically applied in routine data processing.

The bias maps for continuous-clocking mode observations can be corrupted by cosmic rays. If a cosmic ray deposits a lot of charge in most of the pixels in one or more adjacent columns, the bias values assigned to these columns will be too large. As a result, some low-energy events that would have been telemetered will not be telemetered because they do not satisfy the minimum pulse height criterion and the spectrum of a source in the affected columns will be skewed to lower energies. The BI CCDs are relatively insensitive to the problem. A bias algorithm was implemented in Cycle 6 to mitigate the problem.

Occasionally a cosmic ray produces an artifact in a bias map. The pipelines search for these artifacts, and, when found, replace the bias map with another from the same epoch. Work is in progress to use long-term average bias maps, either when there are artifacts in the observation-specific bias map, or for all observations.

6.14 Event Grades and Telemetry Formats

6.14.1 Event Grades

During the first step in the algorithm for detecting X-ray events, the on-board processing examines every pixel in the full CCD image (even in the continuous clocking mode (Section 6.12.3)) and selects as events regions with bias-subtracted pixel values that both exceed the event threshold and are greater than all of the touching or neighboring pixels (i.e., a local maximum). The surrounding 3×3 neighboring pixels are then compared to the bias-subtracted split-event threshold; those that are above the threshold establish the pixel pattern. On the basis of this pattern, the event is assigned a grade. Depending on the grade, the data are then included in the telemetry. On-board suppression of certain grades is used to limit the telemetry bandwidth devoted to background events (see Section 6.16.1).

The grade of an event is thus a code that identifies which pixels, within the 3×3 pixel island centered on the local charge maximum, are above certain amplitude thresholds. The thresholds are listed in Table 6.1. Note that the local maximum threshold differs for the FI and the BI CCDs. A Rosetta Stone to help one understand the ACIS grade assignments is shown in Figure 6.15, and the relationship to the *ASCA* grading scheme is given in Table 6.7.

It is important to understand that most, if not all, calibrations of ACIS are based on a specific subset of ACIS grades. This “standard” set comprises *ASCA* grades 0,2,3,4, and 6 – G(02346). In the absence of pileup, this particular grade selection appears to optimize the signal-to-background ratio, but this conclusion depends on the detailed spectral

32	64	128
8	0	16
1	2	4

Figure 6.15: Schematic for determining the grade of an event. The grade is determined by summing the numbers for those pixels that are above their thresholds. For example, an event that caused all pixels to exceed their threshold is grade 255. A single pixel event is grade 0.

Table 6.7: ACIS and ASCA Grades

ACIS Grades	*ASCA* Grade	Description
0	0	Single pixel events
64 65 68 69	2	Vertical Split Up
2 34 130 162	2	Vertical Split Down
16 17 48 49	4	Horizontal Split Right
8 12 136 140	3	Horizontal Split Left
72 76 104 108	6	“L” & Quad, upper left
10 11 138 139	6	“L” & Quad, down left
18 22 50 54	6	“L” & Quad, down right
80 81 208 209	6	“L” & Quad, up right
1 4 5 32 128	1	Diagonal Split
33 36 37 129	1	
132 133 160 161	1	
164 165	1	
3 6 9 20 40	5	“L”-shaped split with corners
96 144 192 13 21	5	
35 38 44 52 53	5	
97 100 101 131	5	
134 137 141 145	5	
163 166 168 172	5	
176 177 193 196	5	
197	5	
24	7	3-pixel horizontal split
66	7	3-pixel vertical split
255	7	All pixels
All other grades	7	

Table 6.8: Telemetry Saturation Limits

Mode	Format	Bits/event	Events/sec*	Number of Events in full buffer
CC	Graded	58	375.0	128,000
CC	Faint	128	170.2	58,099
TE	Graded	58	375.0	128,000
TE	Faint	128	170.2	58,099
TE	Very Faint	320	68.8	23,273

*(includes a 10% overhead for housekeeping data)

properties of the source. Further, most of the scientifically important characteristics of ACIS (effective area, sensitivity, point spread function, energy resolution, etc.) are grade- and energy-dependent.

6.14.2 Telemetry Formats

There are a number of telemetry formats available. Specifying a format determines the type of information that is included in the telemetry stream. The number of bits per event depends on which mode and which format is selected. The number of bits per event, in turn, determines the event rate at which the telemetry will saturate and data will be lost until the on-board buffer empties. The formats available depend on which mode (Timed Exposure or Continuous Clocking) is used. The modes, associated formats, and approximate event rates at which the telemetry saturates and one begins to limit the return of data, are listed in Table 6.8. The formats are described in the following paragraphs. Event "arrival time" is given relative to the beginning of the exposure.

Faint Faint format provides the event position in detector coordinates, an arrival time, an event amplitude, and the amplitude of the signal in each pixel in the 3 x 3 island that determines the event grade. The bias map is telemetered separately. Note that certain grades may be not be included in the data stream (Section 6.16.1).

Graded Graded format provides event position in detector coordinates, an event amplitude, the arrival time, and the event grade. Note that certain grades may be not be included in the data stream (Section 6.16.1).

Very Faint Very Faint format provides the event position in detector coordinates, the event amplitude, an arrival time, and the pixel values in a 5 x 5 island. As noted in Table 6.8, this format is only available with the Timed Exposure mode. Events are still graded by the contents of the central 3 x 3 island. Note that certain grades may be not be included in the data stream (Section 6.16.1). This format offers the advantage of reduced background after ground processing (see Section 6.16.2) but only for sources with low counting rates that avoid both telemetry saturation and pulse pileup.

Studies (see http://cxc.harvard.edu/cal/Acis/Cal_prods/vfbkgrnd) of the ACIS background have shown that for weak or extended sources, a significant reduction of background at low and high energies may be made by using the information from 5×5 pixel islands, i.e. very faint mode, instead of the faint mode 3×3 island. This screening results in a 1–2% loss of good events. *CIAO* 2.2 and later provides a tool to utilize the VF mode for screening background events. Please note that the rmf generation is the same for very faint mode as it is for faint mode. See the "Why Topic" http://cxc.harvard.edu/ciao/why/aciscleanvf.html.

It is important to realize that VF mode uses more telemetry; the limit is ∼68 cts/s, which includes the target flux and the full background from all chips. Check the calibration web page (http://cxc.harvard.edu/cal/Acis/Cal_prods/bkgrnd/current/background.html) for a discussion of background flares and the telemetry limit. In particular, review section 1.3 of the memo "General discussion of the quiescent and flare components of the ACIS background" by M. Markevitch

In order to reduce the total background rate and the likelihood of telemetery saturation, VF observations should consider using no more than 5 CCDs and an energy filter with a 12 keV upper cutoff. Starting from Cycle 11, the default upper energy cutoff has been decreased from 15 keV to 13 keV. But VF mode observers should consider reducing this threshold further to 12 keV. If the target is brighter than 5-10 cts/s, one has to take more drastic steps, such as turning off more chips or using Faint mode.

This mode should not be used for observing bright sources (see the discussion at the end of Section 6.16.1 for more detail).

6.15 Pileup

Pileup results when two or more photons are detected as a single event. The fundamental impacts of pileup are: (1) a distortion of the energy spectrum - the apparent energy is approximately the sum of two (or more) energies; and (2) an underestimate as to the correct counting rate - two or more events are counted as one. A simple illustration of the effects of pileup is given in Figure 6.16. There are other, somewhat more subtle, impacts discussed below (Section 6.15.1).

The degree to which a source will be piled can be roughly estimated using *PIMMS*. Somewhat more quantitative estimates can be obtained using the pileup models in *XSPEC*, *Sherpa* and *ISIS* . If the resulting degree of pileup appears to be unacceptable given the objectives, then the proposer should employ some form of pileup mitigation (Section 6.15.3) as part of the observing strategy. In general, pileup should not be a problem in the observation of extended objects, the Crab Nebula being a notable exception, unless the source has bright knots or filaments.

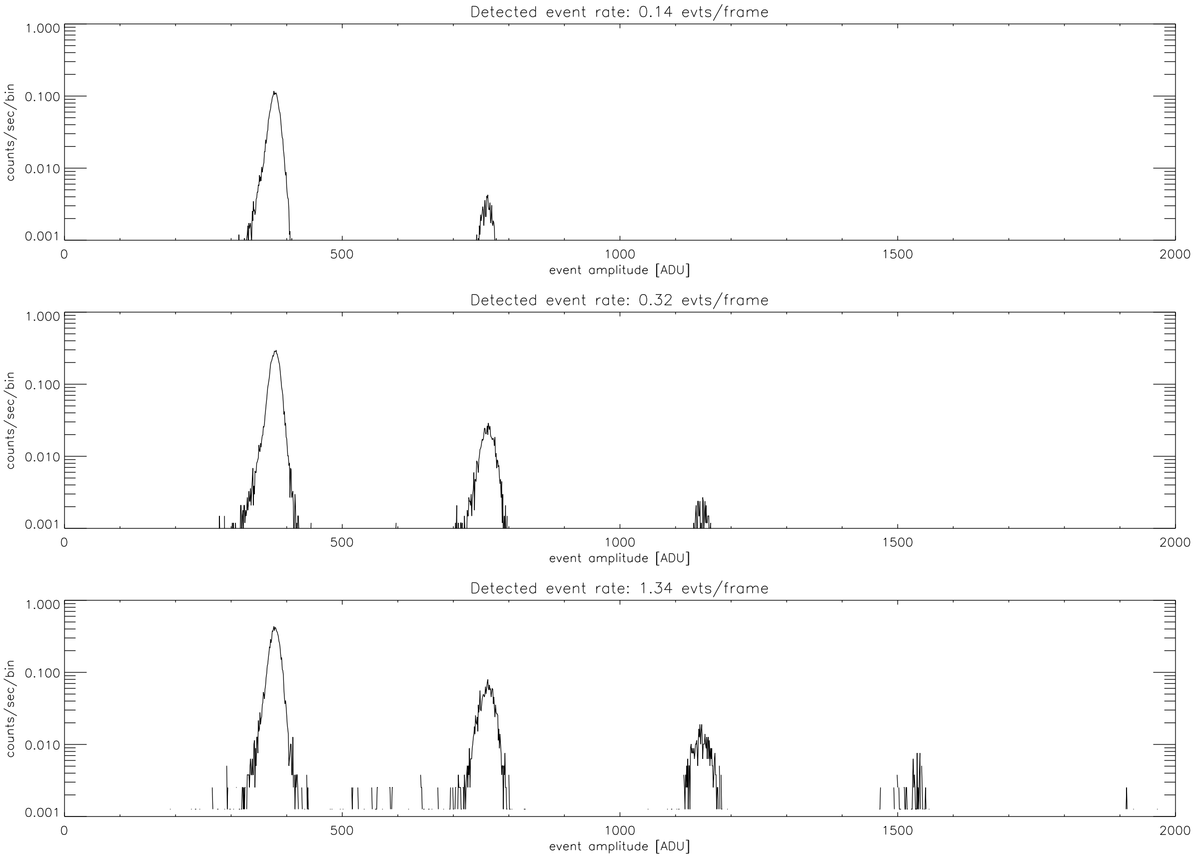

Figure 6.16: The effects of pileup at 1.49 keV (Al Kα) as a function of source intensity. Data were taken during HRMA-ACIS system level calibration at the XRCF. Single-photon events are concentrated near the pulse height corresponding to the Al Kα line ($\sim$ 380 ADU), and events with 2 or more photons appear at integral multiples of the line energy.

Table 6.9: ASCA Grade Distributions for different incident fluxes at 1.49 keV (Al-Kα, based on data taken at the XRCF during ground calibration using chip I3)

Incident Flux*	G0	G1	G2	G3	G4	G5	G6	G7
9	0.710	0.022	0.122	0.053	0.026	0.009	0.024	0.035
30	0.581	0.057	0.132	0.045	0.043	0.039	0.029	0.073
98	0.416	0.097	0.127	0.052	0.050	0.085	0.064	0.108
184	0.333	0.091	0.105	0.040	0.032	0.099	0.077	0.224

*arbitrary units

6.15.1 Other Consequences of Pileup

There are other consequences of pileup in addition to the two principal features of spurious spectral hardening and underestimating the true counting rate by under counting multiple events. These additional effects are grade migration and pulse saturation, both of which can cause distortion of the apparent PSF.

Grade migration Possibly the most troubling effect of pileup is that the nominal grade distribution that one expects for X-ray events changes. The change of grade introduced by pileup has become to be referred to as “grade migration”. Table 6.9 shows an example of grade migration due to pileup as the incident flux is increased. In this simple test, which involved only mono-energetic photons, the largest effect is the depletion of G0 events and the increase of G7 events. In general, as the incident flux rate increases, the fraction of the total number of events occupying a particular event grade changes as photon-induced charge clouds merge and the resulting detected events “migrate” to other grades which are not at all necessarily included in the standard (G02346) set. If one then applies the standard calibration to such data, the true flux will be under-estimated.

Pulse Saturation One consequence of severe instances of pileup is the creation of a region with no events! In this case, the pileup is severe enough that the total amplitude of the event is larger than the on-board threshold (typically 13 keV) and is rejected. Holes in the image can also be created by grade migration of events into ACIS grades (e.g. 255) that are filtered on-board.

PSF distortion Obviously the effects of pileup are most severe when the flux is highly concentrated on the detector. Thus, the core of the PSF suffers more from pileup induced effects than the wings. Figure 6.17 illustrates this point.

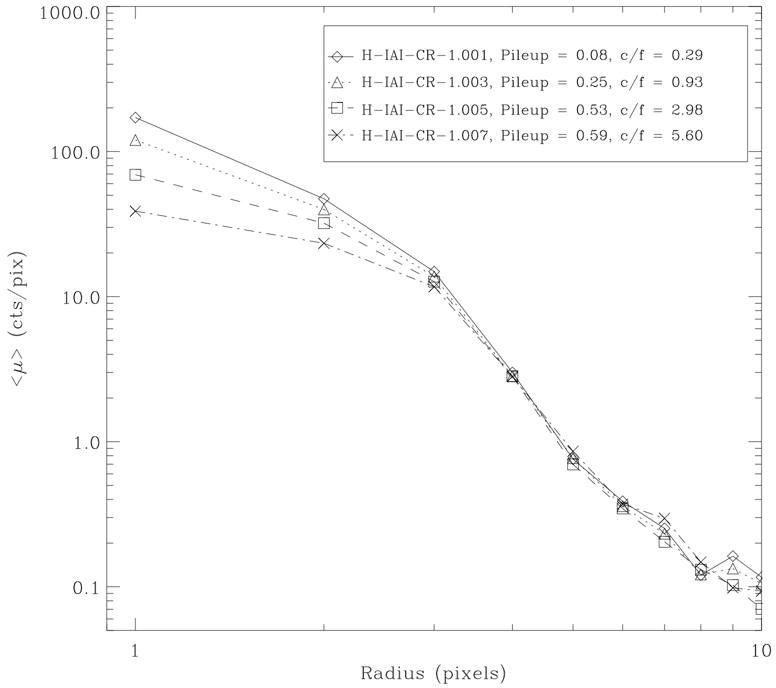

Figure 6.17: The effects of pileup on the radial distribution of the PSF are illustrated. These data were taken during ground calibration at the XRCF. The specific "OBSIDs", the counting rate per CCD frame ("c/f"), and the "pileup fraction" as defined in Section 6.15.2 are given in the inset.

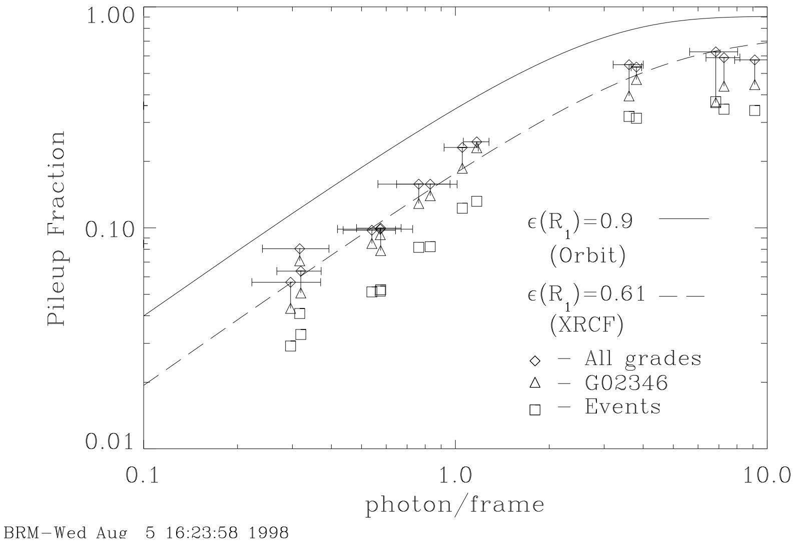

Figure 6.18: The pileup fraction as a function of the the counting rate (in the absence of pileup in units of photons/frame). The solid line is for on-orbit, the dashed line and the data points are for, and from, ground-based data respectively. The difference between the ground and flight functions are a consequence of the improved PSF on-orbit, where gravitational effects are negligible - see Chapter 4. Note that when pileup occurs there are two or more photons for each event, so the fraction of events with pileup is always less than the fraction of photons with pileup.

6.15.2 Pileup Estimation

It is clearly important in preparing a *Chandra* observing proposal to determine if the observation will be impacted by pileup, and if so, decide what to do about it (or convince the peer review why the specific objective can be accomplished without doing anything). There are two approaches to estimating the impact of pileup on the investigation. The most sophisticated uses the pileup models in *XSPEC*, *Sherpa*, and *ISIS* to create a simulated data set which can be analyzed in the same way as real data. A less sophisticated, but very useful, approach is to use the web version of *PIMMS* to estimate pileup or to use Figures 6.17 and 6.18.

Simple Pileup Estimates The pileup fraction is the ratio of the number of detected events that consist of more than one photon to the total number of detected events. An estimate of the pileup fraction can be determined from Figure 6.18. The algorithm parameterizes the HRMA+ACIS PSF in terms of the fraction of encircled energy that falls within the central 3 × 3 pixel event detection cell, and assumes that the remaining energy is uniformly distributed among the 8 surrounding 3 × 3 pixel detection cells. The probabilities of single- and multiple-photon events are calculated separately for the central and surrounding detection cells and subsequently averaged (with appropriate weighting) to obtain the pileup fraction as a function of the true count rate - the *solid* line in Figure 6.18. The model was tested against data taken on the ground under controlled conditions - also shown in Figure 6.18.

As a general guideline, if the estimated pileup fraction is > 10%, the proposed observation is very likely to be impacted. The first panel (upper left) in Figure 6.19 qualitatively illustrated the effect on a simulated astrophysical X-ray spectrum. *However, the degree of pileup that is acceptable for a particular objective will depend on the particular scientific goals of the measurement, and there is no clear-cut tolerance level.* If one's scientific objective demands precise flux calibration, then the pileup fraction should probably be kept well below 10%.

The PIMMS tool provides the pileup fraction using the algorithm described here, both for direct observation with ACIS and also for the zeroth-order image when a grating is inserted.

Simulating Pileup John Davis at MIT has developed an algorithm for modeling the effects of pileup on ACIS spectral data. The algorithm has been implemented as of *XSPEC* V11.1 and *Sherpa* V2.2. The algorithm can be used to attempt to recover the underlying spectrum from a source, or to simulate the effects of pileup for proposal purposes.

The algorithm has been tested by comparing CCD spectra with grating spectra of the same sources. Care should be taken in applying the algorithm - for example, using the appropriate regions for extracting source photons and avoiding line-dominated sources. A description of the algorithm can be found in Davis 2001 (Davis, J.E. 2001, ApJ, 562, 575). Details on using the algorithm in *Sherpa* are given in a *Sherpa* "thread" as of *CIAO* V2.2 on the CXC CIAO web page: http://cxc.harvard.edu/ciao/.

6.15.3 Reducing Pileup

We summarize here various methods which can be used to reduce pileup.

- **Shorten exposure time:** By cutting back on CCD exposure time, the probability of pileup decreases. The user is advised to select the best combination of a subarray and frame time in order to avoid losing data as discussed in Section 6.12.1.

- **Use the Alternating Exposure option:** This option simply alternates between exposures that are subject to pileup and those that are not. The capability was originally developed for use with certain grating observations to allow one to spend some time obtaining useful data from a zeroth order image, which would otherwise be piled up. See Section 6.12.2.

- **Use CC mode** If two-dimensional imaging is not required, consider using CC mode (Section 6.12.3).

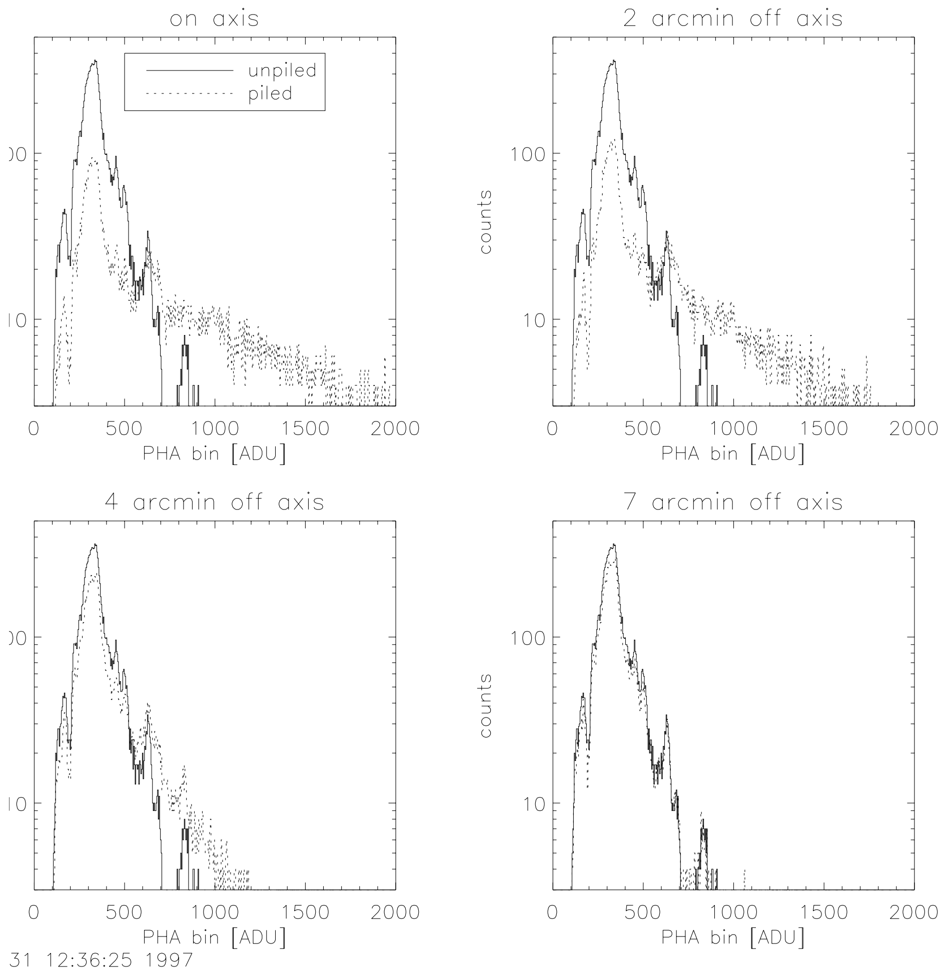

Figure 6.19: MARX simulations of the effect of pileup on the shape of the spectrum. The true (solid line) and the detected (dotted line) spectra are shown for four different viewing angles. The corresponding "pileup fractions" - see Section 6.15.2 - are 46%, 40%, 15%, and 2% as the image is moved progressively further off-axis.

- **Insert a transmission grating:** Inserting either the HETG (Chapter 8) or the LETG (Chapter 9) will significantly decrease the counting rate as the efficiency is lower. The counting rate in the zero order image may then be low enough to avoid pileup.

- **Offset point:** Performing the observation with the source off-axis spreads out the flux and thus decreases the probability of pileup at the price of a degraded image. Figure 6.19 illustrated the impact.

- **Defocus:** The option is only listed for completeness, the option is *not* recommended or encouraged.

6.16 On-Orbit Background

There are three components to the on-orbit background. The first is that due to the cosmic X-ray background (a significant fraction of which resolves into discrete sources during an observation with *Chandra*). The second component is commonly referred to as the charged particle background. This arises both from charged particles, photons, and other neutral particle interactions that ultimately deposit energy in the instrument. The third component is the "readout artifact" which is a consequence of the "trailing" of the target image during the CCD readout; it is discussed in Section 6.12.1.

The background rates differ between the BI and the FI chips, in part because of differences in the efficiency for identifying charged particle interactions. Figure 6.20 illustrates why.

6.16.1 The Non-X-ray Background

Beginning in September 2002, observations have been carried out with the ACIS in the stowed position, shielded from the sky by the SIM structure, and collecting data in normal imaging TE VF mode at -120C. Chips I0, I2, I3, S1, S2, S3 were exposed. The SIM position was chosen so that the on-board calibration source did not illuminate the ACIS chips. This allowed us to characterize the non-celestial contribution to X-ray background (i.e., from charged particles). The resulting spectra from different chips are shown in Figure 6.21. Chip S2 is similar to the ACIS-I chips (denoted I023 in the figure) and not shown for clarity.

In addition, in July-September 2001, *Chandra* performed several short observations of the dark Moon, which blocks the cosmic X-ray background. The dark Moon and stowed background spectra were indistinguishable (except for short periods of flares and variable Oxygen line emission in the Moon observations). We have not observed any background flares in the stowed position. Thus, the ACIS-stowed background is a good representation of the quiescent non-X-ray background in the normal focal position and can be used for science observations.

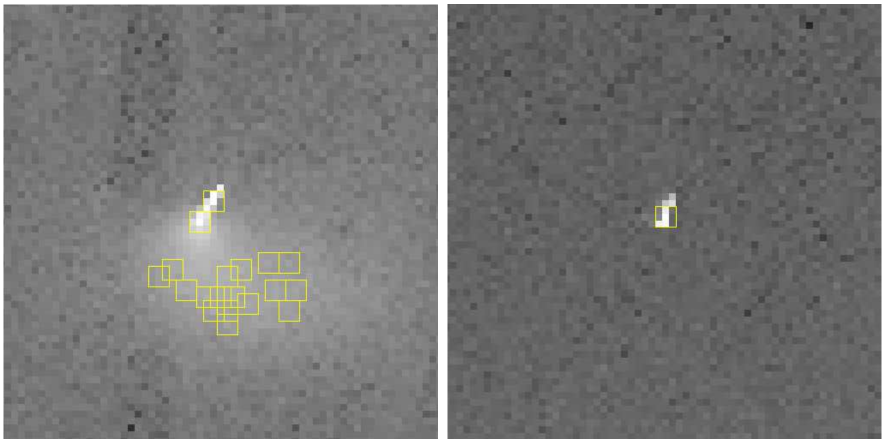

Figure 6.20: Enlarged view of an area of a FI chip I3 (left) and a BI chip (right) after being struck by a charged particle. There is far more "blooming" in the FI image since the chip is thicker. The overlaid 3 × 3 detection cells indicate that the particle impact on the FI chip produced a number of events, most of which end up as *ASCA* Grade 7, and are thus rejected with high efficiency. The equivalent event in the BI chip, is much more difficult to distinguish from an ordinary X-ray interaction, and hence the rejection efficiency is lower.

The flight-grade distributions in early measurements of the non-X-ray background for the two types of CCDs are shown in Figure 6.22. Although subsequent to these early measurements the CCD temperature has been lowered and the FI devices suffered the effects of the radiation damage, the background is still dominated by the same grades. Based on these data, events from flight grades 24, 66, 107, 214, and 255 are routinely discarded on-board. The total rate of the discarded events is available in the data stream. The remaining non-X-ray events telemetered to the ground are still dominated (70-95%) by other bad grades. They are not discarded onboard because some of them may turn out to be valid X-ray events after ground processing.

For data taken using the Very Faint (VF) telemetry format (Section 6.14.2), the non-X-ray background can be reduced in data processing by screening out events with significant flux in border pixels of the 5 × 5 event islands. This screening leaves the data from faint sources essentially the same while reducing the FI background at different energies: a factor of 1.4 (E>6 keV); 1.1 (1-5 keV); and 2 (near 0.5 keV). For the BI chips the reductions are: 1.25 (E>6 keV); 1.1 (1-5 keV); and 3 (near 0.3 keV). The screening algorithm has been incorporated into the *CIAO* tool *acis_process_events*. Further discussion may be found at http://cxc.harvard.edu/cal/Acis/Cal_prods/vfbkgrnd/index.html

Proposers should be aware that telemetry saturation occurs at lower count rates for observations using the VF format, so they may need to take steps to limit the total ACIS count rate (see Section 6.16.2). Proposers should also be aware that if there are bright point sources in the field of view, the screening criterion discussed above is more likely to

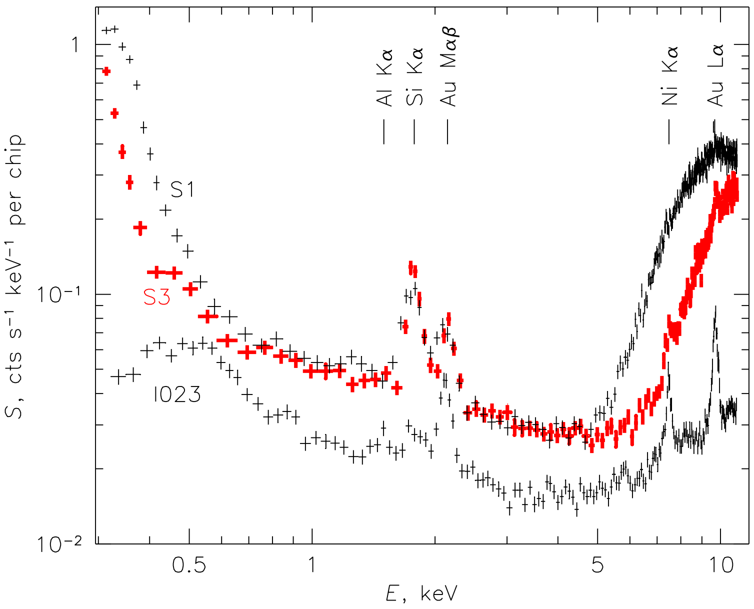

Figure 6.21: Energy spectra of the charged particle ACIS background with ACIS in the stowed position (a 50 ks exposure taken in September 2002; standard grade filtering, no VF filtering). Line features are due to fluorescence of material in the telescope and focal plane.

	Bkgrd rates (cts/s/chip)							
Energy Band (keV)	I0	I1	I2	I3	S1	S2	S3	S4
0.3-10	0.43	0.49	0.43	0.49	2.26	0.46	1.18	0.54
0.5-2	0.10	0.10	0.11	0.10	0.30	0.07	0.11	0.16
0.5-7	0.26	0.26	0.26	0.27	0.70	0.27	0.51	0.33
5.0-10	0.22	0.22	0.21	0.22	0.96	1.54	0.67	0.24
10-12	0.13	0.13	0.13	0.13	1.15	0.13	0.92	0.14

Table 6.10: Approximate on-orbit standard grade background counting rates. The rates are cts/s/chip, using only *ASCA* grades 02346, no VF filtering, excluding background flares and bad pixels/columns and celestial sources identifiable by eye. These values can be used for sensitivity calculations

remove source events due to pileup of the 5×5 pixel event islands. Point sources should have count rates significantly less than 0.1 counts/sec to be unaffected. However, there is no intrinsic increase of pileup in VF data compared to Faint mode, and the screening software can be selectively applied to regions, excluding bright point-like sources. Thus the use of VF mode is encouraged whenever possible.

6.16.2 The Total Background

In real observations, two more components to the background come into play. The first is the cosmic X-ray background which, for moderately long ($\sim$ 100 ks) observations will be mostly resolved into discrete sources (except for the diffuse component below 1 keV) but, nevertheless, contributes to the overall counting rate. The second is a time-variable "flare" component caused by any charged particles that may reflect from the telescope and have sufficient momentum so as not to be diverted from the focal plane by the magnets included in the observatory for that purpose, or from secondary particles (Section 6.16.3). Figure 6.23 compares flare-free ACIS-S3 spectra of the non-X-ray (dark Moon) background and a relatively deep pointing to a typical region of the sky away from bright Galactic features.

The 2007-2008 quiescent detector+sky background counting rates in various energy bands and for the standard good grades are given in Table 6.10. Insertion of the gratings makes little measurable difference in the background rates, but it does block the background flares. The lower-energy rates are very approximate as they vary across the sky. The rates are slowly changing on the timescale of months, so Table 6.10 can only be used for rough sensitivity estimates. Table 6.11 gives total background count rates for each type of chip, including all grades that are telemetered (see Section 6.14.1 and 6.16.1), and can aid in estimating the probability of telemetry saturation.

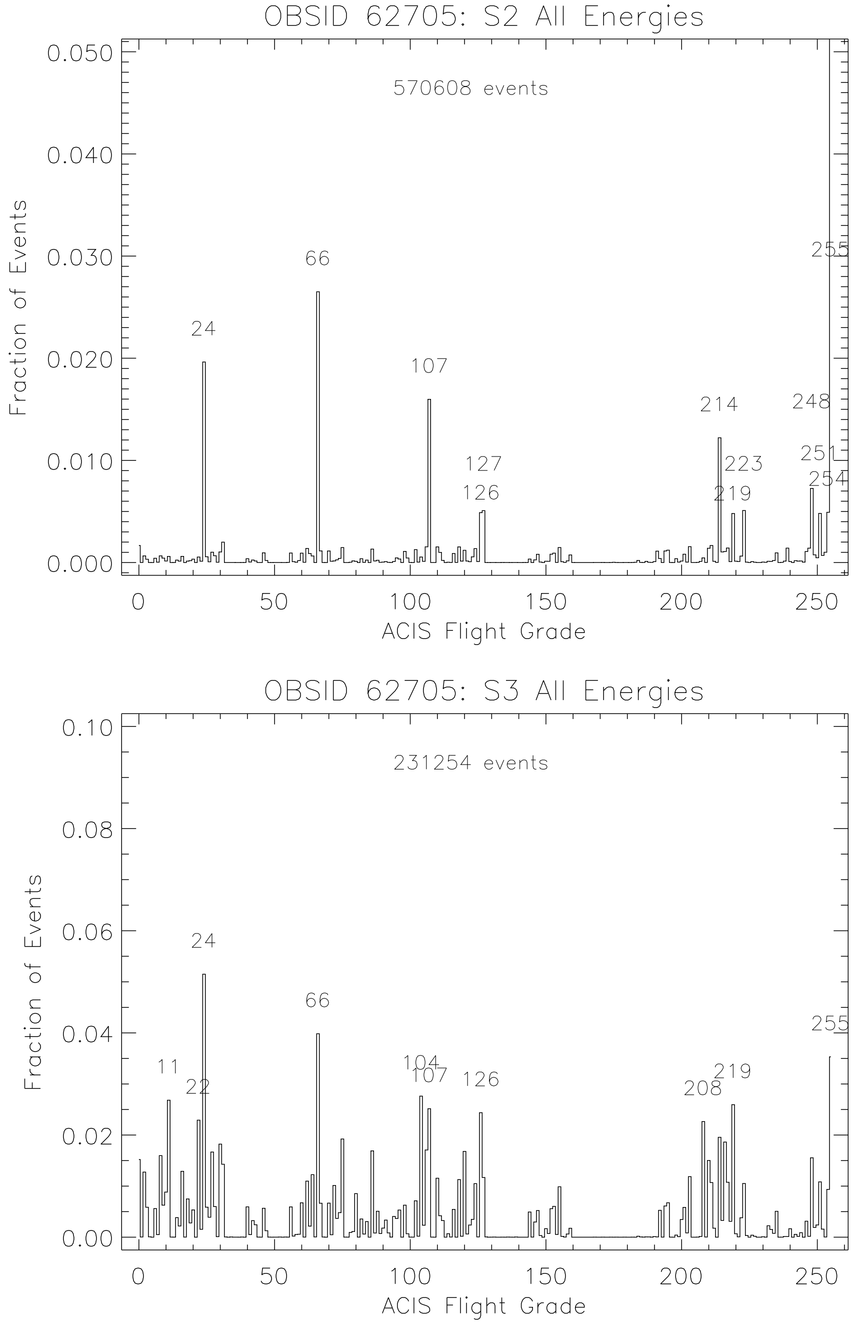

Figure 6.22: Fraction of ACIS background events as a function of grade from early in-flight data for an FI chip (S2) (top) and a BI chip (S3) (bottom).

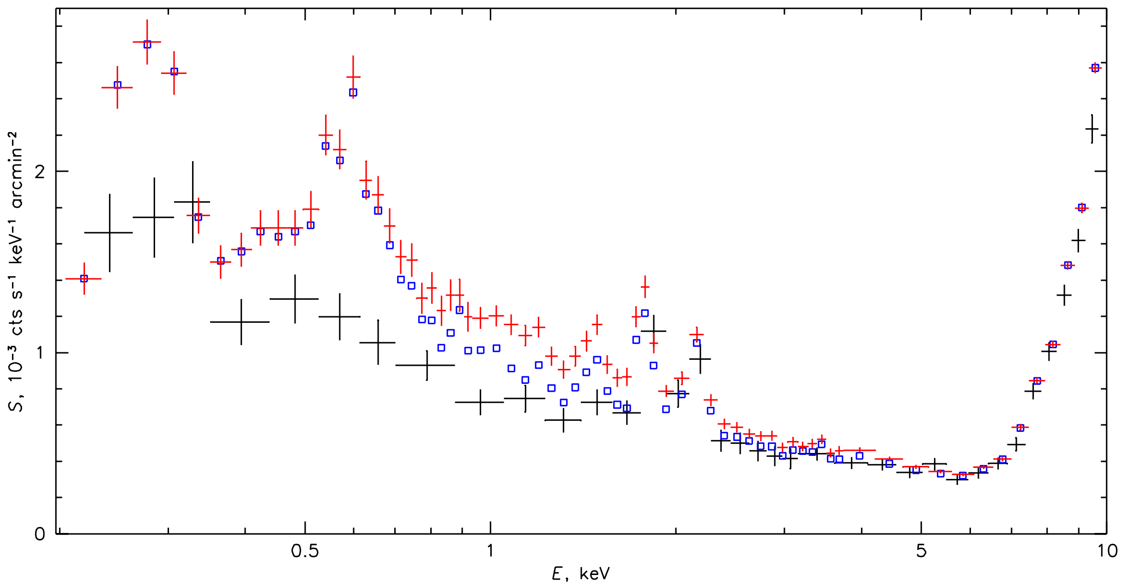

Figure 6.23: ACIS -S3 spectrum of the non-X-ray background (large crosses) overlaid on the quiescent blank sky spectrum. Small crosses show the total sky spectrum, while squares show the diffuse component left after the exclusion of all point sources detectable in this 90 ks exposure. Standard grade filtering and VF filtering are applied. The background and blank-sky spectra are normalized to the same flux in the 10-12 keV band.

Period	Aug 1999	2000-2003	2009	2012			
Upper *E* cutoff	15 keV	15 keV	15 keV	15[†] keV	13 keV	12 keV	10 keV
Chip S2 (FI)	10	6.3	10.7	7.1	5.8	5.7	5.2
Chip S3 (BI)	11	7.7	14.7	10.9	7.4	6.7	4.8

[†] Scaled from 13 keV rate.

Table 6.11: Typical total quiescent background rates (cts/s/chip), including *all* grades that are telemetered (not just standard *ASCA* grades), by chip type and upper energy cutoff. These values can be used to estimate the probability of telemetry saturation.

The background rates have declined in 1999-2000, stayed flat through end of 2003, increased until the end of 2009, and have recently been dropping, following the solar cycle. (Fig. 6.24). By late 2012, the ACIS-S2 rates were approaching the low rates of 2001-2003. The ACIS-S3 rates were declining, but still above the 2001-2003 rates. If the background rate is anti-correlated with the solar cycle, we may expect the decline in the ACIS-S3 rates to continue in 2013, and the ACIS-S2 rates may level off at rates comparable to 2001-2003. The proposer should be cautious in making assumptions about the future background rates for planning purposes.

For aid in data analysis and planning background-critical observations, the *CXC* has combined a number of deep, source-free, flare-free exposures (including all components of the background) into background event files for different time periods. These blank-sky datasets, along with the detector-only (ACIS-stowed) background files (section 6.16.1), can be found in the CALDB.

6.16.3 Background Variability

In general, the background counting rates are stable during an observation. Furthermore, the spectral shape of the non-X-ray background has been remarkably constant during 2000-2012 for FI and, to a lower accuracy, for BI chips, even though the overall background rate showed secular changes by a factor of 1.5. (For chip S3, the shape has been constant during 2000-2005, but a small change is being observed since late 2005.) When the *quiescent* background spectra from different observations are normalized to the same rate in the 10-12 keV interval, they match each other to within ±3% across the whole *Chandra* energy band. The previous discussion assumes that the upper threshold will be set to 13 keV.

Occasionally, however, there are large variations (flares), as illustrated in Figure 6.25. Figure 6.26 shows the frequency of such variations when compared to the quiescent background. An average fraction of the exposure affected by flares above the filtering threshold used for the blank-sky background datasets (a factor of 1.2 above the nominal rate) was about 6% for FI chips and up to 1/3 for BI chips during the first few years of the mission. The average fraction of exposure affected by flaring has declined with time, and was practically zero for a long stretch. Recently, the flare frequency has been increasing, but at

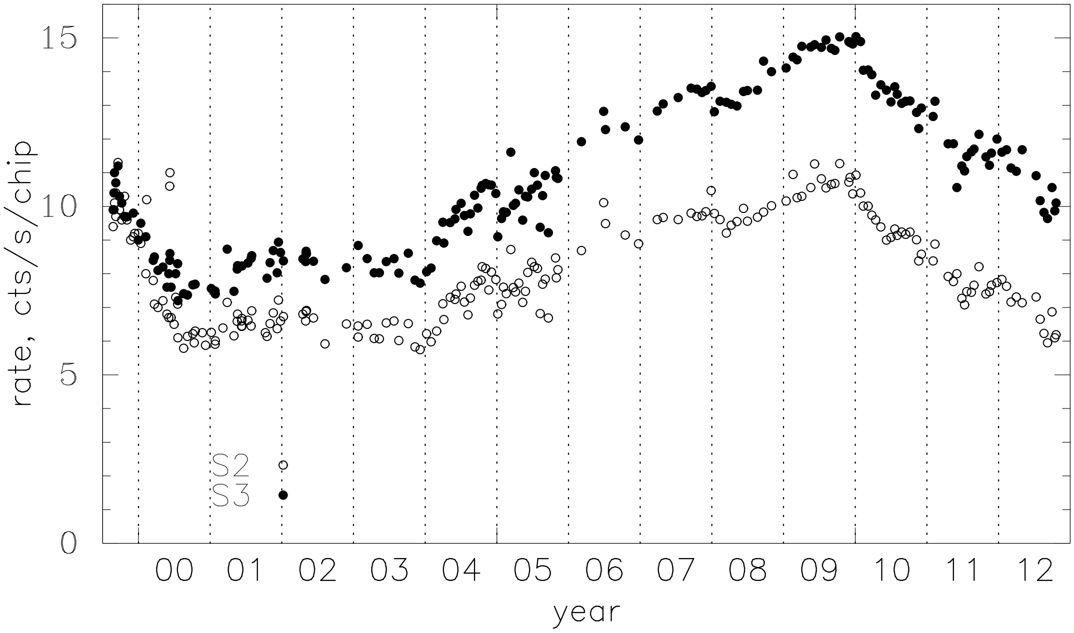

Figure 6.24: Total telemetered background rates (including all grades and the upper event cutoff at 15 keV) for chips S2 (FI) and S3 (BI) as a function of time. Vertical dashed lines are year boundaries.

present (late 2012) it has not reached the frequency seen early in the mission. Thus, given that the quiescent background in FI chips is also lower than that in S3, background-critical observations may best be done with ACIS-I.

Several types of flares have been identified, including flares that are seen only in the BI chips, and flares that are seen in both the FI and BI chips. Figure 6.27 shows the spectra of two of the most common flare species. Both flares have spectra significantly different from the quiescent background. In addition, the BI flares have spatial distribution very different from that of the quiescent background. The BI flares produce the same spectra in S1 and S3.

Users should note that the total counting rate can significantly increase during a flare (although flare events are almost exclusively good-grade so the total rate does not increase by as large a factor as the good-grade rate; details can be found at http://cxc.harvard.edu/cal/Acis/Cal_prods/bkgrnd/current). If the probability of telemetry saturation is significant, users of ACIS-I might consider turning off the S3 chip. However, if ACIS-S is used in imaging mode, the *CXC* recommends that both BI chips be turned on. The advantage is that for most types of flares S1 can be used to determine the flare spectrum which can then be subtracted from the spectrum obtained with S3.

6.16.4 Background in Continuous Clocking Mode

Apart from compressing the data into one dimension (Section 6.12.3), there is essentially no difference in the total background in CC mode and that encountered in the timed exposure mode. The background per-sky-pixel, however, will be 1024 times larger, since the sky-pixel is now 1 x 1024 ACIS pixels.

6.17 Sensitivity

The sensitivity for detecting objects is best estimated using the various proposal tools such as PIMMS, MARX, etc. The "*Chandra* Proposal Threads" web page gives detailed examples of how to use these tools (http://cxc.harvard.edu/proposer/threads)

6.18 Bright Source X-ray Photon Dose Limitations

Pre-Flight radiation tests have shown that ∼200 krads of X-ray photon dose will damage the CCDs. The mechanism for the damage is the trapped ionization in the dielectric silicon oxide and nitride separating the gates from the depletion region. Since the charge is trapped, the damage is cumulative. Because the structure of the BI CCDs differs significantly from that of the FI CCDs, the two types of chips have different photon dose limitations. Specifically, the BI CCDs are more than 25 times as tolerant to a dose of X-ray photons as compared to the FI CCDs since the former have $\sim 40\mu$m of bulk Si protecting the gate layer.

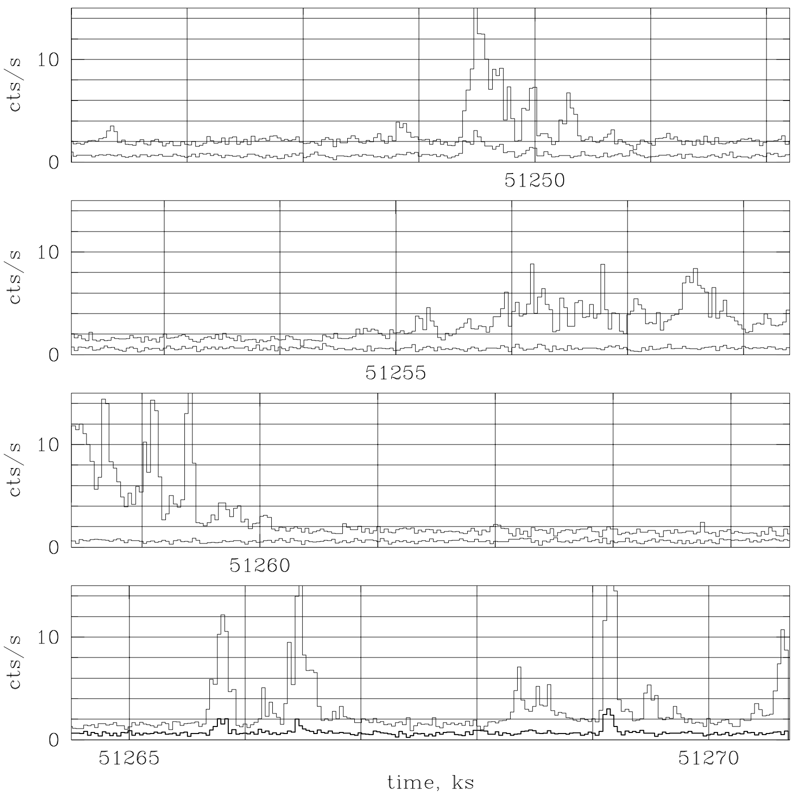

Figure 6.25: An example of the ACIS background counting rate versus time - BI chip (S3; top curve) and an FI chip (I2; bottom curve). These are for the standard grades and the band from 0.3 - 10 keV.

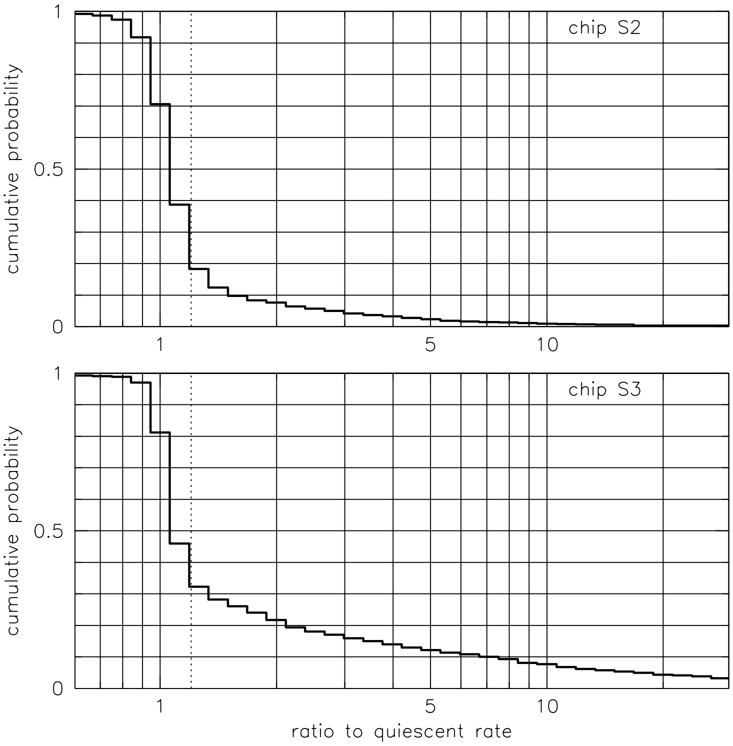

Figure 6.26: An estimate of the cumulative probability that the ratio of the background counting rate to the quiescent background counting rate is larger than a given value. Upper plot for a representative FI chip - S2, and the lower curve for a representative BI chip - S3. The vertical dotted line is a limiting factor 1.2 used in creating the background data sets. These probabilities are relevant for the archival data from the first 2–3 years of the mission. They declined with time to almost zero at present, but may soon increase again as we enter the new solar cycle.

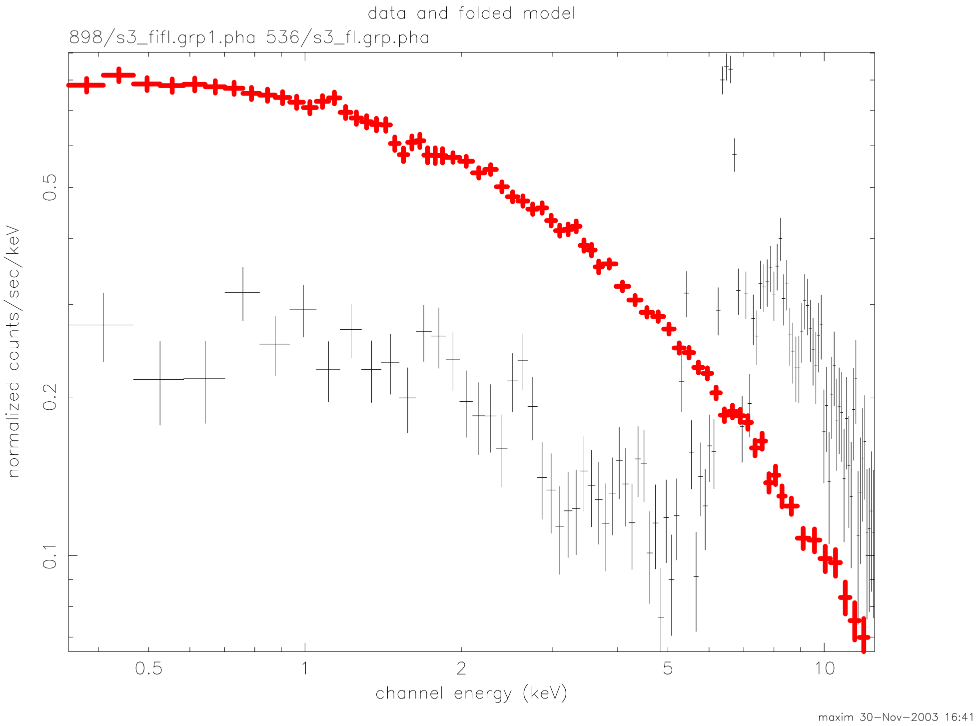

Figure 6.27: Spectra of different background flares in chip S3. Thick crosses show a common flare species that affects only the BI chips. Thin crosses show one of the several less common flare species that affect both the BI and FI chips. Note how both these spectra are different from the quiescent spectrum (see Figure 6.21).

Simulations of astrophysical sources have yielded a very conservative, spectrally-averaged, correspondence of 100 counts/pix = 1 rad. By 'counts' in this context we mean all photons that impinged on the detector, whether or not they were piled-up or discarded onboard.

In consultation with the IPI team the CXC has adopted the following mission allowances, per pixel of the two types of chips:

FI chips:	25 krads	2,500,000 cts/pix
BI chips:	625 krads	62,500,000 cts/pix

If your observation calls for observing a bright point-like source close to on-axis, we suggest you use the *MARX* simulator (with the parameter DetIdeal=yes & dither, typically, on) to calculate whether your observation may reach 1% of the above mission limits in any one pixel. If so, please contact the *CXC* HelpDesk in order to custom design an observational strategy which may accommodate your science aims, while maintaining the health & safety of the instrument.

6.19 Observing Planetary and Solar System Objects with ACIS

Chandra has successfully observed several solar system objects, including Venus, the Moon, Mars, Jupiter and several comets. Observations of planets and other solar system objects are complicated because these objects move across the celestial sphere during an observation and the optical light from the source can produce a significant amount of charge on the detectors (this is primarily an issue for ACIS-S observations). Some information regarding observation planning and data processing is given here. Users are encouraged to contact the *CXC* for more detailed help.

6.19.1 Observations with ACIS-I

Any solar system object can be observed with ACIS-I. Previous solar system observations with ACIS-I have not revealed significant contamination from optical light. However, proposers are encouraged to work with the *CXC* when planning the specifics of a given observation. Since the source moves across the celestial sphere in time, an image of the event data will exhibit a "streak" associated with the source. The *CIAO* tool sso_freeze can be used to produce an event data file with the motion of the source removed.

6.19.2 Observations with ACIS-S

The ACIS-S array can be used with or without a grating. The BI CCDs are more sensitive to soft X-rays than the I array CCDs, but the entire S array suffers from the disadvantage that its OBF is thinner than for ACIS-I and may transmit a non-negligible flux of visible light onto the CCDs. It is thus necessary to estimate the amount of charge produced in the CCDs due to the optical light. More detailed information can be found at http://www.astro.psu.edu/xray/docs/cal_report/ and from the *CXC* via HelpDesk.

If the optical light leak is small enough, it can be mitigated by simply shortening the frame time. This leads to a linear drop in the number of ADU due to optical light. If possible, VF mode should be used, since in this mode the outer 16 pixels of the 5 × 5 region allows a "local" bias to be subtracted from the event to correct for any possible light leakage. However, see the warnings in Section 6.14.2.

The optical light also invalidates the bias taken at the beginning of the observation if a bright planet is in the field. It is therefore desirable to take a bias frame with the source out of the field of view. This bias map is useful even when processing 5 × 5 pixels in VF mode since it can be employed as a correction to the local average "bias" computed from the 16 outer pixels, thereby correcting for hot pixels, cosmetic defects etc.

A more sophisticated approach to dealing with excess charge due to optical light is to make an adjustment to the event and split thresholds. Event grades are described in more detail in Section 6.14.1. Excess charge (in ADU) due to optical light will be added to the event and split counters on-board. Without an adjustment to the thresholds (or a large enough threshold), many of the X-ray events may have all nine pixels of a 3×3 pixel event detection cell above the split threshold, in which case the event will not be telemetered to the ground. If the adjustment is too large, X-ray events may not be detected because they may not exceed the event threshold.

Users should be aware that if the detection thresholds are adjusted, standard *CXC* processing of planetary data will give inaccurate estimates of event pulse heights and grades. To analyze such data, a thorough understanding of the energy calibration process and manual massaging of the data will be required.

6.20 Observing with ACIS - the Input Parameters

This section describes the various inputs that either must be, or can be, specified in order to perform observations with ACIS. The sub-sections are organized to match the RPS form. We have added some discussion as to some of the implications of the possible choices. As emphasized at the beginning of the Chapter, ACIS is moderately complex and the specific characteristics of the CCDs and their configuration in the instrument lead to a number of alternatives for accomplishing a specific objective - *detailed trade-offs are the responsibility of the observer.* Thus, e.g. it might seem obvious that observations of a faint point source may be best accomplished by selecting the ACIS-S array with the aim point on S3, the BI device that can be placed at the best focus of the telescope, and the CCD with the best average energy resolution. On the other hand, perhaps the science is better served by offset pointing (by a few arcminutes) the target onto S2, very near to the framestore, where the FI energy resolution is better than that of S3. On the other hand, if the object is very faint, so that the number total number of photons expected is just a handful – not enough to perform any significant spectroscopy – the advantage of S3 may not be so obvious considering the smaller field of view, and perhaps the ACIS-I array, which would optimize the angular resolution over a larger field, may be more attractive.

6.20.1 Required Parameters

There are certain ACIS input parameters that must be specified: the number and identity of the CCDs to be used, the Exposure Mode, and the Event Telemetry Format. If pileup and telemetry saturation are not considered to be a problem for the observation, then these are the only parameters that need to be specified.

Number and Choice of CCDs Up to six CCDs can be operated at once, if the science objectives require 6 CCDs. Previously in the mission, the *CXC* advised GOs to use 6 CCDs if possible. Given the changes in the thermal environment on the spacecraft around ACIS, the *CXC* now recommends that GOs use 5 or fewer CCDs if there is no impact on their science. Please see the discussion under "Choosing Optional CCDs" that follows for the reasons why we wish the observer to request fewer than 6 if feasible. The identity of the CCDs and the desired aimpoint must be specified.

Choosing Optional CCDs The observer may specify that a given CCD must be on for an observation by entering "Y" for that CCD at the appropriate place in the RPS form. If a CCD must be off, one enters an "N". Finally, one may specify rank-ordered optional CCDs which will be turned on or off at the discretion of the mission schedulers depending on the specific thermal status of the Observatory at the time of the observation. This is done by entering "OPT1-OPT5" ("O1-O5" in RPS). The first to be turned off, if necessary, would be designated by "OPT1", the second to be turned off would be designated by "OPT2", etc. Observers are encouraged to use 5 or fewer CCDs if their science objectives are not significantly affected. Starting in Cycle 14, the RPS forms for proposal submission will no longer allow the proposer to specify "Y" for 6 CCDs. If the observer's science objectives nevertheless require 6 CCDs to be on, the observer should set 5 CCDs to "Y" and 1 CCD to "OPT1". If the proposal is selected, the observer should discuss the configuration with the user uplink support scientist and the optional CCD may be turned on. The CXC will do its best to schedule 6 CCD observations, but proposers should be aware that satisfying the thermal requirements of the Observatory may make the scheduling of such observations more complicated if not impossible.

Using fewer than 6 CCDs is beneficial in keeping the ACIS focal plane and electronics temperatures within the required operating ranges. Because of changes in the Chandra thermal environment, the ACIS Power Supply and Mechanism Controller (PSMC) has been steadily warming over the course of the mission. Under current conditions, and assuming an initial PSMC temperature of less than +30 C, observations at pitch angles less than 60 degrees, longer than 50 ks, and with 6 CCDs operating, are likely to cause the PSMC to approach or exceed the thermal limit. For pitch angles larger than 130 degrees, the ACIS focal plane, the Detector Electronics Assembly (DEA), and the Digital

Processing Assembly (DPA) temperatures can also warm outside of the desired range. As above, each of these temperatures can be reduced by reducing the number of operating CCDs.

If an observer requires the most accurate gain calibration for their observation (provided by a cold and stable focal plane temperature), they should use 5 or fewer CCDs. This is done by setting 5 CCDs to “N”, and 5 CCDs to “Y” or 1 CCD to “Y” and 4 other CCDs to “OPT1-OPT4”. For example, if the observer is using the ACIS-I array for imaging, they could select the four I array CCDs and one of S2 or S3. If the observer is using S3 for imaging, they could select S2, S3, S4, I2 and I3 and turn S1 off or they could select just S1, S2, S3, and S4.

If no optional CCDs are selected, and six CCDs are on and the observation is not constrained in such a way as to prohibit it, the observation is likely to be scheduled at a time for which the pitch angle is between 60 degrees and 130 degrees. The user should be aware that such an observation may be listed in the long term schedule (LTS) at a date for which the pitch angle for this target is less than 60 degrees or greater than 130 degrees. However, when the observation finally appears in the short term schedule, it will be at a date for which the pitch angle will be in the allowed range.

Some Recommended Chip Sets Observers should specify the chip set that is best for their primary science. The following suggestions have proven to be popular, and would facilitate a more useful and homogeneous archive.

```
ACIS-I (5 CCDs) imaging, nominal aimpoint
          --------------------
                I0    I1
                 Y     Y
                I2    I3
                 Y     Y
      S0    S1  S2    S3   S4   S5
       N     N   Y     N    N    N
```

```
ACIS-I (5 CCDs) imaging, nominal aimpoint
          --------------------
                I0    I1
                 Y     Y
                I2    I3
                 Y     Y
      S0    S1  S2    S3   S4   S5
       N     N   N     Y    N    N
```

```
ACIS-I (6 CCDs) imaging, nominal aimpoint
          --------------------
                I0    I1
                 Y     Y
                I2    I3
                 Y     Y
      S0    S1  S2    S3   S4   S5
       N     N  O2    O1    N    N
```

The rationale for the first configuration above is that, in the unlikely event of major background flares, telemetry might saturate more rapidly if S3 were on and the FP temperature and electronics temperatures will be lower with only 5 CCDs on. For the middle configuration, the rationale is that S3 is generally more sensitive and closer to the ACIS-I aimpoint, so more sensitive to serendipitous source detection. The rationale for the third configuration is that it is desired to have both S2 and S3 on, but it is not required. Given the current thermal performance of the spacecraft, it is probable that one of the two optional CCDs would be turned off.

```
ACIS-S (5 CCDs) imaging, nominal aimpoint
          --------------------
                I0    I1
                N     N
                I2    I3
                Y     Y
      S0    S1  S2    S3   S4   S5
      N     N   Y     Y    Y    N
```

```
ACIS-S (5 CCDs) imaging, nominal aimpoint
          --------------------
                I0    I1
                N     N
                I2    I3
                N     Y
      S0    S1  S2    S3   S4   S5
      N     Y   Y     Y    Y    N
```

```
ACIS-S (6 CCDs) imaging, nominal aimpoint
          --------------------
                I0    I1
                N     N
                I2    I3
                O1    O2
      S0    S1  S2    S3   S4   S5
      N     Y   Y     Y    Y    N
```

For this ACIS-S imaging chipset, chips farthest from the aimpoint (where the PSF is degraded) would be turned off first. On the other hand, S4 has significant noise streaks and resulting decreased sensitivity, so some users may prefer to turn it off earlier in the optional sequence. The rationale for the selection on the first set above is that S1 will have a higher count rate than a FI CCD in the case of a background flare and thus it might be desirable to have S1 off. The rational for the middle selection above is that the observer may want to use S1 help model the background on S3, therefore it is desirable to have I2 turned off. The rational for the third configuration is that it is desirable to have 6 CCDs on, but not required. Given the current thermal performance of the spacecraft, it is probable that one of the two optional CCDs would be turned off.

```
ACIS-S (6 CCDs) spectroscopy, nominal aimpoint
             --------------------
                   I0    I1
                    N     N
                   I2    I3
                    N     N
         S0    S1  S2    S3   S4   S5
        O1      Y   Y     Y    Y    O2
```

The optimum ACIS-S spectroscopy chip set depends strongly on the expected spectrum of the target. Typically the maximum signal is desired, so the HETG and LETG observer is most likely to insist on all ACIS-S chips. If the science does depend strongly on the flux received on the S0 and S5 CCDs, the observer may need to specify all 6 ACIS-S CCDs to be on. However, the observer should be aware that the amount of useful flux on S0 and S5 with the LETG is typically quite low given they are both FI CCDs (see Figure 9.6). Given the current thermal performance of the spacecraft, it is probable that one of the two optional CCDs would be turned off.

Further information can be found at the CXC website http://cxc.harvard.edu/acis/optional_CCDs/optional_CCDs.html.

ACIS-I Count Rate and Number of Spectral Lines We want to know the maximum number of counts from the brightest source in the field (not necessarily the target), and if the proposer believes that there will be lines in the spectrum from this source. Both questions are being asked to trigger assessment by the *CXC* of the sensitivity of the experiment to the gain calibration and so that appropriate scheduling may be employed to avoid thermally-induced gain drifts that might impact the observation. If the GO is interested in the optimal spectral performance of the ACIS CCDs, they should seriously consider using only 4 CCDs as discussed above.

Exposure Mode There are only two choices: Timed Exposure (Section 6.12.1) or Continuous Clocking (Section 6.12.3).

Timed Exposure Mode The timed exposure mode with the default nominal (and optimal) frame time of 3.2s is the typical mode for ACIS observations. Note that the option of selecting frame times shorter than nominal reduces observing efficiency, and hence the number of photons collected for a given observation time.

Continuous Clocking Mode The Continuous Clocking mode is useful when timing data are so critical and/or pileup is such a problem that the sacrifice of one dimension of spatial data is warranted. The use of continuous clocking may also lead one to consider specifying a particular satellite roll orientation (see Chapter 3) in order to avoid having two different sources produce events in the same CCD column. (See Section 6.20.4 below.)

6.20.2 Optional Parameters

Alternating Exposures This option applies *only* to Timed Exposures. The parameters specifying an alternating exposure are:

- the number of secondary exposures per primary exposure (1-15)
- the primary exposure frame time

Frame times and efficiencies in TE mode are discussed in Sections 6.12.1 and 6.12.1. The Alternating Exposure option is discussed in Section 6.12.2.

Energy Filtering It is possible to remove events from the telemetry stream, and thus avoid telemetry saturation, by specifying an energy acceptance filter within which detected events will be telemetered. The default discards events above 3250 ADU (nominally 13 keV). The total per-chip background rates for different upper energy cut-offs are in Table 6.11.

Starting September 2006, a new energy to PHA conversion is used for observations with energy filters. Two sets of conversions are used, depending on the aimpoint of the observation. Observations with ACIS-S at the aimpoint use a conversion tailored for the BI CCDs and those with ACIS-I at the aimpoint use FI CCD-specific conversions. The BI and FI specific conversions are more accurate for each type of CCD than the conversion used in previous cycles. The assumption is that it is desirable to have the most accurate gain conversion for the CCD on which the HRMA aimpoint falls. Note that the conversion only impacts the on-orbit energy filtering. *Ground data processing will always apply the appropriate PHA to energy conversion.*

The observer should be aware that for observations which mix CCD type (i.e. BI and FI CCDs on), the selected conversion (based on aimpoint as above), will nevertheless apply to all selected CCDs. This will not affect the observation if the low energy threshold for the energy filter (the “Event filter: Lower” parameter) is 0.5 keV or less as the use of either conversion at these energies results in essentially no difference in the number of accepted events. However, above 0.5 keV, the conversions are significantly different. Finally, observations which apply an energy filter with a low energy threshold greater than 0.5 keV will automatically be assigned spatial windows that allow the FI CCDs to use the FI conversion and the BI CCDs to use the BI conversion regardless of aimpoint. Proposers who need an energy filter above 0.5 keV are encouraged to contact the CXC HelpDesk to discuss their plans with an instrument scientist.

Spatial Windows A more sophisticated approach to removing data from the telemetry stream, and thus avoiding telemetry saturation, is by the use of a Spatial Window. This option offers a good deal of flexibility. One may define up to 6 Spatial Windows per CCD. Each window can be placed anywhere on the chip. Note there is a significant difference between a Spatial Window and a Subarray (Section 6.12.1): Subarrays affect the transmission of CCD data to the on-board ACIS processors; Spatial Windows select events detected by the processors and only impact the telemetry rate. The user may also specify the window energy threshold and energy range.

Spatial windows can specify the sample rate for events inside them. A sample rate of 0 excludes all events; the default rate of 1 includes all events; a rate of $n > 1$ telemeters one out of every n events in the window. A spatial window could be used to eliminate a bright, off-axis source that would otherwise overwhelm the telemetry stream. The order in which the spatial windows is specified is important if they overlap. The earliest specified window including a given pixel will be applied to events at that pixel.

6.20.3 Non-ACIS Parameters Relevant to an Observation with ACIS

There are a small number of additional parameters that need to be considered in specifying an observation with ACIS: (1) the off-axis pointing (if required), which reduces the flux, and spreads out the image; (2) the roll angle (Chapter 4); (3) time constraints (if any); and (4) time monitoring intervals (if any).

6.20.4 Choosing CC-Mode for Bright Source Observation

In the past, the continuous clocking (CC) mode (see Section 6.12.3) has been used to mitigate pileup in very bright sources (see Section 6.15.2). ACIS has offered two standard telemetry formats for observations performed in CC mode, faint (F) and graded (G) (see Section 6.14.2). While the CC-F mode choice has been used on occasion, the CC-G mode has been in the program for over 2 Msec of Chandra observing time, primarily to accommodate HETG spectra of bright X-ray binaries. The objective was to use CC mode in order to effectively mitigate pileup and conserve discrete structures such as emission and absorption lines, and edges in the dispersed spectrum. G mode also reduces the possibility of telemetry saturation.

Spectra in CC-mode, however, carry a number of currently uncalibrated artifacts ranging from a wrong spectral shape at wavelength larger than 10 Å, a smeared Si K edge, and charge losses below 3 Å. For bright sources up to about 300 mCrab we recommend the use of TE faint mode with four CCDs S1 − S4 and a 350 row subarray, at the expense of the spectral range above 12 Å(< 1 keV), some pileup ($< 10\%$), and some moderate amount of frame drops. The latter can be mitigated by using TE graded mode in extreme cases.

We now have developed methods to calibrate modes similar to, but not identical to, the G mode. Starting with Cycle 12, the G mode has been altered to include some of the flight grades that were previously rejected on board. ACIS now telemeters all flight grades except 24, 107, 127, 214, 223, 248, 251, and 255.

Here are a few guidelines for the use of CC-mode and the HETG. Please note, that in any case spectra above above 12 Å(< 1 keV) are always affected by some enhanced background:

- CC-faint mode can be used for sources of about 60 mCrab with no additional measures to restrict event selection
- CC-faint mode can be used for sources of about 90 mCrab and a zero order exclusion window selection of only every 10th (or less) photon
- CC-faint mode can be used for sources of about 105 mCrab and a zero order exclusion window selection of only every 10th (or less) photon and an event energy filter starting at 0.3 keV and a range of 10 keV (or less).

For even brighter sources and in the case of HETG spectra, other mitigating actions can be taken, such as shutting off CCDs or moving half the source and dispersion off the array (i.e. using Z-SIM = -11mm). In these cases sources of over 300 mCrab can be accommodated.

For sources significantly exceeding such flux levels, CC-graded mode may be used. Like in the case of CC-faint mode, ASCA grade 7 events are no longer entirely rejected and similarly additional flight grades enter the telemetry stream causing frame drops to increase by about 10% compared to the previous definition. Mitigating strategies similar to those described above may be used.

Chapter 7

HRC: High Resolution Camera

7.1 Introduction and Instrument Layout

The High Resolution Camera (HRC) is a microchannel plate (MCP) instrument comprised of two detectors, one optimized for imaging (HRC-I), and one (HRC-S) which serves as a readout for the Low Energy Transmission Grating (LETG) discussed in Chapter 9. The HRC-I provides the largest field-of-view ($\sim 30' \times 30'$) of any detector aboard *Chandra*, and its response extends to energies below the sensitivity of ACIS (Chapter 6), albeit without comparable spectral resolution. The time resolution of the HRC detectors (16 μsec) is the best on the observatory, but can only be utilized under certain conditions as discussed in Section 7.11.

A schematic of the HRC layout is shown in Figure 7.1, and a summary of the characteristics is given in Table 7.1. A cross-section of the HRC-S layout and the relationships to the optical axis and the LETG Rowland circle are shown in Figure 7.2.

The HRC is a direct descendant of the Einstein (Giacconi *et al.* 1979) and ROSAT High Resolution Imagers (HRIs) (David *et al.* 1996). The ROSAT HRI had the same coating (CsI) as the HRC.

The Instrument Principal Investigator is Dr. Stephen S. Murray of the Smithsonian Astrophysical Observatory.

7.2 Basic Principles

Figure 7.3 illustrates the features of the HRC MCPs. X-rays enter through a UV/Ion shield, necessary in order to reduce/avoid signals from UV light, ions, and low energy electrons. Most of these X-rays are then absorbed in the CsI-coated walls of the first (input) of two consecutive MCPs. The axes of the millions of tubes that comprise the input and output MCPs are not parallel to the optical axis but are canted ("biased") at an angle of 6° in opposite directions as shown in Figure 7.3. This bias improves the probability of an interaction. The CsI coating enhances the photoemission over that from a bare MCP. The resulting photoelectrons are then accelerated by an applied electric field.

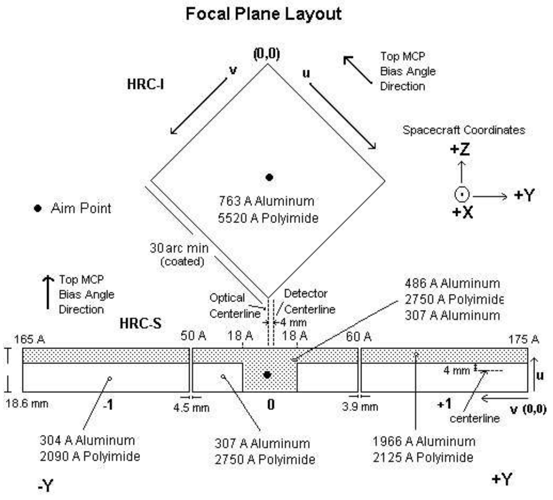

Figure 7.1: A schematic of the HRC focal plane geometry as viewed along the optical axis from the telescope towards the focal plane.

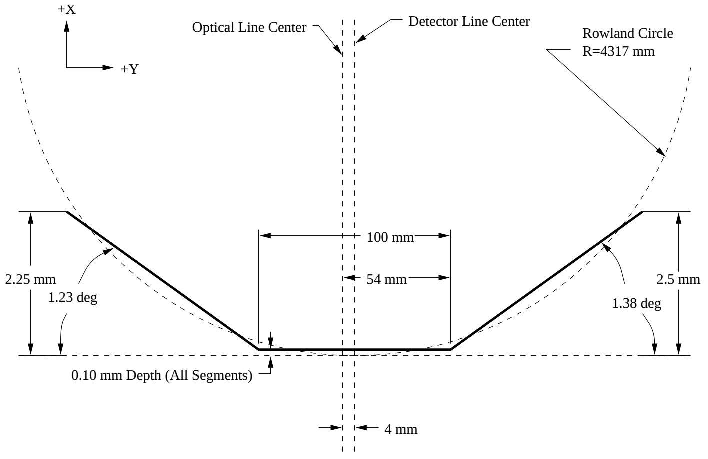

Figure 7.2: A schematic cross-section of the HRC-S MCP (not to scale). The HRC-S is shifted 0.1 mm forward of the tangent plane, so the Rowland circle intersects each segment at two points.

Table 7.1: HRC Parameters

Focal Plane Arrays		
HRC-I:	CsI-coated MCPpair	90 × 90 mm coated (93 × 93 mm open)
HRC-S:	CsI-coated MCPpairs	3-100 × 20 mm
Field of view	HRC-I:	$\sim$ 30 × 30 arcmin
	HRC-S:	6 × 99 arcmin
MCP Bias angle:		6°
UV/Ion Shields:		
	HRC-I:	5520 Å Polyimide, 763 Å Al
	HRC-S:	
	Inner segment	2750 Å Polyimide, 307 Å Al
	Inner segment "T"	2750 Å Polyimide, 793 Å Al
	Outer segment	2090 Å Polyimide, 304 Å Al
	Outer segment (LESF)	2125 Å Polyimide, 1966 Å Al
Spatial resolution	FWHM	$\sim 20\mu$m, $\sim$ 0.4 arcsec
	HRC-I: pore size	10μm
	HRC-S: pore size	12.5μm
	HRC-I: pore spacing	12.5μm
	HRC-S: pore spacing	15μm
	pixel size (electronic readout)	6.42938μm [0.13175 arcsec pixel^{-1}]
Energy range:		0.08 − 10.0 keV
Spectral resolution	$\Delta E/E$	$\sim$ 1 @1keV
MCP Quantum efficiency		30% @ 1.0 keV 10% @ 8.0 keV
On-Axis Effective Area:	HRC-I, @ .277 keV	133 cm^2
	HRC-I, @ 1 keV	227 cm^2
Time resolution		16 μsec (see Section 7.11)
Limiting Sensitivity	point source, 3σ detection in 3×10^5 s (power-law spectrum: $\alpha = 1.4$, $\mathrm{N_H} = 3 \times 10^{20}$ cm^{-2})	9×10^{-16} erg cm^{-2} s^{-1}
Quiescent background	HRC-I	1.7×10^{-5} cts s^{-1} arcsec^{-2}
in level 2 data	HRC-S	6.3×10^{-5} cts s^{-1} arcsec^{-2}
Intrinsic dead time		50 μs
Constraints:	telemetry limit	184 cts s^{-1}
	maximum counts/observation/aimpoint	450000 cts
	linearity limit (on-axis point source)	
	HRC-I	$\sim$ 5 cts s^{-1} (2 cts s^{-1} pore^{-1})
	HRC-S	$\sim$ 25 cts s^{-1} (10 cts s^{-1} pore^{-1})

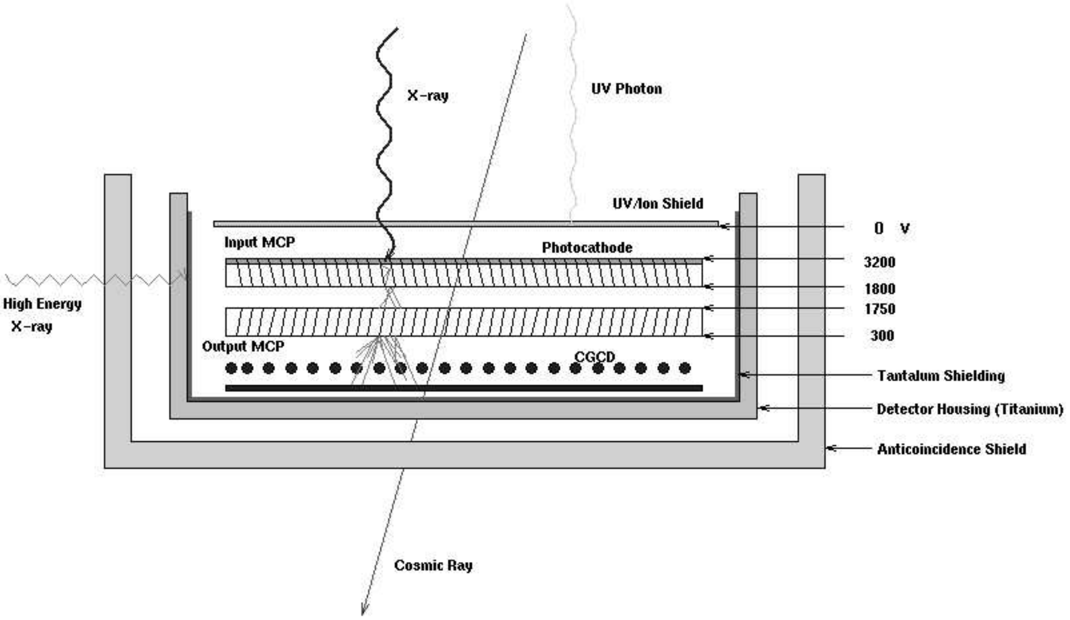

Figure 7.3: A schematic of the HRC Microchannel-Plate detector.

The next interaction with the walls releases several secondary electrons and so on, until a cascade of electrons is produced.

One purpose of the second (output) MCP is to provide additional gain. In addition, reversing the direction of the second MCP's bias angle with respect to the first removes a clear path for positive ions, and hence reduces the possibility of (positive) ion feedback - where an accelerated ion moving in the opposite direction as that of the electrons ends up causing the release of electrons and starts the process all over again.

The electron cloud — typically about 2×10^7 electrons per photon — that emerges from the output MCP is accelerated towards a position-sensitive charge detector. The HRC employs two types of charge detectors: the HRC-I uses a crossed grid charge detector, while the HRC-S uses a hybrid where one axis is comprised of wires and the other has gold lines deposited on a ceramic substrate. Adjacent wires (or lines) are resistively connected and every eighth wire is attached to a charge-sensitive amplifier, referred to as a "tap", as illustrated in Figure 7.4.

The X-ray position is determined by calculating the centroid of the charge cloud exiting the rear MCP via the "three tap algorithm". In short, the three tap algorithm determines the charge cloud centroid using a combination of digital and analog electronics and off-line processing. Fast discriminators and logic circuits first determine a "coarse" position, which is based on the amplifier with maximum detected charge. Analog switches then select the three amplifiers centered on that coarse position and steer them to analog-to-digital converters. The coarse position and three digitized values are then telemetered to the ground and used off-line to calculate the event position. This process is performed for each axis. The reconstructed X-ray position can then be written as the sum of a coarse position and a charge centroid term centered on the coarse position:

$$pos = cp_i + (\frac{Q_{cp_{i+1}} - Q_{cp_{i-1}}}{Q_{cp_{i-1}} + Q_{cp_i} + Q_{cp_{i+1}}}) \times \Delta \tag{7.1}$$

where cp is the coarse position, $Q_{cp_{i+1}}$ is the charge measured on the cp_{i+1} tap, and Δ is the distance between taps. Since the charge cloud extends beyond the two outer taps, each of the outer amplifiers underestimates the amount of charge needed to calculate the true centroid. For an event perfectly centered on the middle tap, the amount of charge missed by the two outer taps cancel in the equation. If however, the event position is not over the center of a tap, the fractional amount of missing charge is different and produces a small systematic error in the reconstructed position. The small systematic positional error combined with the coarse position logic produce "gaps" in the HRC images. These gaps are perfectly aligned with the detector axes and correspond to positions exactly half-way between amplifier taps. The gaps are systematic and are removed in data processing.

The three-tap position algorithm described above can be improved upon by making use of the predictability of the shape of the charge cloud exiting the rear MCP. The spatial distribution of the charge cloud leaving the rear of the second MCP has a very specific shape for X-ray induced events. This shape has often been modeled as the combination of a Gaussian and a Lorentzian distribution. Due to this specific shape, it has been observed and simulated via Monte Carlo techniques that the fine position term:

$$(\frac{Q_{cp_{i+1}} - Q_{cp_{i-1}}}{Q_{cp_{i-1}} + Q_{cp_i} + Q_{cp_{i+1}}}) \tag{7.2}$$

and the complementary term:

$$(\frac{Q_{cp_i}}{Q_{cp_{i-1}} + Q_{cp_i} + Q_{cp_{i+1}}}) \tag{7.3}$$

are highly correlated. In fact, a scatter plot of these two quantities for X-ray induced events closely describes a hyperbola. Non X-ray events, primarily those due to the passage of charged particles, produce charge distributions that are often larger and more spatially extended and complex. As such, it is possible to remove many non-X-ray background events by filtering out those events that do not fit the hyperbola. Furthermore, since the charge distribution is centrally peaked, the complement Q_{cp_i} term is larger and less susceptible to noise-induced errors than the $Q_{cp_{i+1}} - Q_{cp_{i-1}}$ difference term. It is therefore possible to use the complement term, and the best fit hyperbolic locus, to correct those events where instrumental noise has compromised the three-tap fine position. A much more detailed explanation of this technique is presented in Murray, *et al.* (2000).

For more details concerning the HRC see Murray & Chappell (1989) and Zombeck *et al.* (1995).

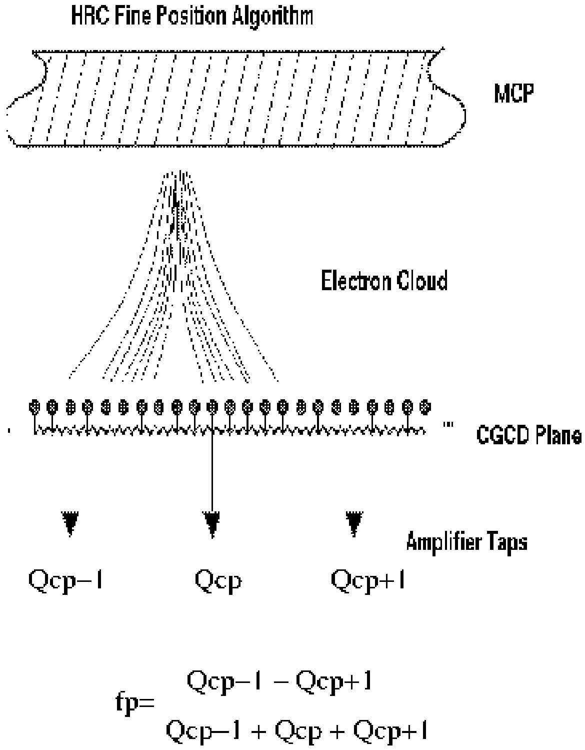

Figure 7.4: Schematic representation of event position determination for one axis of the crossed grid charge detector (CGCD). The electron cloud is divided between several amplifiers. The position of the event relative to the central coarse position is calculated from the difference between the signals on either side of the coarse position divided by the sum of the three signals.

7.2.1 Aimpoints

The aimpoints are the positions on the instrument where the flux from a point source with no commanded offsets is placed. Note that the aimpoint position is offset by $\approx 10 - 20''$ from the optical axis.[1]. There are two nominal aimpoints as indicated in Figure 7.1 - one at the approximate center of the HRC-I, and the other slightly off-center on HRC-S. The HRC-S aimpoint Z-offset places the LETG-dispersed image along the centerline of the thinner part of the UV/Ion Shield (the two white rectangles in the diagram; see Section 7.8). The HRC-S aimpoint Y-offset is slightly off-center, so that the boundaries between the three HRC-S segments correspond to different wavelengths of the grating-dispersed spectrum (see Chapter 9 for details).

7.3 Shutters

Attached to the HRC are two mechanical blades that serve as shutters. These shutters were used to block out portions of the incident flux to aid in focusing the HRC. The blade position settings are variable and were designed to allow one to block the zero-order image of a grating observation. Currently only one blade is functional, and we do not offer use of this shutter as an observing option.

7.4 Dither

The spacecraft is dithered during all observations in a Lissajous figure. For observations with the HRC, the dither amplitude is 40 arcsec peak-to-peak, with nominal periods of 1087 (in Y) and 768 (in Z) seconds. Dithering serves to average out pixel-to-pixel variations in the response. It also eliminates gaps in spectral coverage with the LETG/HRC-S combination caused by the HRC-S intersegment spaces near -50 Å and +60 Å (see Figure 7.3). The effects of dither are removed during ground processing of the data.

7.5 Spatial Resolution & Encircled Energy

Imaging with the HRC is best performed with the HRC-I because of the much lower background (Section 7.10) and larger field of view. The intrinsic PSF of the HRC is well modeled by a Gaussian with a FWHM of ~ 20 μm (~ 0.4 arcsec). The HRC pixels, determined by the electronic readout (*not* the pore size), are 6.42938 μm (0.13175 arcsec). The HRC response is thus well matched to the intrinsic HRMA resolution (Chapter 4).

Approximately 90% of the encircled energy lies within a 14 pixel diameter region (1.8 arcsec) from the center pixel for the observation of AR Lac shown in Figure 7.6. The measured PSF is as good or better than the simulations because a very conservative preflight estimate of the aspect solution was used in the simulations. Analysis of AR Lac and

---

[1] See `http://cxc.harvard.edu/cal/Hrma/OpticalAxisAndAimpoint.html`

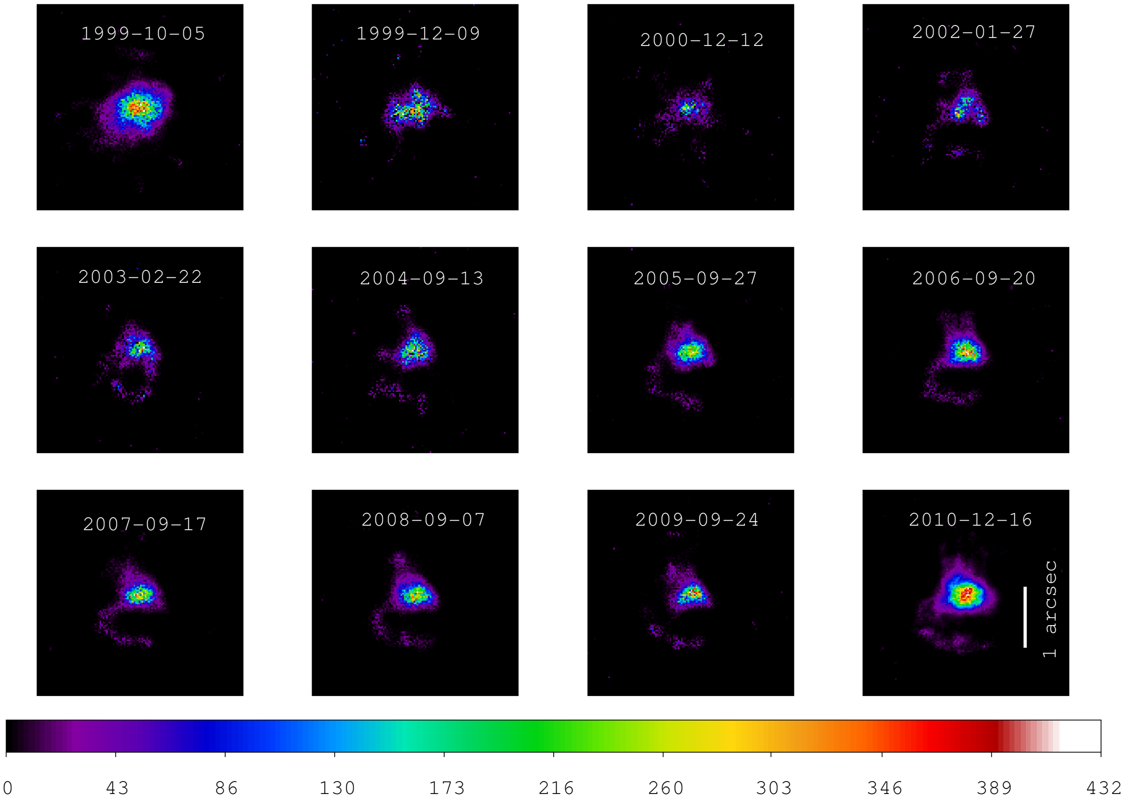

Figure 7.5: Deconvolved images of the calibration point source AR Lac, observed on-axis once each year from 1999 till 2010 (see Juda & Karovska 2010). The images are displayed congruent with the detector (U,V) coordinate system. The vertical white bar is 1 arcsec in length. A hook-like feature is present in all data acquired since 2002; manifestations of such features may also be present in earlier data (Karovska 2011).

Capella observations carried out at different parts of the detector show that a hook-like feature has developed since 2003 (see Figure 7.5; Juda & Karovska 2010). This feature contains $\approx 5\%$ of the flux, and is located $\approx 0.8''$ from the centroid, towards the origin corner of the detector coordinate system, i.e., in the direction towards the ACIS detectors. This does not appear to be a HRC-specific feature (Kashyap 2010; see also the CIAO caveats page on the PSF artifact: http://cxc.harvard.edu/ciao/caveats/psf_artifact.html).

The HRC PSF suffers from a tailgating effect, where photons within the area of the PSF that are recorded rapidly after a previous photon have less accurate positions, leading to the PSF for these events being puffier (Juda 2012, http://cxc.cfa.harvard.edu/contrib/juda/memos/hrc_pileup/index.html). Photons with arrival time differences of < 0.05 sec are affected.

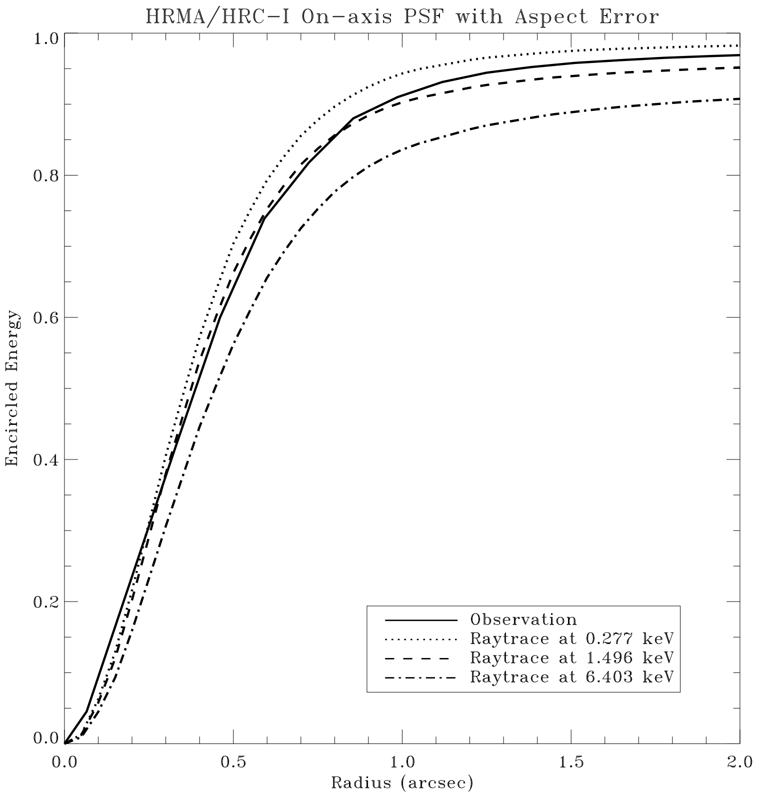

Figure 7.6: The predicted and observed fractional encircled energy as a function of radius for an on-axis point source observed with the HRMA/HRC-I. The calculations (at two energies, 0.277 keV and 6.40 keV) include a very conservative estimate of the aspect solution (FWHM = 20 μm (0.41″)). Flight data from an observation of AR Lac are also shown.

The imaging resolution of the HRC-I degrades off-axis for two reasons: the HRMA PSF increases in size with increasing off-axis angle, and the deviation increases between the flat HRC-I detection surface and the curved HRMA focal surface. The off-axis imaging behavior of the HRC-I is shown in Figure 7.7. The nominal best-focus of the HRC-I is chosen to provide the best image quality in the center of the field-of-view.

7.6 Non-Dispersive Energy Resolution

The intrinsic energy resolution of the HRC is poor (see Figure 7.8, which shows the HRC-I pulse height distributions for six energies obtained during sub-assembly calibration; the distributions for the HRC-S detector are somewhat narrower). Even though the pulse-height amplitude (PHA) of each event is telemetered, spectral fitting cannot be usefully

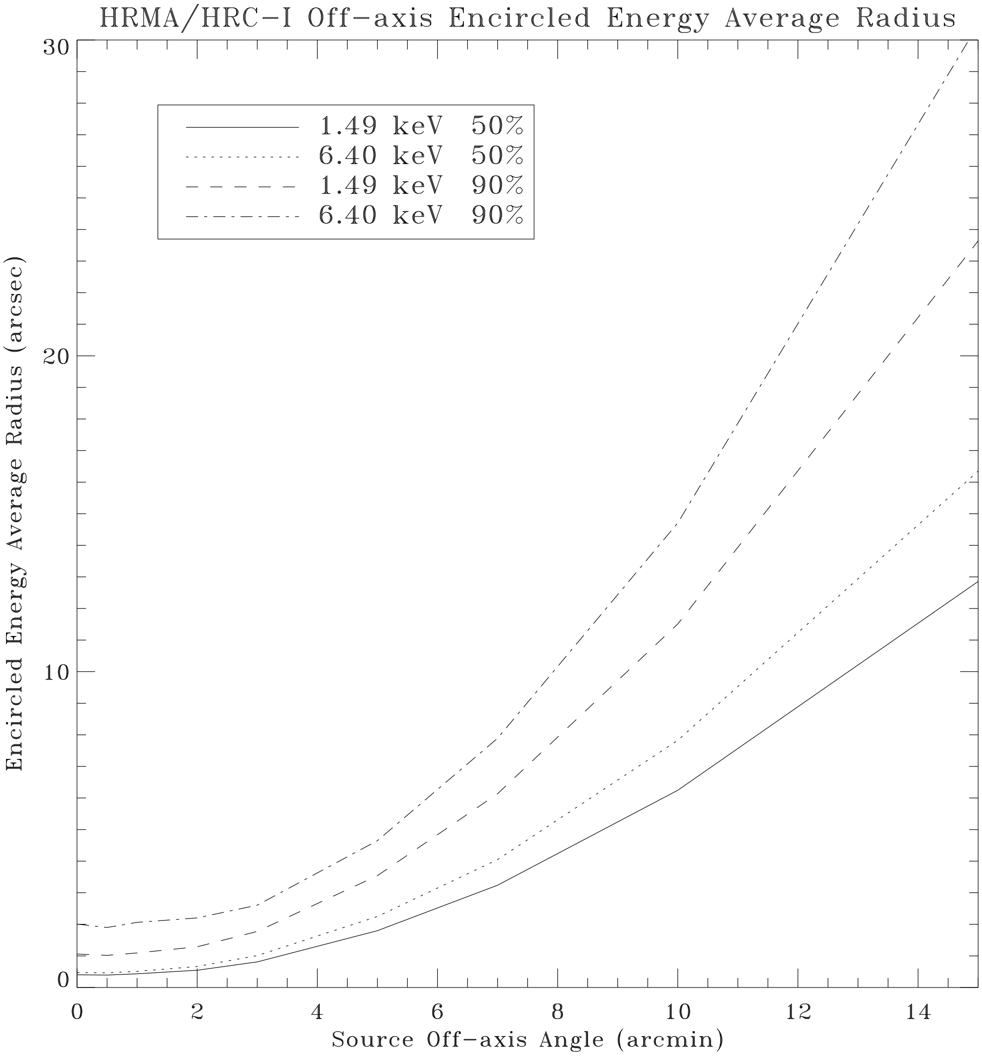

Figure 7.7: Encircled energy as a function of source off-axis angle for 50% and 90% encircled energy for 1.49 and 6.40 keV for the combined HRMA/HRC-I. A conservative contribution from the aspect solution is included (FWHM = 20 μm ($0.41''$)). A plot for the HRC-S would be almost identical since the PSFs of the two instruments are virtually identical.

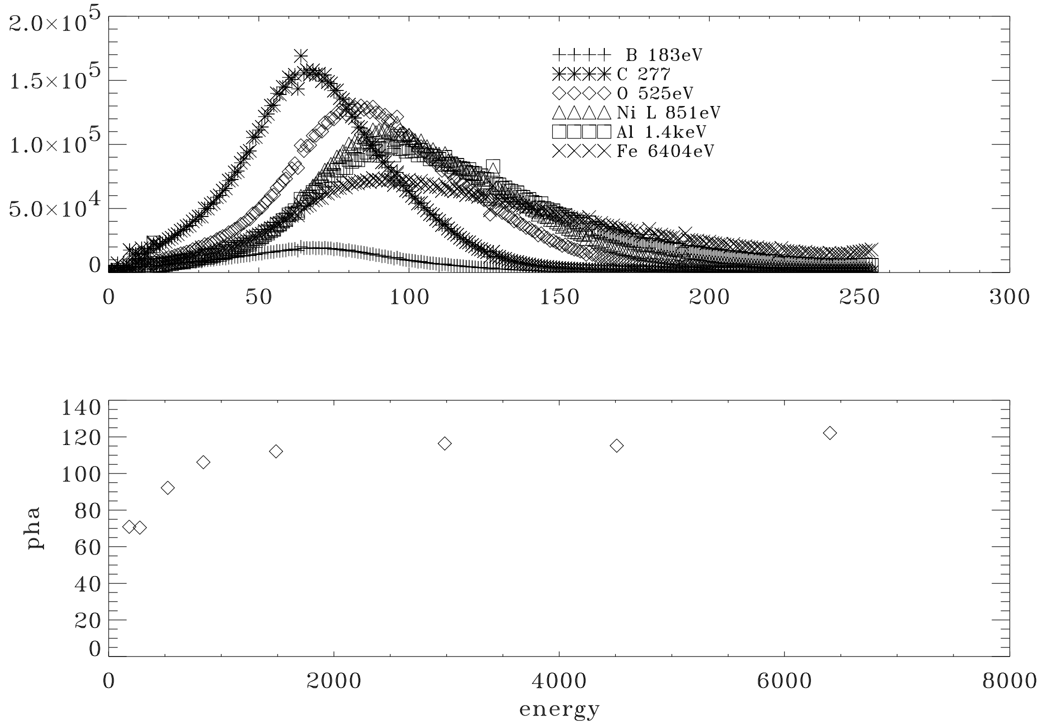

Figure 7.8: Pulse height versus energy for the HRC-I detector (top) and the centroid of the pulse height distribution versus energy (bottom). These data were obtained at SAO during flat field, normal-incidence-illumination tests. The voltage settings have been changed in-flight and thus the applicability of these data is questionable. They are presented here only for illustrative purposes.

carried out for sources observed with the HRC. However, there is sufficient resolution that hardness ratios may be used to distinguish between gross differences in the spectra (see Figures 7.9 - 7.12, which show color-color grids for some common spectral models).

7.7 Gain Variations

There are significant spatial and temporal gain variations present in both instruments (see Figures 7.13, 7.14). Gain correction maps, available since CALDB v3.2.5, correct the spatial variations (for both HRC-I and HRC-S) as well as correct for the temporal gain drop (for the HRC-I). These gain correction files transform the measured PHA values to Pulse Invariant (PI) values that are uniform across the detector (to ≈ 5% over a tap) and correspond to the PHA values seen early in the mission. Note that starting from CIAO v4.2/CALDB v4.2, the gain map is applied to the scaled sum of the amplifier signals

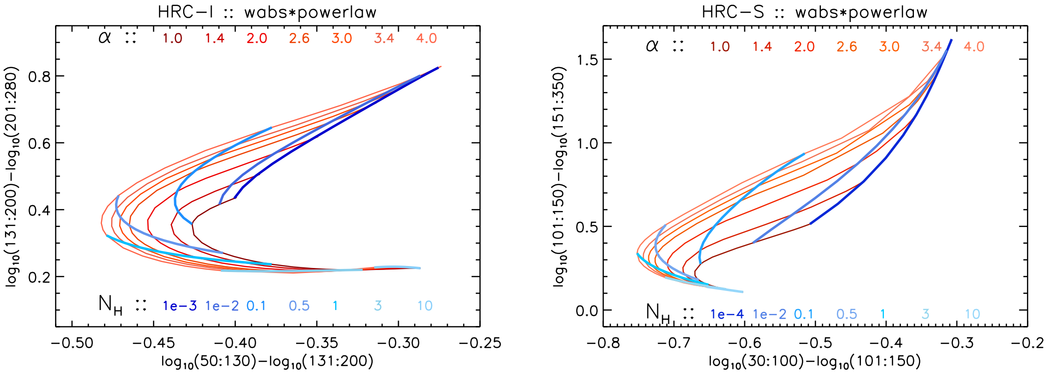

Figure 7.9: The color-color grid for a power-law spectral model, as calculated for the HRC-I (*left*) and the HRC-S (*right*). The PI channels are grouped into three bands, $S = 50:130$, $M = 131:200$, and $H = 201:280$ for the HRC-I and $S = 30:100$, $M = 101:150$, and $H = 151:300$ for the HRC-S, and their logarithmic ratios are plotted along the two axes for specific values of the model parameters α (the index of the power-law function) and N_H (the absorbing column density in units of 10^{22} cm^{-2}). Lines of constant α are depicted in red shades, and lines of constant N_H in blue shades.

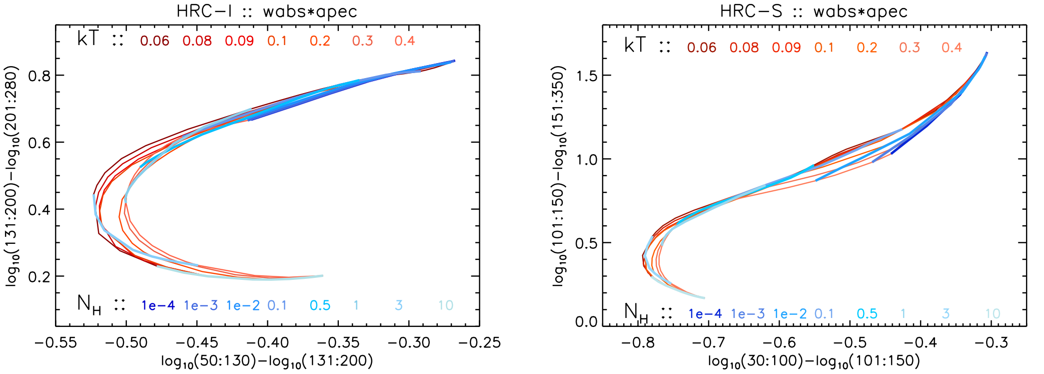

Figure 7.10: As in Figure 7.9, for an APED thermal model at relatively low temperatures. The loci of constant plasma temperature (kT) are in shades of red and are labeled by their value in keV.

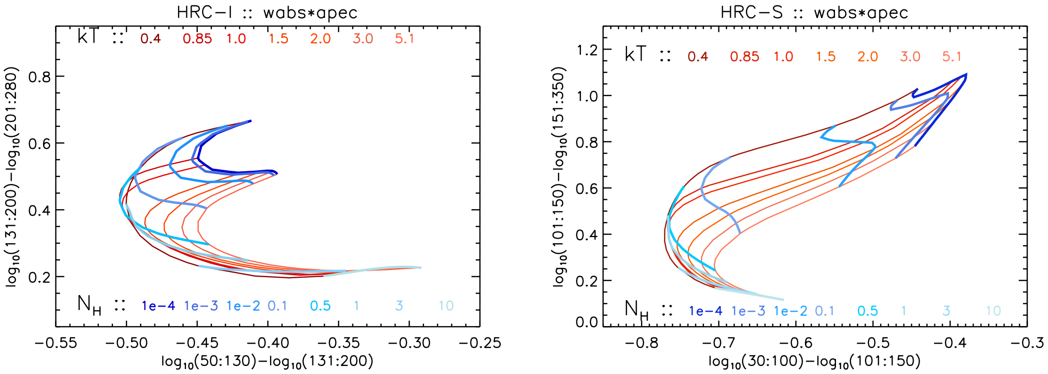

Figure 7.11: As in Figure 7.10, for a set of higher plasma temperatures.

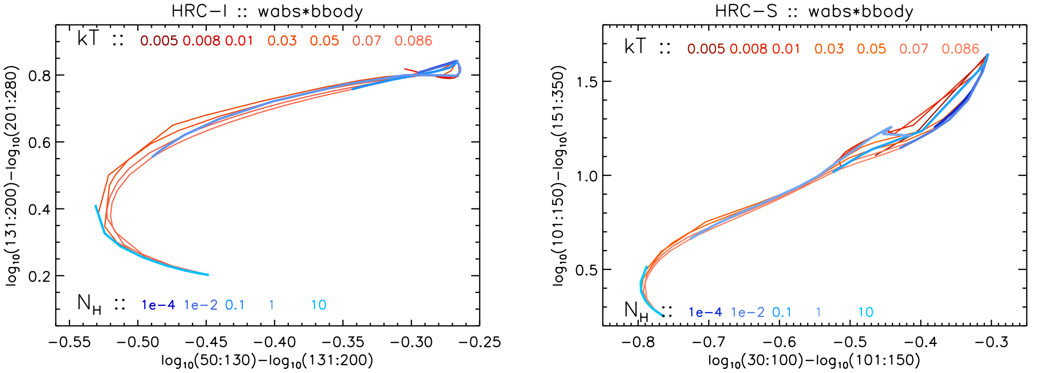

Figure 7.12: As in Figure 7.9, for a blackbody model. The loci of constant temperature (kT) are in shades of red and labeled by their value in keV.

(SUMAMPS) rather than to PHA to generate a better behaved PI distribution (Wargelin 2008, Posson-Brown & Kashyap 2009). In March 2012, the voltage of the HRC-S was increased in order to mitigate the QE loss that was occuring at long wavelengths due to gain decline (Wargelin 2012). See Chapter 9 for details.

7.8 UV/Ion Shields

The placement, composition, and thickness of the various UV/ion shields (filters) are shown in Figure 7.1. Details of the UVIS transmission as a function of energy can be found at http://cxc.harvard.edu/cal/Hrc/detailed_info.html#uvis_trans.

The shields suppress out-of-band (outside the X-ray band) radiation from the ultraviolet through the visible. The detector response to out-of-band light for an object in its field-of-view is a possible source of unwanted signal. Suppressing out-of-band radiation is particularly important for observing sources which have bright XUV and UV fluxes. The HRC has strongly reduced sensitivity in this spectral region, as shown in Figure 7.15. As part of the in-flight calibration program the bright A star Vega (A0V, U=0.02, B=0.03, V=0.03) was observed with both the HRC-I and HRC-S. The predicted count rate for HRC-I was 7×10^{-4} cts s^{-1}. From monitoring observations of Vega, an upper limit to the UV rate of 8×10^{-4} cts s^{-1} is calculated (Pease *et al.* 2005). The image of Vega was also placed on three regions of the HRC-S - the inner segment "T", the thin aluminum inner segment, and on one of the thin aluminum outer segments. The predicted count rates were 1, 400, and 2000 cts s^{-1} respectively. The corresponding observed rates were 0.2, 240, and 475 cts s^{-1}. Sirius was observed with the HRC-S/LETGS in order to obtain a soft X-ray spectrum of Sirius B (white dwarf) and Sirius A (A1V, V=-1.46, B-V=0.01) was seen in zeroth order at about the expected count rate. Based on these sets of observations, the UV/Ion shields are performing as designed. Ongoing monitoring observations of Vega indicate no change in the UV response of HRC-I and HRC-S since launch. For a detailed discussion of the out-of-band response of the HRC to stars, see http://hea-www.harvard.edu/HRC/calib/palermopaper.ps , which allows one to determine the out-of-band count rate produced by a blackbody source with known T_{eff}, m_V, and N_H.

Scattered UV, FUV, and XUV light from the Sun or the bright Earth may cause a background dependence on viewing geometry. The spacecraft was designed to limit the contribution from stray scattered radiation to 0.01 cts cm^{-2} s^{-1} (2.4×10^{-7} cts $arcsec^{-2}$ s^{-1}) on the HRC. The imaged components of scattered radiation are dependent on the solar cycle, but are at most $\sim$ 0.01 cts cm^{-2} s^{-1} for most lines of sight.

7.9 Quantum Efficiency and Effective Area

The efficiency of the HRC detector is the product of the appropriate UV/Ion shield transmission and the quantum efficiency of the CsI coated MCP. Pre-flight flat field measurements show a 10% variation in the efficiency across the HRC-I. The HRC-S also exhibits

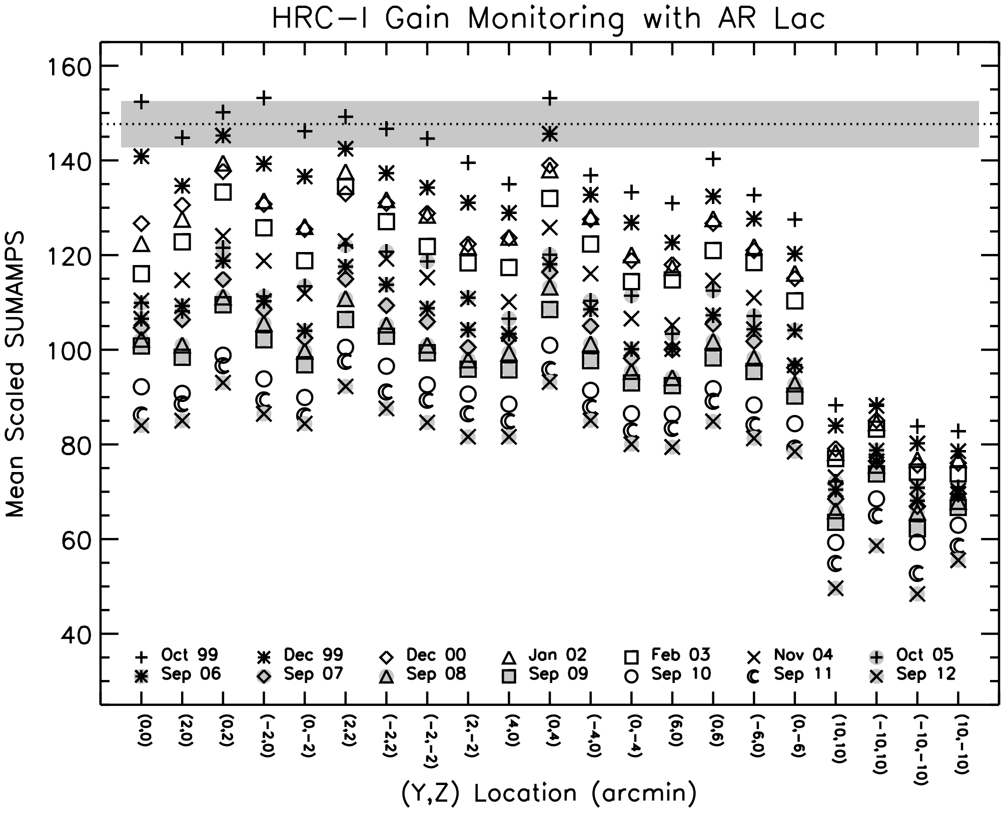

Figure 7.13: Monitoring the gain and gain correction across the HRC-I detector. The mean scaled sum of the amplifier signals (SUMAMPS) for AR Lac observations, carried out at various times and numerous locations across the HRC-I detector, are shown. The scaled SUMAMPS replace PHA. There also exist intrinsic variations in the spectrum which have not been accounted for in this figure. The values from data obtained at different years are shown with different symbols. Note the steady decline in the mean scaled SUMAMPS with time for all pointings; the gain maps in the CALDB can be used to renormalize them such that they are equivalent to an on-axis observation made in October 1999. The horizontal dotted line represents the gain corrected Pulse Invariant (PI) values and the shaded band represents the 1σ scatter on them.

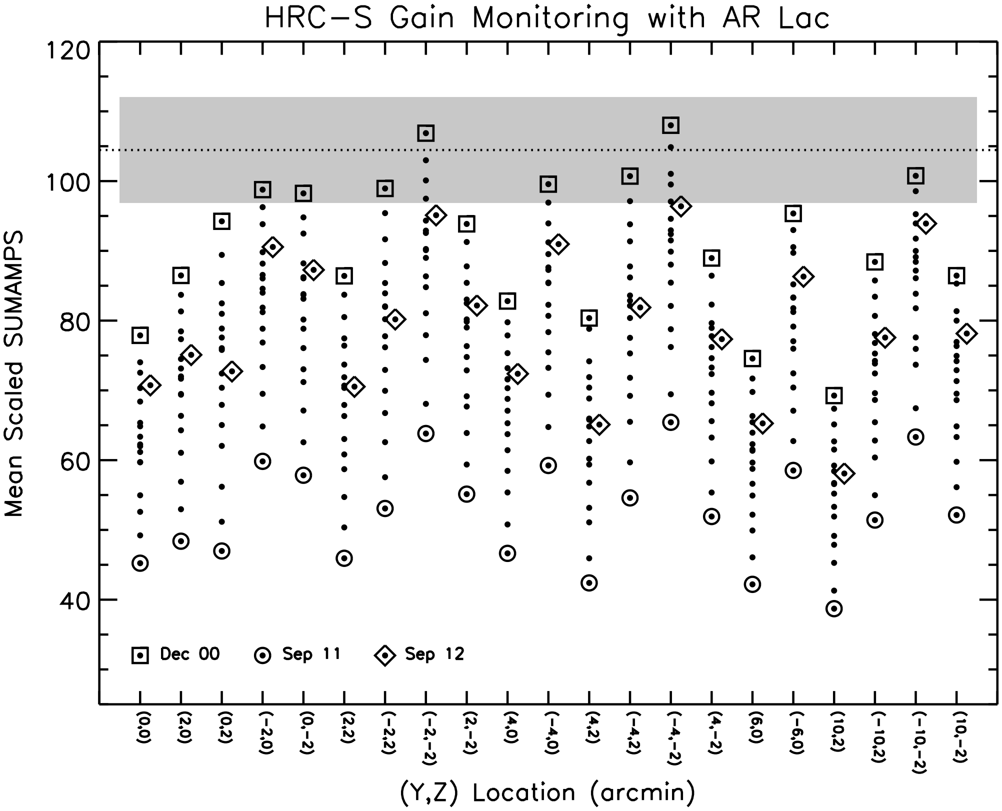

Figure 7.14: Monitoring the gain and gain correction across the HRC-S detector. The mean scaled SUMAMPS at each epoch (solid points) declined with time at all pointings from the beginning of the mission (square symbols) till before the voltage change (circle symbols). After the voltage was increased in March 2012, the mean SUMAMPS incraeased (diamond symbols) to nearly the same level as at the beginning of the mission.

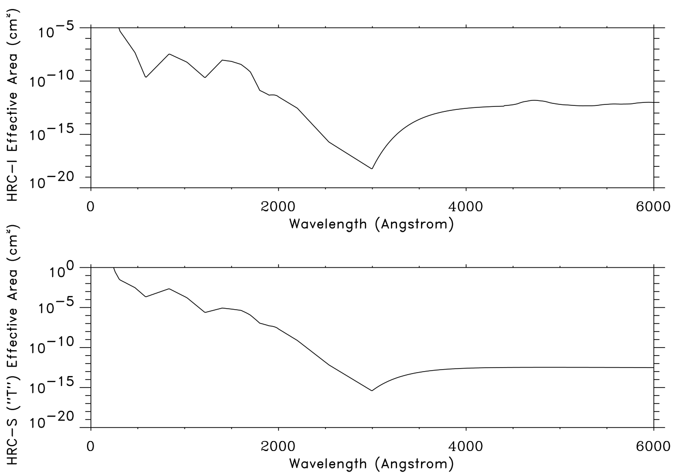

Figure 7.15: The HRC-I (top) and the center section of the HRC-S (bottom) UV/Ion shield effective area as a function of wavelength.

efficiency variations of the same magnitude, with the complex structure of the HRC-S UVIS contributing to the spatial variations. In-flight observations of Capella show that the HRC-I variation is known to better than $\sim 2\%$ at high energies. There are unexplained time dependent decreases in the QE for both HRC-I and HRC-S . The HRC-S decline is $\sim 10\%$ over the course of the mission and is wavelength independent. The HRC-I shows some fluctuations at low energies at large offset locations, ~ 10 arcmin away from the nominal aimpoint (see http://cxc.harvard.edu/ccw/proceedings/2007/presentations/possonbrown3/).

The combined HRMA/HRC effective areas – the product of the HRMA effective area, the quantum efficiency of the HRC-I or the HRC-S and the transmission of the appropriate UV/Ion shield, integrated over the point spread function – are shown in Figure 7.16. Monitoring of the efficiency of both detectors is continuing. The charge extracted since launch has resulted in a small decrease in gain in both detectors, but this has had a negligible effect on the efficiency (See http://cxc.harvard.edu/cal/Hrc/). The HRC-S QE has been declining at a rate of $\lesssim 1\%$ per year. This decline is generally wavelength independent except for certain locations on the detector where the gain decline causes loss of photons below the lower level discriminator. The QE decline in the HRC-I is $< 2\%$ over the duration of the mission at long wavelengths.

7.10 On-Orbit Background

7.10.1 HRC-I

The HRC-I anti-coincidence shield reduces the on-orbit valid event rate by about a factor of 5 to ~100 cts s^{-1} over the field; without on-board anti-co vetoing the rate would greatly exceed the telemetry limit of 184 cts s^{-1}. After standard processing, the Level 2 event file

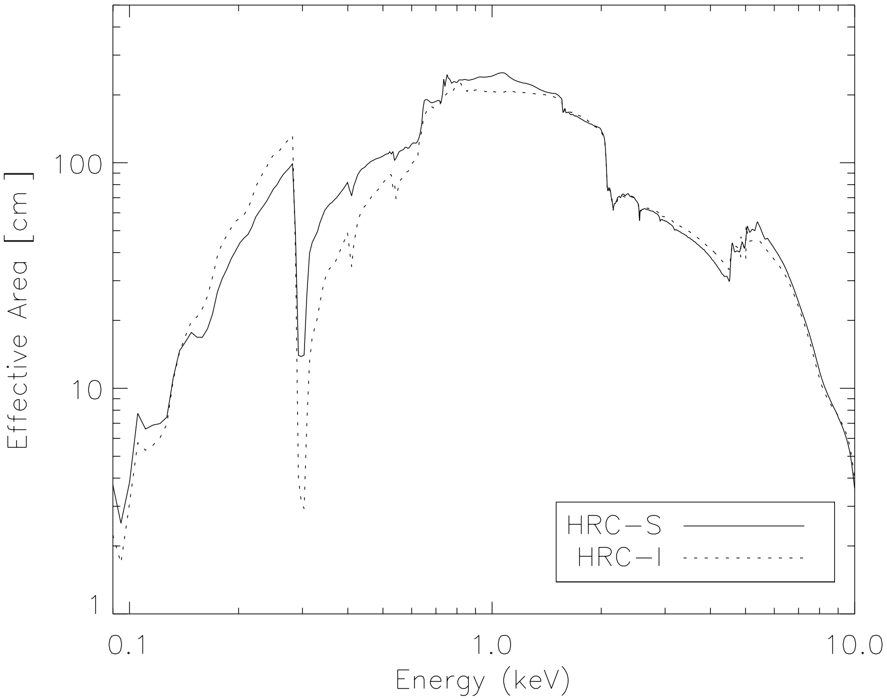

Figure 7.16: The effective area of the HRMA/HRC-I (dashed line) and the central segment of the HRMA/HRC-S in imaging mode (solid line) integrated over the full PSF. Absorption edges are due to the iridium coating on the mirrors, the CsI MCP coating, and the polyimide/Al of the UVIS.

background rate is $\sim 1.7 \times 10^{-5}$ cts s^{-1} $arcsec^{-2}$. The background varies smoothly over the field with no more than a 20% difference between the center (lower) and edges (higher) of the detector. The background is not azimuthally symmetric (see Isobe & Juda 2009). Note, the total event rate remains unchanged, but detector events in coincidence with antico events no longer enter the telemetry data stream. Before launch the expected rate, after vetoing the effects of cosmic rays, was 10-20 cts s^{-1} composed of mainly the internal rate of the MCPs (10-15 cts s^{-1}), and a small contribution from cosmic rays due to antico inefficiency. There is additional background in the HRC-I that is not well understood. For point source detection and exposure times of 100 ks or less the background is virtually negligible. However, for extended low surface brightness objects this relatively low rate can become significant depending on the specific details of the source.

Ground-based filtering further reduces the non-X-ray background in the HRC detectors (see Murray *et al.* 2000, Juda *et al.* 2000 and Wargelin *et al.* 2001; http://cxc.harvard.edu/cal/Letg/Hrc_bg/). After filtering the non-X-ray background for HRC-I data is reduced by $\sim 40\%$ while the corresponding reduction in X-ray events is less than a few percent. For the HRC-S, the non-X-ray background is decreased by $\sim 50\%$ and the X-ray loss is $1 - 2\%$. Furthermore, filtering makes the spatial distribution of the detector background flatter. Filtering also removes saturated events responsible for faint secondary "ghost" images (see Section 7.11).

7.10.2 HRC-S

The anti-coincidence shield of the HRC-S does not work because of a timing error in the electronics. The error is not correctable. As a result the event rate is very high and exceeds the telemetry rate limit. To cope with this problem the HRC team has defined a "spectroscopy region" which is about 1/2 of the full width and extends along the full length of the HRC-S detector. The spectroscopy region ($\sim$10 mm) is implemented using the edge blanking feature of the electronics. With this change, the telemetered quiescent background rate is about 120 cts s^{-1}.

The background can be further reduced in ground data processing by using pulse height filtering that preferentially selects X-rays over cosmic ray events. A reduction in background by a factor of about three is possible for dispersed spectra. Thus there are two relevant background rates for the HRC-S: a telemetry rate of 120 cts s^{-1} and a post-processing rate for calculating signal to noise. The latter is discussed in detail in Section 9.3.6 (see especially Figure 9.22).

7.10.3 Temporally Variable Background

Both the HRC-I and HRC-S experience occasional fluctuations in the background due to charged particles. These times of enhanced background are typically short (a few minutes to a few tens of minutes) and are anywhere from a factor of two to ten over the quiescent rates. The increased background appears to be uniformly distributed over the detector and introduces no apparent image artifacts. On average it seems that no more than about

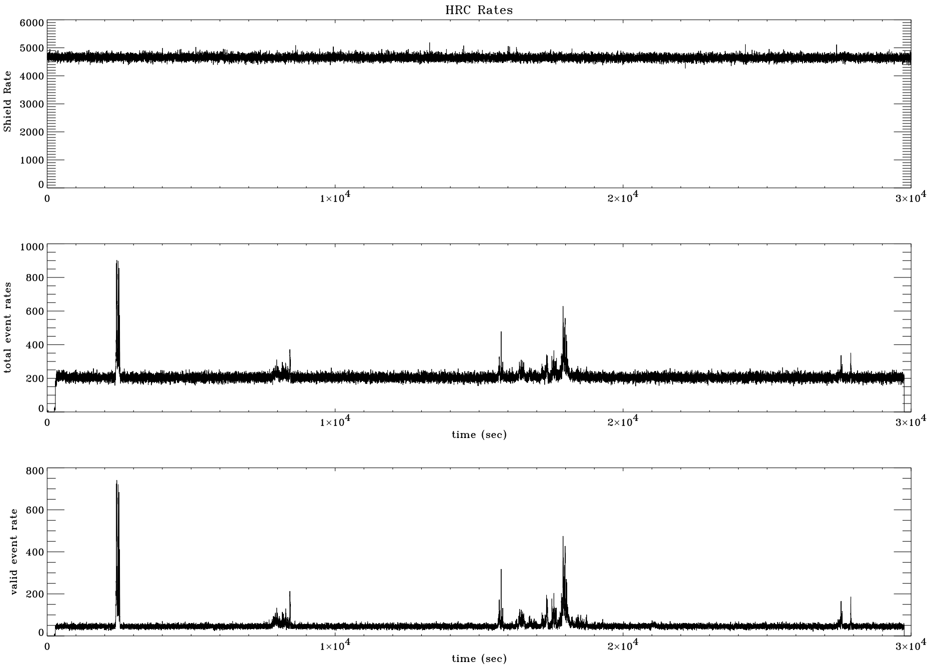

Figure 7.17: An example of the background variability during a ∼30 ks HRC-I observation of the SNR G21.5-09 taken on 1999-10-25. The total event rate (middle) and valid event rate (bottom) show correlated bursts up to ∼800 cts s^{-1}. The bursts are uniformly distributed over the detector. The anti-coincidence shield (top) exhibits no correlated enhancements. The total and valid rates differ by ∼200 cts s^{-1} due primarily to cosmic ray events that are vetoed and don't appear as valid events in the telemetry.

20% of the observing time is affected by these events, and they are easily recognized in the secondary science rate data and so can be filtered out if desired. An example of this behavior is shown in Figure 7.17. See Juda *et al.* (2002) for more information on the HRC background.

When the solar cycle was in minimum, the particle background flux increased (by almost a factor of 2 since launch). However, as we approach a more active portion of the solar cycle, we expect that the particle background will begin to decrease (see Figure 7.19). On-orbit non-sky background data sets are available for use in analysis and modeling. These data are taken when ACIS is viewing the sky but the HRC MCP HV is at the operational level so that the HRC is sensitive to the cosmic ray flux. The data sets are event lists and can be processed and filtered the same as data from a sky observation. The datasets needed to make background images for use in constructing exposure corrected flat-field images are available in CALDB (since v4.3.0). A recipe for their use is described in the CIAO thread http://cxc.harvard.edu/ciao/threads/hrci_bg_events

Furthermore, much of the background can be alleviated by filtering out events with

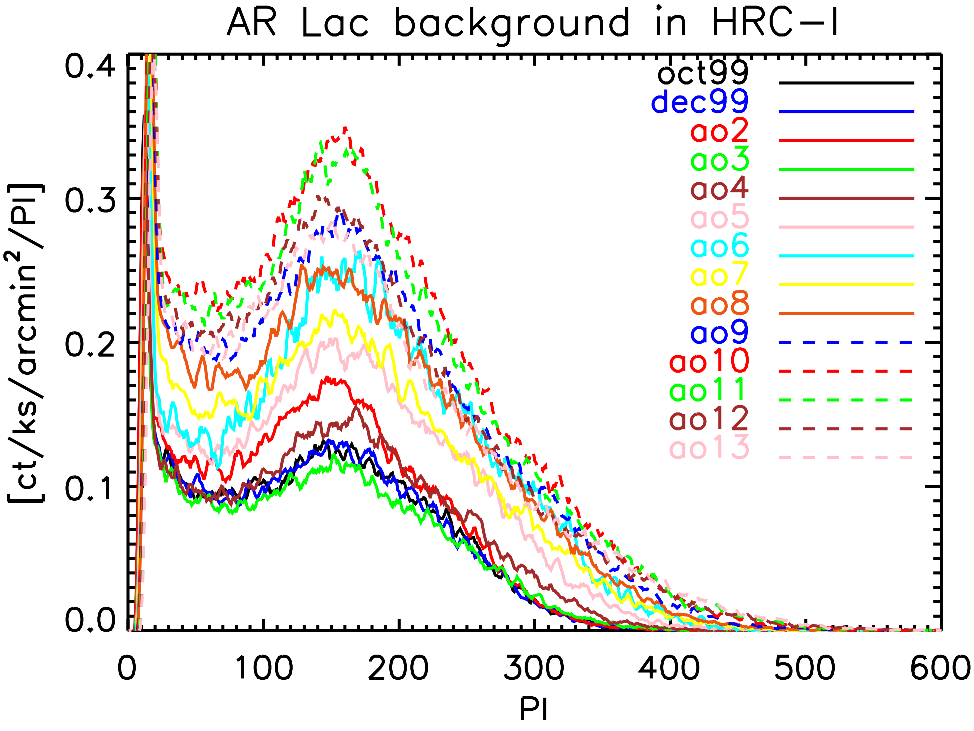

Figure 7.18: Average background spectra in the inner 10′ region of the detector, obtained from yearly observations towards AR Lac are shown. Times of high background flaring have been excluded. The magnitude and shape of the spectra vary considerably with time, but may be interpolated between epochs to estimate the background for any given observation.

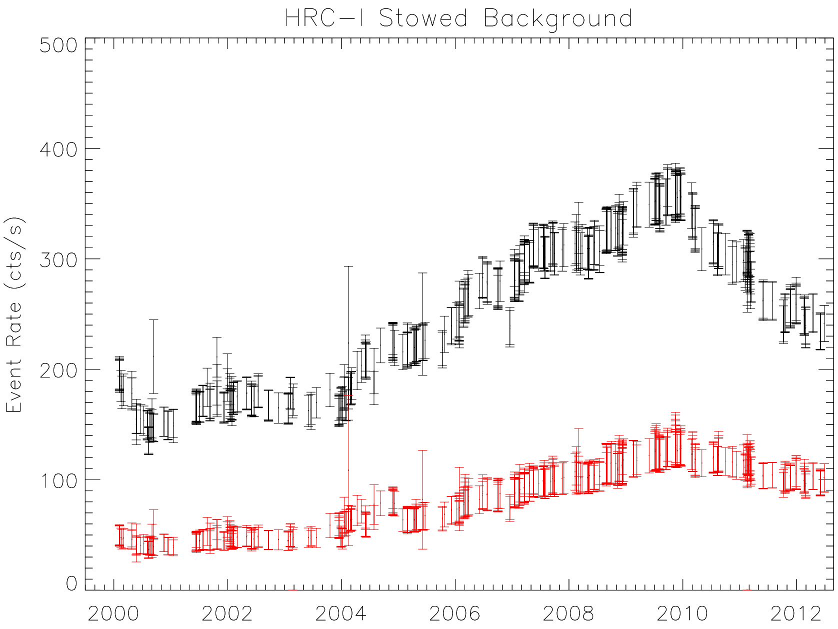

Figure 7.19: The change in HRC-I stowed background rate with time. The total rate (black points and error bars, upper set) and the valid rate (red points and error bars, lower set) are shown. The HRC-S data are similar.

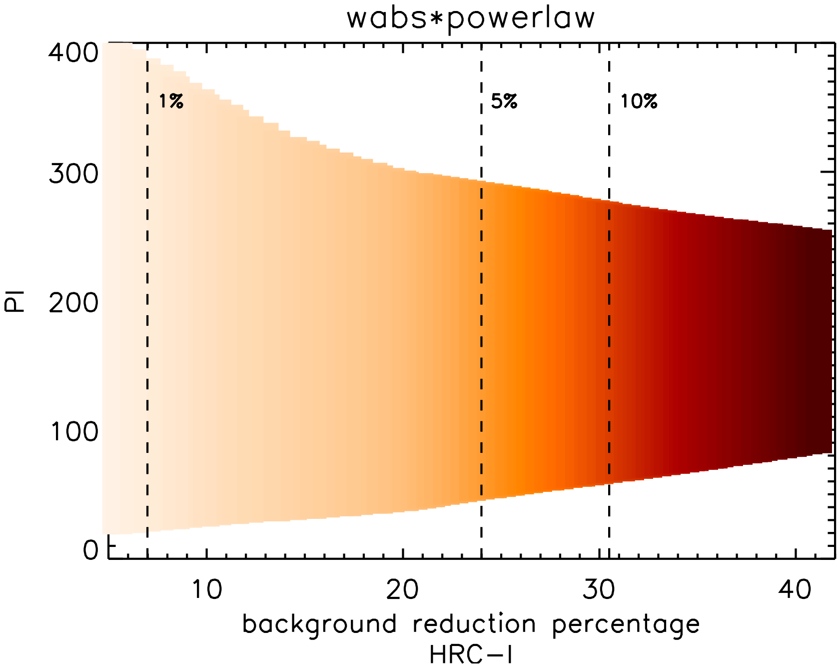

Figure 7.20: The range of PI that should be included to reduce the background by a given percentage is shown in the figure as a shaded band for an assumed absorbed power-law spectrum. All of the parameters included in the grid for Figure 7.9 are considered possible, and these PI ranges can be shrunk if more information is available for a particular source. The depth of the shading indicates how much of the source events are expected to be lost. The vertical dashed lines indicate the background reduction for source event losses of 1%, 5%, and 10%. As shown in Figure 7.18, the background varies with time. Here, for the sake of definiteness, we use the background from the year 2008.

PI $<$ 20 and PI $>$ 350 on the HRC-I. The background is reduced by $\sim$ 20% even as only $\approx 1 - 2\%$ of the source counts are lost (see Figures 7.20 - 7.22). The CIAO thread http://cxc.harvard.edu/ciao/threads/hrci_bg_spectra/ describes how to perform this estimate for different source models background spectra. This thread can also be followed to compute background reduction factors for non-grating HRC-S sources, provided that they are extended or are observed off-axis, and user generated background spectra are used. This approach for improving signal-to-noise is not recommended for sources observed on-axis with the HRC-S, since gain near the aimpoint varies significantly on very small scales and is not well calibrated, potentially leading to undesired filtering effects. The approach should also not be used for data obtained with a grating in place; see Section 9.3.6 for a discussion of background reduction using PI filtering for dispersed spectra.

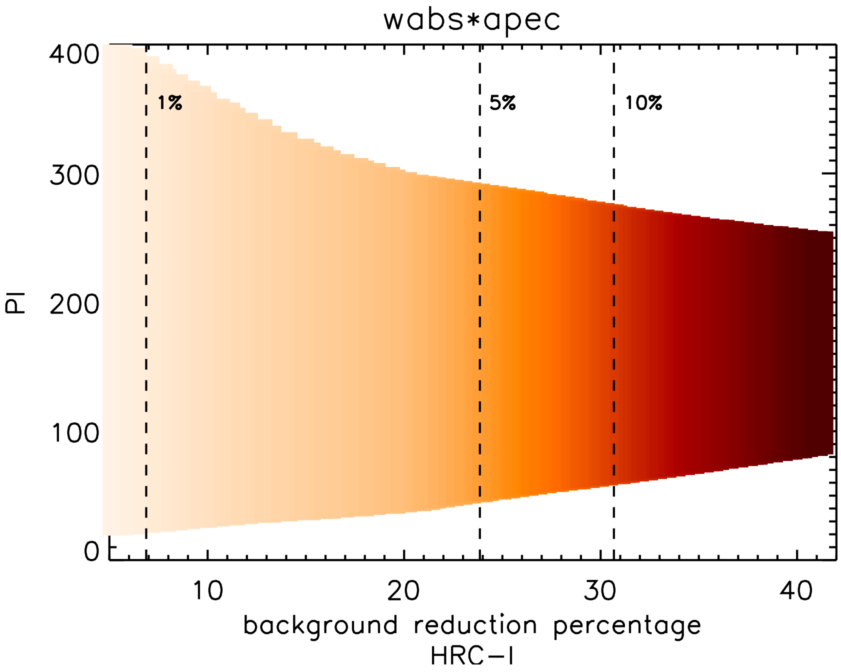

Figure 7.21: As Figure 7.20, but for sources with thermal spectra, for parameter values depicted in Figures 7.10, 7.11.

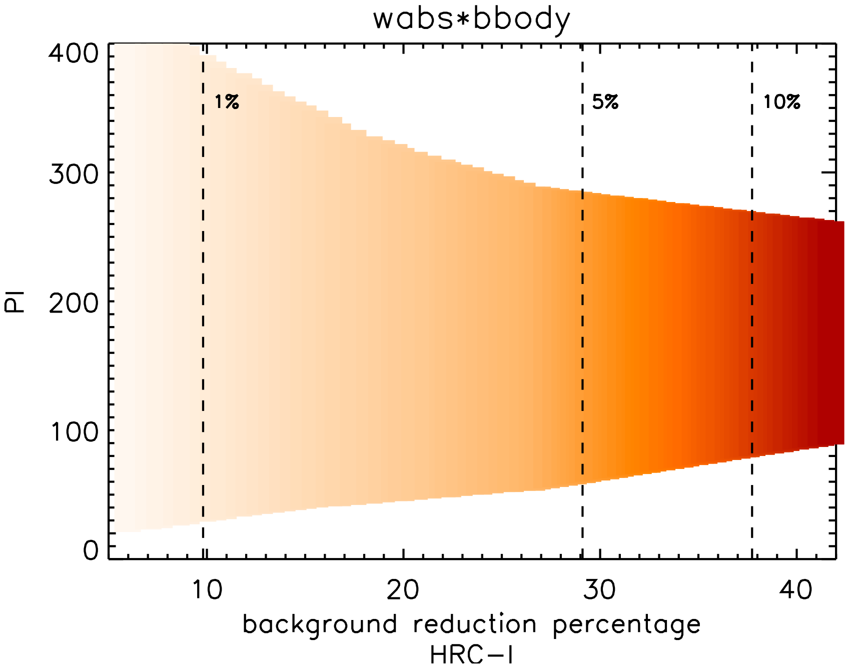

Figure 7.22: As Figure 7.20, but for sources with blackbody spectra, for parameter values depicted in Figure 7.12.

7.11 Instrument Anomalies

Initial observations with the HRC-I showed a faint secondary "ghost" image. This "ghost" image was a displaced, weaker ($\sim 3\%$) image $\sim 10''$ on one side of every source in the HRC-I field of view, generally along the negative U axis of the instrument (Figure 7.1). The cause of this imaging anomaly is saturation of the fine position amplifiers. A change in the HRC-I operating high-voltage reduced the occurrence of saturating events and the previously mentioned event processing algorithms, which are now part of the *CXO*/HRC data pipeline, label these events and filter them out. The combination of the HV change and filtering have reduced the relative intensity of the ghost image to $< 0.1\%$, effectively eliminating it. If the location of the ghost image interferes with features of the source, the *CIAO* tool `obsvis` can be used to determine a roll angle that places the source features away from the ghost image. A similar ghost image existed in the HRC-S but at a much reduced intensity.

The HRC has a hardware problem that corrupts the data from the position taps under a specific set of conditions: 1) the amplifier scale factor is switched to the least sensitive scale, 2) an even number of taps on the axis have signals that are above a set threshold, and 3) the event occurs on the negative side of the tap. When these conditions are met the tap signals are sampled while the amplifiers are still ringing after switching from the initial guess for the event coarse position to the correct one. The ringing results in offsets on the telemetered tap values from their true values, with the smallest signal of the triplet for an axis being most affected. When the event position is calculated from corrupted data, positions are incorrectly determined and can be off by a few pixels. This ringing is partially corrected for in ground processing (Juda *et al.* 2000). These corrections are implemented via the *CIAO* tool `hrc_process_events`. Observers, if they are concerned that the ringing may be producing artifacts, can apply additional filtering to remove events with AMP_SF=3.

A wiring error in the HRC causes the time of an event to be associated with the *following* event, which may or may not be telemetered. The result is an error in HRC event timing that degrades accuracy from about 16 microseconds to roughly the mean time between events. For example, if the trigger rate is 250 events/sec, then the average uncertainty in any time tag is less than 4 milliseconds.

The HRC team has developed a special operating mode that allows high precision timing to be achieved (see Section 7.14.1). This timing mode uses only the central segment of the HRC-S. Disabling the outer two segments lowers the total count rate by two-thirds, dropping it below the telemetry saturation limit for most sources. Thus, there is a high probability that all events will be telemetered. In this case, once the time tag of each event has been appropriately shifted in ground processing, the original timing accuracy (16 microseconds) can be recovered. When using this approach, it is prudent to be sure that the total count rate (source plus background) is somewhat below the telemetry saturation limit to avoid telemetry saturation due to statistical fluctuations in the count rate.

In addition to the primary science data for individual events, the rate of microchannel plate triggers (total rate) and triggers that pass on-board validity tests (valid rate) are telemetered to the ground. The valid rate is used to correct the primary rate for dead-time and telemetry saturation effects. As long as the primary rate is below saturation, the primary rate itself can be used to make the small (<1%) correction, since the event processing dead-time is known. However, when the event rate exceeds saturation, a fairly common occurrence because of background flaring from low energy protons, the valid rate is necessary to correct the event rate. Unfortunately, the total and valid event rates are overestimated by about 15% for normal operation of the HRC-S . This problem is caused by an overshoot in occasional large trigger pulses, resulting in double counting in the total and valid event on-board scalers. The primary science event is not affected, since once event processing starts with the initial trigger pulse, a gate rejects further pulses until processing is complete. The HRC-I does not have this overshoot problem. The HRC-S valid event rate is corrected in standard processing, using the fraction of event pulse amplitudes that are above a given (segment dependent) threshold.

7.12 Calibration

Calibration of the HRC included laboratory calibrations, a system-level ground calibration with the HRMA and HRC at the X-ray Calibration Facility (XRCF) at MSFC, and on-orbit calibration using celestial X-ray sources. The on-orbit calibration of the HRC is an on-going activity. See Tables 7.2,7.3 for a list of HRC calibration targets. All calibration analysis is described in detail at (http://cxc.harvard.edu/cal/Hrc).

7.13 Operational considerations and constraints

In addition to the general Chandra observatory level constraints (Chapter 3), there are a few HRC-specific considerations and constraints that must be taken into account when planning an observation.

7.13.1 Total Count limits

Both the gain and the quantum efficiency are adversely affected by the total amount of charge extracted from the MCP at the point of extraction. To minimize such effects, the high voltage on the detector is lowered during passage through the radiation belts and at times of very high particle radiation. To limit the impact from X-ray sources themselves, a 450,000 count limit distributed over the dither pattern from an on-axis source at a given aimpoint has been imposed. *Users anticipating to exceed this value should so note in the comments section of the RPS form when submitting their proposal.* In this case, the *CXC* will establish new aimpoints as necessary. Offsets in the pointing may be imposed, if necessary, in order to limit the accumulated dose to a given region of the MCP.

Table 7.2: Current and past HRC-I calibration targets

Target	Frequency (per Cycle)	Cycle	Grating	Purpose
2REJ1032+532	11	1	LETG/None	PSF calibration
31 Com	1	>8	None	ACIS undercover; off-axis PSF & gain uniformity
3C273	1	1	None	Cross-calibration with ACIS
AR Lac	21	all	None	Monitor gain at aimpoint & 20 offset locations
Betelgeuse	1	3-6	None	Monitor UV/Ion Shield
Capella	20	7-8	None	Improve de-gap corrections
Cen A	3	1	None	imaging capabilities
Cas A	2	1-8	None	Monitor QE; cross-calibration
Cas A	1/2	8-11	None	Monitor QE; cross-calibration
Coma Cluster	4	1	None	Monitor temporal variations & calibrate de-gap
Coma Cluster	1	2,3	None	Monitor temporal variations & calibrate de-gap
E0102-72.3	1	1	None	Cross-calibration with ACIS
G21.5-0.9	2	1-5	None	Monitor QE; cross-calibration
G21.5-0.9	1	5-8	None	Monitor QE; cross-calibration
G21.5-0.9	1/2	>8	None	Monitor QE; cross-calibration
HR 1099	63	1	LETG/None	PSF and Wavelength calibration
HZ 43	2	1-8	LETG	Monitor low energy response
HZ 43	1	>8	LETG	Monitor low energy response
LMC X-1	16	1	None	PSF calibration
M82	1	1	None	detector imaging
N132D	2	1	None	Cross-calibration with ACIS
NGC 2516	3	1	None	Boresighting & plate scale
NGC 2516	1	2	None	Boresighting & plate scale
PKS2155-304	2	2	LETG	Monitor low energy QE; cross-calibration
PKS2155-304	1	4	LETG	Monitor low energy QE; cross-calibration
Procyon	1	4-5	None	ACIS undercover; off-axis PSF & gain uniformity
PSRB0540-69	5	1	None	Verification of fast timing capability
Ross 154	1	8	None	ACIS undercover; off-axis PSF & gain uniformity
RXJ1856.5-3754	2	4-7	None	ACIS undercover; off-axis PSF & gain uniformity
Vega	2	1-7	None	Monitor UV/Ion Shield
Vega	4	7-11	None	Monitor UV/Ion Shield
Vega	1	>11	None	Monitor UV/Ion Shield
Vela SNR	1	3	None	low energy QE uniformity
Vela SNR	2	4	None	low energy QE uniformity

Table 7.3: Current and past HRC-S calibration targets

Target	Frequency (per Cycle)	Cycle	Grating	Purpose
3C273	1	1	LETG	Cross-calibration
3C273	1	3	LETG	Cross-calibration
AR Lac	2x21	all	None	Monitor gain at aimpoint & 20 offset locations
Betelgeuse	4	1-6	None	Monitor UV/Ion Shield
Betelgeuse	2	7	None	Monitor UV/Ion Shield
Capella	16	1	LETG	Monitor gratings
Capella	1	>1	LETG	Monitor gratings
Cas A	5	1	None	Cross-calibrate HRC MCPs
Cas A	1/2	>9	None	Cross-calibrate HRC MCPs
G21.5-0.9	2	1-4	None	Monitor quantum efficiency; cross-calibration
G21.5-0.9	1	4-9	None	Monitor quantum efficiency
G21.5-0.9	1/2	>9	None	Monitor quantum efficiency; cross-calibration
HR 1099	1	1	None	Wavelength calibration
HZ 43	2	all	LETG	Monitor low energy response
LMC X-1	26	1	None	PSF calibration
Mkn 421	1	8	LETG	Monitor ACIS contamination, cross-calibration
NGC 2516	1	1	None	Boresight and plate-scale
PKS2155-304	1	1-4	LETG	Gratings calibration, monitor ACIS contamination
PKS2155-304	2	4-8	LETG	Gratings calibration, monitor ACIS contamination
Procyon	3	1	LETG	Gratings calibration, cross-calibration
PSRB0540-69	7	1	None	Verification of fast timing capability
PSRB1821-24	1	7	None	Timing calibration
Sirius B	3	1	LETG	Calibrate LETG low-energy QE
Vega	2x4	1-6	None	Monitor UV/Ion Shield
Vega	4x4	6-11	None	Monitor UV/Ion Shield
Vega	1x4	>11	None	Monitor UV/Ion Shield

7.13.2 Count rate limits

There are two count rate limits:

Telemetry Limit

The maximum telemetered count rate is 184 cts s^{-1}. This is a limitation on the total count rate received over the full field-of-view rather than for one individual source within the field. It is possible to exceed this limit and to subsequently correct the total count rate by using the secondary science rates, which keep track of the actual detected rate, to determine the deadtime correction (see Section 7.11). The resulting deadtime fraction increases rapidly with valid event rates above 184 cts s^{-1}. For example, at 200 cts s^{-1} the deadtime fraction is 8%, at 250 cts s^{-1} 26%, and at 300 cts s^{-1} 39%. Listed below are some methods for dealing with situations where the telemetry limit is exceeded.

1. *Bright target:*
   - Insert either the LETG or HETG and analyze the zeroth-order image. This solution may be so dramatic as to substantially increase the required observing time.
   - Offset aimpoint. To be effective, this solution may result in substantially reduced spatial resolution.
2. *Bright nearby source*
   - Depending on the proximity, an appropriate choice of roll angle and/or offset can position the offending source(s) off the detector. Flux from bright sources could be blocked with the HRC shutters, but note that only one blade is functional and this option is unavailable in the standard setup.
   - Request a rectangular window for on-board data so that events produced by the nearby bright source(s) do not contribute to the telemetry limit.

There are of course, other combinations and situations that can lead to telemetry saturation - numerous faint sources on the field, a too-bright extended source, etc.

Linearity limit

During ground calibration, the HRC-I was verified to be linear for incident photon rates at ~ 2 cts s^{-1} pore^{-1}, which translates to ~ 5 cts s^{-1} for an on-axis point source (see Kenter *et al.* 1997, Figure 7). The HRC-S was found to be linear for rates five times greater. At much higher incident fluxes, the measured rate will be lower than expected (see Pease & Donnelly 1998; http://cxc.harvard.edu/cal/Hrc/detailed_info.html#ctrt_lin). Observations of the coronal point source Capella with the HRC-I show that the data are consistent with the nominal correction for a point source of intensity $\sim 19 - 22$ ct s^{-1}.

It is important to be aware that *avoiding telemetry saturation does not guarantee that linearity limits are not exceeded.* There are only three approaches to assure that the linearity limit is not exceeded:

- Offset aimpoint to smear the image out.
- Insert a transmission grating to reduce the flux and offset aimpoint (if also necessary).
- Defocus – this option is not recommended and is only mentioned for completeness.

Note that sources with high count rates will also have smaller photon arrival time differences, which will cause the PSF to be broader (see Section 7.5).

7.14 Observing with HRC - Operating Modes

For many observations, it is only necessary to specify the instrument, the exposure time, and the target coordinates. However, there are a number of optional parameters that might be invoked to optimize a particular observation. Tools such as PIMMS and MARX can be used to plan an observation, e.g., to account for the background when estimating sensitivity. These tools may be found at http://cxc.harvard.edu/proposer/.

7.14.1 Timing Mode

The HRC-S is normally operated in spectroscopy mode, where signals from any of the three MCP segments can be recognized as triggers. An alternate mode of operation (timing) ties the signals from the outer segments to ground so that only signals from the center MCP generate triggers. A key distinction of this mode from using an edge-blanked region (described below) to select only the center MCP segment is that the timing mode selects events without using the on-board veto logic. This preferred method of doing high-precision timing observations reduces the active detector area, minimizing the total trigger rate. Provided that this rate is below telemetry saturation, all events will then be telemetered and the event time tags can be correctly assigned in ground processing (see Section 7.11).

The HRC-S, when used in this mode, provides about a 6 x 30 arcmin field of view.

7.14.2 Edge and Center Blanking

It is possible to define a rectangular region, other than the default region, on both the HRC-I and the HRC-S. Events from either inside (edge-blanking) or outside (center-blanking) the defined regions are telemetered. This could be done, for example, to prevent events from a nearby bright source from contributing to telemetry (see Section 7.13.2). If a proposer wishes to define such a rectangular region, they should state this request in the ”Remarks” field of the RPS form in order to prompt discussions with a *CXC* Support Scientist.

7.15 References

General

David, L.P., Harnden, F.R. Jr., Kearns, K.E, and Zombeck, M.V., *The ROSAT High Resolution Imager (HRI) Calibration Report*, revised (1999).
http://hea-www.harvard.edu/rosat/hricalrep.html

Fraser, G., “X-ray Detectors in Astronomy”, 1989, Cambridge University Press.

Giacconi, R., *et al.*, 1979, Ap. J., 230, 540.

Murray, S.S., Chappell, J.H., Elvis, M.S., Forman, W.R., Grindlay, J.E., Harnden, F.R., Jones, C.F., Maccacaro, T., Tananbaum, H.D., Vaiana, G.S., Pounds, K.A., Fraser, G.W., and Henry, J.P., “The AXAF High Resolution Camera (HRC) and its use for observations of Distant Clusters of galaxies” Astro. Lett. Comm., 26, 113-125, 1987.

Murray, S.S., *et al.*, “In-flight Performance of the Chandra High Resolution Camera”, SPIE, 4012, 2000. http://hea-www.harvard.edu/HRC/calib/ssmspie2000.ps

Zombeck, M.V., Chappell, J. H , Kenter, A, Moore, R., W., Murray, S. S., Fraser, G.W., Serio, S.,“The High Resolution Camera (HRC) on the Advanced X-ray Astrophysics Facility (AXAF)”, Proc. SPIE, 2518, 96, 1995.

Position modeling, de-gap corrections, and event screening

Juda, M., *et al.*, “Improving Chandra High Resolution Camera event positions via corrections to cross-grid charge detector signals”, SPIE Proceedings, 4140, 2000. http://hea-www.harvard.edu/HRC/calib/spie2000_tap_correction.ps

Juda, M., & Karovska, M., “Chandra’s Ultimate Angular Resolution: Studies of the HRC-I Point Spread Function”, AAS/HEAD 2010. http://hea-www.harvard.edu/ juda/memos/HEAD2010/HEAD2010_poster.html

Karovska, M., 2011, “Followup Study of the PSF Asymmetry”, CXC Memo, Jun 2011.

Kashyap, V., “Analysis of Chandra PSF feature using ACIS data”, CXC Memo, Oct 2010. http://cxc.harvard.edu/cal/Hrc/PSF/acis_psf_2010oct.html

Kashyap, V., *et al.*, 2005, “HRC-S Degap Corrections”.
http://cxc.harvard.edu/cal/Letg/Hrc_disp/degap.html

Kenter, A., "Degap as a Transformation of Probability Distribution Problem", 3/1/99.
http://hea-www.harvard.edu/HRC/calib/degap.ps

Murray, S.S., Chappell, J.H., 1989, SPIE 1159, 460-475. "Position Modeling for the AXAF High resolution Camera (HRC)"

Murray, S.S., *et al.*, "Event Screening for the Chandra X-ray Observatory High Resolution Camera (HRC)", SPIE Proceedings, 4140, 2000.
http://hea-www.harvard.edu/HRC/calib/event_screening.ps

http://cxc.harvard.edu/ciao/caveats/psf_artifact.html (CIAO Caveats page on the PSF Artifact)

Count rate limitations and linearity

Juda, M and Dobrzycki, A, "HRC Deadtime and Telemetry Saturation", 6/18/99.
http://cxc.harvard.edu/contrib/juda/memos/tlm_sat.html

Juda, M., "Telemetered vs. Processed Events", memo, 12/7/01.
http://cxc.harvard.edu/contrib/juda/memos/proc2valid/index.html

Juda, M., "HRC-S Double Pulse Fraction", memo, 6/27/02.
http://cxc.harvard.edu/contrib/juda/memos/proc2valid/pha_fraction.html

Kenter, A.T., Chappell, J.H. Kobayashi,K.,Kraft,R.P., Meehan, G.R., Murray, S.S., Zombeck, M.V., Fraser, G.W., Pearson, J.F., Lees, J.E., Brunton, A.N. and Pearce, S.E. Barbera, M., Collura, A., Serio, S., "Performance and Calibration of the AXAF High Resolution Camera I " SPIE 3114, 1997.

Pease, D.P., & Donnelly, H., memo, 5/1998.
http://cxc.harvard.edu/cal/Hrc/detailed_info.html#ctrt_lin
Zombeck, M. V., "Secondary Science Rate Double Counting", memo, 2/12/02.
http://hea-www.harvard.edu/HRC/calib/doublecount.html

Calibration

http://cxc.harvard.edu/cal (CXC calibration site)

http://hea-www.harvard.edu/HRC/calib/calib.html (HRC IPI Team calibration site) http://cxc.harvard.edu/cal/Hrc/(HRC CXC Cal team site)

Juda, M., 2012, CXC Memo, *"Pile-up" Effect on the HRC PSF*
http://cxc.cfa.harvard.edu/contrib/juda/memos/hrc_pileup/index.html

Kenter, A.T., Chappell, J., Kobayashi, K., Kraft, R.P., Meehan, G.R., Murray, S.S., Zombeck, M.V., "Performance and Calibration of the AXAF High Resolution Camera: I. Imaging Readout", SPIE, 3114, 26, 1997.
http://hea-www.harvard.edu/HRC/calib/spie97_kenter.ps

Kenter, A., *et al.*, "In-flight Performance and Calibration of the Chandra High Resolution Camera Spectroscopic Readout (HRC-I)" SPIE, 4012, 2000.
http://hea-www.harvard.edu/HRC/calib/hrci.spie2000.ps

Kraft, R.P., Chappell, J., Kenter, A.T., Kobayashi, K., Meehan, G.R., Murray, S.S., Zombeck, M.V., "Performance and Calibration of the AXAF High Resolution Camera: II. the Spectroscopic Detector", SPIE, 3114, 53, 1997.
http://hea-www.harvard.edu/HRC/calib/spie97_kraft.ps

Kraft, R., *et al.*, "In-flight Performance and Calibration of the Chandra High Resolution Camera Spectroscopic Readout (HRC-S)" SPIE, 4012, 2000.
http://hea-www.harvard.edu/HRC/calib/hrcs.spie2000.ps

Meehan, G.R., Murray, S.S. , Zombeck, M.V., Kraft, R.P., Kobayashi, K., Chappell, J.H., and. Kenter, A.T., "Calibration of the UV/Ion Shields for the AXAF High Resolution Camera", SPIE, 3114, 74, 1997.
http://hea-www.harvard.edu/HRC/calib/spie97_meehan.ps

Meehan, G, "Calibration of the HRC-I UV/Ion Shield", 10/13/99.
http://hea-www.harvard.edu/HRC/calib/hrci_cal_report.ps

Meehan, G.,"Calibration of the HRC-S UV/Ion Shields", 10/13/99.
http://hea-www.harvard.edu/HRC/calib/hrcs_cal_report.ps

Murray, S. S.; Chappell, J.H.; Kenter, A. T.; Kobayashi, K.; Kraft, R. P.; Meehan, G. R.; Zombeck, M. V.; Fraser, G. W.; Pearson, J. F.; Lees, J. E.; Brunton, A. N.; Pearce, S, E.; Barbera, M.; Collura, A.; Serio, S., "AXAF High-Resolution Camera (HRC): calibration and recalibration at XRCF and beyond", SPIE, 3114, 11, 1997.

Background

Isobe, T., and Juda, M., memo, 9/11/2007.
http://cxc.harvard.edu/contrib/cxchrc/Stowed_study/hrc_stowed_position_study.html

Isobe, T., and Juda, M., 2007, "High Resolution Camera Stowed Background Study", Proc. of Chandra Calibration Workshop, October 2007, Huntsville, AL.
http://cxc.harvard.edu/ccw/proceedings/07_proc/presentations/isobe/

Isobe, T., and Juda, M., 2009, "How to Create a Background Map for an Observation", memo, 1/27/2009.
http://cxc.harvard.edu/contrib/cxchrc/Stowed_study/hrci_image_correction.html

Isobe, T., and Juda, M., 2009, "How to Create a Background Map for an Observation", Proc. of Chandra Calibration Review, September 2009, Boston, MA.
http://cxc.harvard.edu/ccr/proceedings/09_proc/presentations/isobe/

Juda, M., "Time History of the HRC Background", memo, 5/22/01.
http://cxc.harvard.edu/contrib/juda/memos/hrc_bkg/time_history.html

Juda, M., "HRC Rates and High Solar Activity", memo, 5/21/01.
http://cxc.harvard.edu/contrib/juda/memos/hrc_bkg/high_solar.html

Juda, M., *et al.*, "Characteristics of the On-Orbit Background of the Chandra X-ray Observatory High Resolution Camera", Proc. SPIE 4851, August 2002
http://cxc.harvard.edu/contrib/juda/memos/spie2002/spie2002.html,
http://cxc.harvard.edu/contrib/juda/memos/spie2002/spie2002.ps

Detector coordinate systems

McDowell, J., "Coordinate Systems for Analysis of On-orbit Chandra Data, Paper I: Imaging", http://cxc.harvard.edu/contrib/jcm/ncoords.ps

Counts lifetime

Kenter, A.T., K.A. Flanagan, G. Meehan, S.S. Murray, M.V. Zombeck, G.W. Fraser, J.F. Pearson, J.E. Lees, A.N. Brunton, and S.E. Pearce, "Microchannel plate testing and evaluation for the AXAF high resolution camera (HRC)", Proc. SPIE, 2518, 356, 1995.

Gain, spectral response, out-of-band response

Kashyap, V., Posson-Brown, J., 2005, "Spectral Response of the HRC-I", Chandra Calibration Workshop, Oct 31-Nov 1 2005,
http://cxc.harvard.edu/ccw/proceedings/05_proc/presentations/kashyap2/

Kashyap, V. Posson-Brown, J., 2009, “The Imaging and Spectral Performance of the HRC”, Chandra Calibration Review, 2009.14,

http://cxc.harvard.edu/ccr/proceedings/09_proc/presentations/kashyap/

Pease, D.O., Drake, J.J., & Kashyap, V.L., 2005, “The Darkest Bright Star: Chandra X-Ray Observations of Vega”, ApJ, 636, 426

Pease, D., Kashyap, V., Drake, J., Juda, M., 2005, “Monitoring the HRC-S UV Rate: Observations of Vega”, CXC Memo, May 2005,
http://cxc.harvard.edu/cal/Hrc/Documents/hrcs_vega_05.ps

Posson-Brown, J., Kashyap, V., 2005, “Monitoring the Optical/UV Transmission of the HRC with Betelgeuse”, CXC Memo, June 2005,
http://cxc.harvard.edu/cal/Hrc/Documents/betelgeuse.ps

Posson-Brown, J., Kashyap, V., 2005, “Monitoring the Optical/UV Transmission of the HRC with Betelgeuse”, Chandra Calibration Workshop, Oct 31-Nov 1 2005,
http://cxc.harvard.edu/ccw/proceedings/05_proc/presentations/possonbrown/

Posson-Brown, J., Kashyap, V., 2009, “SUMAMPS-based gain maps and RMF for the HRC-I”, Chandra Calibration Review, 2009.16,
http://cxc.harvard.edu/ccr/proceedings/09_proc/presentations/possonbrown2/

Wargelin, B., 2012, CXC Memo, *HRC-S Voltage Change*,
http://cxc.cfa.harvard.edu/cal/Letg/newHRCShv/

Wilton, C., Posson-Brown, J., Juda, M., Kashyap, V., 2005, “The HRC-I Gain Map”, Chandra Calibration Workshop, Oct 31-Nov 1 2005 ,
http://cxc.harvard.edu/ccw/proceedings/05_proc/presentations/wilton/

Zombeck, M.V., “HRC-I out of band response.”
http://hea-www.harvard.edu/HRC/calib/hrci_cal.html

Zombeck, M.V., “HRC-S out of band response.”
http://hea-www.harvard.edu/HRC/calib/hrcs_cal.html

Zombeck, M.V., *et al.*, “Vega calibration observations.”
http://hea-www.harvard.edu/HRC/calib/vega/vega.html

Zombeck, M.V., *et al.*, “The Out-of-band Responses of the HRC on Chandra”, X-ray 2000 Proceedings, Palermo, 2000.

http://hea-www.harvard.edu/HRC/calib/palermopaper.ps

Zombeck, M. V., “Response of the HRC to Vega”, memo, 10/28/02. http://hea-www.harvard.edu/HRC/calib/vega/vega_trend.html

Chapter 8

HETG: *Chandra* High Energy Transmission Grating

8.1 Instrument Overview

HETG is the High-Energy Transmission Grating (Canizares *et al.* 2005). In operation with the High Resolution Mirror Assembly (HRMA) and a focal plane imager, the complete instrument is referred to as the HETGS — the High-Energy Transmission Grating Spectrometer. The HETGS provides high resolution spectra (with $E/\Delta E$ up to 1000) between 0.4 keV and 10.0 keV for point and slightly extended (few arc seconds) sources. Although HETGS operation differs from proportional counter and CCD spectrometers, standard processing of an HETGS observation produces familiar spectrometer data products: *PHA*, ARF, and RMF files. These files can then be analyzed with standard forward-folding model fitting software, e.g., *Sherpa*, *XSPEC*, *ISIS* , etc.

The HETG itself consists of two sets of gratings, each with different period. One set, the Medium Energy Grating (MEG), intercepts rays from the outer HRMA shells and is optimized for medium energies. The second set, the High Energy Gratings (HEG), intercepts rays from the two inner shells and is optimized for high energies. Both gratings are mounted on a single support structure and therefore are used concurrently. The two sets of gratings are mounted with their rulings at different angles so that the dispersed images from the HEG and MEG will form a shallow X centered at the undispersed (zeroth order) position; one leg of the X is from the HEG, and the other from the MEG. The HETG is designed for use with the spectroscopic array of the *Chandra* CCD Advanced Imaging Spectrometer (ACIS-S) although other detectors may be used for particular applications. A summary of characteristics is given in Table 8.1.

The Instrument Principal Investigator for the HETG is Dr. Claude Canizares of the MIT Center for Space Research. See Canizares *et al.* (2005) for a thorough description of the instrument and its performance.

Table 8.1: HETG(S) Parameters

HETGS Range:	0.4 – 10.0 keV, 31 – 1.2Å
HEG Range:	0.8 – 10.0 keV, 15 – 1.2 Å
MEG Range:	0.4 – 5.0 keV, 31 – 2.5 Å
Effective Area (see Figures 8.7 8.8):	7 cm^2 @ 0.5 keV
(MEG+HEG first orders,	59 cm^2 @ 1.0 keV
with ACIS-S)	200 cm^2 @ 1.5 keV
	28 cm^2 @ 6.5 keV
Resolving Power ($E/\Delta E$, $\lambda/\Delta\lambda$)	
HEG:	1070 – 65 (1000 @ 1 keV, 12.4 Å)
MEG:	970 – 80 (660 @ 0.826 keV, 15 Å)
Resolution:	
ΔE:	0.4 – 77 eV FWHM
$\Delta\lambda$, HEG:	0.012 Å FWHM
$\Delta\lambda$, MEG:	0.023 Å FWHM
Absolute Wavelength Accuracy: (w.r.t. ”theory”)	
HEG	±0.006 Å
MEG	±0.011 Å
Relative Wavelength Accuracy: (within and between obs.)	
HEG	±0.0010 Å
MEG	±0.0020 Å
HEG angle on ACIS-S:	$-5.235^\circ \pm 0.01^\circ$
MEG angle on ACIS-S:	$4.725^\circ \pm 0.01^\circ$
HETGS Rowland spacing	8632.65 mm (flight installed)
Wavelength Scale:	
HEG	0.0055595 Å / ACIS pixel
MEG	0.0111200 Å / ACIS pixel
HETG Properties:	
Diffraction Efficiency:	2.5% @ 0.5 keV (MEG)
(single-side, first order)	19% @ 1.5 keV (MEG & HEG)
	9% @ 6.5 keV (HEG)
HETG Zeroth-order Efficiency:	4.5% @ 0.5 keV
	8% @ 1.5 keV
	60% @ 6.5 keV
Grating Facet Average Parameters	
HEG and MEG bar material:	Gold
HEG / MEG period:	2000.81 Å, / 4001.95 Å
HEG / MEG Bar thickness:	5100 Å, / 3600 Å
HEG / MEG Bar width:	1200 Å, / 2080 Å
HEG / MEG support:	9800 Å, / 5500 Å polyimide

8.1.1 Examples of Observations with the HETGS

An example of an HETGS observation is presented in Figure 8.1 using data from an observation of Capella, Obsid 1318. The top panel shows an image of detected events on the ACIS-S detector with the image color indicating the ACIS-determined X-ray energy (see WWW version if this is not in color.) In this detector coordinate image (TDETX, TDETY), the features are broad due to the nominal dither motion which serves to average over detector non-uniformities. The ACIS-S chips are numbered S0 to S5 from left to right, with the aim point in S3 where the bright zeroth-order image is visible and includes a vertical frame-transfer streak (a trailed image). The HRMA optical axis passes through S3 approximately 6 mm from the S2-S3 chip gap. For further information see Figure 6.1 and related text.

HETG-diffracted photons are visible in Figure 8.1 forming a shallow "X" pattern; the full opening angle between the HEG and MEG spectra is 9.96°. The back illuminated (BI) chips are S1 and S3. The S1 location was chosen to enhance the first order MEG spectrum since back illumination provides higher efficiency below 1 keV. The location of the zeroth-order for any particular observation, however, may be adjusted by offset pointing in order to select the energies of the photons that will be placed in the gaps between the chips. Details on gaps are presented in Section 8.2.1.

The middle panel of Figure 8.1 shows an image after the data have been aspect corrected and data filters applied to include only valid zeroth and first-order events. Note that this image was created using Sky coordinates that were rotated and had their y-axis sign "flipped" in order to match the detector coordinates view in the top panel. The lower set of panels shows an expanded view of the MEG minus-first-order spectrum with emission lines clearly visible. Wavelengths are assigned based on the diffraction angle of the events, that is, how far the events are from the zeroth-order image. Using the grating equation in Section 8.1.3, absolute wavelengths can be assigned based on the dispersion angle. A spectrum of the source is then created by binning the events into energy or wavelength bins; the spectrum from another Capella observation is shown in Figure 8.2.

Note: The dispersion distance on the detector is essentially linear in wavelength. Thus, wavelength is the natural unit for this high-resolution x-ray spectrometer. The conversion between energy and wavelength is provided by the relation: $E \times \lambda = hc = 12.39852$ keVÅ.

Each of the "arms" of the HETGS diffracted X pattern yields a first-order spectrum identified by type (HEG or MEG) and sign of the order (plus or minus.) Using ARF's (ancillary response files) and RMF's (response matrix files) these spectra can be analyzed in an *XSPEC*-like framework. Additionally, the *CXC* software package "Interactive Spectral Interpretation System" (ISIS, http://space.mit.edu/ASC/ISIS/) can be used to identify spectral lines, e.g., as seen in Figure 8.2.

8.1.2 Scientific Objectives and Grating Heritage

The HETGS allows one to probe the physical parameters of emitting regions of all classes of X-ray sources, including stars, X-ray binaries, supernova remnants, galaxies, clusters

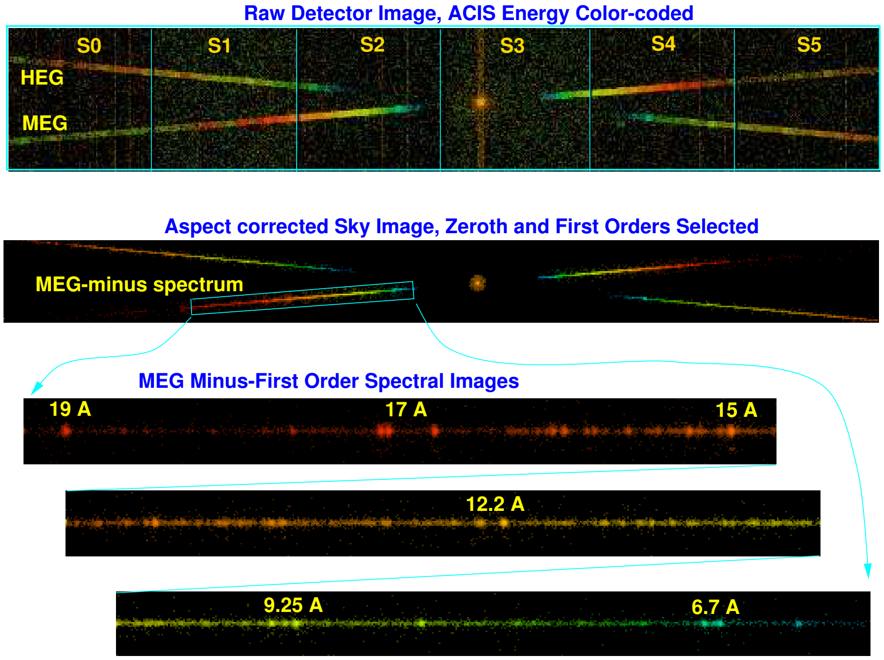

Figure 8.1: HETGS observation of Capella, Obsid 1318. The top panel shows an image of detected events on the ACIS-S detector with the image color indicating the ACIS-determined X-ray energy. The bright zeroth-order image is visible on CCD S3 and includes a trailed image (the vertical frame-transfer streak). Diffracted photons are visible forming a shallow "X" pattern; the HEG and MEG spectra are indicated. The images are broad due to dither of the spacecraft. The middle panel shows an image after the data have been aspect corrected and selections applied to include only valid zeroth and first-order events; note that the Y axis has been flipped from the normal Sky view to match the detector coordinates view in the top panel. Finally, the lower panel shows an expanded view of the MEG minus-first-order spectrum with emission lines clearly visible.

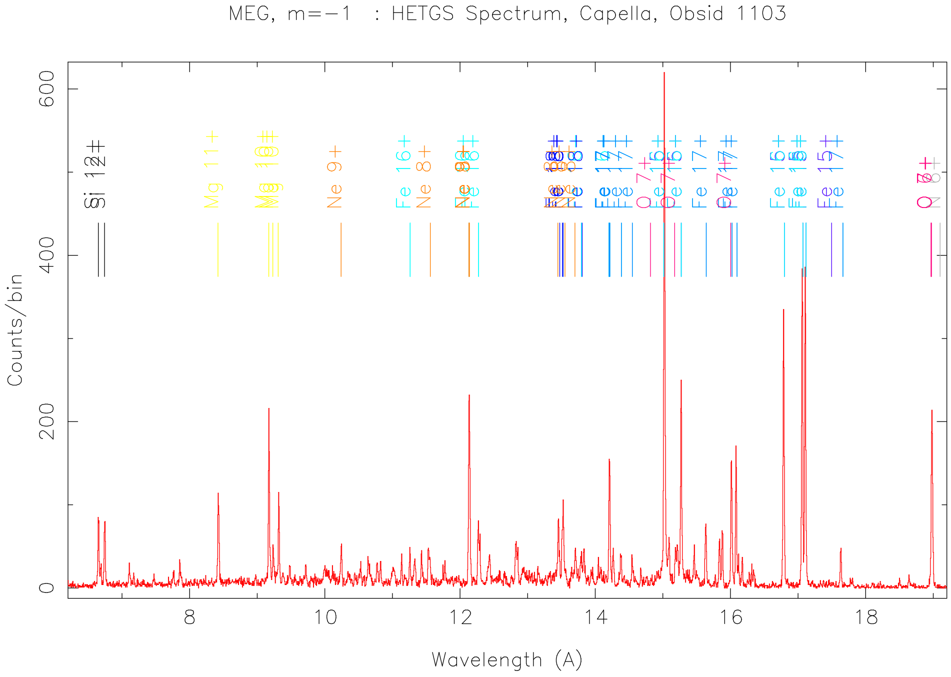

Figure 8.2: HETGS Capella spectrum, MEG $m = -1$, Obsid 1103. The first-order events identified in the MEG minus-side "arm" of the HETG *X* pattern are assigned wavelengths by *CXC* pipeline software according to the grating equation and known instrument parameters. These values are then binned to produce a pulse height analysis spectrum (`pha2.fits` file) which is plotted here. The `ISIS` software package available from the *CXC* has also been used to indicate the location of expected emission lines based on a simple source model.

of galaxies, quasars, and interstellar and intergalactic material. Plasma diagnostic techniques applied to emission lines, absorption lines and absorption edges will convey source properties such as temperatures, ionization states, densities, velocities, elemental abundances, and thereby structure, dynamics, and evolution of various classes of sources. The energy band amenable to observation is extremely rich in lines from both coronal and photo-ionized plasmas, containing the L-shell lines from ionization stages of Fe XVII to Fe XXIV and the K-shell lines of hydrogenic and helium-like ions of oxygen through nickel. The 6 keV Fe K lines are well within the observable band. The highest resolutions available will also allow detailed study of motions through Doppler line shifts in supernova remnants, X-ray binaries, turbulent intra-cluster or intra-galactic gas, or early-type galaxies in clusters.

Although gratings have flown on *Einstein* and *EXOSAT*, the HETGS shares only the basic operating principles with these. Advanced grating technology has enabled achievement of greater efficiency and increased dispersion. The Rowland geometry of the grating plate and spectroscopic arrays maintains the telescope focal properties in the dispersion direction by minimizing dispersed image aberrations and hence contributes to improved spectral resolution.

8.1.3 HETGS Operating Principles

The HETG is mounted, and can be inserted, just aft of the HRMA as shown in the schematic of the HRMA-HETG-detector system, Figure 8.3. The HETG provides spectral separation through diffraction. X-rays from the HRMA strike the transmission gratings and are diffracted (in one dimension) by an angle β given according to the grating equation,

$\sin\beta = m\lambda/p$,

where m is the integer order number, λ is the photon wavelength in angstroms, p is the spatial period of the grating lines, and β is the dispersion angle. A "normal" undispersed image is formed by the zeroth-order events, $m = 0$, and dispersed images are formed by the higher orders, primarily the first-order, $m = 1$.

The HETGS-faceted Rowland design is shown in Figure 8.4. The "Rowland circle" is a circle whose diameter is simply the distance from the grating that would lie on the optical axis to the point in the focal plane where the zeroth order image is placed. The "Rowland torus" is formed by rotating the circle about the line in the dispersion direction going through the on-axis focus. Individual grating facets are mounted such that their centers lie on the torus. In the figure, the axis of the torus is perpendicular to the page for the side view and lies in the plane of the top view. Ideally, the detector is shaped to follow the counterpart Rowland torus in the image plane. The result is that the telescope focal properties in the dispersion direction are maintained for a large range of diffraction angles, β, thereby minimizing any grating-added optical aberrations.

An important parameter of the HETGS is the Rowland spacing, the distance from the outer intersection of the HETG axis and Rowland Circle to the HRMA focus. This Rowland spacing is what determines the value of β in the grating equation. The value of the Rowland spacing is listed in Table 8.1.

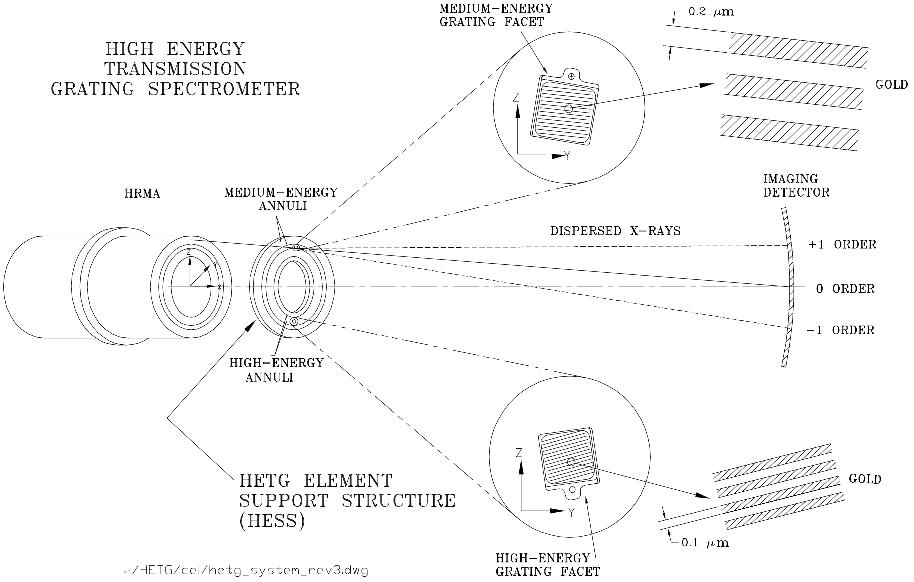

Figure 8.3: A schematic layout of the High Energy Transmission Grating Spectrometer. (Dimensions shown are approximate.)

Order overlap and source confusion can be discriminated by the intrinsic energy resolution of the CCD detector (ACIS-S is the preferred detector for HETG spectroscopy since it has intrinsic energy resolution and so can separate orders; the HRC may be used if high time resolution is desired, but this choice is at the price of using the focal plane detector's energy resolution to aid in order separation). The form of a spectral image on the ACIS-S array is shown in Figure 8.1. The spectroscopic array spans about 8 arc minutes × 48 arc minutes of the sky, though image quality and resolving power degrade rapidly for sources more than about 4 arcmin off-axis. For an on-axis source, the detector edge in the dispersion direction causes a low energy cutoff of the spectrum at about 0.4 keV for the MEG and 0.8 keV for the HEG. Order selection and chip gaps are described more fully in Section 8.2.1.

8.1.4 HETG Physical Configuration

The HETG support structure (HESS) is a circular aluminum plate (110 cm diameter by 6.35 cm thick) which can be swung into position behind the HRMA. Mounted on the HESS are 336 grating facets, each about 25 mm square. The position and orientation of the HESS mounting surfaces have been designed and machined to place each grating center on a Rowland torus of diameter 8633.69 mm. A detailed drawing of the HETG (HESS plus facets) is shown in Figure 8.5.

The gratings cover the annular regions through which the X-rays pass. The 192 grating

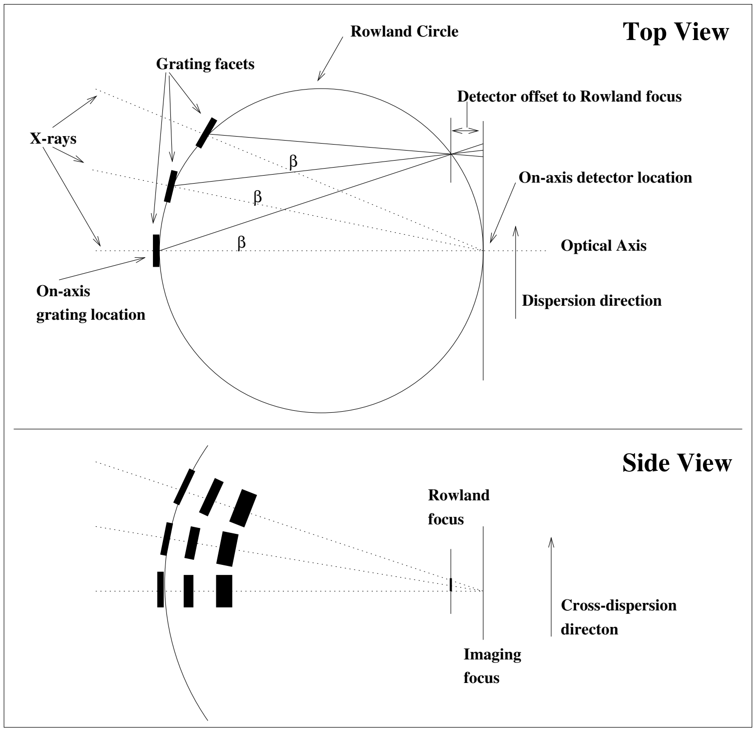

Figure 8.4: The Rowland geometry is shown schematically. In the "Top" view, we are looking across the dispersion direction. The diffraction angle is β. The geometry is such that converging rays diffracted at a specific angle by the gratings (which are located on the Rowland circle) will converge to a point that is also on the Rowland circle. The dotted lines represent zeroth-order rays and the solid lines represent the grating-diffracted first-order rays. The bottom panel ("Side" view) looks along the dispersion direction at rays from a set of gratings arranged perpendicularly to those in the "Top" view and schematically shows the astigmatic nature of the spectrally focused image: since the converging rays have not yet reached the imaging focus, they are extended across the dispersion (by less than 100 microns).

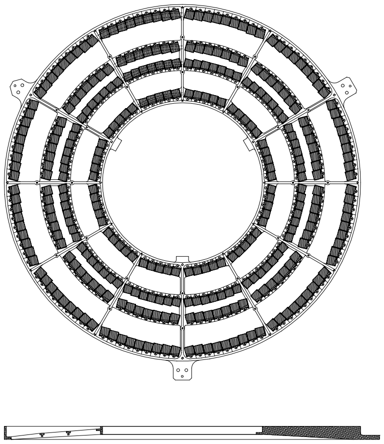

Figure 8.5: A front (upper) and side (lower) view of the HETG support structure (HESS). The grating facets are mounted to intercept the X-rays as they exit the HRMA; the front view is from the HRMA i.e., what an approaching X-ray would see. In the side view, the left cross-section shows that the four support rings are in different planes due to the Rowland curvature. The right cross-section is through a radial rib at one of the three mounting "ears".

facets on the outer two annuli (MEG) have a period of 4001.95 Å. Tiling the inner two annuli are 144 (HEG) gratings, which have a period of 2000.81 Å (see Table 8.1). The two sets of gratings are mounted with their rulings at different angles so that the dispersed images from the HEG and MEG will form a shallow *X* centered at the undispersed (zeroth order) position; one leg of the *X* is from the HEG, and the other from the MEG. See Figure 8.1 for an example.

The HETG grating facets are composed of electro-plated gold bars supported on a polyimide substrate, as shown schematically in Figure 8.6. The grating bar design parameters, height and width, are nominally chosen to reduce zeroth-order and maximize first-order intensities. Choosing to have the bar width one-half of the grating period suppresses even orders and provides maximum 1st order efficiency for a rectangular profile; this is closely achieved for the MEG gratings. For the HEG gratings, the bar is wider and results in a higher 2nd order efficiency and reduced 3rd order efficiency. The bar height choice "tunes" the efficiency peak in energy by allowing X-rays to constructively interfere in first order in the region where the gold is partially transparent, primarily above 1.2 keV.

8.2 Instrument Characteristics

When observing a point source, the HETGS can be viewed as a black-box spectrometer characterized by its *Effective Area* and *Resolution*. More specifically an HETGS count

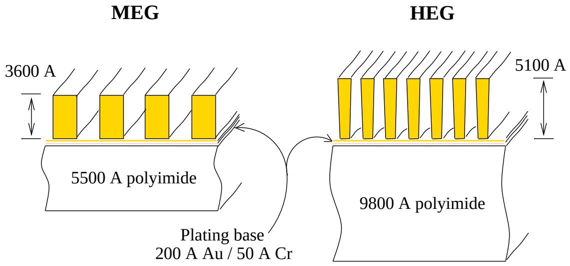

Figure 8.6: Cross-sections of the MEG and HEG membranes. The soap-bubble-thin membranes of the HETG consist of gold bars attached to a polyimide support layer. The MEG grating bars are close to rectangular, typically with a height of 3600 Å and a bar-to-period fraction of 52%. The HEG bars have a crudely trapezoidal shape, narrower on the polyimide side as shown, typically 5100 A high with an effective bar-to-period fraction around 60%.

spectrum produced by standard analysis (a *PHA* file) can be related to the source spectrum through a grating ARF and grating RMF; because of the spatially-dispersive operation of the HETGS, the RMF is also referred to as the Line Response Function, LRF. Four first-order spectra are obtained from an observation corresponding to the four whiskers of the dispersed "X" pattern: the plus and minus first-orders of the HEG and MEG gratings. Standard CIAO tools produce these *PHA* files, ARFs, and RMFs for observers' use.

In the sections that follow, information on the HETGS Effective Area (ARFs) and Resolution (RMFs/LRFs) are given with an examination of the components and effects that contribute to them. In addition two other characteristics of the HETGS are briefly presented: the *Background* event rate for an extracted spectrum and the *Absolute Wavelength* accuracy.

8.2.1 HETGS Effective Area

The HETGS effective area, as encoded in the ARF, depends on the HETG efficiency coupled with the HRMA effective area and the ACIS efficiency. Additional effects can arise from the process of selecting events, the effect of chip gaps, and the use of "ACIS ENERGY" to do order sorting. In this chapter we use the term ACIS ENERGY to describe the energy deduced from the ACIS pulse height.

Nominal HETGS ARFs

Combining the HETG diffraction efficiencies with the HRMA effective area and the ACIS-S detection efficiency produces the system effective area as a function of energy, described by an "ancillary response file" or ARF. Plots of HETGS ARF's are shown in Figures 8.7 and 8.9 which are plotted with log vertical axes; the same plots with linear vertical scale are shown in Figures 8.8 and 8.10. The values are plotted from ARF files created by the *CXC CIAO* tool `fullgarf`. The effective area includes the effect of molecular contamination on the ACIS filter (projected to the middle of the Cycle).

The nominal plots shown here are for qualitative reference only; because the `fullgarf` tool also accounts for a variety of other effects, *e.g.*, dither motion, bad pixels, QE non-uniformity, etc., grating ARFs are custom made for a given observation. The details of the calibration of the ARF are discussed in Section 8.3.

Since first-order photons from both the HEG and MEG gratings provide information, to compare the HETGS with other instruments, it is useful to plot the total HETGS effective area (the combined plus and minus first-order areas of both the HEG and MEG); this is shown by the solid curve in Figure 8.11. During an observation the zeroth-order photons from HEG and MEG form a single zeroth-order image; the effective area for this zeroth-order image is also plotted on this figure (dotted line).

Note the dips caused by the gaps between chips in these figures. The observatory is dithered in order to spread the signal across a large number of pixels. For HETGS observations, sinusoidal motions with 8 arc second amplitude in spacecraft Y and Z axes are used with periods of 1000.0 and 707.0 seconds, respectively, creating a Lissajous pattern (see Section 5.8.2). When the combination of the chip gaps and dither are accounted for, a "pitch fork" dip occurs at each gap region in the ARFs. Although effects of this motion are removed in on-ground processing, observers are advised to *avoid placing spectral features of interest near the gaps*. More information concerning gaps are in the next section. The effective areas shown in Figure 8.7-8.11 are based on an integration over the full LSF. Most of the flux in a line will be contained within a circle of diameter 4 arcsec. The user might wish to note that in data processing, the pipeline software keeps only events that are in a spatial window that lies within 3 arcsec of the dispersion axis. This aperture guarantees that a high fraction, 97-99%, of the signal flux is retained while minimizing the contribution of the background. Further discussion of the spatial distribution of events can be found for the HRMA PSF in Chapter 4 and for the HETGS in Section 8.2.2 below.

HETG Grating Efficiency

The HETG contribution to the effective area comes in through the efficiencies of the HETG gratings; the values of these are shown in Figure 8.13. All calibration data support the modeling assumption that the positive order efficiencies are equal to the negative order efficiencies. These efficiencies are primarily based on laboratory measurements of each facet, synchrotron reference grating corrections, improved polyimide transmission models, and updated gold optical constants as described in Flanagan et al., (2000). Slight adjustments to the HETG efficiencies have been determined using in-flight data by comparing the HEG and MEG spectra of many sources. The adjustments are mostly less than 10%; see Marshall (2005) for details. In an update (Marshall 2012) included in CalDB 4.4.7 and later, the HEG and MEG agree now at the $\sim 1\%$ level.

A number of systematic effects at the 10% level have now been accounted for in the HETGS effective area via adjustments to the grating efficiencies. Observations of blazars (Marshall 2012) have been used to verify these corrections. Relative systematic errors

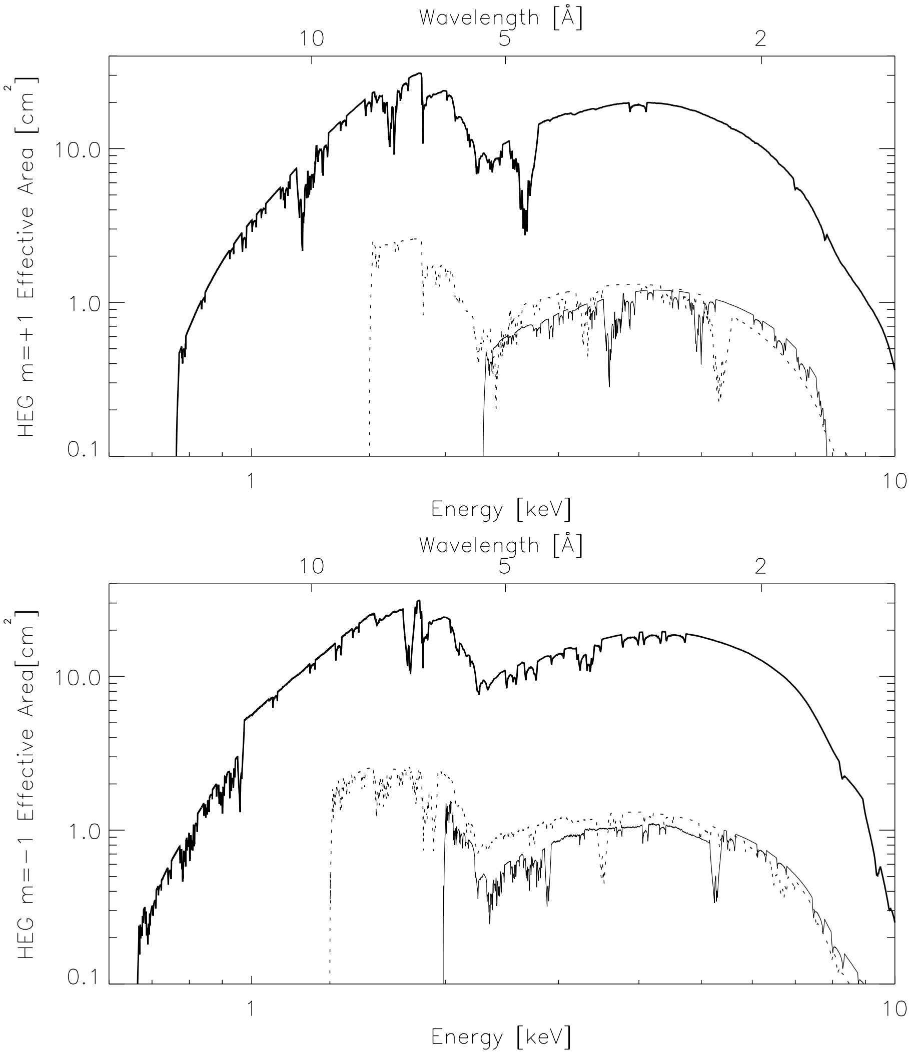

Figure 8.7: The HETGS HEG effective area, integrated over the PSF, is shown with energy and wavelength scales. The $m = +1, +2, +3$ orders (falling on ACIS chips S5, S4, S3; left to right) are displayed in the top panel and the $m = -1, -2, -3$ orders (falling on ACIS chips S0, S1, S2; left to right) are in the bottom panel. The thick solid lines are first order; the thin solid line is third order; and the dotted line is second order.

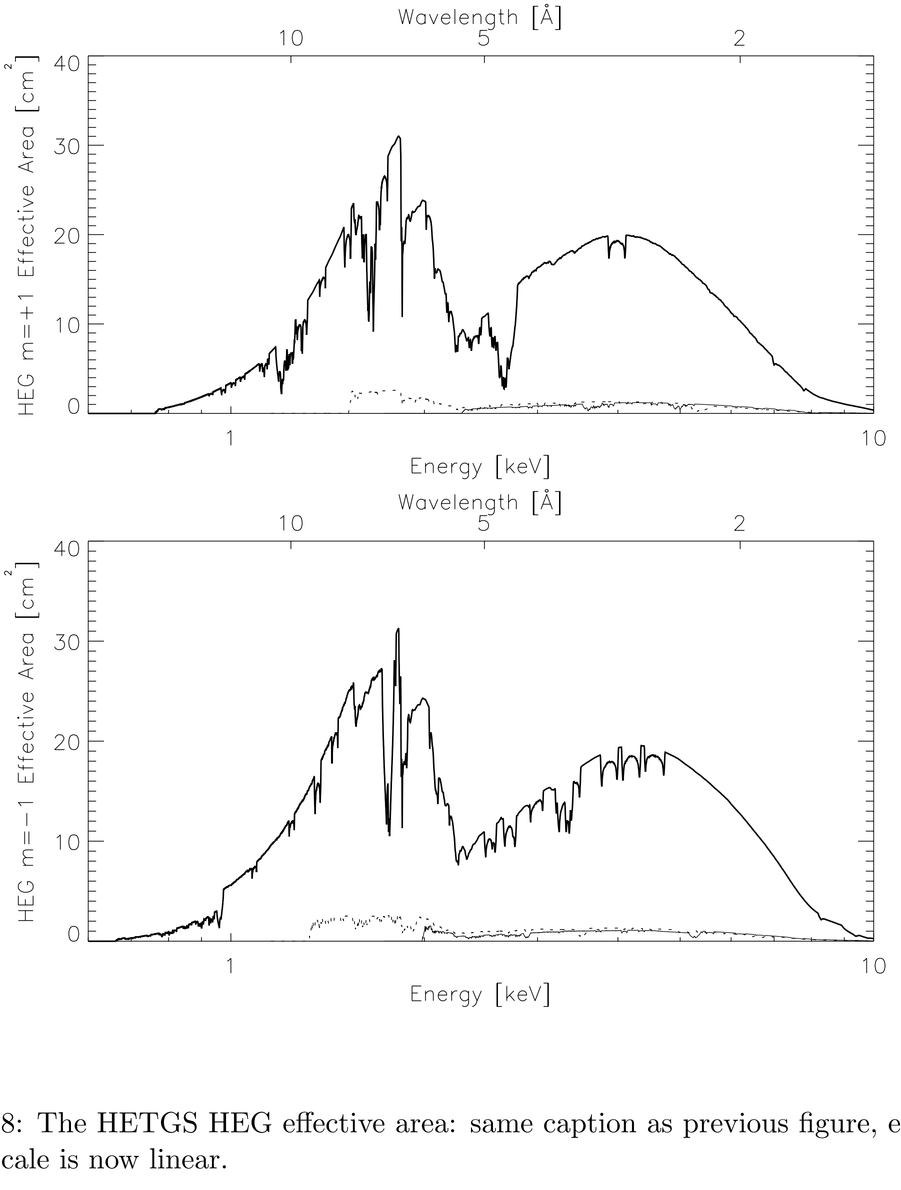

Figure 8.8: The HETGS HEG effective area: same caption as previous figure, except the vertical scale is now linear.

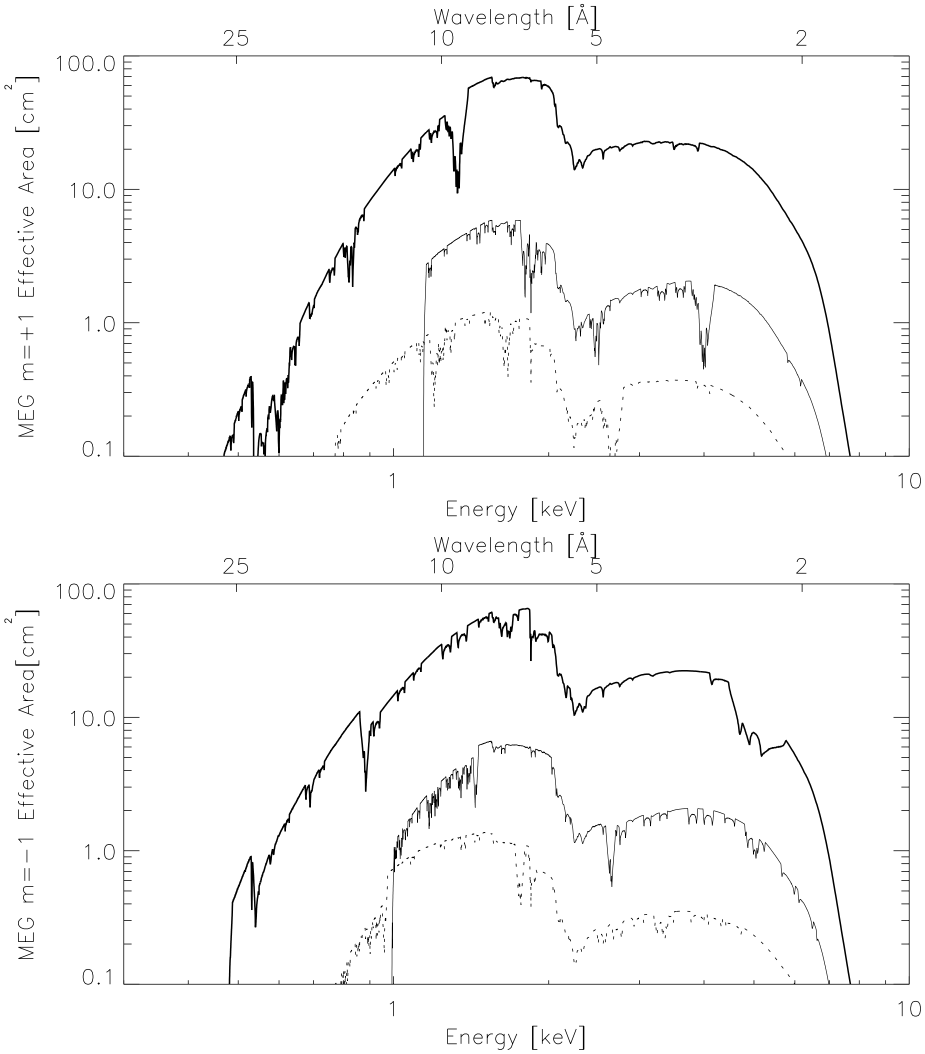

Figure 8.9: The HETGS MEG effective area, integrated over the PSF is shown with energy and wavelength scales. The $m = +1, +2, +3$ orders (falling on ACIS chips S5, S4, S3; left to right) are displayed in the top panel and the $m = -1, -2, -3$ orders (falling on ACIS chips S0, S1, S2; left to right) are in the bottom panel. The thick solid lines are first order; the thin solid line is third order; and the dotted line is second order.

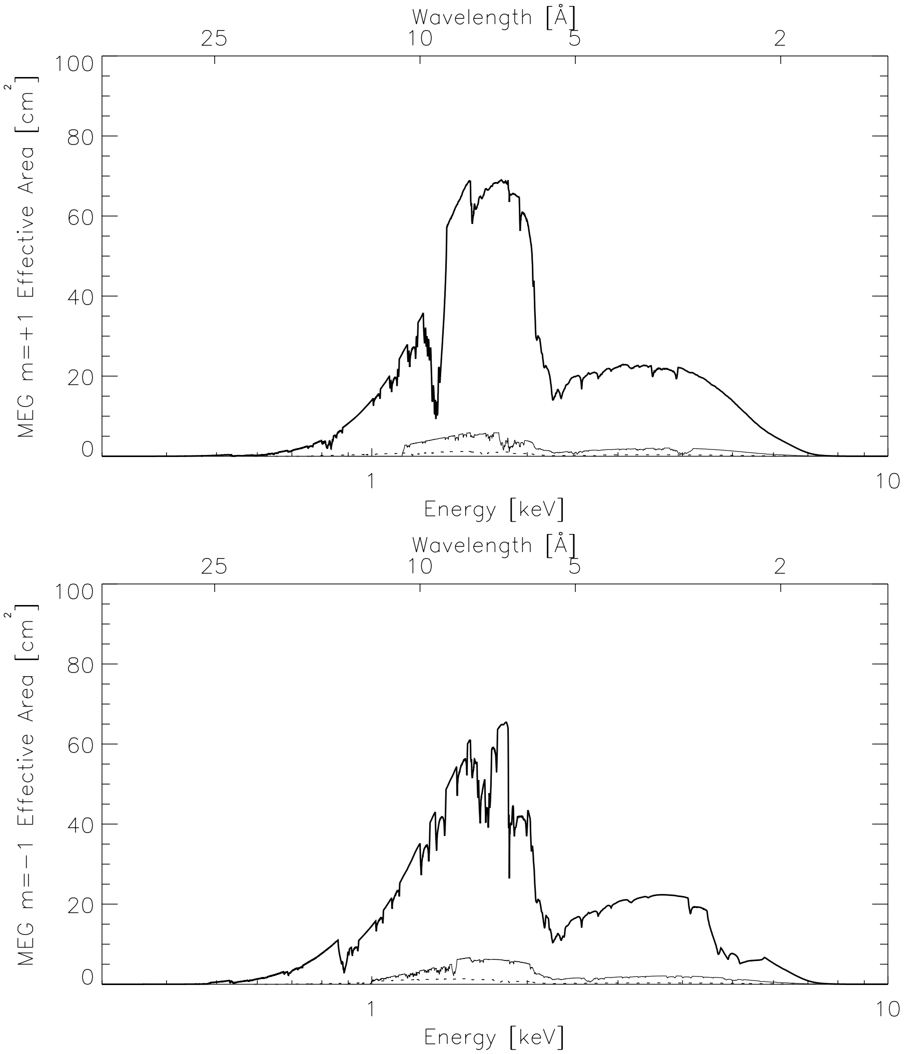

Figure 8.10: The HETGS MEG effective area: same caption as previous figure, except the vertical scale is now linear.

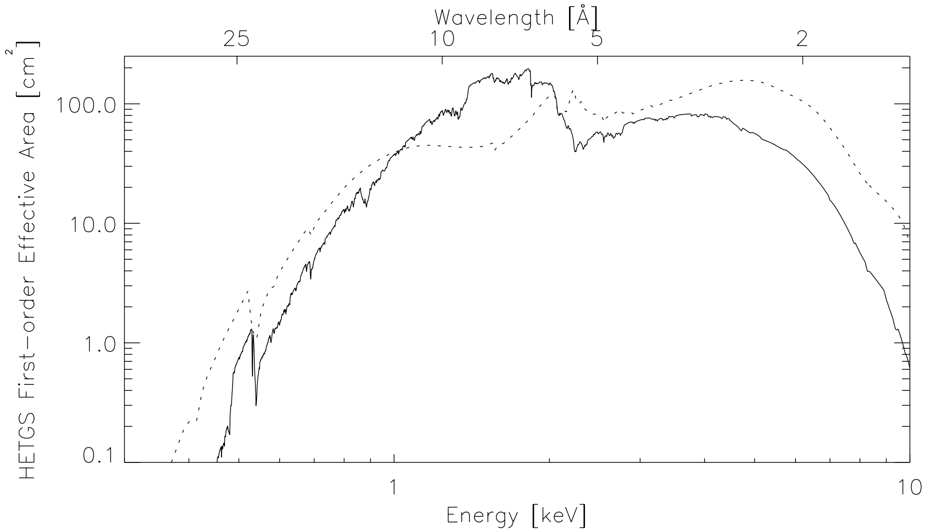

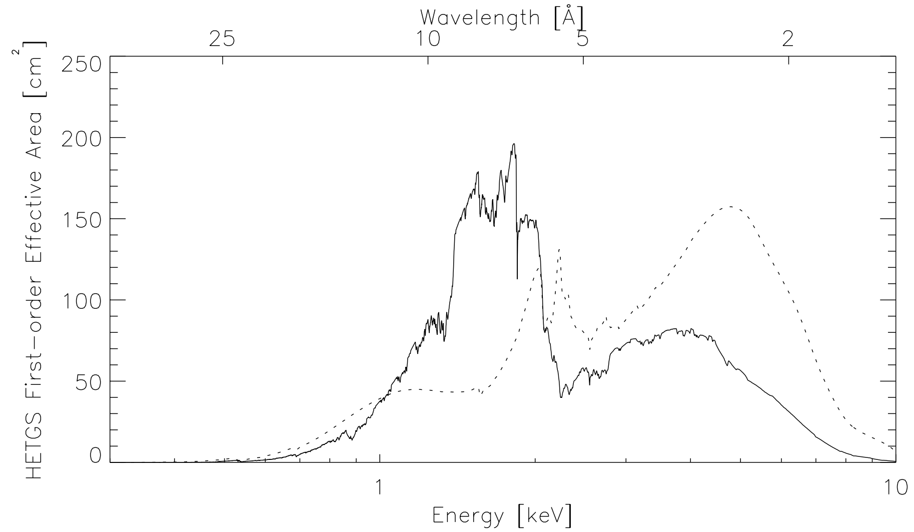

Figure 8.11: The modelled total first-order (solid curve) and zeroth-order (dotted curve) effective area, integrated over the PSF, of the **HRMA**-HETG-ACIS-S combination, as a function of energy. The first-order data are the same as those plotted in Figures 8.7 and 8.9. The plotted first-order values are the sums of the area at a particular energy from both orders (+/-) of both MEG and HEG spectra. Both a log-log and a log-linear version are shown.

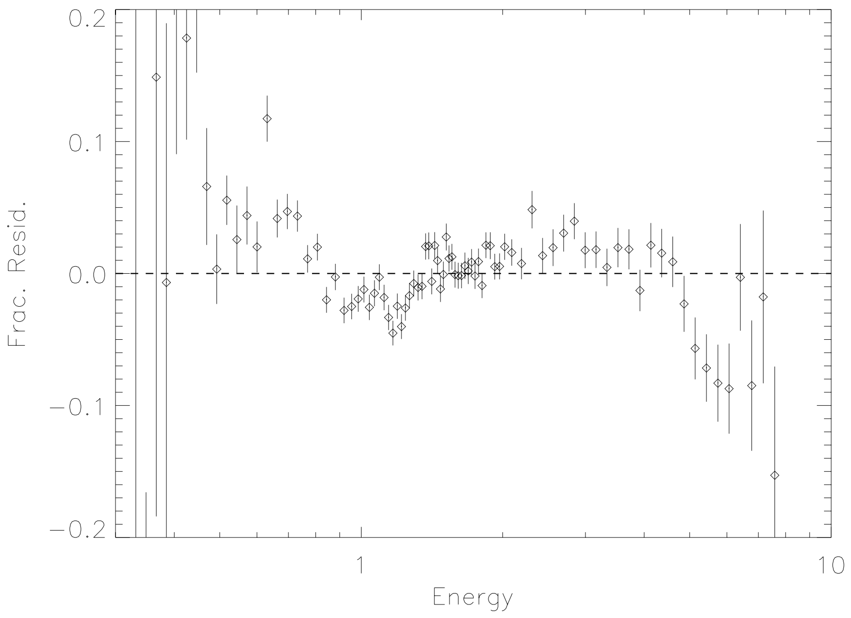

Figure 8.12: The average residuals for curved power-law fits to the HETGS data for BL Lac objects. For most of the HETGS range, the systematic deviations are not significant or are less than 3%. See Marshall (2012) for details.

from curved power-law spectral fits are generally less than 3% (0.5 - 8.0 keV) on small scales (see Figure 8.12). Preliminary results from cross-calibration with XMM-*Newton* indicate that measured fluxes agree to better than 10% (Smith & Marshall 2012).

ACIS-S Order Sorting Effects

One of the advantages of using the ACIS-S as the HETG readout detector is the ability of ACIS to determine the energy of detected X-rays. This crude (by HETGS standards) energy measure can be used to determine the diffraction order of the photon, i.e., perform "order sorting", as shown in the "banana plot" of Figure 8.14.

During data analysis, this filtering is accomplished by utilizing two of the data columns supplied in the level 1.5 (or 2.0) FITS data file: the ACIS-determined energy, ENERGY, and the dispersion distance, $m\lambda$ = TG_MLAM. Ideally this order sorting would have perfect efficiency, that is, all first-order events would be correctly identified. In practice, a high sorting efficiency is achieved by accurately calibrating the ACIS ENERGY values

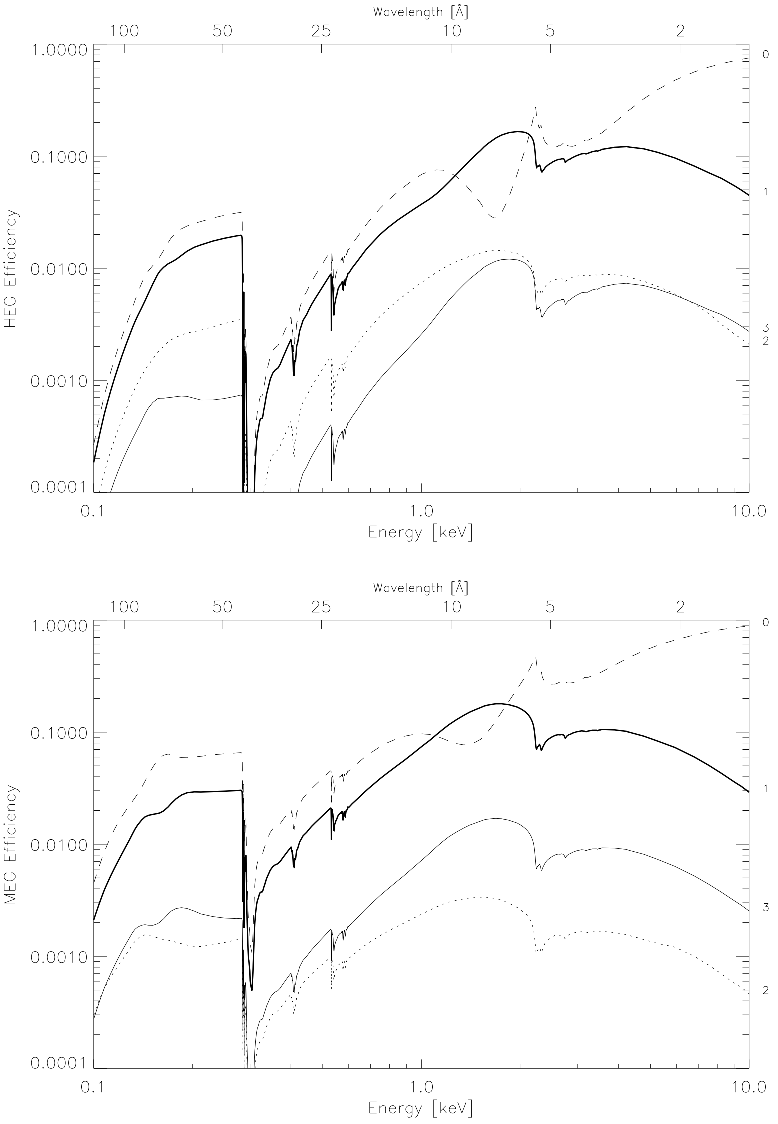

Figure 8.13: HEG (upper panel) and MEG (lower panel) efficiencies as a function of energy. The values plotted are the mirror-weighted efficiency into a single plus, minus, or zero order (labelled on the right edge). The dashed line is zeroth order; the thick solid line is first order. Note that the relative strengths of the third orders (thin solid lines) are comparable, whereas the second order strengths (dotted lines) are significantly different between the HEG and MEG.

and by accepting events in a large ENERGY range. The slight efficiency corrections that do arise are included in the ARF through values in an order sorting integrated probability (osip) file.

ACIS-S Pileup Effects

Figure 8.15 shows a closeup of the "banana plot" (ACIS-determined energy versus the dispersion distance in units of wavelength) for MEG minus-order events for an observation which exhibits pileup (see Section 6.15) and thus mimics higher-order photons. One can encounter pileup even in the dispersed spectra. The effect is most likely seen in first order spectra when observing bright continuum sources such as those found in the Galactic bulge. Pileup, when it occurs, is most usually found in the MEG first order spectrum near the iridium edge at 2 keV where the HETGS effective area is the highest. Users analyzing data should note that not correcting for pileup may introduce an artificial absorption edge. In these cases users may well wish to examine the spectrum in the third order to either salvage or correct a result.

ACIS-S BI / FI QE Effects

The ACIS-S array is made up of both back-illuminated (BI) and front-illuminated (FI) CCDs; chips S1 and S3 (see Figure 8.1) are BI devices and the rest are FI devices. These devices have different quantum efficiencies (QE) with the BI having greater sensitivity at lower energies; most notably the S1 BI device gives an increased effective area in the MEG minus first order between about 0.5 to 0.8 keV. The grating ARFs are created taking these QE differences into account.

ACIS-S Chip Gap Effects

The nominal ACIS-S aim point is on chip S3, about $2.0'$ from the gap between chips S2 and S3. Energies of gap edges in both dispersed spectra for the default aim point and for 3 offsets in both (+/-) Y directions are given in Table 8.2. For example, with zeroth order at the -0.66 arc minute Y-offset position, the gap between chips S1 and S2 spans the energy range 0.808-0.821 keV in the MEG spectrum (lower energies on S1). The observer is advised to *try to avoid placing known features of interest within three gap widths of the tabulated gap edges.* All HETGS observations are nominally dithered with an amplitude of ±8 arc seconds. There will be reduced coverage in the spectral regions within one gap-width on either side of the gaps. The web-based Spectrum Visualization Tool http://cxc.harvard.edu/cgi-gen/LETG/alp.cgi displays where spectral features fall on the ACIS-S detector as a function of Y-offset and source redshift.

The values in the table are based on an effective gap size of 0.502 mm, corresponding to $10''$ on the sky. It is "effective" in the sense that the gap includes columns 1 and 1024 of the devices from which no events are reported. This value for gap size is approximate and accurate to about 2 pixels. The actual gap sizes vary slightly; more accurate values of the

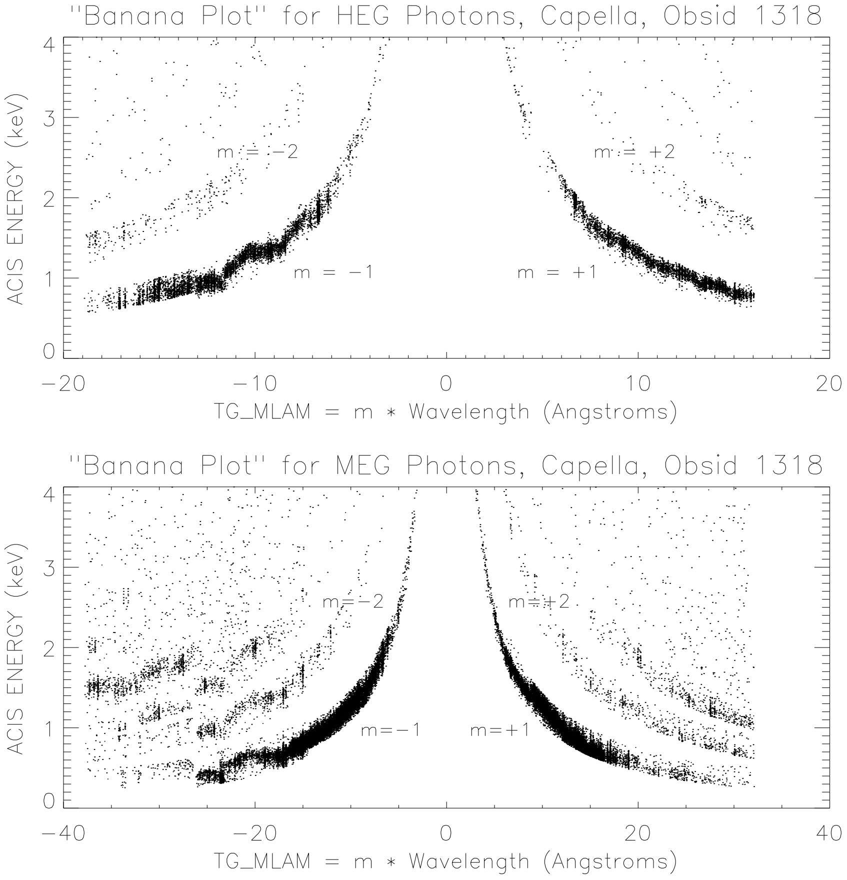

Figure 8.14: HEG (upper panel) and MEG (lower panel) "Banana Plots". A useful look at the HETGS data is obtained by plotting the ACIS-measured event ENERGY as a function of $m\lambda$ = TG_MLAM (or versus dispersion distance.) These "banana plots" are shown here for HEG and MEG parts of the Obsid 1318 Capella observation. The various diffraction orders show up as hyperbolae. Events can be assigned to a diffraction order based on their location in this space. By accurately calibrating the ACIS ENERGY and by taking an appropriate acceptance region, events can be sorted by order with high confidence and efficiency. A "zig-zag" in the $m = -1$ events pattern is visible around -10 Å in the HEG plot and is due to uncorrected serial charge transfer inefficiency in the BI device S1, which produces a slow variation of gain across a node.

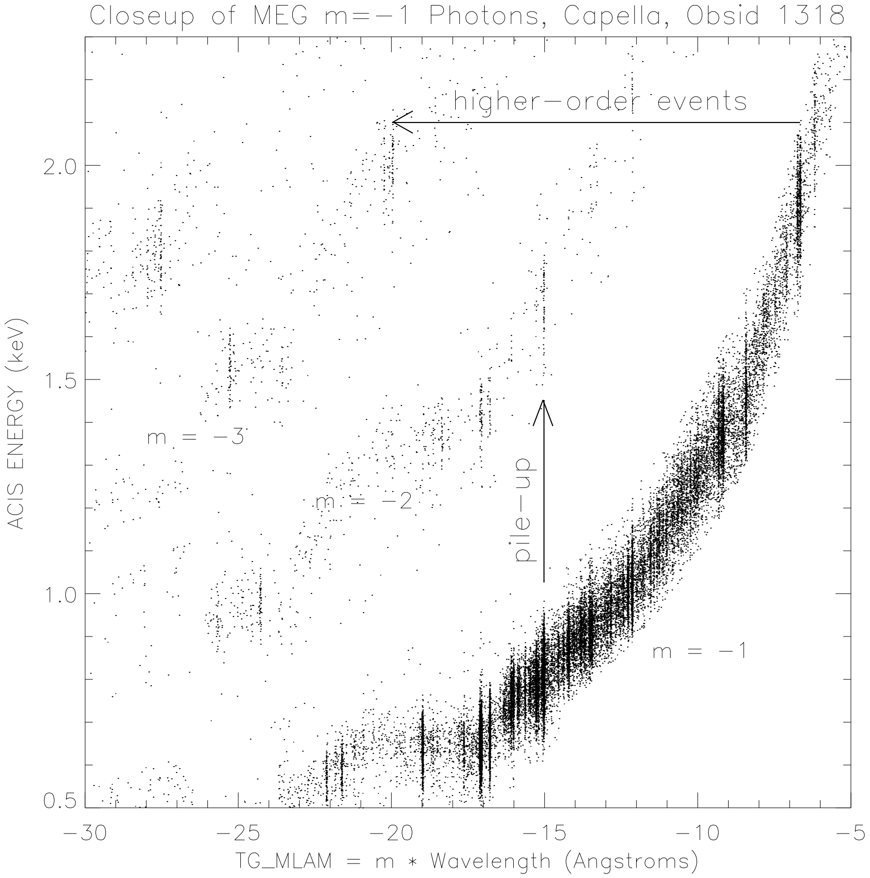

Figure 8.15: HETGS pile-up and higher-order events. Taking a close look at the MEG "banana plot" demonstrates how the ACIS ENERGY can be used to identify higher-order events and pileup in an HETGS spectrum. The 3rd order of the ≈ 6.7 Å lines are clearly visible; the lines are only weakly present in 2nd order because the MEG 2nd order is suppressed. In comparison, the 15 Å line (and others) are so bright in 1st order that a fraction of the events (≈ 6 % here) pile-up and produce events with twice the ACIS ENERGY. Note that the 6.7 Å lines are better resolved in the high order spectrum.

Table 8.2: Table of HETGS Gap Locations

Y Offset		Grating	HETGS Gaps (keV)						
arc min.	mm		S0	S0-S1	S1-S2	S2-S3	S3-S4	S4-S5	S5
1.00	2.93	MEG		0.505	0.959	9.611	1.198	0.564	0.369
			0.345	0.510	0.977	11.736	1.172	0.558	
		HEG		1.009	1.917	19.209	2.395	1.127	0.737
			0.689	1.018	1.952	23.455	2.342	1.115	
0.50	1.46	MEG		0.491	0.911	6.290	1.283	0.582	0.376
			0.338	0.496	0.927	7.135	1.252	0.576	
		HEG		0.982	1.821	12.570	2.564	1.163	0.752
			0.676	0.991	1.853	14.260	2.503	1.151	
0.15	0.44	MEG		0.482	0.880	5.064	1.349	0.595	0.382
			0.334	0.486	0.895	5.598	1.316	0.589	
		HEG		0.963	1.759	10.122	2.697	1.190	0.763
			0.667	0.972	1.789	11.189	2.630	1.177	
-0.33	-0.97	MEG		0.470	0.841	3.997	1.453	0.615	0.390
			0.328	0.474	0.855	4.322	1.414	0.608	
		HEG		0.939	1.681	7.988	2.903	1.228	0.779
			0.656	0.948	1.708	8.638	2.826	1.214	
-0.66	-1.93	MEG		0.462	0.816	3.491	1.534	0.629	0.395
			0.324	0.466	0.829	3.736	1.490	0.621	
		HEG		0.924	1.631	6.977	3.065	1.256	0.790
			0.648	0.932	1.657	7.467	2.979	1.242	
-1.00	-2.93	MEG		0.454	0.792	3.088	1.627	0.644	0.401
			0.320	0.458	0.804	3.279	1.578	0.636	
		HEG		0.908	1.583	6.172	3.251	1.287	0.802
			0.640	0.916	1.607	6.553	3.155	1.271	

ACIS-S chip geometry are given in a CXCDS CALDB file 'telD1999-07-23geomN006.fits' (and higher versions) and incorporated in *MARX* version 3.0 and higher. Relative to S3, where zeroth order is normally placed, the ACIS-S chip locations are calibrated to better than 0.2 pixels allowing accurate relative wavelengths.

8.2.2 HETGS Line Response Function

A high-resolution spectrum is created by the projection of events along the dispersion axis and binning the events into energy or wavelength bins as shown in Figure 8.2. The HETGS line response function (LRF) at a given wavelength is the underlying distribution which would result if the source were monochromatic at that wavelength. The LRF function is encoded in the grating RMF files. Examples from flight data are shown in Figures 8.16 and 8.17. To a good first approximation the core of the LRF can be modeled as a Gaussian, parameterized by a *Resolution*, ΔE or $\Delta\lambda$, given as the full-width at half-maximum of the Gaussian, 2.35σ. For the HETG the resolution is roughly constant when expressed as a wavelength. The *Resolving Power*, $E/\Delta E = \lambda/\Delta\lambda$, is a useful dimensionless measure of the spectrometer performance. Plots of the HETGS resolving power are presented in Figure 8.19.

Of course the HETGS LRF is not simply a Gaussian and, as for other spectrometers, the response can be encoded at a higher level of fidelity through the use of response matrix files, RMF's. As explained below, the LRF (RMF) of the HETGS depends on all system components as well as the source spatial properties. Thus, LRF creation is carried out using a system model, e.g., the *MARX* ray trace software. A set of RMF's for a point source and nominal telescope properties can be created based on the latest LRF library in the *Chandra* CALDB which includes two Gaussian and two Lorentzian components to describe the LRF as derived from realistic MARX simulations; for examples, see the fitted LRF models in Figures 8.16 and 8.17. Note that "canned" grating RMFs are provided for observation planning but should not be used to analyze real data. They can be found at: http://cxc.harvard.edu/caldb/prop_plan/index.html

The line response function can be decoupled approximately into three contributing components: the telescope PSF, the HETG effects in the dispersion direction, and HETG effects in the cross-dispersion direction. These are described below. With the exception of "HEG scatter", all effects described here are included in *MARX* version 3.0 (and higher) ray trace software.

LRF: Telescope PSF and Zeroth Order

The HETG itself does not focus the X-rays emerging from the HRMA. Rather, *the Rowland design attempts to maintain the focal properties of the HRMA in the dispersion direction even as the focus is deflected by the diffraction angle β.* The 1-D projection of the telescope PSF onto the dispersion axis is thus at the heart of the HETGS LRF and can be thought of as the "zeroth-order LRF". Ground testing showed no measurable effect on the telescope PSF due to the HETG insertion; this was used to good advantage for the now famous image of the Crab Nebula and its pulsar, Obsid 168, where the jet and swirling structure are seen in the zeroth-order HETGS image. Thus, the zeroth-order image in an HETGS observation can be used to determine the telescope contribution to the LRF.

Image quality depends on many factors, and so, while a nominal LRF can be modeled, the detailed LRF will be observation dependent at some level. Factors in the telescope PSF performance include: source size and spectrum, HRMA properties, focus setting, detector effects (e.g., pixel quantization), aspect solution and reconstruction effects, and data analysis operations (e.g., pixel randomization.) While all of these effects can be modeled, the "proof of the pudding" is in the as-observed zeroth order image.

As an example, we show the results of the observation of Capella (Obsid 1318, Figure 8.1) in Figure 8.18. Both the zeroth-order event distribution and its 1-D projection indicate that the zeroth-order is heavily piled up with an unpiled event rate of order 10 events per frame time (per few square ACIS pixels). The wings of the PSF are visible but the core shape and intensity have been severely distorted. However, because the ACIS-S CCDs have their columns perpendicular to the (average) dispersion axis, the "frame-transfer streak" events or "trailed image" (see Section 6.12.1 in Chapter 6) can be used to create an accurate zeroth order LRF that is not affected by pileup, as shown. For point-sources such as Capella, measurements of the FWHM of the zeroth-order streak events for selected observations over the first two years of HETGS operation show FWHM values generally in the range 1.46 to 1.67 ACIS pixels with an average of 1.57 ACIS pixels. Thus, by appropriately examining the zeroth-order image and its LRF, one can get a good idea of the expected width of a truly monochromatic spectral line, and determine whether or not any broadening seen in a dispersed order is a spectral property of the X-ray source.

LRF: Dispersion Direction

As mentioned, the profile in the dispersion direction defines the instrument spectral resolution, ΔE or $\Delta\lambda$. The resolution function has two main terms with different dependences on energy: the image blur from the mirror described above and that caused by grating period variations which come in through the dispersion relation and are described here.

From the grating equation, $m\Delta\lambda = p\Delta\beta cos\beta + \Delta p sin\beta \approx y\Delta p/R_s + p\Delta y/R_s$, where p is the grating period, β is the dispersion angle, y is the dispersion distance and R_s is the (fixed) Rowland spacing. The two terms of interest are on the right side of $\lambda/\Delta\lambda = (\Delta p/p + \Delta y/y)^{-1}$. The grating fabrication process produced tightly distributed grating periods ($\Delta p/p < 2.5 \times 10^{-4}$) so that the first term is important in the spectral resolution only at very high dispersion (low energy). The mirror point response function has a nearly constant size Δy and dominates the resolution over most of the HETGS band, as shown in Figure 8.19. At very low energies there is a contribution from variation in the grating periods. These variations are taken into account in the *MARX* simulator.

During ground testing, we discovered that there is a low level of incoherent dispersion (or "scattering") in HEG spectra. This scattering effect distributes a small amount of the flux along the dispersion direction. The total power involved is only 1.0% of the total in first order but the light is irregularly distributed between the coherently dispersed orders. Assuming that the power distribution scales with the first order dispersion distance, there is no more than 0.02% of the first order flux in any bin of width 0.01λ. There has been no scattering detected in the MEG spectra to a level of order 100 times fainter than in the HEG. See the HETG Ground Calibration Report listed at the end of this chapter for further details. The effects of scattering from the grating are likely to be negligible for most observations.

LRF: Cross-Dispersion Direction

The profile in the cross-dispersion direction is dominated by three effects: mirror blur, grating roll variations, and astigmatism (as a by-product of the Rowland design which optimizes spectral resolution). The cross-dispersion profile that results from astigmatism is slightly edge brightened, but quasi-uniform, with a length at the Rowland focus of $2R_f y^2/R_s^2$, where y is the dispersion length and R_f is the radius of the ring of facets

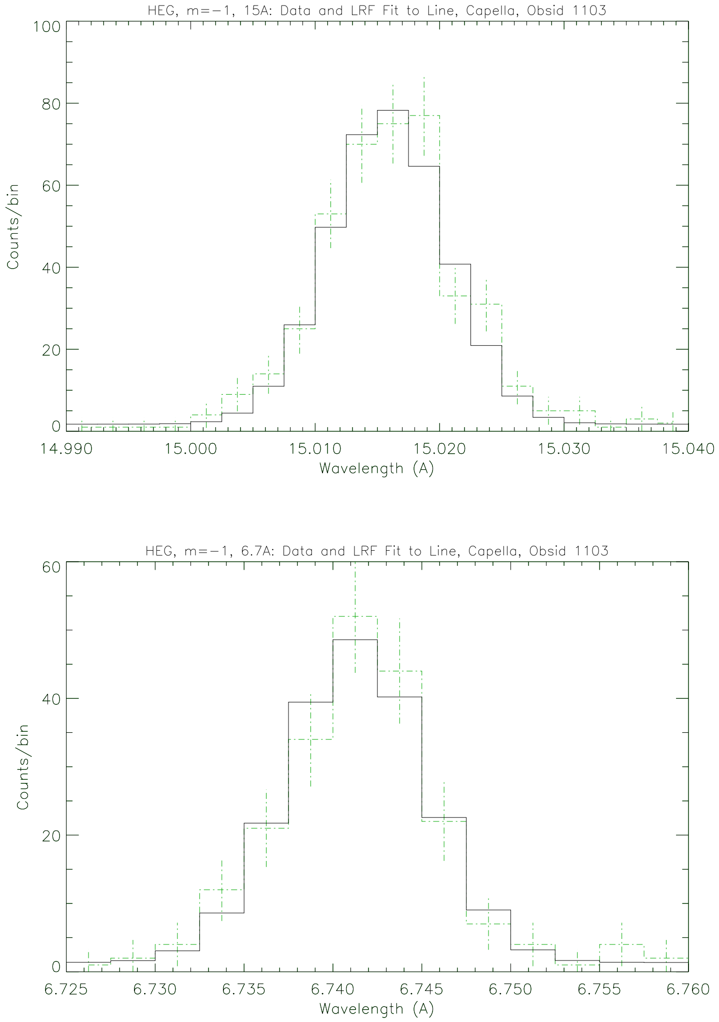

Figure 8.16: Representative Line Response Functions at two wavelengths for the HEG; 15 Å top, 6.7 Å bottom. Two of the bright lines in the HEG counterpart to the MEG Capella spectrum shown in Figure 8.2 have been fit by the instrumental LRF. The LRF is encoded in the HEG RMF created using *CXC* software and calibration parameters.

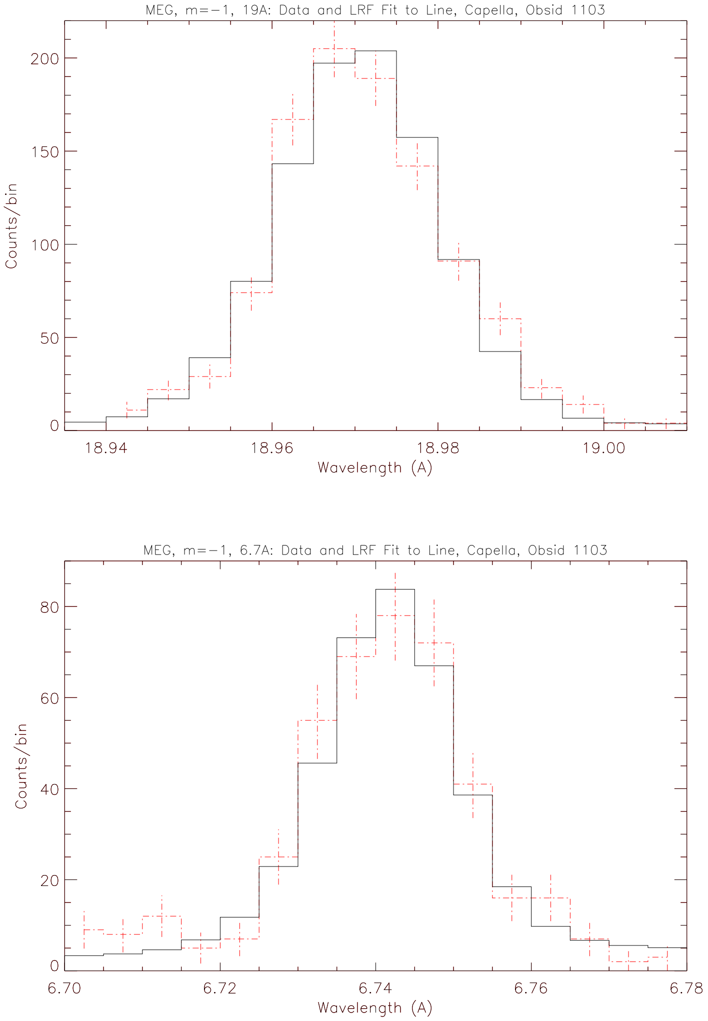

Figure 8.17: Representative Line Response Functions at two wavelengths for the MEG; 19 Å top, 6.7 Å bottom. Two of the bright lines in the MEG Capella spectrum shown in Figure 8.2 have been fit by the instrumental LRF. The LRF is encoded in the MEG RMF created using *CXC* software and calibration parameters.

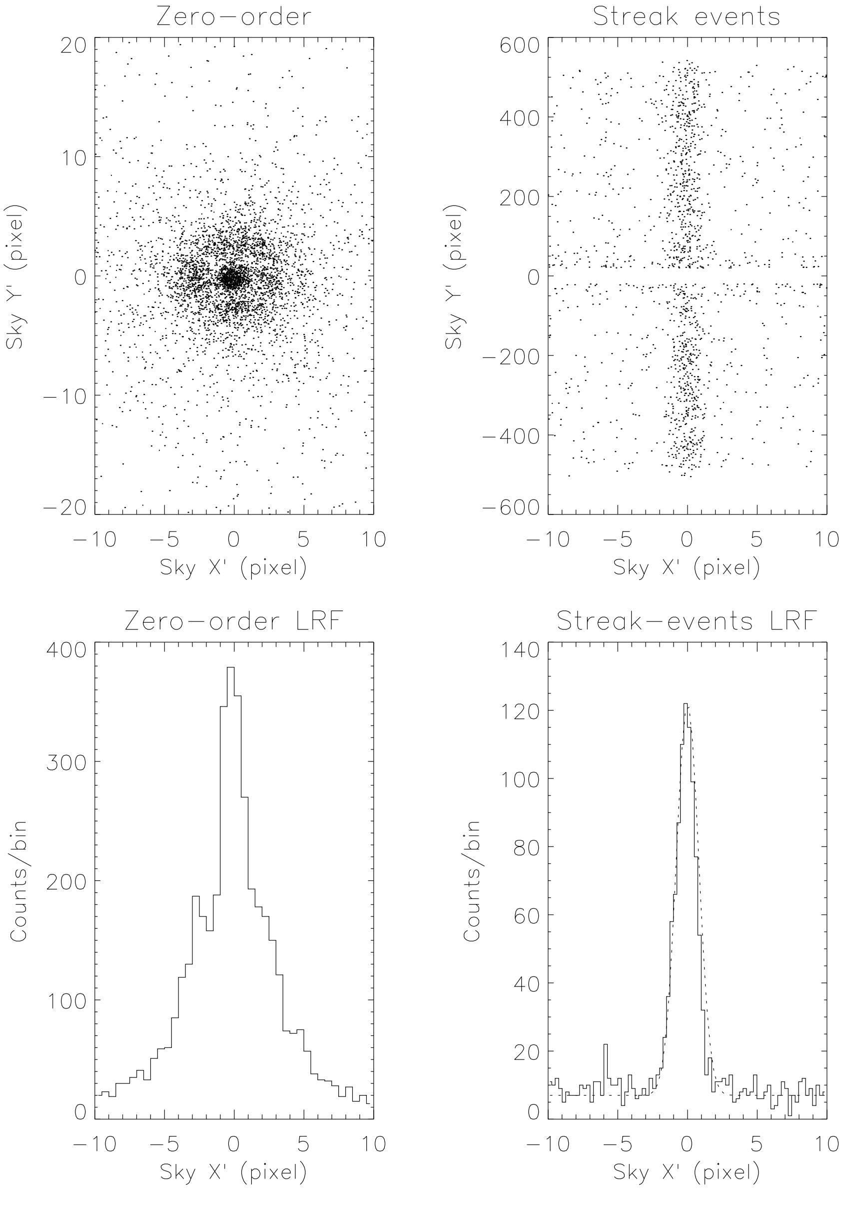

Figure 8.18: HETGS zero order and Frame transfer Streak (trailed image) for Obsid 1318 of Capella. The sky coordinates, X, Y, have been rotated so that the frame-transfer streak is along the Y' axis, hence Y' is parallel to the CCD detector Y axis (`CHIPY`) and X' is approximately along the average HEG-MEG dispersion axis. The left-side panels show the detected zero-order events and their 1-D projection; pileup is evident by the enhanced wings relative to the suppressed PSF core. The right-side panels show the frame-transfer streak events and their 1-D projection; the dotted line is a Gaussian fit to the data.

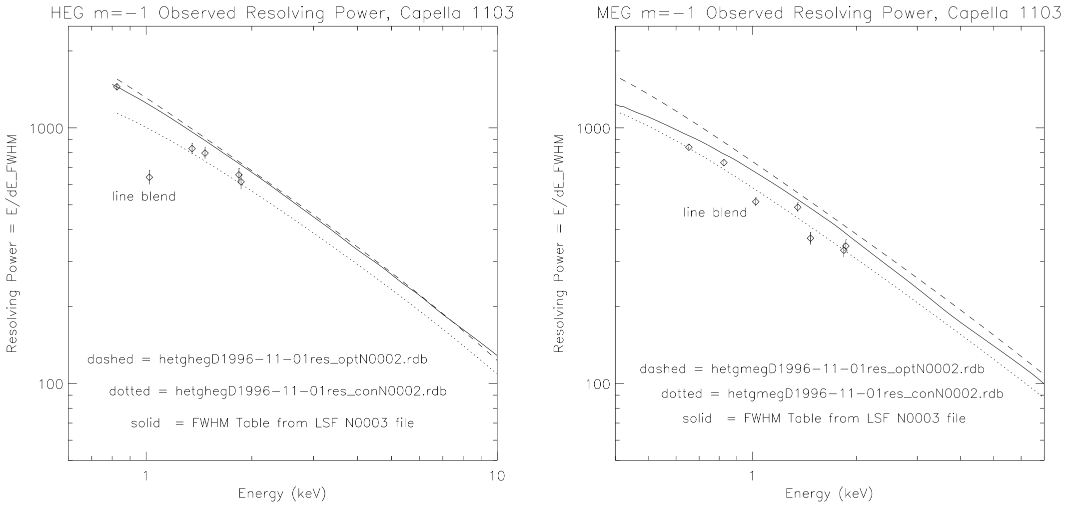

Figure 8.19: HEG and MEG resolving power ($E/\Delta E$ or $\lambda/\Delta\lambda$) as a function of energy for the nominal HETGS configuration. The resolving power at high energies is dominated by the telescope PSF; at low energies grating effects enter but do not dominate. The "optimistic" dashed curve is calculated from pre-flight models and parameter values. The "conservative" dotted curve is the same except for using plausibly degraded values of aspect, focus, and grating period uniformity. The cutoff at low-energy is determined by the length of the ACIS-S array. Measurements from the HEG and MEG $m = -1$ spectra, e.g., Figure 8.2, are typical of flight performance and are shown here by the diamond symbols. The values plotted are the as-measured values and therefore include any natural line width in the lines; for example, the "line" around 12.2 Å is a blend of Fe and Ne lines. The solid line gives the resolving power encoded in the RMFs generated using the current CALDB.

on the HETGS structure and dominates the size of the cross dispersion profile at large dispersion.

The spread of facet roll angles (defining the dispersion direction for each facet, and not to be confused with the spacecraft roll angle), $\Delta\phi$, contributes a cross-dispersion term of order $y\Delta\phi$. Sub-assembly measurements predicted $\Delta\phi = 0.42$ arc minutes rms. However, analysis of ground test measurements lead to a somewhat larger and more complex roll angle distribution for the gratings. In addition, six misaligned MEG facets were discovered during ground testing. The inferred facet roll angles were misaligned from the average dispersion direction by 5-23 arc min. On average, each facet contributes only 1/192 of the flux at any given energy, so the cross dispersion profile has small deviations in the form of peaks displaced from the main distribution.

To include explicitly the MEG misaligned gratings, *MARX* uses “sector” files which allow the specification of grating alignment and period parameters for certain regions (sectors) of each of the four shells. Using these files, the agreement between ground calibration and flight data is very good. For the MEG the misaligned gratings are explicitly included and the rest of the gratings' $\Delta\phi$ term is modeled as the sum of two Gaussian distributions centered at +1 and -1 arc minute w.r.t. the nominal axis, each with an rms value of 1.5 arc minutes. For the HEG a more pronounced bi-gaussian distribution is observed and modeled: the Gaussians are offset by -1.35 and +1.65 arc minutes, each with a 1 arc minute rms, and in a relative ratio of 55:45.

In each case, these effects are accurately included in *MARX* version 3.0 (and above). Flight data for the Crab pulsar (Obsid 168) are shown in Figure 8.20 for the MEG and in Figure 8.21 for the HEG. Note that these profiles are on top of a significant baseline due to the presence of the Nebula. The asymmetry in the MEG profile caused by misaligned gratings is quite clear at large dispersions.

Finally, we show in Figure 8.22 how the total observed flux depends on the width of the extraction region in the cross-dispersion direction. The figure can be used to estimate the reduction in flux if analysis using a narrow extraction window, smaller than the nominal 4 arcsec full width, is planned.

Extended and Off-Axis Targets

The observation of extended sources with the HETGS adds complexity. Chiefly, the position of an event in the focal plane is not a unique function of the position within the source and the photon energy. The source extent, measured by the zeroth-order image size, can effectively increase in several ways: the telescope is out of focus, the source is off-axis, or there is a natural extent to the astrophysical source. Figure 8.23 illustrates the chief consequence for extended sources - a degradation of the apparent spectral resolution. In Figure 8.24 similar resolution curves are shown as a function of the source off-axis angle.

The discussion and plots above assumed that the source has no spatially dependent variations in the spectrum. The more general case of extended sources with spatially varying spectra is briefly discussed below in Section 8.5.3.

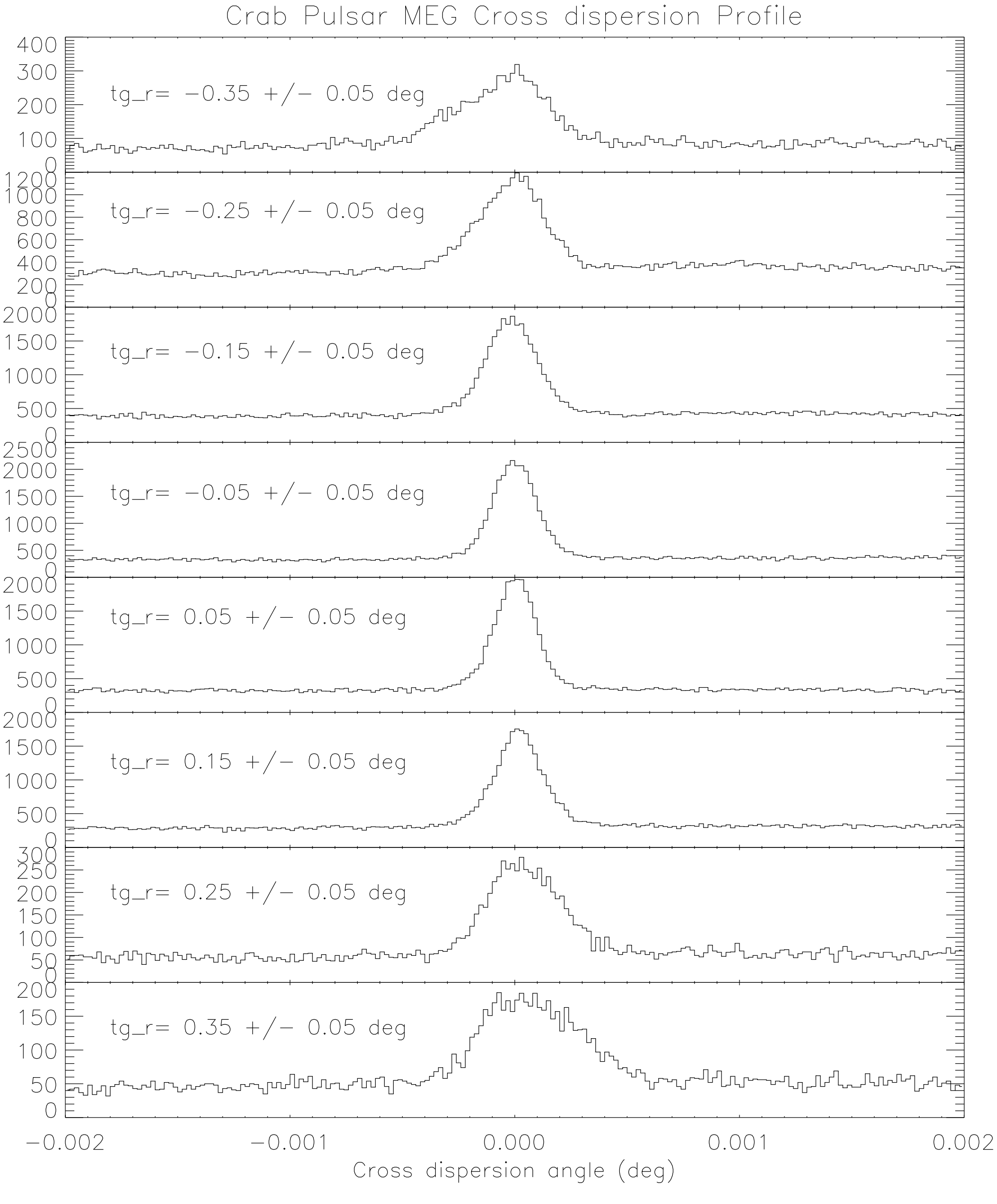

Figure 8.20: The cross dispersion profile is shown for eight slices of the dispersed MEG spectrum of the Crab pulsar. There is an asymmetry caused by misaligned gratings that becomes most evident at large dispersion.

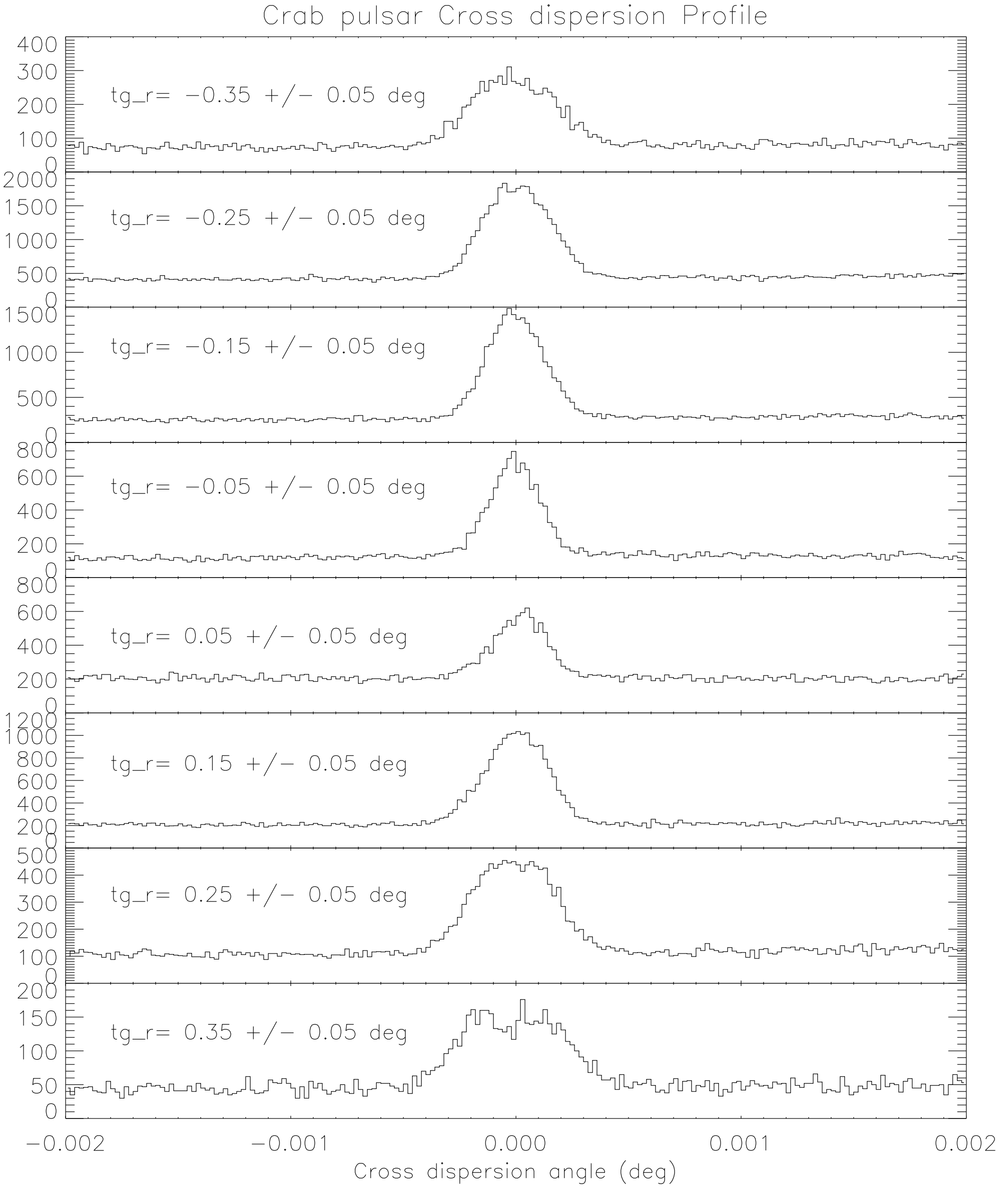

Figure 8.21: As in Figure 8.21, the cross dispersion profile is shown for the HEG spectrum of the Crab pulsar. The profile is symmetric but broadens significantly at large dispersion.

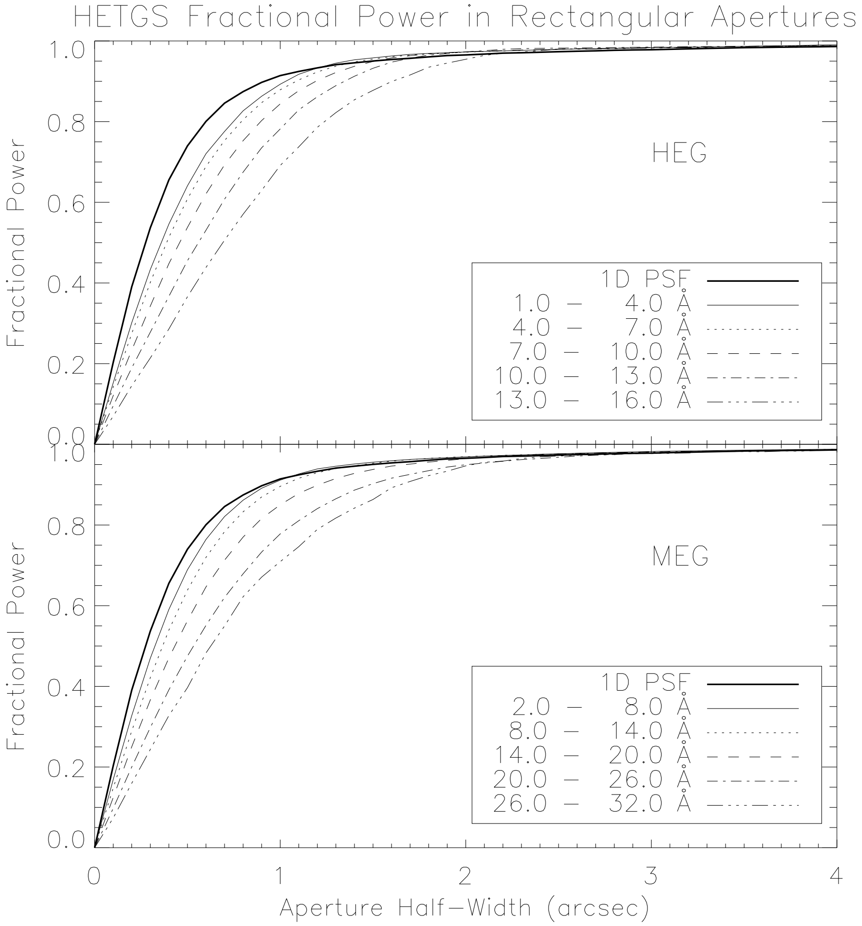

Figure 8.22: Enclosed power distributions are computed for five wavelength intervals for both the HEG (top) and the MEG (bottom). The observation of Mk 421 (observation ID 1714) was used.

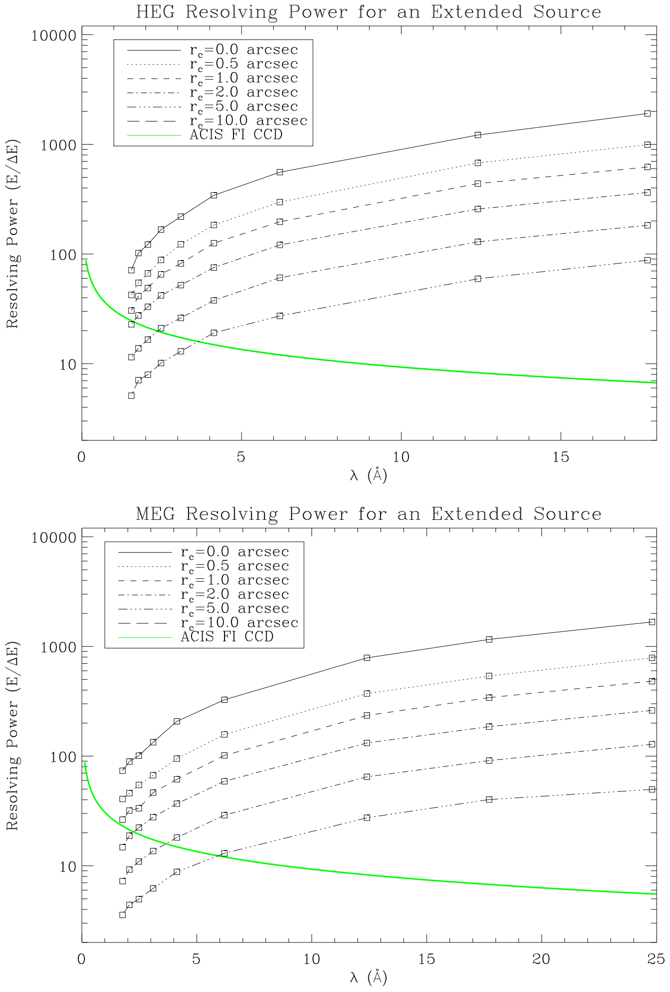

Figure 8.23: The effects of source size on the apparent HETGS spectral resolution. This *MARX* simulation uses a cluster (of galaxies) Beta model for the surface brightness profile. The Beta model is parameterized by a core radius (r_c) which represents the extension of the source. The effect on the apparent resolving power (E/ΔE) is shown as a function of photon energy for source sizes of $0'', 0.5'', 1'', 2'', 5''$, and $10''$. The spectral resolution of an ACIS FI CCD near the framestore region is shown for comparison.

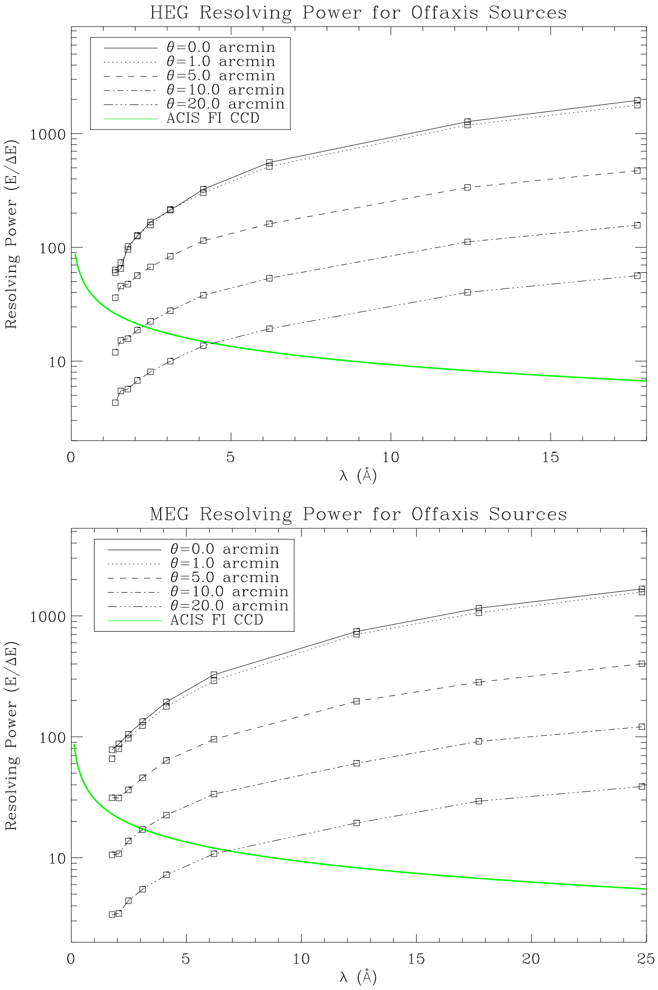

Figure 8.24: The effects of off-axis pointing on the HETG grating spectral resolution. Using *MARX*, we have simulated an observation of a point source at increasing off-axis positions. The effect on the resolving power (E/ΔE) is shown as a function of photon energy for off-axis angles of $0', 1', 5', 10'$, and $20'$. The spectral resolution of an ACIS Front Illuminated (FI) CCD at a point near the framestore region is shown for comparison.

8.2.3 Background

Since the HETG is always used in conjunction with a focal-plane detector, spectra from the HETGS will have background events determined by the detector's intrinsic and environmental backgrounds. The cosmic background, folded through the HETGS response, will likewise contribute background events. In addition to these detector-dependent backgrounds, there are additional grating-dependent effects such as scattering from the gratings which will produce extraneous photons in locations unexpected on the basis of the simple grating equation. One such effect is the scattering along the dispersion direction described in Section 8.2.2.

Figure 8.25 shows the HEG and MEG spectra of the background for a long calibration observation of HR 1099 (observation ID 62538). The background was selected from regions 8-50 arcsec from the dispersion line in the HEG and 11-50 arcsec from the dispersion line in the MEG. The pulse height selection was simple, accepting events that satisfy the relation $|E_{ACIS}/E_{TG} - 1| < 0.30$, where E_{ACIS} is the energy derived from the ACIS-S pulse height and E_{TG} is the energy based on the dispersion distance. The background was normalized to an aperture of ± 3 arcsec (full size of 6 arcsec) and averaged at 0.1 A intervals. This plot can be used to estimate the background in a dispersed spectrum at a particular wavelength for proposal purposes.

There is considerable structure in the background. For $\lambda < 2$ Å ($E > 6$ keV), the background is dominated by high energy events that are included in the relatively wide pulse height selection. This background can be further reduced in data analysis because the pulse height selection can be somewhat narrower at high energies. As one would expect (see Section 6.16), the background is higher in the region near 8 Å in -1 order as this portion of the dispersed spectrum is detected with a BI chip (S1). "Streaks", short-lived events observed in the S4 detector, have been removed; otherwise, the background in +1 order would be significantly higher and would show more structure.

8.2.4 Absolute Wavelength

The HETGS-measured wavelength depends, as the grating equation implies, on knowing the diffraction angle, the diffraction order, and the grating average period. The angle depends on knowing the HETGS geometry, specifically the Rowland spacing and the ACIS-S pixel size and configuration. Preliminary comparisons between measured and expected emission line wavelengths indicates an agreement to the accuracies listed in Table 8.1. Systematic wavelength errors are now at the 100 km/s level.

8.3 Calibration Status

The calibration of the HETGS is based on extensive laboratory tests, system-level ground measurements, and flight data and analyses. Because the HETGS involves the HRMA, HETG, and ACIS-S as well as aspect system properties, calibration of all these components

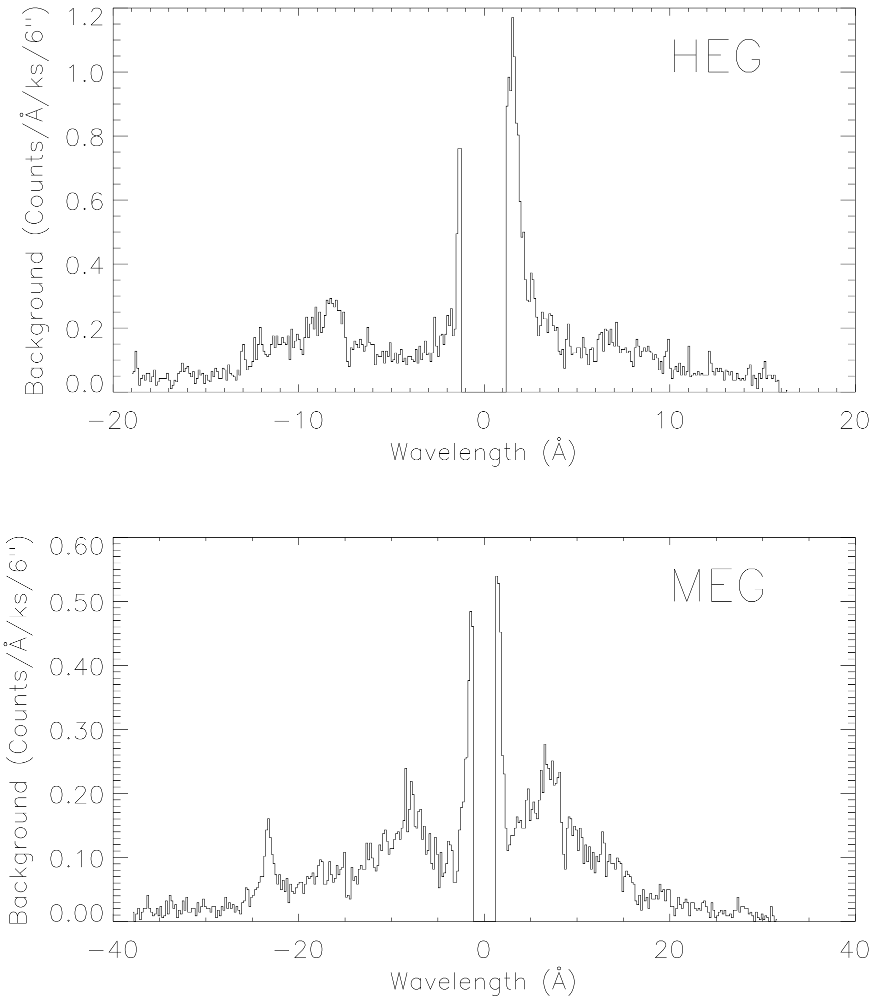

Figure 8.25: The background spectrum is plotted for the HEG (top) and MEG (bottom) for a long observation of the late-type star HR 1099 (observation ID 62538). The background was normalized to a 6 arcsec wide aperture but determined from a substantially larger region out to 50 arcsec from the source dispersion line. The spectrum was binned to 0.1 Å to show details of structure that may be observed in a typical HETGS observation. The spikes near zeroth order are due to increased background included in the pulse height selection at high energies.

is important to the HETGS calibration. Details of the present state of the HETGS calibration are available at http://space.mit.edu/ASC/calib/hetgcal.html; see also Marshall *et al.* (2004), Weisskopf *et al.* (2004), and Marshall (2012).

8.4 HETG Operations

8.4.1 Flight Events and Anomalies

There have been no flight anomalies with the HETG *per se.* There have been some problems with the HETG and LETG grating insertion/retraction mechanisms. To date these have been limited to failure of some of the limit switches which are used to sense the gratings' position. In May 2000 there was failure of the HETG A-side electronics retraction limit switch indicating that the HETG was not retracted, when in fact it was. Switching to the redundant B-side limit switch worked until June 2000 when it too would not indicate that the HETG was retracted. Subsequently operational procedures have been changed in order to determine when the gratings are properly retracted. There have been no impacts to the science program.

Because the HETG insert limit switches continue to function and because the HETG is inserted against a hard stop, **these anomalies have had no effect on the HETG wavelength scale.**

8.4.2 Operational Constraints

With the exception of operational constraints on the focal plane detectors, there are no operational constraints for the use of the HETGS from the proposer's point of view. The HETG is placed in the stowed position during passage through the radiation belts, a time when no data can be taken. Additional functional constraints include preventing both the HETG and LETG from being simultaneously commanded into position, which could cause a mechanical interference. Finally, a "failsafe" command, once used, will permanently retract the grating. A decision to issue the failsafe command will not be taken without a thorough review including the Chandra Project and NASA Headquarters.

8.4.3 Output Data

There are no data from the HETG itself. The data are generated by the focal-plane imager in its format (e.g. Figure 8.1).

8.4.4 Performance Monitoring, Health and Safety

The HETG itself has only a few thermal and mechanical switch sensors associated with it. These sensors are examined routinely as part of the health and safety monitoring of the Observatory. HETGS performance is monitored by means of the calibration observations (Section 8.3).

8.4.5 Thermal Response Time

There is a negligible thermal time constant for the HETG to equilibrate from "near-wall" storage to "in-use" temperature environments. The temperature dependence of the resolution and energy scales have been minimized through use of low-expansion material ("Invar") and single-point-mounted facet-frames. Thus, the support structure may expand or contract, but the facets will not.

8.4.6 Observation Frequency/Duty Cycle

Currently, the longest continuous observations are limited to the time between passage through the radiation belts (section 3.4.2).

8.4.7 Radiation Considerations

The main radiation concern for the HETG concerns the polyimide support material. Thin membranes of this material, used for proportional counter windows operating under a pressure differential, have been tested for the effects of radiation damage on leak rate. No increased leak rate was encountered after a dosage of 9 krad. In these tests the mechanical integrity of the material, the key issue for the HETG, was severely tested by the ability of the window to maintain the pressure differential of order one atmosphere. Loss of mechanical integrity has been reported in the literature, but only after exposures of 1000 MRads. The estimated proton dose to the HETG polyimide is of order 1 kRad per orbit when the HETG is inserted, and much lower values when HETG is in its stowed position. Current practice is to have the HETG retracted during radiation passages; however, even if it were left inserted the total exposure would be ≈ 1 MRad over 10 years, well below the 1000 MRad level.

A secondary concern would be changes to the Gold grating bars (which, when in place, face the HRMA) due to sputtering by particles, particularly for the high-aspect ratio HEG gratings. Diffraction order ratios are sensitive to these changes. To date, after flight experience and laboratory radiation tests, there is no evidence that this concern is other than intellectual.

8.5 Observation Planning

The following sections provide assorted information and topics relevant to planning an HETGS observation. See also the HETGS observation planning web page: http://space.mit.edu/ASC/calib/hetg_GO_info.html

8.5.1 Focal Plane Detector Considerations

The HETG was designed for use with the ACIS-S detector, although other detectors may be used for certain applications. Details concerning the detectors may be found in Chapters 6 and 7. Some considerations are:

- ACIS or HRC: ACIS provides energy resolution which is useful for order separation, background suppression, and discrimination between multiple sources. The HRC is likely to be useful if high time resolution is necessary especially if the ACIS mode is not helpful for the observation in question. The HRC has not yet been used with the HETG and no calibration verification has yet been performed, so this detector is not recommended for general use.

- Operating mode of ACIS-S: The ACIS-S array can operate in many modes, giving control over e.g., the read-area, pixel-binning, and read-frequency. The selection of the appropriate operating mode and its ramifications for the experiment is one of the most important that the user faces. A careful reading of Chapter 6 is recommended. The proposer should *pay special attention to the pros and cons of designating optional CCDs* for their HETGS observation, as opposed to simply requesting the entire ACIS-S chip set.

- Selecting the aimpoint: The capability of moving the SIM along the spacecraft Z-axis (the cross-dispersion direction) is useful for placing the image (dispersed spectra and zeroth order) closer to the ACIS chip readouts. This placement minimizes the effects of the row-dependent energy resolution of the FI chips. For a point source, the recommended placements, stated as offsets from the nominal position are -3 mm and -4 mm for ACIS TE and CC modes respectively. The recommended shift in TE mode allows space for background data to be obtained on the readout side of the dispersed image. The CC mode, however, integrates over the columns, and so there is no advantage gained, and thus the the image can be placed even closer to the readout. NB: Shifting the aimpoint may not be desirable if the target is extended or when there are several sources in the field.

- Orientation of multiple (or extended) sources: One may need to specify a restricted range of spacecraft roll-angles to avoid overlapping spectra from multiple targets in the field, or to arrange that the dispersed spectra from particular features of an extended target do not similarly overlap. Note that roll angle constraints usually will lead to restrictions on the dates dates of target availability. See Chapter 3.

- Offset pointing: Pointing offsets may be specified and used to include or exclude nearby sources, to keep an important spectral feature clear of the gaps between chips, to put a particular low-energy feature on the higher efficiency BI chip S1, etc. Offsets greater than one or two arc minutes will, however, degrade the image quality - Chapter 4 - which in turn broadens the LRF (Section 8.2.2).

- ACIS subarray modes: One might wish to reduce the ACIS-S frame time e.g. in order to minimize the effects of pileup. The user might consider using a subarray with the HETG, as described at
  http://space.mit.edu/ASC/calib/hetgsubarray.html.)
  If the source is point-like, then a -3 mm SIM shift can be used. In this case, there

are at least 6 mm of ACIS-S rows that may not be scientifically interesting (unless the user desires data from serendipitous sources). The reduced array could have 1024 - 250 = 774 rows starting at row 1 thus reducing the frame time to 2.5 s. The size of the minimal subarray depends on the low energy cut-off, E, below which the spectra are not of interest. To understand this better, please refer to Figure 8.1. The subarray must be large enough to encompass both HEG and MEG "arms". Larger subarrays are needed at lower energies where the arms are furthest apart. The minimal subarray size is $y_{\rm sub} = 2 * y_{\rm bg} + 32 + 389/E$, where E is in keV, 32 pixels allow for dither, and $y_{\rm bg}$ is the size of a background region on either side of the spectrum. The background region might be of order 70 pixels (about 10 times the spectrum's extraction width). The SIM should be shifted to center the spectra in the subarray by SIM_Z $= 0.024 * (y_{\rm sub}/2 - 497 + 122\theta_z)$ mm, where 497 is the row of the ACIS-S aimpoint and θ_z is the telescope Z offset that places the target precisely on the optical axis. For $E = 1$ keV and $\theta_z = 0.25'$, then $y_{\rm sub} = 561$ rows and the SIM shift is -5.93 mm.

- Example of a set of parameters: It is instructive to examine the obscat entry for observation ID 9703 which shows observation parameters and values.
  (See
  http://cda.harvard.edu/chaser/startViewer.do?menuItem=details&obsid=9703.)
  The main target is a quasar. The AGN is mildly absorbed, so there is flux of interest down to the MEG limit, hence chip S0 (where the low energy flux will fall) is designated as "yes", while S5, which is redundant with S1 and S0, is designated as "optional". A subarray is used to eliminate pile-up. The SIM has been shifted in the Z direction to place the spectrum closer to the readout and to center the spectrum in the subarray. This will minimize the impacts of the row-dependent CTI on the FI-chips. Finally, a Y offset of 0.0 arcmin is used to keep the Fe-Kα region of the spectrum out of the S2-S3 chip gap in the HEG. The telescope Z offset is set to bring the zeroth order closer to the current optical axis.

- Use of continuous clocking (CC) mode: this mode can be applied in order to mitigate pileup in very bright sources. Most high resolution features will be unaffected. However, there are some calibration issues that have not yet been resolved:

  - The Si K edge can have a distorted shape and incorrect optical depth
  - A broad feature may appear at about 5.4 Å (2.3 keV)
  - There can be significant charge losses below 3 Å ($>$ 4 keV)
  - The spectrum may have the wrong shape above 10 Å ($<$ 1.2 keV)

  For further details, see ACIS section 6.20.4 and links therein.

8.5.2 Complications from Multiple Sources

Multiple sources in the field of view can also lead to effects which impact the observation.

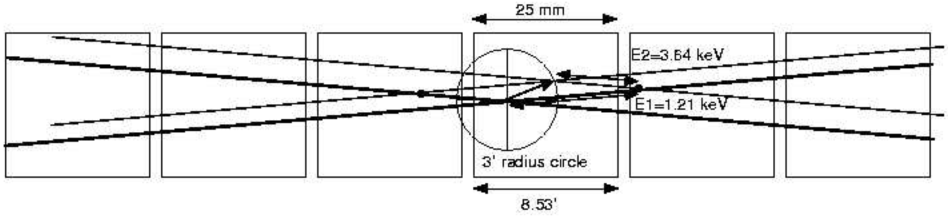

Figure 8.26: An idealized sketch of a ‘collision’ between two sources separated by 3 arcmin. At the ‘collision’ point, third-order photons from the on-axis source will have an energy 3x1.21=3.63 keV and ACIS can not distinguish these from the second source’s first order photons, at 3.64 keV.

Faint Background Sources

The position of a faint second source might be such that the zeroth-order image falls directly on the dispersion pattern from the prime target. In this case, the zeroth-order image of the second source appears as a line in the dispersed image of the prime target. The ACIS energy spectrum can be used to minimize the contribution to the measured dispersed spectrum of the target. Also, the lack of a feature in the other side of the dispersion pattern will indicate that the “line” is spurious.

Two Point Sources of Comparable Intensity

The dispersed MEG and HEG spectra of two sources will cross if the objects are fairly close. When the two targets are less than about $3'$ apart, both will be nearly in focus, so the spectra appear like two flattened “X”s. Normally, the ACIS-S pulse heights of the events will be significantly different in the regions of overlap, so that one may distinguish the events from two sources in data analysis. There are specific roll angles, however, where the identification of the source is ambiguous; a rare occurrence, but one the user should be aware of.

An example is shown in Figure 8.26, where the MEG spectrum of the brighter object (source 1) overlaps the HEG spectrum of the fainter target (source 2). The first order energies at the overlap positions are a factor of 3 apart, so that $E_2 = 3 \times E_1$. An ambiguity arises from 3rd order photons from source 1 at $3 * E_1$, which cannot be discriminated by ACIS from photons of about the same energy but from source 2. For a given angular distance between sources, it is possible to specify the observatory roll angle so that collisions like the one shown in the top of Figure 8.27 are avoided.

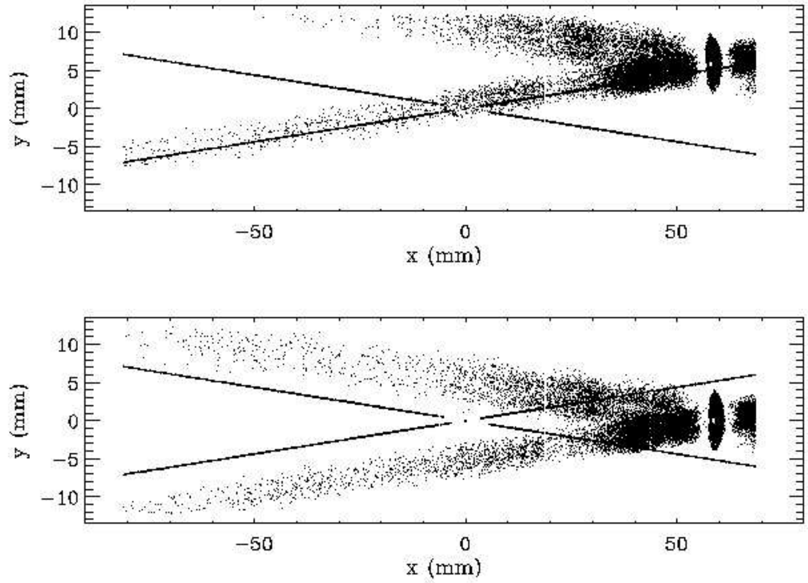

Figure 8.27: A simulation of spectral contamination caused by a second source in the field. The image of the dispersed spectrum from the second source is seen in the upper right hand corner for particular choice of roll angle. Note that the image is highly extended as the source is 20 arcmin off-axis. For this roll angle, there is significant overlap of the two images. In the lower panel we show the same situation, but for a different choice of roll angle. Here the overlap of the images is minimal and data analysis will be further aided through the use of energy discrimination provided by the ACIS-S detector.

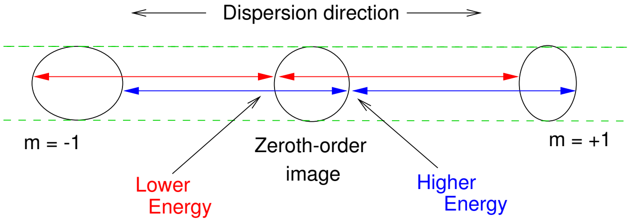

Figure 8.28: HETGS spatial-spectral effect example. In this schematic, a zeroth-order ring image emits at an energy which varies across the ring's diameter in the dispersion direction emitting lower-energy photons on the left and higher-energy photons on the right. The resulting diffracted images in ±1st orders have different appearances due to the spatial-spectral interaction. In the cross-dispersion direction, however, the images have the same extent.

A Strong Source Lying Outside the Field

The proposer should also take into consideration sources, other than the target, that are within the field of view of the telescope, but out of the field of view of the detector. Parts of the image of the dispersed spectrum may still fall onto the detector. If this presents a problem; a sensible choice of a range of allowable roll angles might ameliorate the situation.

8.5.3 Extended Sources and Spatial-Spectral Effects

The case of a simply extended, spectrally homogeneous source was described in Section 8.2.2, under the heading, "Extended and off-axis targets". Here more complex cases are briefly considered; generally these must be treated on a case-by-case basis.

For extended sources with multiple condensations, careful selection of the roll angle (see e.g. Section 8.5.2) might make the data easier to analyze and interpret. It may also be possible to model the spectrum given information from the zero order image and/or a short ACIS exposure with the grating retracted. The ACIS spectrum can then be used as an initial guess in modeling the dispersed HEG and MEG spectra.

The diffracted images of extended objects which lead to position-dependent spectra are complicated. The complexity indicates that information is present but extracting the information is more difficult than for a point or an extended source with a uniform spectrum. For example, the plus and minus order images may not have the same appearance. An example of this effect was seen in ground test data using the double crystal monochromator source; e.g., test image H-HAS-EA-8.003 which is schematically presented and described in Figure 8.28. For astrophysical sources, variations in temperature, abundances, Doppler velocities, cooling flows, etc. can all create spatial-spectral variations. For these complex objects general analysis techniques are not available and forward folding of the spatial-spectral model through *MARX* is the best way to study these effects and to plan potential observations.

8.5.4 Optimizing Detection of Isolated Emission Lines: Choice of Spectrometer

If the scientific objectives require detecting emission lines against a moderately bright source continuum, then the signal/noise ratio depends on the effective area of the instrument in combination with the spectrometer resolving power. Here, we compute the relative merits of each *Chandra* spectrometer in this context. Three cases where this analysis will not apply are when: (1) detecting weak lines that may blend with stronger lines, (2) observing significantly extended sources, and (3) observing lines that are substantially broadened. In case 1, the highest resolving power at the energy of interest would be indicated. Case 2 will require that the reduction of the grating resolution for extended sources, discussed in Section 8.2.2, be included.

When a line is isolated and appears against a "background" due primarily to the source continuum, then the signal/noise ratio is given by:

$$\frac{C_L}{\sigma_C} = \frac{A_E T W n_E}{[A_E T (dE)_E n_E]^{1/2}} \tag{8.1}$$

where C_L is the number of counts in the emission line, σ_C gives the uncertainty in this number, A_E is the instrumental effective area, T is the integration time, n_E is the photon flux in the continuum in units of photon cm^{-2} s^{-1} keV^{-1}, W is the equivalent width of the line in keV, and $(dE)_E$ is the spectral resolution of the spectrometer in keV. The signal-to-noise ratio per fractional equivalent width, $W_f = W/E$, is then:

$$\frac{C_L/\sigma_C}{W_f} = (T n_E E)^{1/2} [\frac{A_E\ E}{(dE)_E}]^{1/2} \tag{8.2}$$

This last instrument-specific term is the figure of merit for the spectrometers:

$$F_E \equiv [A_E\ (E/dE)_E]^{1/2} \tag{8.3}$$

which can be compared for different instruments at the desired energy. Of course, all these considerations are tempered by the additional features of each instrument setup. For example, this calculation does not take into account instrumental background effects nor the additional continuum that may result from higher energy flux detected in higher orders when the LETG is used with the HRC-S. The reduction of the line detectability then depends on the source spectrum.

8.6 Simulations with *MARX*

For sources with spatial or spectral complexity, observation planning is best carried out using the *MARX* simulator to create a simulated data set. These data can then be analyzed with the same tools as flight data in order to demonstrate the feasibility of extracting useful results from a proposed observation.

MARX is a suite of programs designed to simulate the on-orbit performance of *Chandra*. It is built around a core program or engine which performs a ray trace of photon paths through all elements of the *Chandra* observatory. The user specifies a file containing the spectral energy distribution of the source to be simulated and then selects a model for the spatial distribution of the source, which can be a FITS image. More complicated "user source models" allow simulation of sources with spatial-spectral variations.

Once the source has been specified, *MARX* traces the path of photons through a model of the HRMA. Models for the High Energy Transmission Grating (HETG) and Low Energy Transmission Grating (LETG) can also be included and, in the focal plane, the user has the choice of all four *Chandra* detectors. The result of the simulation is converted with `marx2fits` into a FITS event file which can then be processed with standard CIAO tools.

The latest capabilities and instructions for use of *MARX* are given in the *MARX* User Guide at the *MARX* web site, http://space.mit.edu/CXC/MARX/ and in analysis threads available at http://cxc.harvard.edu/ciao/threads/index.html.

8.7 REFERENCES

WWW resources:

http://cxc.harvard.edu/cal/- *CXC* Instruments and Calibration page
http://cxc.harvard.edu/caldb/ - *CXC* CALDB page
http://space.mit.edu/HETG/- HETG home page
http://space.mit.edu/CXC/ - *CXC* at MIT, focusses on gratings
http://wwwastro.msfc.nasa.gov/xray/xraycal/ - MSFC ground cal site

Canizares, C.R., Schattenburg, M.L. and Smith, Henry I. 1985, "The High Energy Transmission Grating Spectrometer for AXAF", SPIE, **597**, 253.

Canizares, C.R. *et al.* 2000, "Initial Results from the Chandra High Energy Transmission Grating Spectrometer", Atomic Data Needs for X-ray Astronomy, M.A. Bautista, T.R. Kallman, and A.K. Pradhan, eds. http://heasarc.gsfc.nasa.gov/docs/heasarc/atomic/

Canizares, C.R. *et al.* 2000, ApJ, **539**, L41.

Canizares, C.R. *et al.* 2005, PASP, **117**, 1144.

Davis, J.E., H.L. Marshall, M.L. Schattenburg, and D. Dewey, 1998, "Analysis and Modeling of Anomalous Scattering in the AXAF HETGS", SPIE, **3444**, 76.

Dewey, D., Drake, J.J., Edgar, R.J., Michaud, K., and Ratzlaff, P., 1998, "AXAF Grating Efficiency Measurements with Calibrated, Non-imaging Detectors", SPIE, **3444**, 48.

Dewey, D., Humphries, D. N., McLean, G. Y., and Moschella, D. A. 1994, "Laboratory Calibration of X-Ray Transmission Diffraction Gratings", SPIE, **2280**, 257.

Edgar, R.J., 2003, Chandra X-ray Center memo dated 6/9/2003, http://cxc.harvard.edu/cal/Acis/Cal_prods/qe/ACIS_QE_O_S23.ps.

Edgar, R.J., & Vikhlinin, A.A., 2004, Chandra X-ray Center memo dated 8/11/2004, http://cxc.harvard.edu/cal/Acis/Cal_prods/qe/qe_memo.ps.

Flanagan, K. A., Dewey, D. and Bordzol, L. 1995, "Calibration and Characterization of HETG Grating Elements at the MIT X-ray Grating Evaluation Facility", SPIE, **2518**, 438.

Flanagan, K.A., et al., 2000, "Modeling the Chandra High Energy Transmission Gratings below 2 keV" SPIE, **4140**, 559.

Markert, T.H., Canizares, C.R., Dewey, D., McGuirk, M., Pak, C., and Schattenburg, M.L. 1994, "The High Energy Transmission Grating for AXAF", SPIE, **2280**, 168.

Markert, T. H. et al., 1995, "Modeling the Diffraction Efficiencies of the AXAF High Energy Transmission Gratings", **SPIE**, **2518**, 424

Marshall, H.L. et al. 1997, "Towards the Calibration of the HETGS Line Response Function", SPIE, **3113**, 160.

Marshall, H.L., Dewey, D., Schulz, N.S., and Flanagan, K.A., 1998, "Spectral Features in the AXAF HETGS Effective Area using High-signal Continuum Tests", SPIE, Vol. **3444**, 64.

Marshall, H.L., D. Dewey, and K. Ishibashi, 2004, "In-Flight Calibration of the *Chandra* High Energy Transmission Grating Spectrometer", Proc. SPIE, Vol. **5165**, 457.

Marshall, H.L., Tennant, A., Grant, C., Hitchcock, A.P., O'Dell, S., and Plucinsky, P.P., 2004, "Composition of the ACIS Contaminant", SPIE, **5165**, 497.

Marshall, H.L., 2005, Chandra X-ray Center memo dated 10/14/2005, http://space.mit.edu/ASC/calib/heg_meg/meg_heg_report.pdf.

Marshall, H.L., 2012, "Updating the Chandra HETGS Efficiencies using In-Orbit Observations", SPIE, **8443**, in press, http://arxiv.org/abs/1211.0017.

Schattenburg, M.L. et al. 1991, "Transmission Grating Spectroscopy and the Advanced X-ray Astrophysics Facility", Optical Engineering, **30**, 1590.

Schattenburg, M.L., Ancoin, R.J., Flemming, R.C., Plotnik, I., Porter, J., and Smith, H.I. 1994, "Fabrication of High Energy Transmission Gratings for AXAF", SPIE, **2280**, 181.

Schulz, N.S., Dewey, D., Marshall, H.L. 1998 "Absolute Effective Areas of HETG", SPIE, **3444**, 160.

Smith, M.J.S., & Marshall, H.L., 2012, "XMM-Newton – Chandra Blazar Flux Comparison", presented at the 7th IACHEC meeting http://web.mit.edu/iachec/meetings/2012/Presentations/Smith.pdf.

Weisskopf, M.C. et al. 2004, "An Overview of the Performance of the Chandra X-Ray Observatory", Experimental Astronomy, Vol. **16**, no. 1, 1.

"X-ray Spectroscopy in Astrophysics", 1999, Springer-Verlag, ed. van Paradijs, J., & Bleeker,

Chapter 9

LETG: Low Energy Transmission Grating

9.1 Instrument Description

The Low Energy Transmission Grating (LETG) was developed under the direction of Dr. A.C. Brinkman in the Laboratory for Space Research (SRON) in Utrecht, the Netherlands, in collaboration with the MPE für Extraterrestrische Physik (MPE) in Garching, Germany. The grating was manufactured in collaboration with Heidenhaim GmbH.

The Low Energy Transmission Grating Spectrometer (LETGS) comprises the LETG, a focal plane imaging detector, and the High Resolution Mirror Assembly discussed in Chapter 4. The *Chandra* High Resolution Camera spectroscopic array (HRC-S) is the primary detector designed for use with the LETG. The spectroscopic array of the *Chandra* CCD Imaging Spectrometer (ACIS-S) can also be used, though with lower quantum efficiency below ~0.6 keV and a smaller detectable wavelength range than with the HRC-S. The High Energy Transmission Grating (HETG) used in combination with ACIS-S offers superior energy resolution and quantum efficiency above 0.78 keV. The HRC is discussed in Chapter 7, the ACIS in Chapter 6, and the HETG in Chapter 8.

The LETGS provides high-resolution spectroscopy ($\lambda/\Delta\lambda > 1000$) between 80 and 175 Å (0.07–0.15 keV) and moderate resolving power at shorter wavelengths. The nominal LETGS wavelength range accessible with the HRC-S is 1.2–175 Å (0.07–10 keV); useful ACIS-S coverage is 1.2 to roughly 60 Å ($\sim$ 0.20–10 keV).

A summary of LETGS characteristics is given in Table 9.1.

9.1.1 Scientific Objectives

The LETGS provides the highest spectral resolving power (> 1000) on *Chandra* at low (0.07–0.2 keV) energies. High-resolution X-ray spectra of optically thin plasmas with temperatures between 10^5 and 10^7 K, such as stellar coronae, reveal a wealth of emission lines that provide diagnostics of temperature, density, velocity, ionization state, and elemental

Table 9.1: LETGS Parameters

Wavelength range	1.2–175 Å (HRC-S)
	1.2–60 Å (ACIS-S)
Energy range	70–10000 eV (HRC-S)
	200–10000 eV (ACIS-S)
Resolution ($\Delta\lambda$, FWHM)	0.05 Å
Resolving Power ($\lambda/\Delta\lambda$)	$\geq$ 1000 (50–160 Å)
	$\approx 20 \times \lambda$ (3-50 Å)
Dispersion	1.148 Å/mm
Plate scale	48.80 μm/arcsecond
Effective area (1st order)	1–25 cm^2 (with HRC-S)
	4–200 cm^2 (with ACIS-S)
Background (quiescent)	Typically 10 (25) cts/0.07-Å/100-ksec @ 50 (175) Å (with HRC-S after filtering)
	$\ll$ 0.01 cts/pixel/100-ksec (with ACIS-S, order sorted)
Detector angular size	3.37' × 101' (HRC-S)
	8.3' × 50.6' (ACIS-S)
Pixel size	6.43 × 6.43 μm (HRC-S)
	24.0 × 24.0 μm (ACIS-S)
Temporal resolution	16 μsec (HRC-S in Imaging Mode, center segment only)
	$\sim$10 msec (HRC-S in default mode)
	2.85 msec–3.24 sec (ACIS-S, depending on mode)
Rowland diameter	8637 mm (effective value)
Grating material	gold
Facet frame material	stainless steel
Module material	aluminum
LETG grating parameters	
Period	0.991216 ±0.000087 μm
Thickness	0.474 ±0.0305 μm
Width (at bar middle)	0.516 ±0.0188 μm
Bar Shape	symmetric trapezoid
Bar Side Slope	83.8 ±2.27 degrees
Fine-support structure	
Period	25.4 μm
Thickness	2.5 μm
Obscuration	< 10%
Dispersion	29.4 Å/mm
Material	gold
Coarse-support structure	
Triangular height	2000 μm
Width	68 μm
Thickness	< 30 μm
Obscuration	< 10%
Dispersion	2320 Å/mm
Material	gold

abundances and allow precise studies of structure, energy balance, and heating rates. Absorption features provides similar information in cases where bright compact X-ray sources are embedded in cooler, extended gas clouds.

The high resolution ($\Delta\lambda \approx 0.05$ Å) of LETGS spectra at longer wavelengths ($\gtrsim 100$ Å) also permits detailed studies of spectral line *profiles* in the X-ray region. These studies may provide non-thermal velocities of stellar coronae, flow velocities along active-region loops, orbital velocities in X-ray binaries, and upflow velocities in stellar flares. The LETGS also allows time resolved spectroscopy, 1-D spatially resolved spectra, and spectra of multiple point sources within its ∼4 arcmin field of best focus.

Since the ultimate spectral resolution can only be achieved for point sources, the prime candidates for study in our Galaxy mainly comprise stellar coronae, white dwarf atmospheres, X-ray binaries, and cataclysmic variables. Extragalactic sources include relatively bright active galactic nuclei (AGN) and cooling flows in clusters of galaxies.

9.1.2 Heritage

Flat transmission gratings were flown aboard *Einstein* and *EXOSAT*. The LETG grating elements are produced using a technique similar to that used for production of the *EXOSAT* gratings. However, the LETG shares only basic operating principles with earlier instruments. Advanced grating technology has enabled the achievement of greater efficiency and increased dispersion. The Rowland geometry (see Figure 8.4) of the grating plate and spectroscopic arrays reduces dispersed image aberrations and hence contributes to improved spectral resolution.

9.1.3 Operating principles

When inserted behind the HRMA, the LETG diffracts X-rays into a dispersed spectrum according to the grating diffraction relation, $m\lambda = p \sin\theta$, where m is the integer order number, λ the photon wavelength, p the spatial period of the grating lines, and θ the dispersion angle. Parameters are summarized in Table 9.1. The grating facets are mounted on an aluminum support plate which has been machined so that the centers of individual grating facets lie on a Rowland torus. The grating facets are aligned to produce a single dispersed image. Spectral resolution is determined, among other factors, by grating line density, line density variations, HRMA point-spread function, pointing stability, alignment accuracy, pixel size of the readout detector, and detector geometry.

9.1.4 Physical configuration

When the LETG is used, the Grating Element Support Structure (GESS), an aluminum frame approximately 110 cm in diameter and 6 cm thick, is inserted ∼300 mm behind the exit aperture of the HRMA and 1.4 m behind the HRMA mid-plane. The GESS holds approximately 180 trapezoidal grating modules, which measure about 13 × 50 mm. A design drawing of the full GESS is shown in Figure 9.1; a closer view, showing some

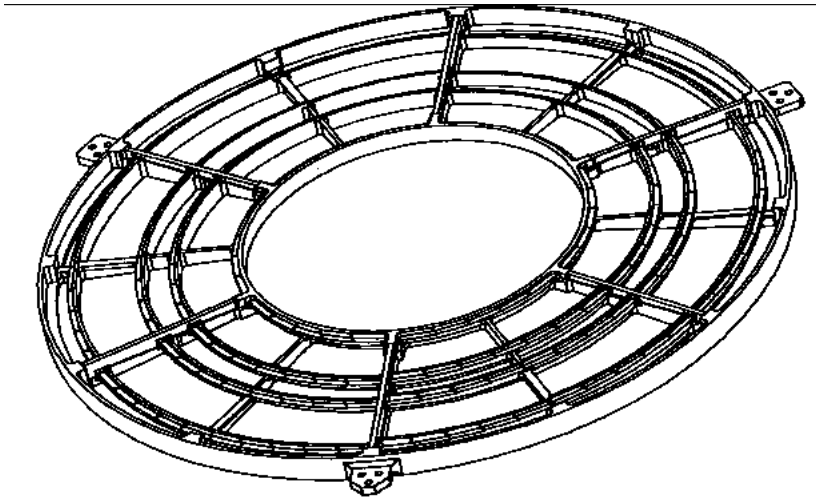

Figure 9.1: LETG Grating Element Support Structure, a machined aluminum plate approximately 110 cm in diameter that holds grating modules on a Rowland torus behind the *Chandra* mirrors.

mounted modules, is seen in Figure 9.2. Figure 9.3 shows empty grating modules mounted on the GESS. Each grating module holds three circular grating facets, each of which comprises approximately 80 of the triangular grating elements seen in Figure 9.4.

In contrast to the HETG gratings, which have a thin polyimide substrate, the LETG gratings are free-standing wires held by a support mesh. Within each grating facet the grating bars are supported by perpendicular "fine support" bars and triangular "coarse support" bars. The parameters of these structures are given in Table 9.1. A schematic of the grating structure is shown in Figure 9.4. Both the fine and coarse grating supports act as long-period transmission gratings themselves. The fine support produces a dispersion pattern perpendicular to the grating dispersion direction and the coarse support produces a six-pointed star pattern. These are discussed in more detail in Section 9.4 (see Figures 9.23 and 9.27, respectively).

Since the gratings are produced from a single master mask, there is negligible variation in the period between facets. The thickness of the gold of the grating bars on top of the support mesh determines the "phasing," or efficiency of redistribution of photons into each spectral order in wavelengths where the gold is partially transparent. The thickness is designed to optimize the 1st order response at energies of interest.

To reduce aberrations, the GESS is shaped to follow the Rowland torus. The basics of the Rowland geometry are shown in Figure 8.4. The primary readout detector (HRC-S) is made of three tilted array segments which also follow the Rowland circle in the image plane (see Figures 7.2 and 9.5). Because the detector array elements are flat, the distance from the Rowland circle changes with position, and so the spectral resolution changes very slightly with wavelength. The secondary readout detector, ACIS-S, has 6 CCDs, each of

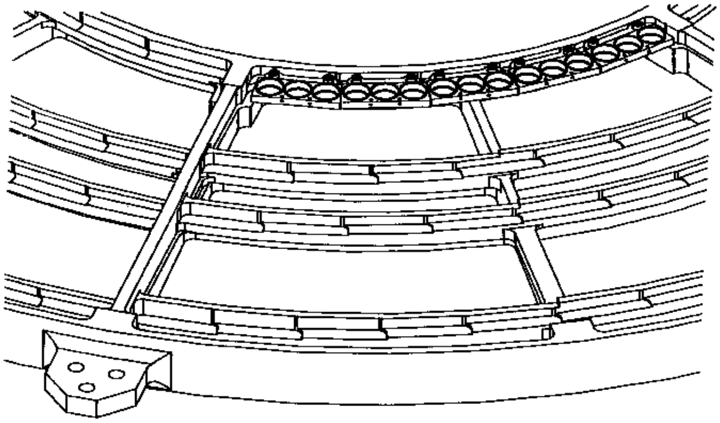

Figure 9.2: Detail of the LETG Grating Element Support Structure showing grating modules mounted on the inner annulus.

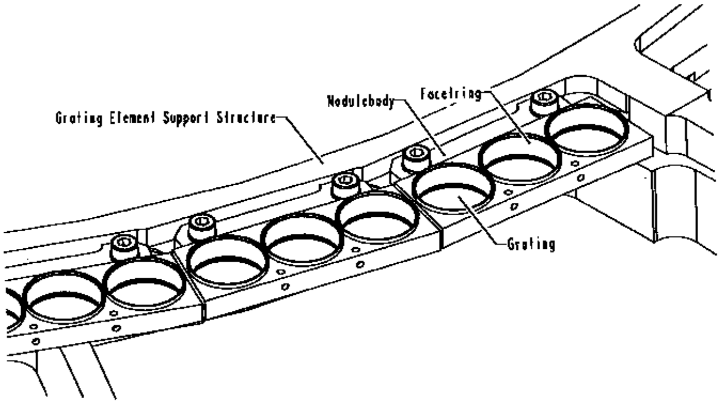

Figure 9.3: A closeup view of the LETG GESS showing nearly three complete grating modules. Each module holds three circular grating facets, and each facet contains approximately 80 triangular grating elements.

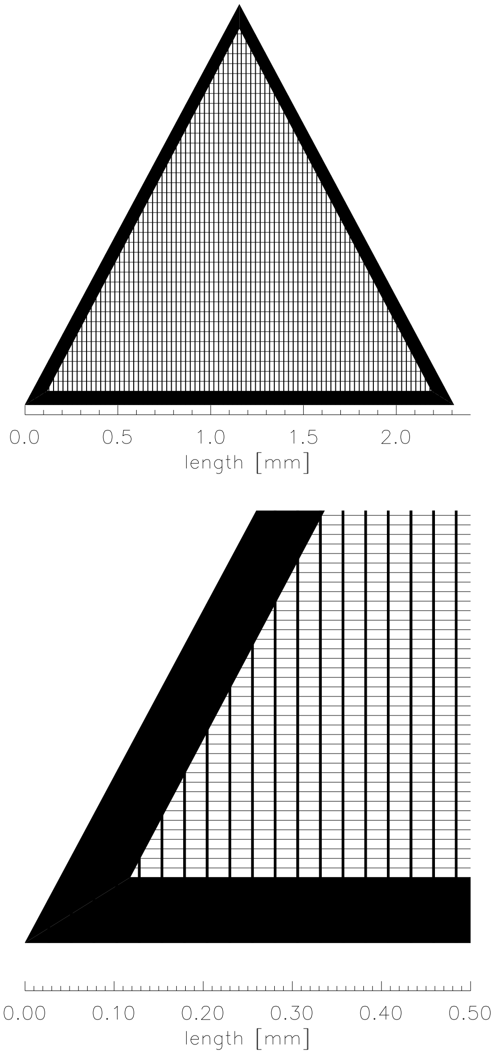

Figure 9.4: LETG facet structure schematic showing the basic shape of the individual grating elements and the relative sizes of the support structures. The upper view shows the complete grating element, which comprises the triangular coarse support, the vertical fine supporting bars, and the (horizontal) grating bars. The grating bars themselves are not shown to scale. In the upper view every 50th grating bar is drawn, in the lower view every 10th bar.

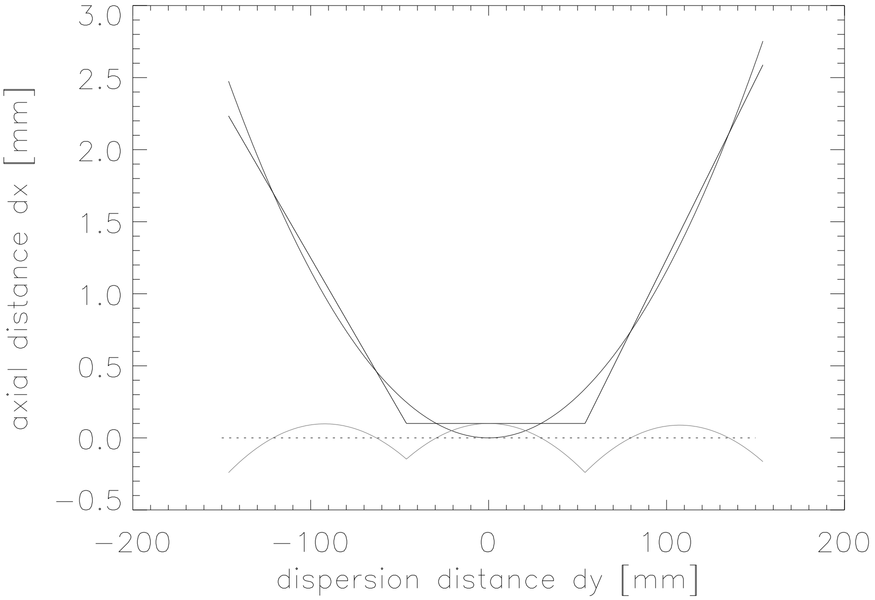

Figure 9.5: The front surfaces of the HRC-S detector segments and their relationship to the Rowland circle are shown schematically. The scalloped line beneath them is the difference between the detector surface and the Rowland circle.

which is only one-quarter as long as an HRC-S segment, so the ACIS-S array follows the Rowland circle even more closely.

9.2 Calibration

9.2.1 Pre-launch Calibration

Prior to assembly, individual grating elements were tested using a visual light spectrograph at the MPE. Laboratory calibration of grating period and resolution was performed for individual grating elements at optical wavelengths, and extrapolated to the X-ray range. Grating efficiencies at X-ray wavelengths were modeled using near-infrared spectrophotometry, and verified by X-ray measurements of a sample of facets. Grating facet and module alignment was also tested. LETGS efficiency, resolution, and line response function were tested at the X-ray Calibration Facility at MSFC in Huntsville, AL for both ACIS-S and HRC-S configurations. Absolute energy scale and off-axis response were also measured. Efficiency and the Line Spread Function (LSF) of the LETG and HRMA/LETG subsystem were characterized using a detector system designed for HRMA calibration, the HRMA X-ray Detection System (HXDS). Details may be found in the XRCF Final Report

Table 9.2: Routine LETGS Calibration Monitoring Observations

Target	Freq. (yr^{-1})	Purpose
Capella	1	LETG/HRC-S LRF, dispersion relation, QE, EA
PKS 2155-304	1	LETG/ACIS-S EA, ACIS-S contam, cross calib with *XMM*, *Suzaku*
Mkn 421	1	LETG/ACIS-S and LETG/HRC-S EA, ACIS-S contam, HRC-S gain
RX J1856-3754	1	LETG/ACIS-S EA and ACIS-S contam
HZ 43	1	LETG/HRC-S EA and HRC-S gain

at http://cxc.harvard.edu/cal/Hrma/XRCFReport.html.

9.2.2 In Flight Calibration

In-flight calibration of the LETGS, along with its primary detector, the HRC-S, is planned and executed by the *CXC* LETG team. LETG first-light and focus observations were of the active late-type binary Capella whose coronal spectrum is rich in narrow spectral lines (see Figure 9.26). Spectra of Capella, the late-type star Procyon (F5 IV), and serendipitous Guest Observer targets have been used in calibration of the LETG dispersion relation, resolving power, line response function, and grating-detector alignment.

Calibration of the LETGS effective area (EA) and HRC-S quantum efficiency (QE) at energies above the C-K edge (0.28 keV, 44 Å) relies primarily on observations of the quasar continuum source PKS 2155-304 and (earlier in the mission) 3C 273 and Capella. PKS 2155-304 also has been regularly observed with LETG/ACIS-S to monitor contamination buildup on ACIS (see Section 6.5.1) and for cross calibration with other X-ray missions. Mkn 421 largely replaced PKS 2155-304 as an ACIS contamination monitoring source starting in 2010, and RX J1856 (neutron star continuum source) was recently added for the same purpose. For calibration of the LETG/HRC-S EA at longer wavelengths, observations of the hot DA white dwarfs HZ 43 and Sirius B are used.

Early in the mission, most calibration targets were observed at least twice per year to monitor LETGS operation, but calibration observations are now less frequent. Regularly observed sources and monitoring frequencies are listed in Table 9.2. Other targets are occasionally observed to meet specific calibration needs that might arise, and ACIS-S and HRC-S (see Table 7.3) are routinely calibrated by themselves (i.e., without gratings).

9.3 LETGS Performance

9.3.1 Usage

Overview

The primary use of the LETG is for on-axis observations of point sources, which produce a zero-order image and a dispersed spectrum. Typical LETGS observations range from a few tens to several hundred ksec. To reduce the (small) risk that the grating mechanism might fail, its frequency of use is minimized by grouping grating observations into consecutive time blocks whenever possible.

The net LETG transmission is ∼28% at energies below ∼1 keV (about 12.5% for zeroth order, the same for 1st order, and a few percent for all other orders) so counting rates are usually not a concern with respect to exceeding detector limits or telemetry saturation. However, some bright sources (e.g. Sco X-1) if observed for long exposure times could cause significant charge depletion in the HRC MCPs (see Chapter 7, especially Section 7.13), and even moderate rates may cause pileup problems when using ACIS-S (see Sections 6.15 and 9.4.1). Some observers may find it useful to insert the LETG for imaging observations simply to reduce the detected photon counting rate.

Detectors

In standard operation, the LETGS uses either the HRC-S or ACIS-S as its detector. The LETG+HRC-S covers a wavelength range of approximately -165 to $+175$ Å in 1st order for on-axis sources. This wavelength range can be shifted somewhat by offset pointing, but image quality degrades substantially beyond about $2'$. The HRC-S does not have sufficient energy resolution to allow sorting of overlapping spectral orders.

In rare cases it might be useful to use the HRC-S Low Energy Suppression Filter (LESF), as discussed in Section 9.4, in order to obtain a predominantly higher-order ($m > 1$) spectrum. The LESF is a region on the HRC-S UV/Ion Shield (UVIS) where the aluminum coating is relatively thick, and corresponds to the upper part of the “T” in Figure 7.1. Note that the Al coating on the LESF is thicker on the outer plates than on the central plate. See Figures 9.17 and 9.19 for the effect of the LESF on 1st and higher order effective areas.

When used with the ACIS-S detector, the effective LETGS wavelength coverage is reduced because of the smaller detector size in the dispersion direction (ACIS-S is only half as long as the HRC-S) and the fact that the two outermost chips (S0 and S5) have essentially zero QE for detecting 1st order LETG photons (see Figure 9.6). Another consideration is that ACIS has lower temporal resolution than HRC, which may be important when observing periodic or rapidly varying sources. In some cases, however, those disadvantages may be outweighed by the lower effective background rate and intrinsic energy resolution of ACIS, which can be used to separate diffraction orders. Note that the CTI-degraded energy resolution of the ACIS FI CCDs (Section 6.7) does not pose a problem for LETG point-source observations, since the source can be placed close to the ACIS readout, where the energy resolution is best.

In some special cases, the HRC-I may also be used with the LETG. A detailed discussion of the various merits of LETGS detector choices from a point of view of proposal planning is given in Section 9.4.

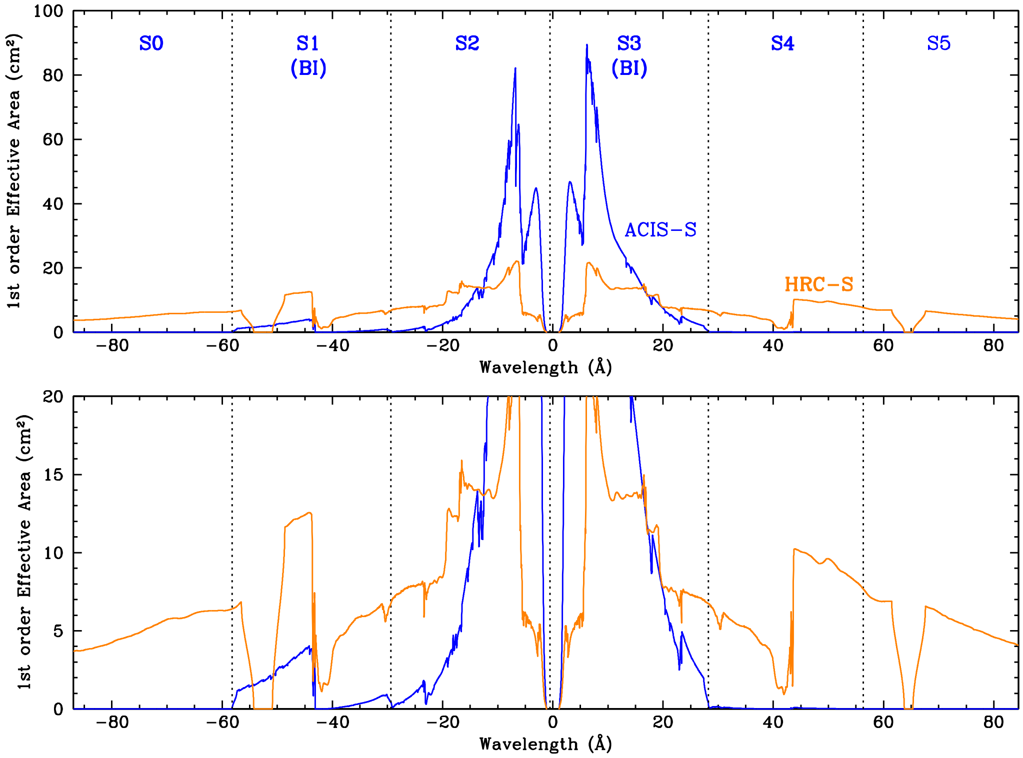

Figure 9.6: LETGS 1st order effective area (EA) with ACIS-S and HRC-S, showing plus and minus orders separately; lower panel shows low-EA regions in more detail. The effects of dither and ACIS bad columns are explicitly included. Dotted lines mark ACIS chip boundaries, and HRC plate gaps appear near −53 and +65 Å. ACIS curve is for Y-offset=+1.5′ and HRC curve is for Y-offset=0’. EAs are taken from mid-2012; the LETG+ACIS EA is very slowly decreasing over time because of increasing contamination. Note its abrupt decline beyond ∼28 Å as longer wavelengths fall on the FI S4 chip, whereas the BI S1 chip provides useful EA well beyond 50 Å. Y-offsets may be chosen to tailor the coverage of BI chips (S1 and S3), which have significantly higher QE at low energies than the FI chips. See Section 9.4.2/Offset Pointing for more information regarding the choice of Y-offset. See also Figure 9.17 which plots effective areas for combined plus and minus orders.

Off-Axis and Multiple Sources

Because the LETGS is essentially an objective-grating system, it is possible to do multi-object spectroscopy, although as noted above, the point-spread function degrades rapidly off-axis. To include or reject secondary sources, or to avoid overlapping diffraction from multiple sources, observers may specify the orientation (roll angle) of the grating dispersion direction on the sky (see Chapter 3). Observations of extended sources are also possible, but at the expense of resolving power and with the loss of the simple relation between position and energy. In angular extent, the standard HRC-S spectroscopy readout region is $3.37'$ x $101'$, and the full ACIS-S array covers $8.3' \times 50.6'$. In special cases, a different HRC-S detector "window" (up to twice as wide in cross-dispersion) may be selected, as described in Section 9.4.

9.3.2 Wavelength Coverage and Dispersion Relation

The active extent of the HRC-S in the dispersion direction is 296 mm, almost exactly twice that for the ACIS-S. The nominal zeroth-order aimpoints for each detector are slightly offset from the detector center so that gaps between the three HRC-S segments (six ACIS-S segments) will occur at different wavelengths in negative and positive orders. A Y-axis offset (along the dispersion axis) of $+1.5'$ is usually used with LETG+ACIS-S observations to shift coverage of longer wavelengths onto the backside-illuminated S1 and S3 chips, which have higher QE at low energies than the other ACIS-S chips.

With a dispersion of 1.148 Å/mm for the LETG, the standard wavelength range of the LETGS with HRC-S is -164 Å to $+176$ Å. Physical coverage with ACIS-S extends from -87 to $+84$ Å when using Y-offset=$+1.5'$, but the poor low-E response of the outlying front-illuminated chips limits the effective wavelength range to -60 Å for negative 1st order and less than about $+30$ Å for the positive order (see Figure 9.6). Outlying chips may be useful, however, for collecting higher-order spectra.

Off-Axis Pointing and Detector Gaps

Wavelength coverage can be adjusted (increasing the wavelength range on one side and decreasing on the other) by changing the central offset (the observatory Y coordinate—see the discussion in Chapter 3) although spectral resolution degrades rather quickly beyond about $4'$ from the optical axis. From the information in Table 9.1, one can derive the relationship between angular offset (in the dispersion direction) and wavelength as 3.36 Å per arcminute, so an offset of $10'$ would stretch the positive order HRC-S coverage to approximately 210 Å (60 eV). While the vast majority of LETG observations have been made with offsets of less than $2'$, flight LETG calibration data have been collected at $5'$ off-axis (for resolution testing) and $10'$ off-axis (for effective area calibration).

As noted in Section 9.3.2, there are gaps between detector segments which create corresponding gaps in the wavelength coverage of each order. The gaps in + and − orders do not overlap so that the combined wavelength coverage is continuous. The location of the

Detector	Section	Energy (eV)	Wavelength (Å)
HRC-S	UVIS Inner T (thick Al)	(690) – 690	(18) – 18
HRC-S	seg-1 (neg. $m\lambda$)	(75) – (220)	(164) – (56)
HRC-S	seg0	(240) – 200	(51) – 62
HRC-S	seg+1 (pos. $m\lambda$)	185 – 70	67 – 176
ACIS-S	S0 (neg. $m\lambda$)	(142) – (210)	(87.1) – (58.9)
ACIS-S	S1 (Back-illuminated)	(212) – (410)	(58.5) – (30.2)
ACIS-S	S2	(417) – (7700)	(29.7) – (1.6)
ACIS-S	S3 (Back-illuminated)	(11000) – 459	(1.1) – 27.0
ACIS-S	S4	451 – 223	27.5 – 55.7
ACIS-S	S5 (pos. $m\lambda$)	221 – 147	56.2 – 84.3

Table 9.3: LETG Position-Dependent Spectral Coverage (1st Order). Energies and wavelengths for the negative order are given in parentheses. Listed values are for the most commonly used pointing (on-axis for HRC-S and Y-offset = +1.5′ for ACIS-S) without dither. Standard dithering affects 1.1 Å on the edge of each HRC-S segment and 0.45 Å on the edge of each ACIS chip. Typical uncertainties are of order 0.3 Å and arise from aimpoint drifts and target acquisition errors. Energies and wavelengths for the negative order are listed in parentheses. Note that the QE for FI ACIS chips is much lower than for BI chips at low energies, rendering S0, S4, and S5 of limited use (see Figure 9.6). Please see http://cxc.harvard.edu/cal/Letg/ACIS_params for up-to-date and detailed information regarding offset pointing and wavelength ranges.

gaps (neglecting the effects of dither) are listed in Table 9.3, which also lists the location of the HRC-S UV/Ion Shield inner "T" filter edge. Dithering the spacecraft will partially smooth these gaps, but observers may wish to adjust the source pointing if a favorite line falls in a gap, or to tune the wavelength coverage of the higher-QE back-illuminated (S1 and S3) ACIS-S chips. Standard HRC dither amplitude (full width, in both directions) is 40″ (1.95 mm), which covers 2.3 Å, and standard ACIS dither is 16″ (0.78 mm), or 0.9 Å.

Please see the "Checking your LETG/ACIS Obscat Setup" web page at http://cxc.harvard.edu/cal/Letg/ACIS_params. An interactive tool for visualizing spectral feature placement on the ACIS array as a function of Y-offset and source redshift is available there.

Dispersion Calibration

Overall wavelength calibration is accurate to a few parts in 10000 across the full wavelength range of the instrument, and the Rowland diameter has remained stable since launch. The RMS deviation between observed and predicted wavelengths for a set of relatively unblended lines observed in Capella spectra amounts to 0.013 Å, after correction for the relative spacecraft and Capella radial velocity differences. Through analysis of accumulated calibration and GO observations, some remaining differences between predicted and observed line wavelengths have been found to be caused by small event position errors at some locations on the HRC-S detector.

Position errors occur in both dispersion and cross-dispersion axes, though for spectroscopy the latter are usually not important because data are generally summed in the cross-dispersion direction. The magnitude of position errors in the dispersion axis for the central HRC-S plate range from 0 to ~ 0.05 Å, with typical errors of ~ 0.01–0.02 Å. The outer plates (> 60 Å) tend to exhibit larger errors of typically ~ 0.02–0.08 Å. The size of the position errors changes over spatial scales of the HRC readout taps, which are 1.646 mm apart (see Chapter 7 for details of the HRC). Spacecraft dither moves dispersed monochromatic photons of a given order over a region of the detector that is roughly 2mm square. Within any given dither region, then, monochromatic light will fall on detector regions that have different position determination errors. As a result, a narrow spectral line could suffer some distortion of its line profile and/or a small shift of its apparent wavelength. Such distortions or shifts could occur at the spacecraft dither frequency (see Chapter 5); observers should therefore exercise caution in interpretation of such periodic effects. Care should also be taken when interpreting the results of combined spectra from $+$ and $-$ orders, since these effects are not symmetrical about zeroth order.

The position errors appear to be stable *in detector coordinates* and to repeat in different observations for which the aim points are very similar. An empirical correction for the effect based on accumulated calibration and GO observations has been derived and is implemented in CALDB 3.2.0 as part of the HRC-S degap map. Details on the derivation of the wavelength corrections can be found on the "Corrections to the Dispersion Relation" page at http://cxc.harvard.edu/cal/Letg/Corrlam. After correction, the RMS deviation between observed and predicted wavelengths lines observed in Capella are reduced from 0.013 to 0.010 Å across the entire wavelength range of the instrument. Corrections for the outer plates (> 60 Å) are much less effective owing to a lack of reference lines with adequate signal-to-noise ratio. For the central plate alone, the RMS deviation amounts to 0.006 Å.

For the purposes of observation planning, it should be assumed that individual observed line wavelengths could be in error by up to about 0.02 Å for $\lambda < 60$ Å, and 0.05 Å for $\lambda > 60$ Å. Despite the observed repetition in pattern from observation to observation, observers are reminded that the exact wavelength error for any given line depends on the exact position of the target on the detector. Small differences in actual aim point that occur naturally between observations as a result of uncertainties in aspect and target acquisition (see Chapter 5) mean that wavelength shifts for a specific line are not generally repeatable from one observation to another and might also be subject to small secular trends.

9.3.3 Resolving Power

The dominant contribution to the LETGS line response function (LRF) and instrument resolving power is the HRMA point-spread function (PSF), which is ~ 25 μm FWHM, depending on energy. The next most important factor is the detector PSF, which is

$\sim 20\ \mu$m FWHM for the HRC-S, with 6.43-μm-wide pixels; ACIS pixels are 24 μm wide. Uncertainties in correcting photon event positions for the observatory aspect, which occurs during ground data processing, adds a small contribution of order a few μm. Finally, the small errors in event position determination resulting from HRC-S imaging non-linearities described in Section 9.3.2 can lead to some distortion of spectral line profiles. These effects are difficult to quantify in detail but are estimated to affect the line FWHM by less than 25%.

When all these effects are combined, the LETGS line response function is generally $\sim 40\ \mu$m FWHM. With a conversion of 1.148 Å/mm for the LETG, a good figure of merit for LETGS resolution is therefore 0.05 Å. Because the three segments of the HRC-S can not perfectly follow the Rowland circle (see Figure 9.5), however, resolution varies slightly along the detector, and is lowest near the ends of each detector segment. Resolution degradation is almost negligible when using the ACIS-S, since its six segments more closely follow the Rowland circle, although the coarser ACIS pixel size (24 μm vs. $\sim$ 40-μm-FWHM LRF) means that line profiles are barely adequately sampled. A plot of LETGS resolving power for an on-axis point source, based on results from an observation of Capella, is shown in Figure 9.7.

Plots of fits to the LETG+HRC-S LRF at zeroth order and of Fe XVII and XVIII lines at $\sim$ 17 and 94 Å are given in Figures 9.8 and 9.9. The fitted form is a Moffat function:

$$I(\lambda) = \frac{I_0}{\left[1 + \left(\frac{\lambda - \lambda_0}{\Gamma}\right)^2\right]^{\beta}} \tag{9.1}$$

where λ_0 is the wavelength of the line center and Γ is a measure of the line width. The relation between Γ and the line FWHM depends on β. For a Lorentzian profile, or $\beta = 1$, the profile FWHM is $\Gamma/2$. For the value $\beta = 2.5$ recommended here, FWHM $\approx 1.13\Gamma$.

Figure 9.10 illustrates the χ^2 of fits to the zeroth order profile vs. β, and shows a best-fit profile with an index of $\sim$ 2.5. (Note that $\beta = 1.0$ yields a Lorentzian profile.) The best fit to the very high signal-to-noise-ratio zeroth order profile is far from being statistically satisfactory. However, spectral lines seen in first order generally contain orders of magnitude fewer counts than in the zeroth order of the well-exposed calibration spectrum shown, and the Moffat function nearly always provides a good match. Line response functions can also be generated within CIAO in the RMF FITS format. These are based on ray trace simulations using the MARX program and generally match observed line profiles to a level of 10% or better once intrinsic source broadening terms have been taken into account. Observers wishing to use line profile shapes as a diagnostic tool should keep in mind that, in the case of LETG+HRC-S observations, non-linearities in the HRC-S imaging can lead to significant distortions of observed line profiles (see Section 9.3.2).

Extended Sources

If a source is extended, there is no longer a unique mapping between the position of an event in the focal plane and wavelength, and this results in the apparent degradation of

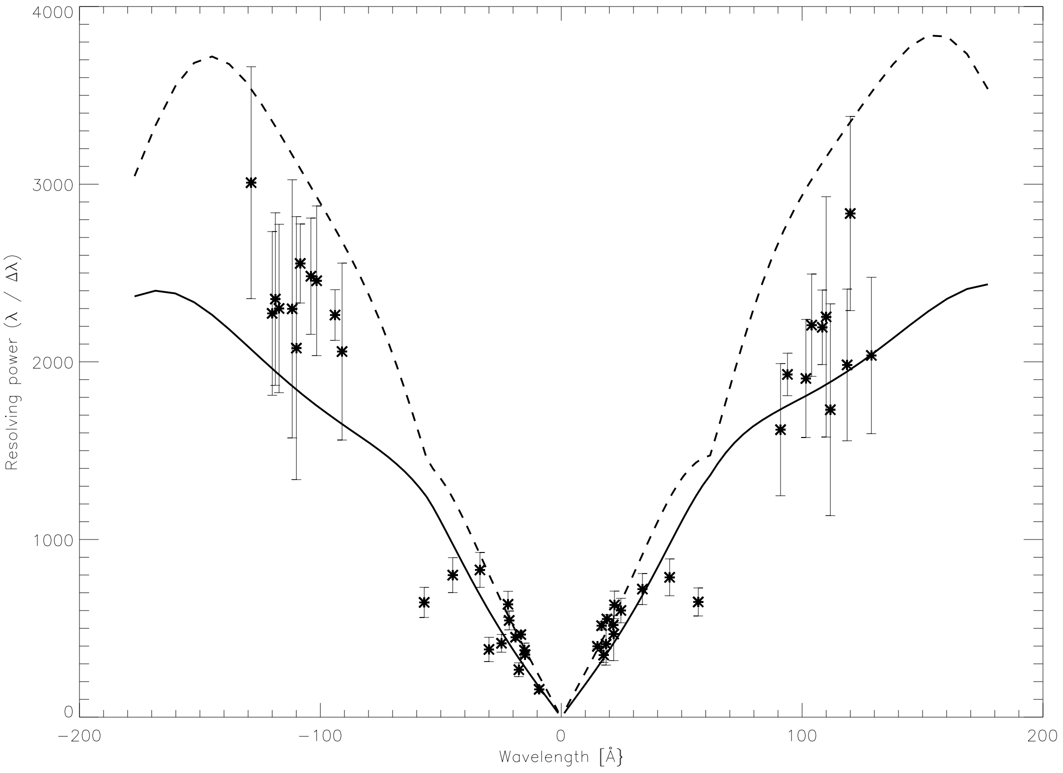

Figure 9.7: LETG spectral resolving power, as derived from observations of Capella (Obs ID's 1248, 1009, 58) and Procyon (Obs ID's 63, 1461) with the HRC-S. The analysis is based only on spectral lines thought not to be affected significantly by blending at the LETGS resolution. Measured line widths were corrected for source orbital, rotational, and thermal motions. The dashed line is an optimistic error budget prediction calculated from pre-flight models and instrument parameters. The conservative solid curve is based on in-flight values of aspect, focus, and grating period uniformity. The deviations from approximate linearity near ±60 Å and at the longest wavelengths arise from deviations of the HRC surface from the Rowland circle (see Figure 9.5). Deviations in the experimental data from a smooth curve are likely caused by hidden blends not predicted by the radiative loss model and by detector imaging nonlinearities discussed in Section 9.3.2.

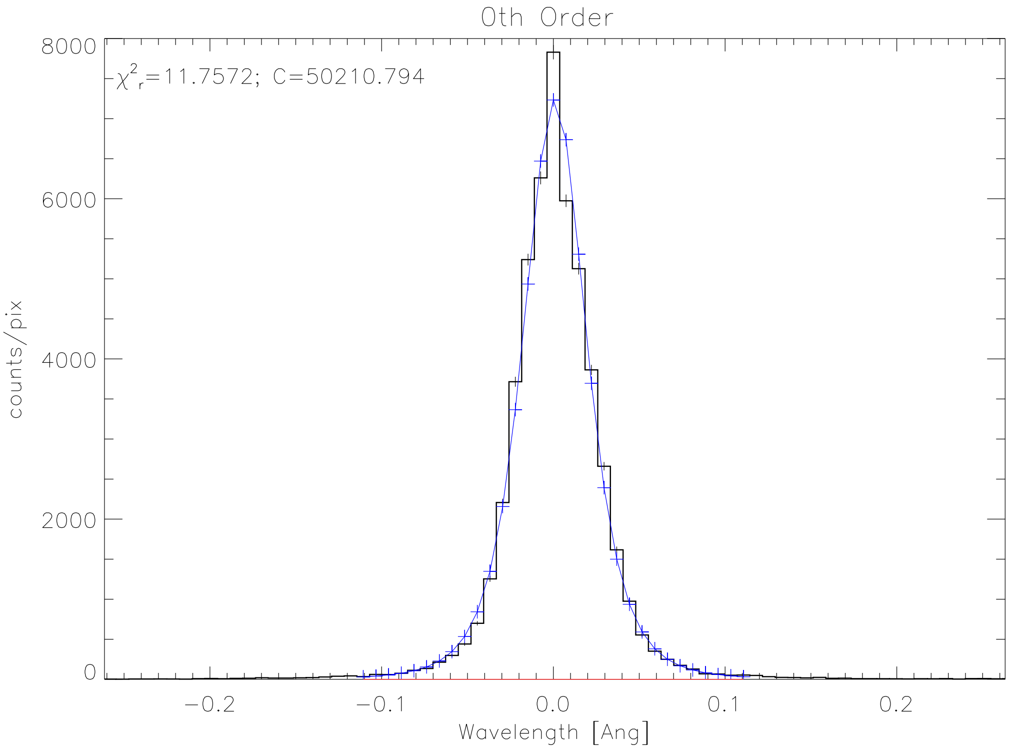

Figure 9.8: Observed LETG zeroth-order LRF from in-flight calibration observations of the active late-type binary Capella. The model profile, the continuous curve, is a Moffat function (see Equation 9.1) corresponding to the best-fit value of $\beta = 2.5$. While this function represents a statically-poor fit to this extremely high S/N zeroth-order profile, it is a good approximation to the LRF for lines in the dispersed spectrum containing many fewer counts.

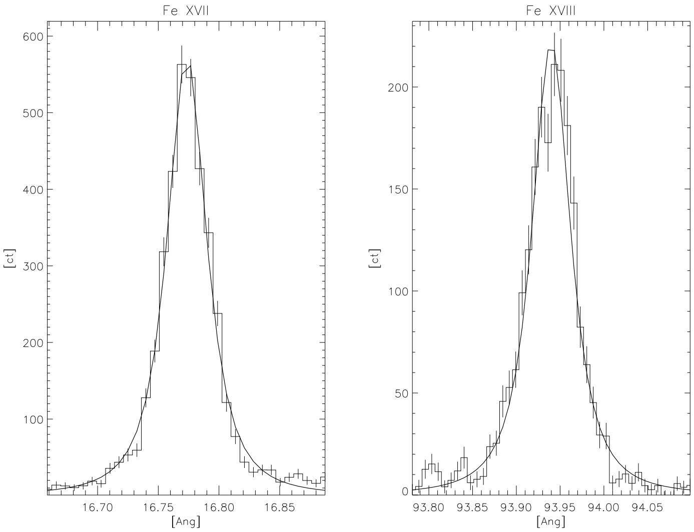

Figure 9.9: LETGS line response function as illustrated by two bright Fe lines (Fe XVII at ∼ 17 Å and Fe XVIII at ∼ 94 Å) using in-flight calibration observations of Capella. The solid curves are best-fit Moffat functions with $\beta = 2.5$.

Figure 9.10: LETGS zeroth order profile goodness of fit vs. β, showing a best-fit profile with an index of ∼ 2.5 (see Equation 9.1).

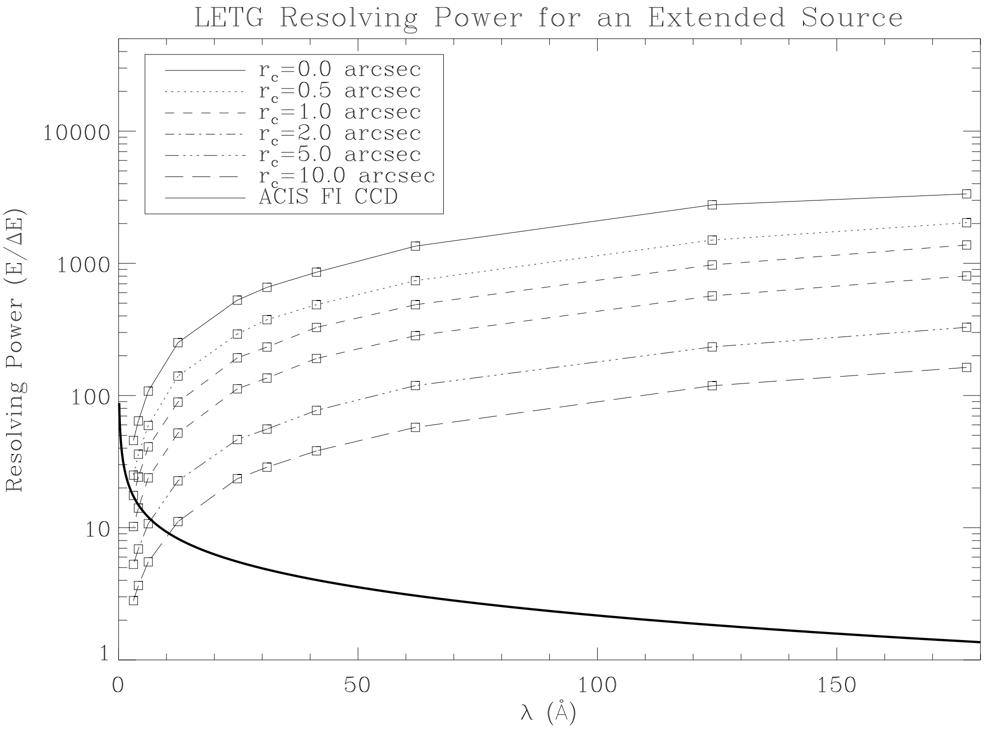

Figure 9.11: LETG spectral resolving power for extended sources. The predicted LETG resolving power ($E/\Delta E$) is shown versus wavelength for several source sizes. The *MARX* simulator has been used, and the source is represented by a β model (Equation 9.2). For comparison, the spectral resolution for ACIS front-illuminated CCD chips is shown (thick solid line). Note that the ACIS/FI curve does not include the effects of CTI, which progressively degrades resolution away from the readout edge (most of this degradation can be compensated for in data analysis).

spectral resolving power. For very large sources, the grating resolution may be no better than the intrinsic ACIS energy resolution.

The effect of increased source size on the apparent LETG spectral resolving power has been simulated using the *MARX* program, and results are shown in Figure 9.11. Another illustration of the effect of source extent may be seen in Figure 9.30 (Section 9.4), which shows model spectra over a small wavelength range.

In each case, extended sources were modeled using a Beta model for the surface brightness profile. Beta models are often used to describe the distribution of emission in galaxies and clusters of galaxies, and have an identical form to the Moffat function used to describe the line profile above, except that the intensity dependence is radial:

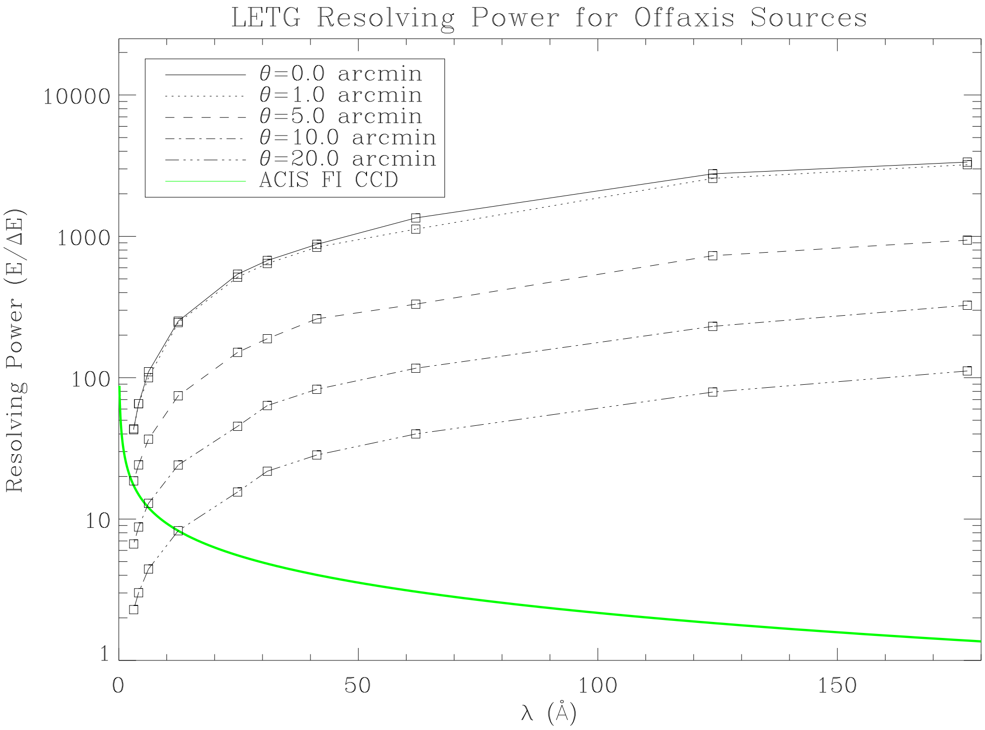

Figure 9.12: LETG spectral resolving power for off-axis sources. The predicted LETG resolving power ($E/\Delta E$) is shown versus wavelength for various off-axis distances. For comparison, the spectral resolution for ACIS front-illuminated CCD chips is shown. Note that the ACIS/FI curve does not include the effects of CTI, which progressively degrades resolution away from the readout edge.

$$I(r) = \frac{I_0}{\left[1 + \left(\frac{r}{r_c}\right)^2\right]^\beta} \tag{9.2}$$

where $I(r)$ is the surface brightness, r is the radius, and r_c characterizes the source extent. The value of β was set to a typical value of 0.75 and simulations were performed for different values of the source extent, r_c.

Off-Axis Sources

Similarly, for sources off-axis, the increased point-spread function decreases the spectral resolving power. The effect on off-axis sources has been simulated with *MARX* and is shown in Figure 9.12.

As with extended sources, an ACIS pulse-height spectrum may, in extreme cases, provide energy resolution comparable to or better than the LETG for a source far off-axis.

9.3.4 Grating Efficiency

Fine and Coarse Support Structure Diffraction

As explained in Section 9.1, the LETG has fine and coarse support structures which are periodic in nature, and have their own diffraction characteristics. The fine support structure disperses photons perpendicularly to the main spectrum, with about 1/26 the dispersion of the main grating. The coarse support is a triangular grid, and creates a very small hexagonal diffraction pattern which is generally only discernible in zeroth order or for very bright lines. Examples of this secondary diffraction are visible in Figures 9.23, 9.24, and 9.27, all in Section 9.3.7.

The two support structures each diffract roughly 10% of the X-ray power, but the coarse-support diffraction pattern is so small that essentially all its photons are collected along with the primary spectrum during spectral-region extraction in data analysis. A significant fraction of the fine-support diffraction pattern, however, may lie outside the spectral extraction region, resulting in a loss of several percent of the total X-ray intensity (see, *e.g.*, Figure 9.23). The fractional *retention* of X-ray power in the source extraction region is referred to as the *spectral extraction efficiency* and is discussed in Section 9.3.5.

Total Efficiencies

The zeroth, 1st, and selected higher-order grating efficiencies, based on a rhomboidal grating bar analytical model and verified by ground calibration, are shown in Figure 9.13. The efficiency for each order is defined as the diffracted flux with the grating assembly in place divided by the flux if the grating assembly were not in place. Plotted values are for the total diffraction efficiency (including photons diffracted by the coarse and fine support structures), with negative and positive orders summed. Even orders are generally weaker than odd orders up through roughly 6th order.

The wiggles near 80 Å, and the stronger features near 6 Å, arise from partial transparency of the gold grating material to X-ray photons. Note that there are no absorption-edge features from C, N, or O in the LETG efficiency as there are in the HETG, because the LETG does not use a polyimide support film.

9.3.5 Effective Area

The LETGS effective area for any diffraction order is equal to the product of the HRMA effective area, the net LETG efficiency for that order (including spectral extraction efficiency), and the overall detector efficiency (which varies slightly depending on exactly where the diffracted spectrum falls on the detector). For LETG/ACIS-S there is an additional factor, the Order Sorting Integrated Probability (OSIP), which is determined by the width of the ACIS-S energy filter for each diffraction order. All these quantities vary with wavelength.

Of the contributors listed above, the HRMA EA (see Chapter 4) is the best calibrated within the LETGS energy band. The largest contributor to the LETG/HRC-S effective

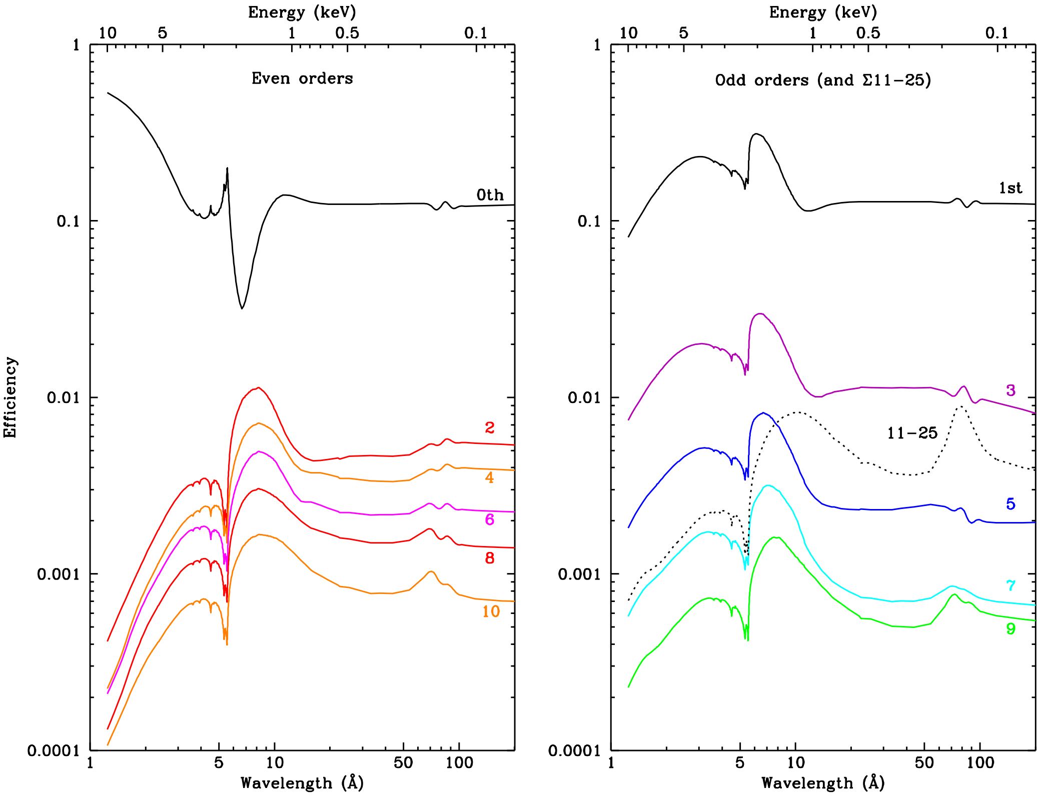

Figure 9.13: LETG grating efficiency. Combined positive and negative order efficiency is plotted versus wavelength and energy. For clarity, even and odd orders are plotted separately; the sum of orders 11–25 is also shown. Plotted values include all support structure diffraction. Net efficiency when using a spectral extraction region (see Figures 9.14 and 9.15) is 10-15% lower. Features near 6 and 80 Å are due to the partial transparency of the gold grating material at these wavelengths.

area uncertainty is the efficiency of the HRC-S, especially at longer wavelengths (> 44 Å; < 0.28 keV) where ground calibration is very difficult or impossible. In-flight calibration (see Section 9.2.2), particularly of the net 1st order effective area, has provided the best and most extensive data, and the effective area is now believed to be accurate to a level of approximately 10–15% or better across the entire bandpass.

Effective areas for orders 2–10 have been calibrated relative to 1st order to an accuracy of 5–10% (best for 3rd order and generally worsening with increasing m), using both ground and flight data. Uncertainties for $\lambda \lesssim 6$ Å, $m\lambda \gtrsim 80$ Å, and orders beyond 10th may be larger but are usually unimportant.

Instrument Spectral Features

In addition to fixed-position detector features (primarily detector segment gaps—see Section 9.3.2) there are instrumental spectral features which occur at fixed energies because of absorption edges in the materials comprising the HRMA, LETG, and HRC-S or ACIS-S. The edges are tabulated in Table 9.4 and can be seen in the effective area curves (such as Figure 9.17) as decreases or increases in effective area depending on whether the material is part of the mirror, the filter, or the detector. Every effort has been made to adequately calibrate *Chandra* over its entire energy range, but it should be understood that effective areas near absorption edges are extremely difficult to quantify with complete accuracy and uncertainties in these regions are inevitably higher.

Spectral Extraction Efficiency

In practice, it is impossible to "put back" photons which undergo secondary diffraction (from the coarse and fine support structures) in a real observation. Instead, one defines an extraction region for the observed spectrum and adjusts the derived spectral intensities to account for the fraction of total events that are contained within the extraction region.

The default extraction region for the LETG+ACIS-S configuration is a rectangle; that for the LETG+HRC-S configuration is "bow-tie" shaped, comprising a central rectangle abutted to outer regions whose widths flare linearly with increasing dispersion distance (see Figure 9.14). The shape of the bow-tie has been optimized to match the astigmatic cross-dispersion that is a feature of Rowland-circle geometry, with the goal of including as much of the diffracted spectrum as possible while minimizing the included background. Extraction efficiencies for LETG+ACIS are illustrated in Figure 9.15. For custom analysis (such as when narrower or wider extraction regions are needed), *CIAO* permits adjustment of spectral and background regions by the user. Whatever spectral region is chosen, *CIAO* computes the extraction efficiency and includes it as a factor in the *Response Matrix File* (RMF). Users then apply this RMF together with the effective area from the *CIAO*-computed *Ancilliary Response File* (ARF) during subsequent analysis.

Table 9.4: Instrumental Absorption Edges

Instrument	Element	Edge	Energy (keV)	Wavelength (Å)
HRC	Cs	L	5.714	2.170
HRC	Cs	L	5.359	2.313
HRC	I	L	5.188	2.390
HRC	Cs	L	5.012	2.474
HRC	I	L	4.852	2.555
HRC	I	L	4.557	2.721
LETG	Au	M	3.425	3.620
LETG	Au	M	3.148	3.938
HRMA	Ir	M	2.909	4.262
LETG	Au	M	2.743	4.520
HRMA	Ir	M	2.550	4.862
LETG	Au	M	2.247	5.518
LETG	Au	M	2.230	5.560
HRMA	Ir	M	2.156	5.750
HRMA	Ir	M	2.089	5.935
ACIS	Si	K	1.839	6.742
HRC, ACIS	Al	K	1.559	7.953
HRC	Cs	M	1.211	10.24
HRC	I	M	1.072	11.56
HRC	Cs	M	1.071	11.58
HRC	Cs	M	1.003	12.36
HRC	I	M	0.931	13.32
HRC	I	M	0.875	14.17
HRC	Cs	M	0.7405	16.74
HRC	Cs	M	0.7266	17.06
HRC	I	M	0.6308	19.65
HRC	I	M	0.6193	20.02
ACIS	F	K	0.687	18.05
HRC,ACIS	O	K	0.532	23.30
HRMA	Ir	N	0.496	25.0
HRC	N	K	0.407	30.5
HRC,ACIS	C	K	0.284	43.6
HRC	Al	L	0.073	170

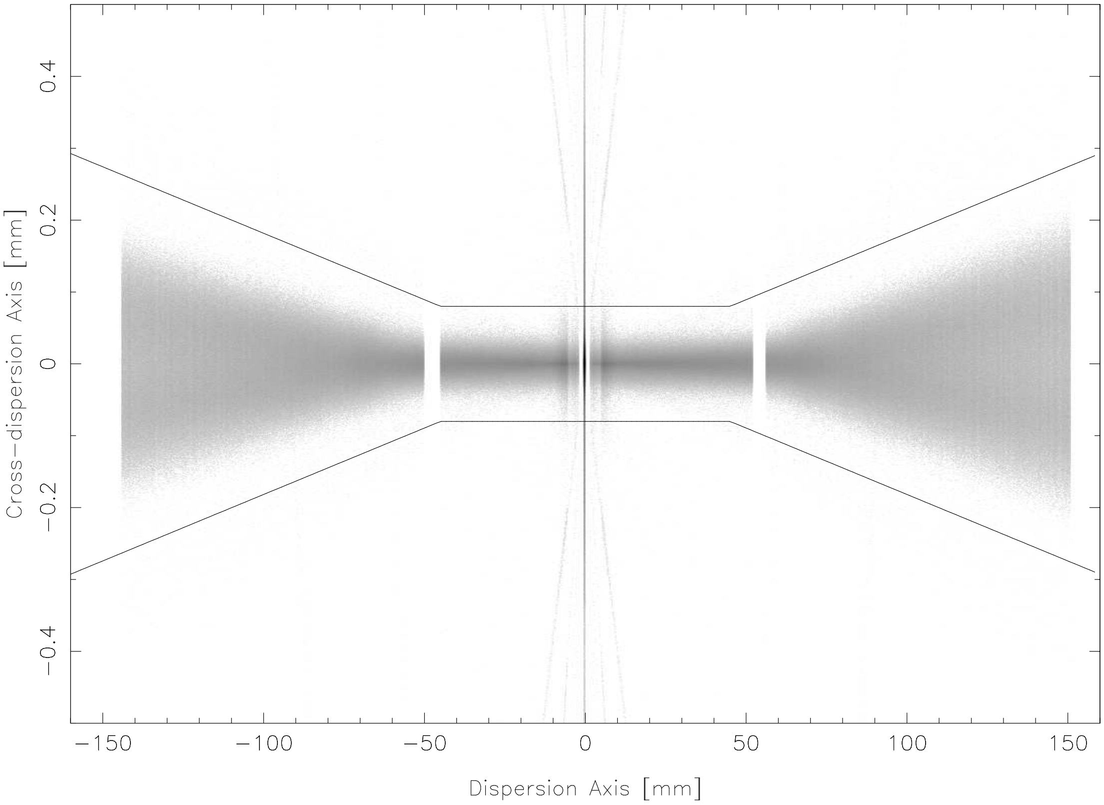

Figure 9.14: A MARX simulation of a flat spectrum illustrating the broadening of the LETG+HRC-S profile in the cross-dispersion direction, and showing the "bow-tie" spectral extraction window. Note that the vertical axis is highly stretched. The cross-dispersion profile of an LETG+ACIS-S spectrum is approximately constant across its smaller wavelength range and the default extraction window (not shown) is rectangular.

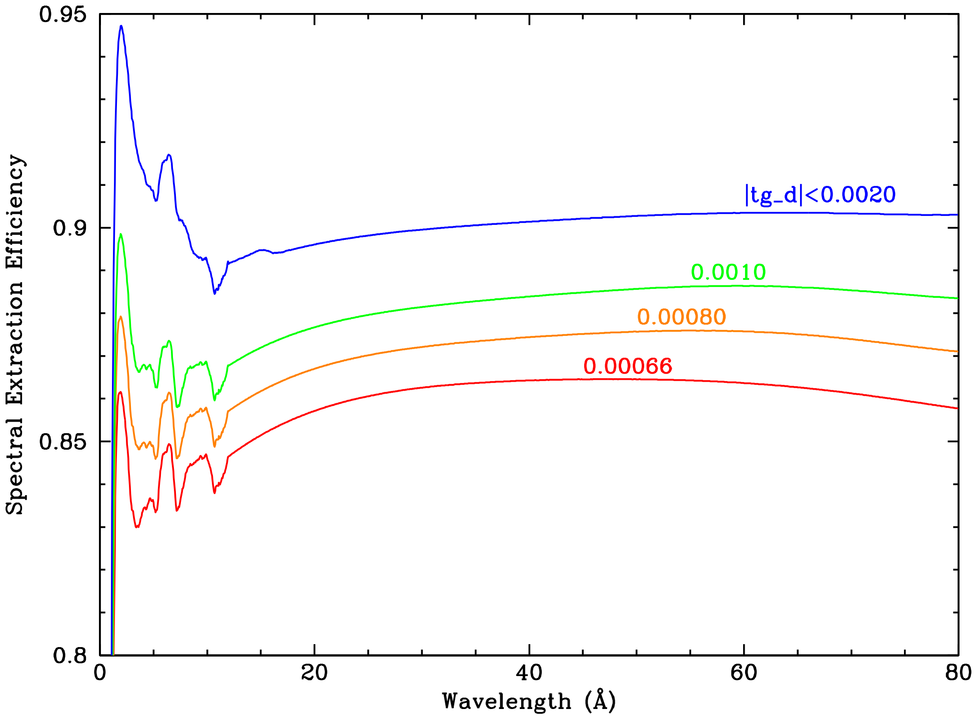

Figure 9.15: Spectral extraction efficiencies for LETG+ACIS for various extraction region half-widths (tg_d values listed in degrees). Approximately 10% of the total power is diffracted by the fine-support structure and most of it falls outside the extraction region; the peaks toward shorter wavelengths reflect the inclusion of progressively higher orders of cross-dispersed events within the extraction region. The otherwise general trend of declining efficiency toward short wavelengths is caused by increased scattering. The slight fall-off beyond ∼60 Å is due to astigmatism, i.e., an increasing fraction of events are lost as the dispersion pattern broadens (see Figure 9.14). In 2010 the default spectral extraction region was narrowed from $| tg\_d |< 0.0020$ to 0.0008 degrees after a slight misalignment between the dispersed spectrum and the extraction region was corrected.

Zeroth and First-Order Effective Areas

Although the HRC-S is the default detector for the LETG, other detector configurations are possible. Figures 9.16 and 9.17 show effective areas for the LETG zeroth and 1st orders, respectively, when using the HRC-S, HRC-S with LESF, or ACIS-S as the readout detector. Based upon these and other plots, the various tradeoffs as to the use of each detector are thoroughly discussed in Section 9.4. Users interested in the low energy response using ACIS should read carefully the discussion in Section 6.5.1.

Off-Axis and Extended Sources

Differences in the LETGS effective area for off-axis and significantly extended sources compared to the on-axis point source case are primarily determined by the HRMA vignetting function (see Chapter 4).

High-Order Diffraction Effective Areas

Although the LETG (and HETG) have been designed to reduce complications from higher-order diffraction by suppressing even orders, many grating spectra will have overlapping diffraction orders. When ACIS-S is used as the detector, its intrinsic energy resolution can be used to separate orders. The situation is more complicated, however, with HRC-S, which has very little energy resolution. Detector options and various data analysis techniques are described in Section 9.4.

The relative contribution of higher-order photons with different detector configurations can be estimated by inspection of Figures 9.18, 9.19, and 9.20. As an example, say an observer plans to use the LETG/HRC-S configuration and wants to determine the intensity of a line at 45 Å, but knows that line may be blended with the 3rd order of a 15 Å line which has 10 times the emitted intensity of the 45 Å line. Looking at Figure 9.18, we read the 1st- and 3rd-order curves at $m\lambda = 45$ Å and see that the 3rd-order value is about one-tenth the 1st-order value. Multiplying by 10 (the ratio of the emitted intensities of the 15 and 45 Å lines), we compute that ∼50% of the feature at $m\lambda = 45$ Å will come from the 15 Å line. A fuller explanation, with color figures and more examples for the LETG/HRC-S with line and continuum sources, can be found at http://cxc.harvard.edu/ciao/threads/hrcsletg_orders/.

9.3.6 Background

The LETG is always used in conjunction with a focal-plane detector, so LETGS spectra will exhibit that detector's intrinsic, environmental, and cosmic background. The components of the background of the HRC are discussed in Section 7.10. The quiescent background rate over the full detector varies with the solar cycle (see Figure 9.21) but is always a significant fraction of the 183 cts s^{-1} telemetry limit. Imposition of the HRC-S spectroscopy window reduces the rate to between 55 and 130 cts s^{-1}, as discussed below.

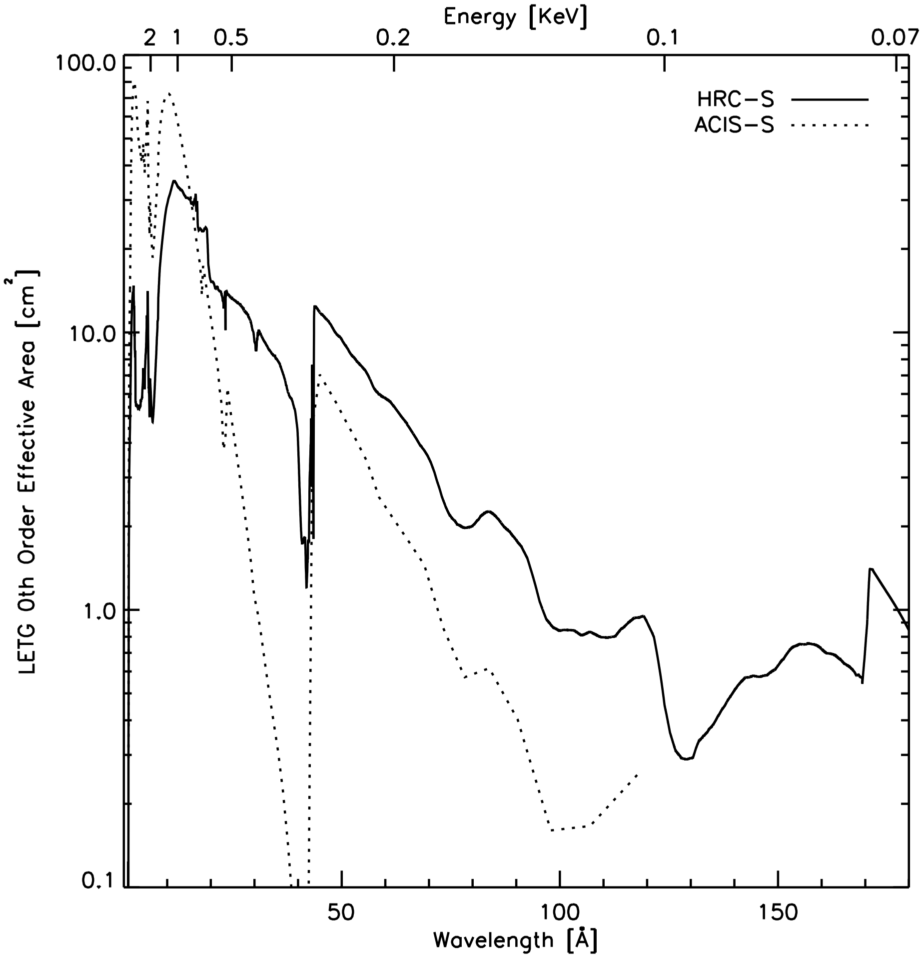

Figure 9.16: LETGS zeroth-order effective area for an on-axis point source for the LETG with HRC-S and ACIS-S detectors. The zeroth-order effective area for the HRC-S/LESF combination is the same as for the HRC-S. LETG+ACIS-S areas were computed using an effective area model that included the effects of contamination build-up extrapolated to the level expected in mid-2013.

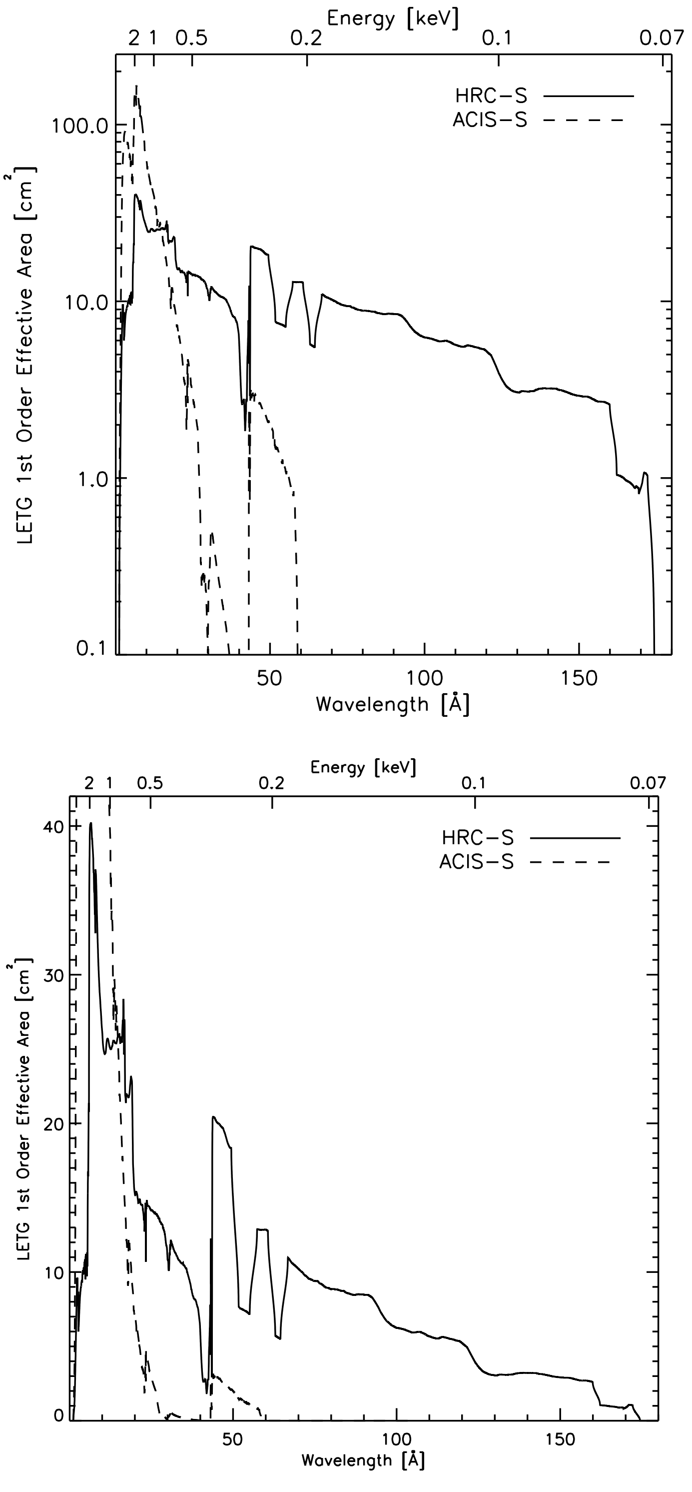

Figure 9.17: LETGS 1st-order effective area for an on-axis point source, with HRC-S and ACIS-S detector configurations with log (top) and linear (bottom) scaling. Positive and negative orders are summed. LETG+ACIS-S areas were computed using an effective area model that included the effects of contamination build-up extrapolated to the level expected in mid-2013. Note that the vertical scale of the linear plot has been truncated.

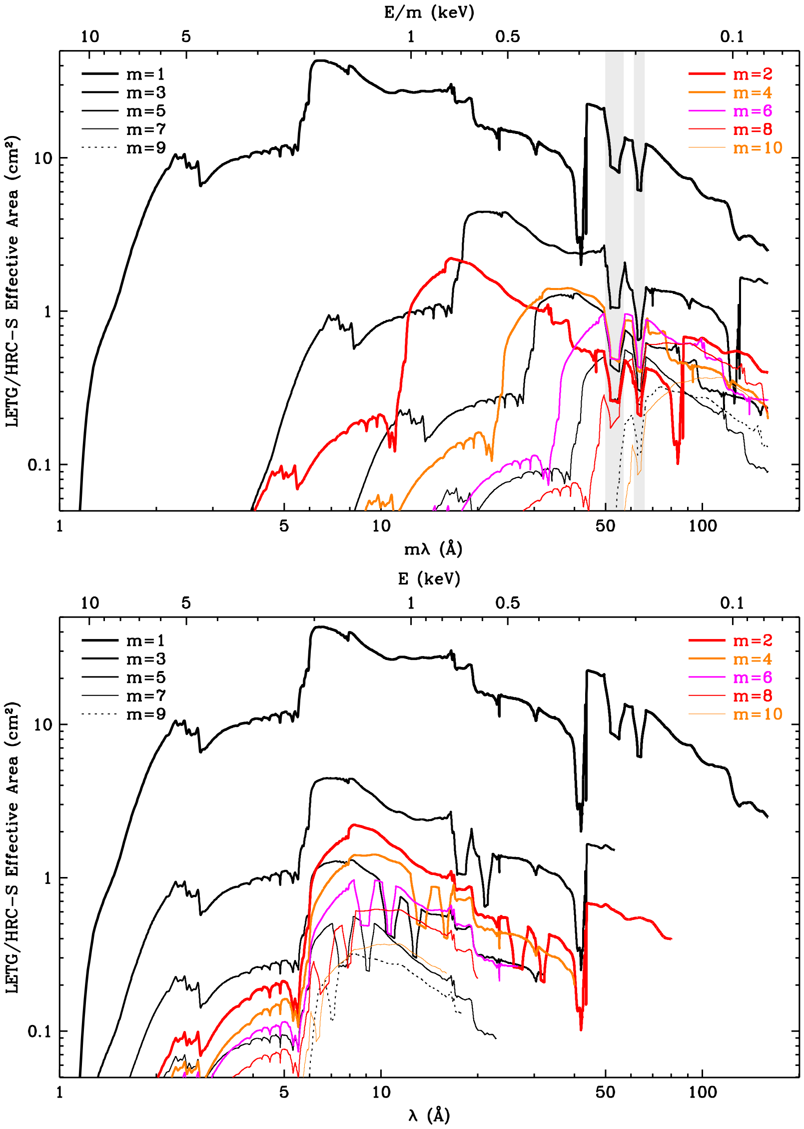

Figure 9.18: The combined LETG/HRC-S effective area, illustrating the relative strengths of 1st and higher orders, plotted versus $m\lambda$ (top) and λ (bottom). Positive and negative orders are summed. Light shading in top panel marks plate gaps around $m\lambda = -53$ and $+64$ Å. See the text for an example of how to determine the relative strength of overlapping lines from different orders, and http://cxc.harvard.edu/ciao/threads/hrcsletg_orders/ for color figures and further information.

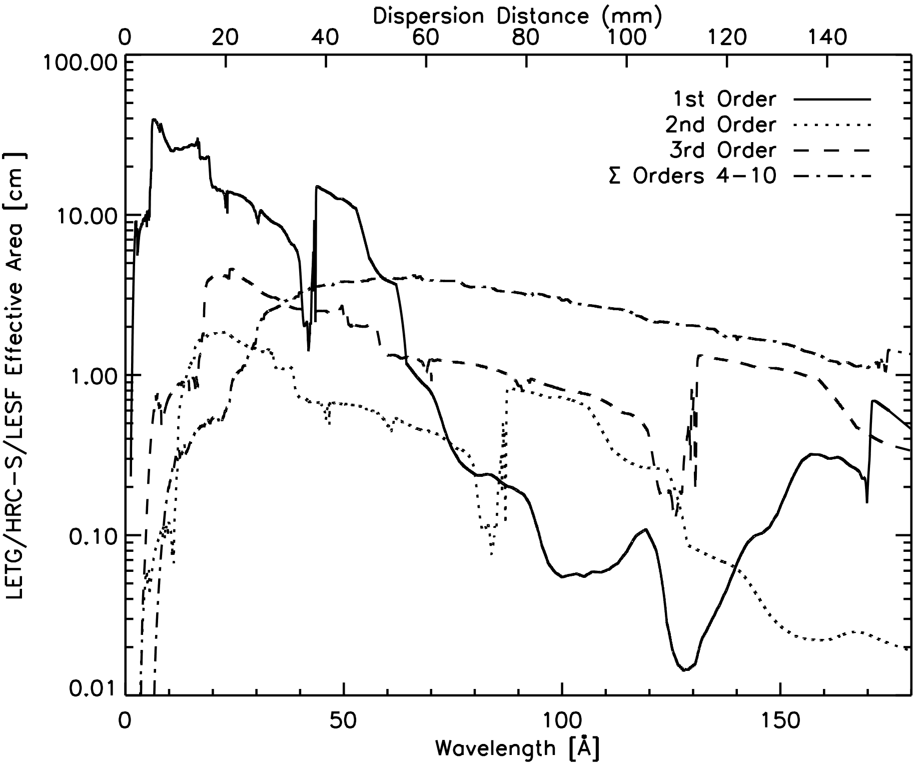

Figure 9.19: The combined HRMA/LETG/HRC-S/LESF effective areas for 1st and higher orders. Positive and negative orders are summed.

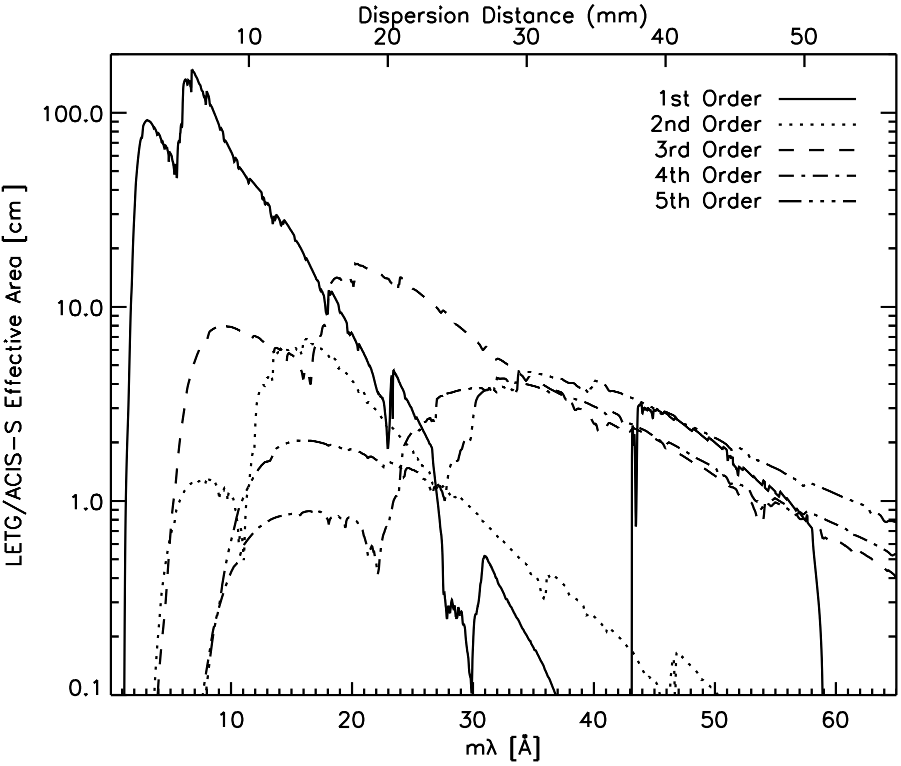

Figure 9.20: The combined HRMA/LETG/ACIS-S effective areas for 1st and higher orders. LETG+ACIS-S areas were computed using an effective area model that included the effects of contamination build-up extrapolated to the level expected in mid-2013. Positive and negative orders are summed.

HRC-S Exposure Windows, Deadtime, and Timing Resolution

To avoid constant telemetry saturation, the HRC-S is operated in a default, windowed down "edge-blanking" configuration, in which data from only 6 of the 12 coarse taps in the center of the detector in the cross-dispersion direction are telemetered (see Section 7.10.2). The edge-blanking creates an active detector area slightly less than 10 mm, or 3.4 arcmin, in the cross-dispersion direction. This window easily accommodates the (dithered) dispersed spectra of point sources; other windows may be specified for extended sources or other special cases. When Solar Maximum occurs around 2013, the total quiescent background rate using the default configuration will be near its solar-cycle minimum.

As long as the total counting rate is below the 183 cts s^{-1} telemetry limit, detector deadtime is negligible (and recorded as a function of time in the secondary science `.dtf` files—net exposure time is recorded in the image FITS file header). During background "flares" arising from an increased flux of solar wind particles, however, the background rate may rise above the 183 cts s^{-1} telemetry limit. During these times detector deadtime may become significant. Current data processing algorithms correct for this deadtime with a typical accuracy of $\sim$10% or better.

Time resolution approaching 16 μsec can be achieved with the HRC if the data rate is below telemetry saturation. To leave ample margin for telemetry in case of background flares, a special Imaging Mode (see Section 7.11) is used for high-resolution timing observations. This mode utilizes only the central region of the HRC-S detector and provides a field of view of approximately $7' \times 30'$. However, if telemetry saturation does take place then the time resolution with HRC-S is approximately the average time between events.

HRC-S Background Reduction Using Pulse-Height Filtering

The quiescent background rate in HRC-S Level 2 data varies by more than a factor of two over a solar cycle (see Figure 9.21). A "typical" rate of 1.0×10^{-6} cts s^{-1} pixel^{-1} corresponds to 5.76×10^{-5} cts s^{-1} arcsec^{-2}, or 0.10 counts per pixel in 100 ks. The extent of a dispersed line in the LETGS spectrum is approximately 0.07 Å (9.5 pixels) and the spectral extraction region is 25 to 85 pixels wide in the cross-dispersion direction; the typical background rate therefore yields 24 to 81 background counts beneath the line in a 100 ks exposure. However, the HRC-S pulse height distribution is sufficiently narrow that a large fraction of pulse-height space can be excluded from the data to further reduce the background, which has a relatively broad pulse-height distribution.

Data collected or reprocessed in the Archive after June 2010 were processed with a time-dependent HRC-S gain map, which allows use of an associated pulse-height filter. This filter removes more than half of the Level 2 background at wavelengths longer than 20 Å, with a loss of only 1.25% of X-ray events (see Figure 9.22). Details, including instructions on how to reprocess older data, may be found at http://cxc.harvard.edu/cal/Letg/Hrc_bg.

Note that the HRC-S high voltage was raised in Mar 2012. The gain map for observations after this date is not as accurate as before because temporal trends are not yet well established. The background filter is still safe to use but will be slightly less effective on these post-HV-change data. The gain map will be refined as more calibration data become available.

Relevance for Higher Orders The mean of the pulse-height distribution increases weakly with photon energy, such that a factor of two difference in energy corresponds to a shift in the mean of ∼8%. The mean of 8th order will therefore be about 25% higher than 1st order; the new PI filter removes 1.25% of 1st order at 160 Å, and about 11% of 8th order ($\lambda = 20$ Å, $m\lambda = 160$ Å). Extra filtering of higher orders will have negligible effect for nearly all analyses, but should be considered if deliberately studying wavelength ranges with very heavy higher order contamination.

Relevance for Observation Planning There are two backgrounds relevant for the LETG/HRC-S. The first is the Level 1 data event rate over the 3-plate standard spectroscopy region, which is 55–130 cts s^{-1} during quiescence (see Figure 9.21), but can rise during background 'flares' to cause telemetry saturation when the total (background plus sources) rate reaches 183 cts s^{-1}. The other is the filtered Level 2 background rate in the extracted spectrum. A "typical" rate of 1.0×10^{-6} cts s^{-1} pixel^{-1} (see Figure 9.21) corresponds to ∼10–25 counts (depending on wavelength—see Figure 9.22) in a 0.07 Å spectral bin per 100,000 s integration during quiescence, which may be used for estimating signal-to-noise (see also the discussion in Section 9.5.1).

There is a third background rate which will be of interest when high time resolution (sub-msec) is required, which is the counting rate before any on-board screening is applied. See Sections 7.11 and 7.14.1 for more information on the HRC-S Timing Mode.

ACIS-S Background

As with the HRC-S detector, background rates in ACIS are somewhat higher than expected, but lower than in the HRC. Pulse-height filtering applied during order separation further reduces the effective ACIS-S background to extremely low levels when used with gratings. The reader is directed to Chapter 6 for further discussion.

9.3.7 Sample Data

Figure 9.23 is a detector image from an 85 ksec LETGS observation of Capella (ObsID 1248). The central 30 mm of the dispersion axis and the full extent of the telemetered cross-dispersion window (9.9 mm) is shown. The image is in angular grating coordinates (TG_D, TG_R), which have been converted to Å. The lines radiating from zeroth order above and below the primary dispersion axis are due to fine-support structure diffraction. Star-shaped coarse support structure diffraction is seen around zeroth order. Figure 9.24

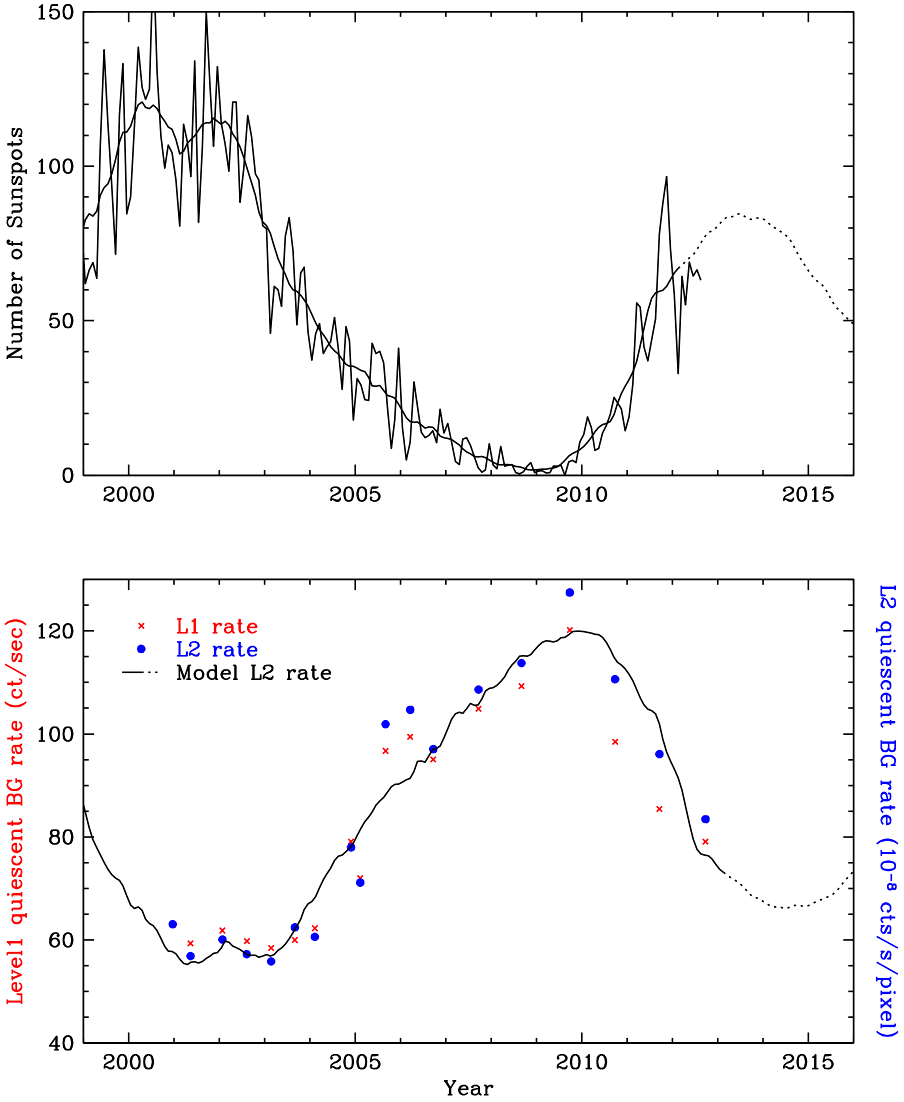

Figure 9.21: Solar cycle and HRC-S background. Top: Monthly sunspot numbers and with 6-month smoothing; dotted curve is predicted. Bottom: Level 1 background rate is for the LETGS standard spectroscopy region, derived from AR Lac monitoring data. The "typical" Level 2 (L2) rate is 1.0×10^{-6} cts s^{-1} $pixel^{-1}$, but this varies with the solar cycle. A simple model of the HRC-S background rate based on sunspot number (with a 1-year lag corresponding to the approximate time for the solar wind to reach the heliopause, where its magnetic field helps deflect cosmic rays from entering the solar system) is shown by the solid and dotted curve. Rates in Figure 9.22 correspond to a Level 2 rate of 1.1×10^{-6} cts s^{-1} $pixel^{-1}$.

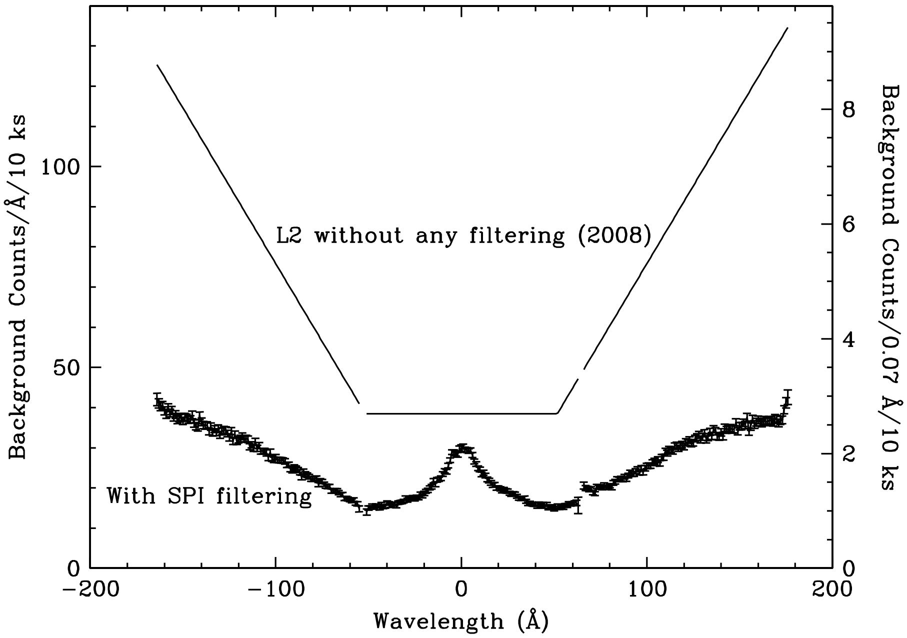

Figure 9.22: The Jan 2008 LETG+HRC-S background rate with and without pulse-height filtering. These Level 2 rates correspond to 1.1×10^{-6} cts s^{-1} $pixel^{-1}$ (see Figure 9.21). Data are shown using the standard 'bowtie' spectral extraction region (see Figure 9.14). X-ray losses from the observed spectrum as a result of the filtering for 1st order are ∼1.25%; losses will be slightly higher for higher orders. See http://cxc.harvard.edu/cal/Letg/Hrc_bg for more information.

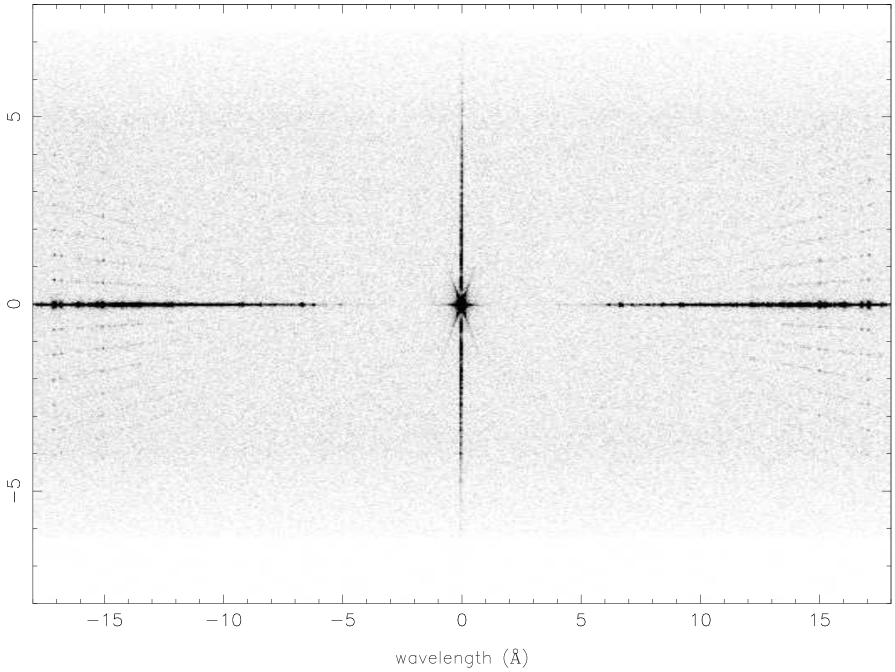

Figure 9.23: HRC-S detector image of LETGS observation of Capella. In order to illustrate the stretching of the cross-dispersion axis, both axes are in Å with 1.148 Å/mm; only the central 30 mm of the central plate is shown. The full extent of the telemetered six-tap cross-dispersion window is shown and measures 9.9 mm. The areas of reduced background at top and bottom are due to dither effects. Star-shaped coarse support structure diffraction is seen around zeroth order, and "cat's whiskers" fine support structure diffraction is seen above and below the primary dispersion axis, as well as in the vertical line through zeroth order.

is a close-up of the bright Fe XVII, Fe XVIII, and O VIII lines between ∼ 15–17 Å, in which many orders of fine support diffracted flux can be seen.

Figure 9.25 is an HRC-S image of a second Capella observation (ObsID 1420, 30 ksec), showing positive order dispersion. The increasing cross-dispersion extent of lines at longer wavelengths is due to astigmatism in the HRMA/LETG system (see also Figure 9.14). The positive order HRC-S plate gap is seen at ∼ 63 Å. An extracted Capella spectrum (ObsID 62435, 32 ksec), is shown in Figure 9.26. Positive and negative order flux has been summed.

Figure 9.27 is a zeroth-order image of summed Sirius AB observations (ObsIDs 1421, 1452, 1459) with a total exposure time of 23 ksec. The star-shaped pattern is due to coarse support structure diffraction. Sirius A and B are separated by $\sim 4''$. The flux from Sirius A is due to the small, but non-zero, UV response of the detector.

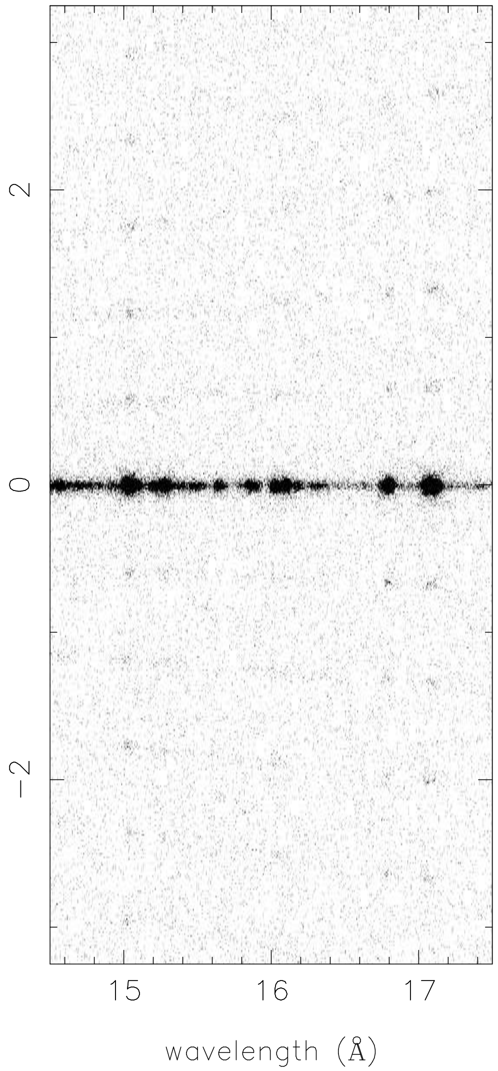

Figure 9.24: Detail of Figure 9.23, showing the LETG/HRC-S image of bright lines in Capella. Both axes are in Å with 1.148 Å/mm. The Fe XVII lines at ∼ 15 and 17 Å are the brightest in the LETG Capella spectrum. Faint features above and below the primary spectrum are due to fine support structure diffraction.

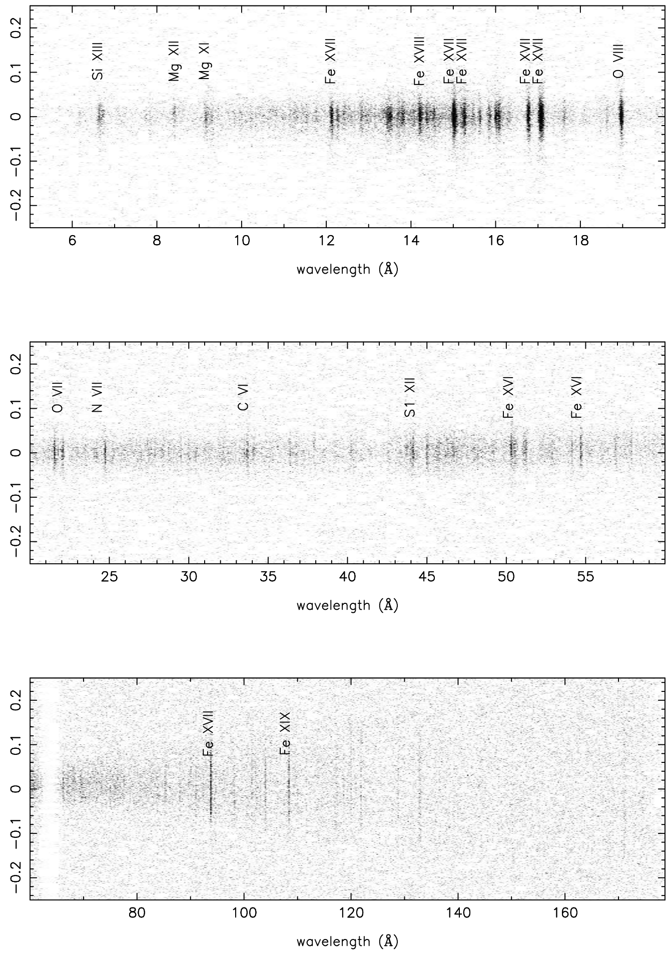

Figure 9.25: HRC-S detector image of a Capella observation, showing positive order dispersion. Both axes are in Å with 1.148 Å/mm. The increasing cross-dispersion extent of lines at longer wavelengths is due to astigmatism in the HRMA/LETG system. The positive-order HRC-S plate gap is at ∼ 63 Å.

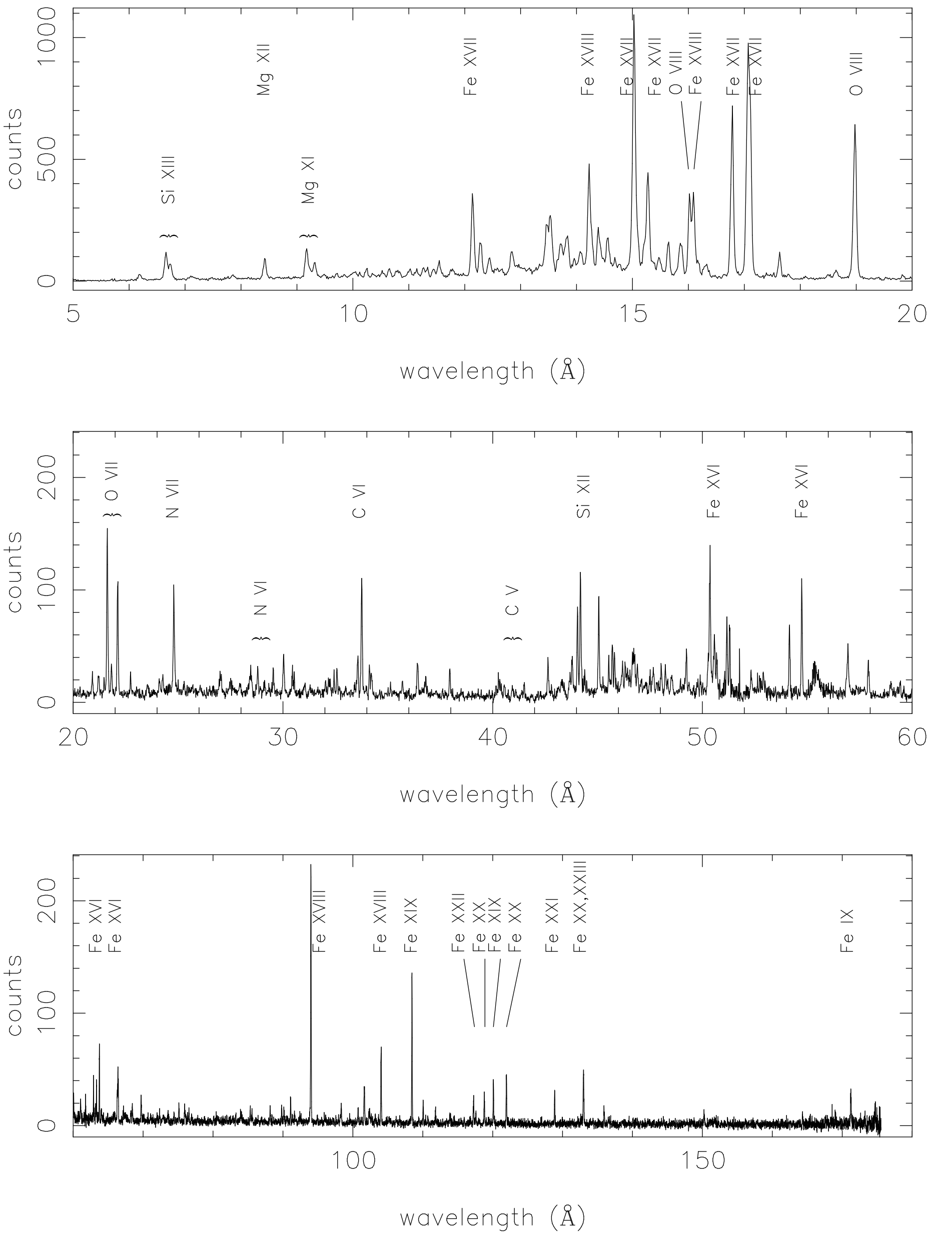

Figure 9.26: Extracted LETGS spectrum of Capella with some line identifications (from Brinkman et al. 2000, ApJ, 530, L111). Many of the lines visible between 40 and 60 Å are 3rd order dispersion of the strong features seen in 1st order in the uppermost panel.

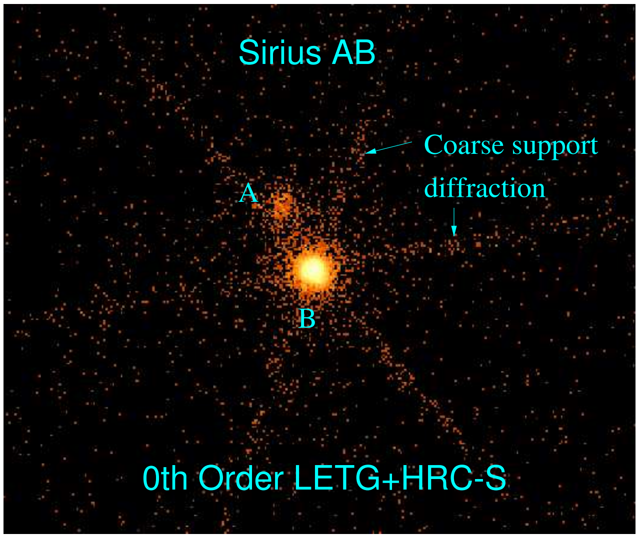

Figure 9.27: LETG/HRC-S zeroth order image of Sirius A and B. The two stars are separated by $\sim 4''$. Flux from Sirius A is due to the small but finite UV response of the detector. The star-shaped structure is due to coarse support diffraction.

9.4 Observation Planning

The purpose of this Section is to provide further information directly related to planning LETGS observations that is not explicitly presented in Sections 9.1 and 9.3, and to reiterate the most relevant issues of instrument performance that should be considered when preparing an observing proposal.

9.4.1 Detector Choices

The best choice of detector will depend on the exact application; some considerations are listed below. For further details concerning the HRC and ACIS detectors, refer to Chapters 7 and 6, respectively. We remind readers that contamination build-up on the ACIS detector has significantly reduced the effective area of the LETG+ACIS-S combination for wavelengths > 20 Å compared to that at launch. In this regard please be sure to read the discussion in Section 6.5.1.

HRC-S

- The HRC-S provides wavelength coverage from 1.2–175 Å (10–0.07 keV).
- The HRC-S QE is smaller than that of ACIS-S in the 1.2–20 Å (∼10–0.6 keV) range, but larger at longer wavelengths (see Figure 9.17).

- The HRC-S provides the highest time resolution at 16 μs when telemetry saturation is avoided. The probability of avoiding saturation is significantly improved if only the central plate is utilized (see Section 7.11).
- The HRC-S suffers from small position non-linearities which may slightly distort or shift spectral features (see Section 9.3.2).
- HRC-S has essentially no intrinsic energy resolution and so overlapping spectral orders cannot be separated.
- The Level 1 HRC-S background count rate is typically 100 cts s^{-1} in its windowed-down spectroscopic configuration during quiescence. (See Figure 9.21 for how this varies over the solar cycle). However, this can rise to exceed the HRC telemetry saturation limit of 183 cts s^{-1} during background "flares". During telemetry saturation, deadtime is determined to an accuracy of 5–10%. Background flares can also be filtered out using *CIAO* or other software tools. These flares have been seen to affect 10–20% of some observations. Typical fractions are smaller than this; larger fractions are rare. If observing a very bright source where telemetry saturation is a concern, one can use a smaller than standard region of the detector (see Section 9.4.2).
- The LESF filter region in principle can be used to obtain a higher-order spectrum relatively uncontaminated by 1st order for wavelengths above 75 Å ($E < 0.17$ keV; see Figure 9.17). This could be useful either for observing features in a high order for high spectral resolution that cannot be easily observed with the HETG/ACIS-S combination, or for providing a direct observation of higher order contamination in conjunction with an LETG+HRC-S observation in its nominal configuration. NB: the LESF configuration has never been used in flight.

Summary HRC-S is probably the best detector choice for spectroscopic observations in which one or more of the following observational goals apply:
—signal longward of 25 Å is of significant interest (see Figure 9.17);
—the highest time resolution is required.

HRC-I

- When used with the LETG, the HRC-I provides wavelength coverage from 1.2–73 Å (10–0.17 keV).
- The raw HRC-I quiescent background event rate per unit area is lower than that of the HRC-S by about a factor of 4. After moderate filtering in both detectors, the ratio is about a factor of 2. This may be important for very weak sources.
- The HRC-I imaging capabilities are similar to those of the HRC-S, but its single flat detector plate cannot follow the Rowland geometry as well as the HRC-S. At nominal focus this results in slightly poorer spectral resolution for wavelengths > 50 Å. In

principle, small focus offsets can be used to optimize the focus of the dispersed spectrum either within a specific wavelength range, or to average defocus blurring over the full wavelength range. No simple focus optimization prescription currently exists; interested readers should contact the CXC for assistance.

- The details of the LETG+HRC-I effective area have been less well-studied in general than for the LETG+HRC-S combination. The polyimide used in the HRC-I UV/Ion shield is about twice as thick as that used with the HRC-S, resulting in lower transmission at long wavelengths.
- The HRC-I offers a broad detector in the cross-dispersion direction and this might be a consideration for observation of sources with extended components exceeding ~ 2 arcmin or so. Note, however, that the *Chandra* spectrographs are slitless, and the effective spectral resolution is severely degraded for large sources (see Figure 9.11).

Summary HRC-I is possibly the best detector choice for sources in which signal longward of 73 Å (0.17 keV) is not of primary interest and accurate effective area knowledge for > 44 Å (< 0.28 keV) is not a strong concern, and in addition one or more of the following observational goals apply:

—the source is very weak with interesting spectral features at wavelengths beyond the limit of the LETG+ACIS-S coverage;
—high resolution timing is *not* required;
—a larger detector area in the cross-dispersion direction than is provided by the HRC-S is required.

ACIS-S

- Contamination build-up on the ACIS-S detector has significantly reduced the effective area of the LETG+ACIS-S combination longward of ~ 20 Å since launch (see Section 6.5.1 for details). ACIS-S provides an effective LETG 1st order wavelength limit of about 60 Å (0.20 keV) because longward of this the ACIS-S QE is essentially zero (see Figures 9.6 and 9.17). ACIS-S is not as well-calibrated for wavelengths longward of the C edge (~ 44 Å).
- The intrinsic energy resolution of ACIS-S allows for discrimination between different and otherwise overlapping spectral orders. For dispersion longward of $m\lambda \sim 60$ Å the LETG+ACIS-S response is dominated by higher order throughput (Figure 9.17) and ACIS-S can therefore be useful for observing these higher spectral orders.
- ACIS-S allows several modes of operation (see Section 6.12) including continuous clocking (CC) if high time resolution is desired, or to avoid pileup.
- If using the full frame 3.2 s exposure of ACIS-S in TE mode, photon pileup can be a serious consideration, especially in zeroth order. Proposers should also be aware

that there is a potential for pileup in bright lines and continua and not assume that, because of dispersion, the flux is too spread out to be affected. For observations using Y-offset= $+1.5'$, the fraction of 1st order events lost to pileup in a continuum spectra can be estimated as event rate (in counts/frame/dispersion-axis-pixel) times 3 for FI chips; times 4 for BI chips. As an example, if the counting rate of the 1st order spectrum is expected to be 0.01 counts/frame in a wavelength interval of 0.0275 Å (one pixel wide along the dispersion axis), about 3% of those events will be lost to pileup (in FI chips). While the example rate is observed only in very bright continuum spectra (such as Mkn 421 near 6.5 Å), pileup can be a concern for bright features in line-dominated spectra. Some of these events can be recovered by examining higher order spectra but most pileup events will have "migrated" out of the standard grade set. Pileup can affect both the shape of the PSF and the apparent spectral energy distribution of your source. Pileup may be reduced by opting for a "sub-array" that reads out a smaller area of the detector for a decrease in the frame time. See Section 9.4.2 and also Section 6.15 for details concerning pileup, its effects, and how best to avoid it.

- ACIS-S time resolution is lower than that of HRC and depends on the control mode adopted. In timed exposure (TE) mode the full frame exposure is 3.2 s. This is reduced when using a subarray due to the shorter read-out time for the smaller detector region (see Section 6.12 for details). Using fewer chips (e.g., dropping S0 and S5 because of their negligible effective area for 1st-order photons) may also slightly reduce the frame time. The highest time resolution possible with ACIS-S (2.85 ms) is obtained in continuous clocking (CC) mode, but imaging information in the cross-dispersion direction is lost and the background will be higher due to the implicit integration over the entire cross-dispersion column of the detector.

- The energy resolution of the FI chips degrades as distance increases from the CCD readout because of CTI (see Section 6.7). The LETG dispersion axis is parallel to the ACIS-S readout and the spectrum of a point source can be placed close to the readout such that the energy resolution degradation is no longer a significant problem; a default SIM-Z offset of -8 mm is routinely applied to LETG+ACIS-S *point source* observations. If observations with extended sources are under consideration, or if for other reasons a SIM offset is undesirable, the resolution in the FI CCDs of the ACIS-S array might be a point to consider. From an LETG perspective, the effects of concern are a degradation of the CCD energy resolution that is employed for order sorting, grade migration that can make for difficult calibration of detector quantum efficiency, and, at longer wavelengths ($\gtrsim 50$ Å), a loss of events that have pulse heights below that of the ACIS event lower level discriminator. These effects render the effective area at wavelengths longward of the C edge (~ 44 Å) less well-calibrated than at shorter wavelengths.

- The ACIS-S energy resolution enables removal of the vast majority of background events in LETG spectra; the effective ACIS-S background is consequently much lower than that of HRC-S or HRC-I.

Summary ACIS-S is possibly the best detector choice for sources for which signal longward of 25 Å (0.5 keV) is of little interest and one or more of the following observational goals apply:
—Particular spectral features of interest occur where the LETG+ACIS-S effective area is higher than that of LETG+HRC-S
—High time resolution beyond the 3.2 s exposure of TE mode (less if a subarray is used), or the 2.85 ms of CC mode (if applicable), is not important
—A low resolution zeroth order spectrum from the S3 BI chip is of high scientific value, in addition to the dispersed LETG spectrum
—Order separation is important
—Pileup can either be avoided or mitigated or is not likely to be a problem.

9.4.2 Other Focal Plane Detector Considerations

Instrument Features and Gaps

Attention should be paid to the locations of instrument edge features and detector gaps to make sure that spectral features required to achieve science goals are not compromised by these. Calibration in the vicinities of these features is generally much more uncertain. These features and gaps are listed for both HRMA+LETG+HRC-S and HRMA+LETG+ACIS-S combinations in Tables 9.3 and 9.4. Note that intrinsic instrumental features, such as edges, are not affected by dithering and offset pointing (see below), but chip gaps in ACIS-S and HRC-S plate gaps, as well as the boundaries between “thick” and “thin” regions of Al that make the “T” shape of the HRC-S UVIS, are.

Dither

The standard LETG+HRC-S dither amplitude is 20 arcsec (40 arcsec peak-to-peak; 2 mm in the focal plane or 2.3 Å) and that of LETG+ACIS-S is 8 arcsec (16 arcsec peak-to-peak; 0.8 mm or 0.9 Å), in both axes. Spectral features in dispersed LETG spectra will experience the same dither pattern, and allowance for the size of the dither must be made when considering if spectral features of interest will encounter detector gaps.

In special cases, different dither amplitudes can be specified by the observer, though it must be kept in mind that detector safety constraints, such as accumulated dose per pore in the HRC (see Section 7.13), must not be violated.

SIM-Z Offsets

The SIM permits movement of the focal plane detectors in the spacecraft z direction (perpendicular to the LETG dispersion axis). This can be used to better position a source on the ACIS-S or HRC detectors, for example to accommodate multiple sources, or to place a source over the HRC-S LESF filter region. The nominal aim point for the LESF requires a SIM-Z offset of +7 mm.

In the case of LETG+ACIS-S, a standard SIM-Z offset of −8 mm is applied to point source observations, *unless otherwise requested by the observer*, in order to place the source closer to the ACIS readout. In the case of extended sources, this offset might not be desirable as it could place part of the source off the detector. The effects of spacecraft dither should always be considered when choosing a SIM-Z offset.

Offset Pointing

In Feb 2007, as a result of accumulated aimpoint drift, the default Z-offset when using ACIS-S (with or without a grating) was changed from 0 to −0.25 arcmin in order to put the aimpoint closer to the best focus (highest resolution) position. *This Z-offset value will be used unless otherwise requested by the observer.*

Pointing off-axis in the observatory y axis can be used to change the wavelengths at which detector gaps occur, or to change the wavelength corresponding to the ends of the detectors. Examples of offset pointings are shown in Chapter 3. When choosing offsets, an increase of +1 arcmin in Y-offset corresponds to a shift of +3.36 Å in wavelength. As an example, by invoking a +2 arcmin offset pointing (see Chapter 3 for the convention), the long-wavelength cut-off of the HRC-S can be extended in the + order from approximately 176 Å for on-axis pointing to 183 Å. This, of course, is obtained at the expense of a commensurate shortening of coverage in the − order.

Offset pointing leads to degradation of the PSF, and consequently the spectral resolution—see Figure 9.12. For offsets of 2 arcmin or less this degradation is very small. For offsets of > 4 arcmin, spatial and spectral resolution will be considerably degraded.

In the case of the LETG+ACIS-S configuration, certain offsets might be useful, e.g., in order to place features of interest on (or off) backside-illuminated chips for better low energy quantum efficiency. Table 9.3 and Figure 9.6 can be used to determine what offsets are required. There is also an extremely useful visualization tool on the 'Checking Your LETG/ACIS-S Obscat Setup' page (http://cxc.harvard.edu/cal/Letg/ACIS_params), which incorporates the latest detector aimpoint calibration (see Section 6.10). Four particularly important Y-offsets are the following:

$+0.15'$ This is the default Y-offset value and provides the highest possible resolution while avoiding dither across the node0/node1 boundary on the S3 chip.

$+1.50'$ This is the most commonly used offset, as it keeps O K-edge features on the S3 backside chip. Zeroth order is moved toward the S2 chip by 4.5 mm and changes the S3 coverage to −0.7 to +26.5 Å (after excluding 0.45 Å on each dithered edge of the chip). Spectral resolution is ∼20% worse than with Y-offset=0.

$+1.55'$ This is the largest offset that can be used and still have zeroth order ∼completely on S3 (using the standard $16''$ dither and an extraction region with 5-pixel ($2.5''$)

radius) while allowing an adequate margin (∼5″) for errors in target acquisition and aimpoint scatter. Resolution is very slightly worse than with +1.50′.

+1.91′ This puts zeroth order in the gap between S2 and S3; a small fraction of zeroth order events will fall on each chip because of dither. There will be uninterrupted spectral coverage (apart from chip-edge dither effects around 29 Å) by the BI chips (S1 and S3) from 0 to 57 Å. Spectral resolution is degraded by ∼25% (see Figure 9.12).

ACIS-S Modes

When using the LETG+ACIS-S configuration, a mode must be selected for the ACIS detector. The ACIS detector is very flexible but deciding the best set-up can be complicated. Prospective observers considering using ACIS-S for the focal plane detector are urged to read Chapter 6 carefully. The most common modes used for LETG+ACIS-S observations are those using sub-arrays. The shorter frame times of subarrays can be a good way to both increase the time resolution and decrease pileup. Care must be taken when defining subarrays to make sure that the choice of SIM-Z plus any offset pointing in the z direction places the source comfortably inside the subarray. Modes with 256 rows ($\frac{1}{4}$ subarray) or fewer are recommended for observations of point (or small) sources, provided that the source position is known to within a few arcseconds. Subarrays permit the use of shorter frame times, and thus less pileup. As an example, a $\frac{1}{8}$ subarray (using 6 chips and with the standard SIM-Z offset of −8 mm) requires a frame time of 0.7 s (vs 3.2 s for the full array).

Frame times as short as 0.6 s can be used with four ACIS-S chips, or 0.5 s with three chips. See Section 6.12.1 for further information on ACIS frame times. Users should always refer to “Checking your LETG/ACIS-S Obscat Setup” (http://cxc.harvard.edu/cal/Letg/ACIS_params) for the most current information regarding subarray setups, including the optimal ACIS Start Row parameter, which slowly drifts with the telescope aimpoint over time (see Section 6.10).

Optional ACIS-S Chips and Scheduling Flexibility

As described in more detail in Section 6.20.1, the continuing gradual degradation of the *Chandra* thermal environment means that a steadily increasing fraction of observations are experiencing scheduling constraints with regard to the allowable exposure time per orbit. One way to increase the scheduling flexibility of LETG+ACIS-S observations is to use fewer than the full array of 6 CCDs, which reduces the temperature of the ACIS electronics and focal plane. To achieve this, users may denote some ACIS chips as “Optional.” In cases where thermal limits might otherwise be breached, Optional chips will be turned off for an observation; this allows Mission Planning more flexibility when setting up observing schedules and makes the process more efficient. Problematic observations with Optional chips are thus less likely to be split into multiple pieces than they would be if all the chips are required.

Note that chips S0 and S5 have negligible QE for LETG 1st order dispersed photons; those outermost chips are only useful for collecting higher-order spectra, or perhaps in other very special circumstances. The web page “Checking your LETG/ACIS-S Obscat Setup” (http://cxc.harvard.edu/cal/Letg/ACIS_params) and the Spectrum Visualizer tool linked there are helpful in determining which CCDs may be unnecessary. As of Cycle 13, **the S0 chip will turned off in all LETG+ACIS-S observations** unless the observer provides a compelling reason for its use. We also recommend that S5 be turned off or marked as Optional.

HRC-S Windowing

As described in Section 9.3.6, the HRC-S has a default spectroscopic “window” defined that limits the detector area from which events are telemetered to the ground. The window is a rectangle based on coarse position tap boundaries; the default rectangle comprises the central 6 taps in the cross-dispersion direction (corresponding to ~ 9.9 mm) and the whole detector length in the dispersion direction. This window can be defined to suit special observational goals, such as if the source is extended and the width of the readout region must be increased (with increased risk of telemetry saturation during background flares).

Likewise, a smaller detector region can be used if, for example, the source is very bright and telemetry saturation is a concern. In such a case, the number of cross-dispersion taps could be reduced, since the source only dithers across 2 or 3 taps. There would be less area for the background extraction region, but with a bright source this would not be a problem.

One can also specify that a subset of taps along the dispersion direction be used, particularly if the source spectrum is expected to be cut off at long wavelengths and higher-order spectra are not needed. The most commonly used (though still rare) non-default configuration is simply to use only the central plate with the standard 6 cross-dispersion taps, usually referred to as the Imaging Mode.

When considering defining a special HRC-S window, it is reasonable to assume that the detector background is spatially uniform for the purposes of computing the total source plus background count rate. The telemetry capacity of 183 cts s^{-1} should be kept in mind to avoid telemetry saturation by using a window that is too big.

9.4.3 General Considerations

Complications from Other Sources

Field sources coincident with the target source dispersed spectrum should be avoided. While some flexibility in roll angle of order several arcminutes can often be accomodated in observation execution, this avoidance is most rigorously accomplished by imposing a roll angle constraint (see below). Note that it is also desirable to retain a pristine region either side of the dispersed spectrum to enable an accurate estimation of the background within the spectral extraction window.

In some circumstances, photons from bright sources outside of the direct field of view of the HRC or ACIS might be dispersed by the LETG onto the detector.

Particular attention should be paid to optically-bright and UV-bright sources, even if these are some distance off-axis. The ACIS-S and HRC-S filters are much more transparent to optical and UV light than are those of HRC-I and ACIS-I (the HRC-S central "T" segment is closer in performance to that of HRC-I, but has completely different thicknesses of polyimide and Al layers). As an example, an observation of the bright A0 V star Vega ($V = 0.03$) in one of the outer HRC-S UVIS segments gave a count rate of about 475 count s^{-1}.

The energy resolution of the ACIS-S detector enables removal by filtering of all photons except those in a fairly narrow wavelength or energy range corresponding to the wavelength or energy of photons in a spectrum dispersed by the LETG. This means that contamination of the dispersed spectrum by, for example, the zeroth order or dispersed spectrum of other sources *might* not be a significant problem.

However, a much better solution to problems of source contamination is, if it is possible within other observation constraints, to choose a roll angle (Chapter 3) that avoids the source contamination issue.

Roll Angle Considerations

Roll angle constraints can be specified to avoid contamination by off-axis sources, as described above, or to help separate the dispersed spectra of multiple sources in the cross-dispersion direction. The maximum separation between dispersed LETG spectra of two sources is obviously one that places the sources in a line perpendicular to the dispersion axis.

Owing to spacecraft thermal degradation and increasing difficulty in scheduling constrained observations, proposers are reminded that only a very limited number of constrained observations can be accomodated. Technical justification for requested constraints must be provided. It is also important to remember that roll angle constraints will also impose restrictions on the dates of target availability as discussed in Chapter 3. Exact restrictions depend on celestial position. Their impact can be examined using the observation visualizer tool, downloadable from the *CIAO* home page at http://cxc.harvard.edu/ciao/.

High Order Throughput

It is expected that the majority of observations with the LETG will make use of the HRC-S as the readout detector because of its wavelength coverage and high quantum efficiency at long wavelengths. Since the HRC-S has very little energy resolution, the overlapping of spectral orders could be a significant issue and prospective observers should assess the degree to which their observation might be affected. The following list summarizes some considerations:

Scientific Utility: Higher spectral orders provide higher spectral resolving power than the 1st order spectrum by the approximate factor of the order number m. For observations in which features are expected to be seen in higher orders, this capability could be scientifically useful.

LESF: The LESF (the region of thicker Al coating on the HRC-S UVIS) is untested in flight, but could be useful for obtaining a spectrum containing mostly higher order flux.

Source Spectrum: For some sources higher orders will contain very little flux and will not be an issue. Typical examples are hot white dwarfs or relatively cool stellar coronae with $T \sim 10^6$ K. Sources whose spectra are fairly weak in the region where the effective area of the LETG+HRC-S is highest (∼ 8–20 Å; 1.5–0.6 keV) but gain in strength toward longer wavelengths will also be less affected by higher order throughput. Typical examples are blackbody-type spectra with temperatures $T \sim 10^6$ K or less, such as might characterize novae or isolated neutron stars.

Estimates: Figure 9.18 can be used to estimate high order contamination. *PIMMS* can be used for gross estimates of higher order count rates; the *PIMMS* higher order calculation uses an effective area curve for orders $m > 1$ combined.

Instrumental Capabilities: Order separation is straightforward with ACIS-S. With HRC-S orders cannot be separated.

Spectral Modeling and Higher Orders: Unlike ACIS-S, the HRC-S does not have enough energy resolution to allow order sorting of LETG spectra. However, by folding a spectral model through an LETG+HRC-S instrument response that includes all significant higher orders (generally ≤ 10), the whole spectrum can be modeled at once. The capability to generate and simultaneously utilize response matrices for multiple orders (which can be created for plus and minus orders 1–25) is available within *Sherpa/CIAO*, and these response matrices can also be used with other spectral analysis software such as *XSPEC*. Note that the response matrices do not include the small-scale wavelength distortions discussed in Section 9.3.2, and hence care must be taken when analyzing some details of line-dominated spectra, particularly line profiles.

ISM Absorption

The long wavelength cutoff of the LETGS in tandem with the HRC-S detector of ∼175 Å (which can be extended with offset pointing as described in Section 9.4.2), reaches well into the extreme ultraviolet (EUV). In this wavelength regime, the spectra of even very nearby sources with relatively low ISM absorbing columns can be appreciably attenuated by H and He bound-free photoionizing transitions. Therefore observers should be aware that the effective long wavelength cutoff for anything but the nearest sources (∼ 100 parsec

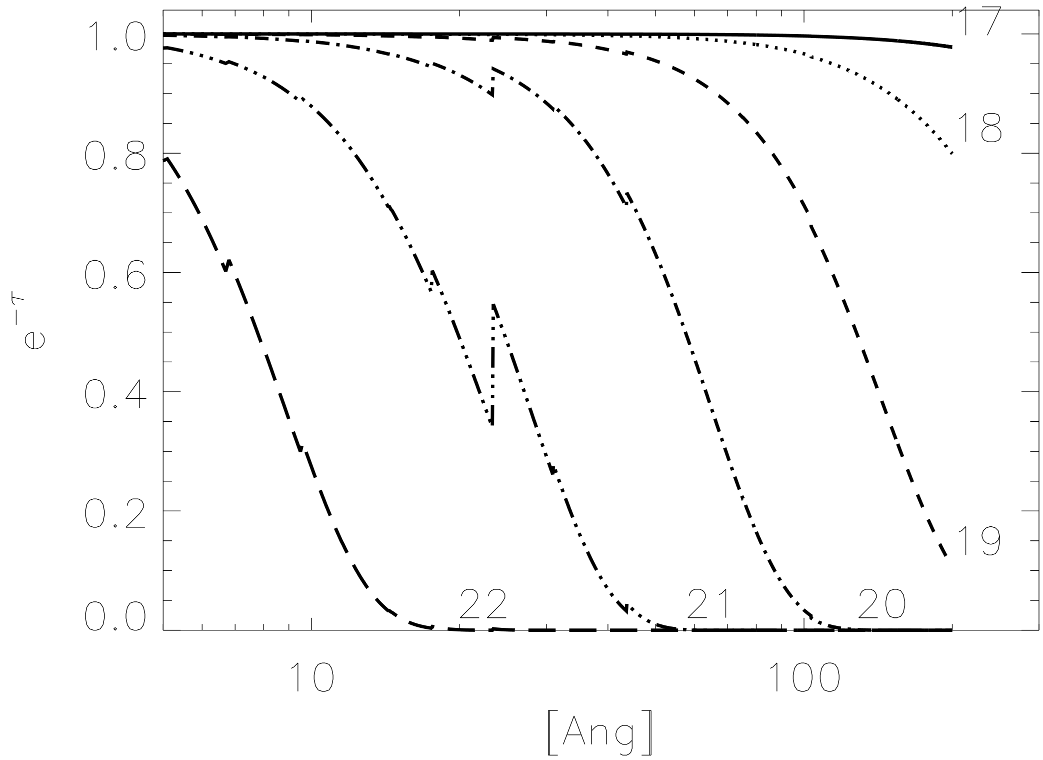

Figure 9.28: The ISM transmittance within the LETGS bandpass for different values of neutral hydrogen column density 10^{17}–10^{22} cm^2.

or less) will probably be determined by ISM absorption. It is also important to remember that neutral and once-ionized He can dominate the ISM absorption cross-section in the 44–200 Å (0.28–0.062 keV) range, and consideration of the neutral H absorption alone is generally not sufficient. Shortward of the C edge near 44 Å (0.28 keV), metals become the dominant absorbers. For illustration, the ISM transmittance for a "typical" mixture of neutral and ionized H and He with H:He:He$^+$ ratios of $1 : 0.1 : 0.01$ is shown in Figure 9.28 for the 5–200 Å range with different values of the neutral hydrogen column.

The *CXC* web page has a tool *Colden* (http://cxc.harvard.edu/toolkit/colden.jsp) that provides the total *galactic* neutral hydrogen column for a given line-of-sight. The Ahelp page for *Colden* is located at http://cxc.harvard.edu/ciao/ahelp/colden.html. An IDL routine from the PINTofALE data analysis package for computing the ISM optical depth is available from http://hea-www.harvard.edu/PINTofALE/pro/ismtau.pro.

9.5 Technical Feasibility

Proposers should always be aware of possible limitations in the physical models and methods they are using for observation planning purposes. For example, older *XSPEC* versions might not include ISM absorption edges or spectral models at the high resolutions appropriate for *Chandra* grating observations. Available optically thin, collision-dominated plasma radiative loss models have also generally only been tested in any detail for strong lines of abundant elements. Some prominent transitions in Fe ions with n=2 ("L-shell") and n=3 ("M-shell") ground states are not yet well-represented by some models. The spectral region 25–75 Å (0.5–0.17 keV) still remains largely unexplored, and both total radiative loss and predicted strengths of lines in this region are more uncertain than at shorter wavelengths.

Some additional technical limitations in *MARX* modeling of LETG+HRC-S spectra are detailed below.

9.5.1 Simple Calculation of Exposure Times and Signal-to-Noise Ratio for Line and Continuum Sources

There is a discussion in Chapter 8 (HETG), Section 8.5.4, concerning the detection of an isolated emission line or absorption line that is also relevant to the LETG+HRC-S combination. This discussion is based on line equivalent width, which is appropriate for broadened lines and continuum features but which is more difficult to apply to simple modeled estimates of expected line fluxes. Additional formulae which are simple to apply are presented below. The units are Å rather than keV, Å being a much more natural unit of choice for dispersed spectra, and especially for the LETG range.

Emission Line Sources The source signal S in a bin is the difference between the total counts and the background counts B. The estimated standard deviation of the source counts S in a spectral bin is given by Poisson statistics as:

$$\sigma_S = \sqrt{S + B} \tag{9.3}$$

Here we have made the important assumption that there is effectively no additional uncertainty in the estimation of the background B. Such an assumption may only be valid if, for example, the detector region used to estimate the background within the spectrum extraction window is much larger than the window itself.

Spectrometer count rates for emission features are given by

$$s_l = A_{eff}(\lambda)\mathcal{F}_l(\lambda) \tag{9.4}$$

where s_l is the source count rate in the resolution element centered at λ, in cts s^{-1}, A_{eff} is the effective area in cm^2, and $\mathcal{F}_l$ is the source flux at the telescope aperture, in photons/cm^2/s. For A_{eff}, it is reasonable to use the total area obtained from the sum of + and − orders as illustrated in Figure 9.17. Raw source counts are estimated by multiplying this instrument count rate by an integration time.

Using Equations 9.3 and 9.4, the signal-to-noise ratio for an integration time t is then

$$\frac{S}{\sigma_S} = \frac{s_l\sqrt{t}}{\sqrt{s_l + b}} \tag{9.5}$$

where b is the background count rate *within the spectrum extraction window* (i.e. "underneath" the spectrum) in the same resolution element centered at λ, in cts s^{-1}. Equation 9.5 provides the expected relation that is valid in the limit where the background count rate b is small compared with the source count rate s_l, that the signal-to-noise ratio scales with the square root of the exposure time.

The exposure time required to achieve a given signal-to-noise ratio is then provided by inversion of equation 9.5,

$$t = \left(\frac{S}{\sigma_S}\right)^2 \frac{s_l + b}{s_l^2}. \tag{9.6}$$

In order to make the exposure time estimate one needs to determine the background count rate, b. Since the spectrometer does not have infinite resolution, the flux from an otherwise narrow spectral line is spread over a typical line width, w_l. For LETG+HRC-S spectra, a good estimate for w_l is 0.07Å. This is somewhat larger than the FWHM value of 0.05Å listed in Table 9.1, but is more appropriate for calculations of signal-to-noise because it includes more of the line flux. For lines that are additionally broadened, simply use a value of w_l that covers the region under the feature of interest. The background rate b is then given by the quantity $b = w_l b'$, where b' is the background rate in units of cts/Å/s. Background spectra for LETG+HRC-S from which one can readily estimate b are illustrated in Figure 9.22 Two scales are shown, one corresponding to b' and one corresponding to b where a width $w_l = 0.07$ Å was assumed. Note the y-axis units are per 10 ks.

Using the signal count rate s_l, provided by the product of source flux (at the telescope aperture) and effective area as stated in equation 9.4, we then obtain the two equations for the signal-to-noise ratio S/σ_S resulting from an exposure time t,

$$\frac{S}{\sigma_S} = \frac{\mathcal{F}_l A_{eff} t}{\sqrt{\mathcal{F}_l A_{eff} t + b' w_l t}} \tag{9.7}$$

and for the exposure time t required for a signal-to-noise ratio S/σ_S

$$t = \left(\frac{S}{\sigma_S}\right)^2 \frac{\mathcal{F}_l A_{eff} + b' w_l}{(\mathcal{F}_l A_{eff})^2}. \tag{9.8}$$

These simple equations, which include the effects of instrumental background, can also be easily applied to observations of lines on top of continua, as well as to situations in which features of interest lie on top of higher (or lower) spectral orders (HRC). In these cases, the continuum or higher order flux acts as an additional background term—the count rate/Å due to these additional terms is simply added to b'.

Continuum Sources Model fluxes for continuum sources can be expressed as flux densities in units of photons/cm^2/s/Å. To compute instrument count rates s_c from a continuum source spectrum, the A_{eff} function and spectrum must be partitioned with some bin size w, large enough to give adequate count rates. The product of the source spectrum with the A_{eff} function is then summed over some wavelength region of interest. Equation 9.4 becomes the sum

$$s_c(\lambda) = \sum_{j=1}^{N} \mathcal{F}_c(\lambda_j)\, A_{eff}(\lambda_j)\, w \tag{9.9}$$

where $\mathcal{F}_c$ is the model source flux in photons/cm^2/s/Å, $A_{eff}(\lambda_j)$ is the effective area of the jth bin in cm^2. The region of interest spans bins 1 through N, and w is the bin width in Å. In using this formula for planning purposes, proposers must choose a spectral bin width that will demonstrate the viability of the program proposed. For fairly narrow spectral ranges in which A_{eff} is nearly constant, the sum over 1-N reduces to

$$s_c(\lambda) = \mathcal{F}_c(\lambda_j)\, A_{eff}(\lambda_j)\, Nw \tag{9.10}$$

In this case one can of course simply chose a new bin size $w' = Nw$.

The difference between the continuum and the emission line case above lies in the units of $\mathcal{F}_c$, which is a flux density. The equations corresponding to the line source Equations 9.7 and 9.8 are, for the signal-to-noise resulting from an exposure time t

$$\frac{S}{\sigma_S} = \frac{\mathcal{F}_c A_{eff} w t}{\sqrt{\mathcal{F}_c A_{eff} w t + b' w t}} \tag{9.11}$$

and for the exposure time t required for a signal-to-noise ratio S/σ_S

$$t = \left(\frac{S}{\sigma_S}\right)^2 \frac{\mathcal{F}_c A_{eff} w + b' w}{(\mathcal{F}_c A_{eff} w)^2}. \tag{9.12}$$

Note also in the above equations that the background b' is in units of counts/Å/s.

PIMMS for Rough Planning Purposes

PIMMS is best suited to performing rough estimates of total or zeroth order count rates, or estimating the fraction of zeroth order events that would be piled up. Some degree of caution should accompany *PIMMS* calculations of detailed quantities such as count rates within narrow spectral bands using the Raymond-Smith model. For example, line positions and intensities in this model were only designed to represent total radiative loss and do not stand up to high resolution scrutiny. Calculations using power-law and featureless continua are not prone to such difficulties, but are susceptible to other *PIMMS* limitations. One particular limitation concerns the background model for HRC-S, which in *PIMMS* is assumed to be a single average number per spectral resolution element of 20 counts/100 ks. This approximation overestimates the background at medium energies, and underestimates the background at lower and higher energies; see Figure 9.22.

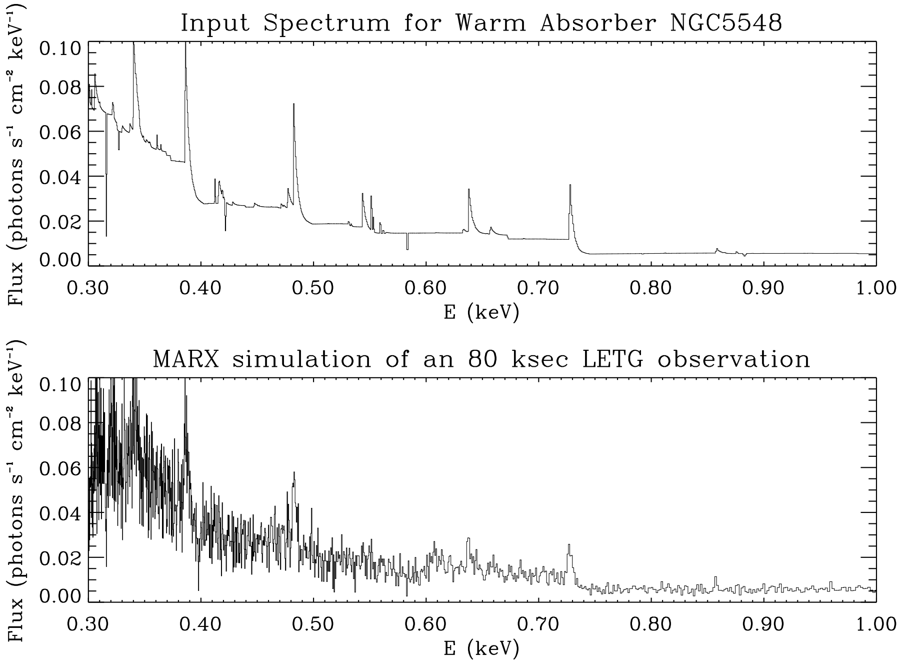

Figure 9.29: This figure shows the extracted 1st order spectrum for an 80 ksec observation of the AGN NGC5548. The input spectrum consists of a power-law plus a "warm" absorber (shown in the top panel). The simulated spectrum (bottom panel) has been corrected for the instrument response to give the flux from the source.

MARX **Simulations**

The best tool for simulating LETG observations, including cases where there are multiple targets in the field of view, is the *MARX* ray trace simulator, which permits study of any of the available *Chandra* instrument combinations. For cases requiring higher fidelity modeling of the PSF, simulations can be performed by first simulating the response of the HRMA using ChaRT (http://cxc.harvard.edu/chart) and then feeding those ray trace results into *MARX* to simulate the LETG and detector responses.

MARX has an important limitation for LETG+HRC-S observations in that instrument, sky, and particle backgrounds are almost always significant (see Section 9.3.6 and Figure 9.22) but are *not* directly included and need to be simulated or otherwise accounted for by the user. Background can be simulated by approximating it as a flat field and adding this simulation to that of the source (see http://space.mit.edu/CXC/MARX/). Another way of simulating background is to scale the background in Figure 9.22 after adjusting for solar-cycle variations in the background rate.

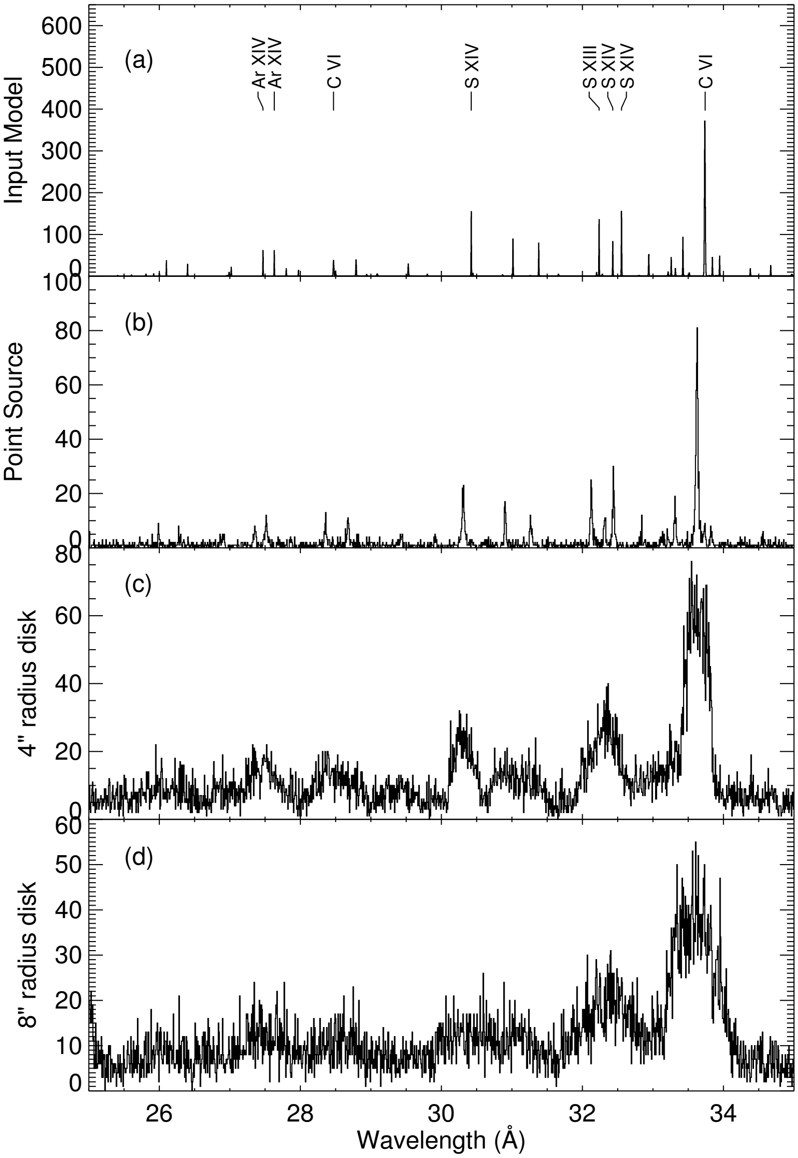

Figure 9.30: *MARX* simulation of spectra showing the effect of source extent. The panels show (a) computed input spectrum, (b) a *MARX* output of LETG spectrum of a point source, (c) the same as (b) except that the source is a disc of uniform brightness with radius of 4″, and (d) the same but with radius of 8″. See Figure 9.11 and Section 9.3.3 for a discussion of extended sources.

9.6 References

Further information on LETGS performance and calibration, along with relevant Chandra Newsletter articles, can be found on the LETGS Observer Information page off the Instruments & Calibration website (http://cxc.harvard.edu/cal/).

Part I

Appendices

Appendix A

Contact Information

A.1 Contact Information

The Proposal Review is organized for NASA by the *CXC* Director's Office (*CDO*) under the direction of Dr. Belinda Wilkes (Assistant Director). Questions should be submitted to the *CDO* via our HelpDesk (http://cxc.harvard.edu/helpdesk/) (preferable) or by email: (cxchelp@cfa.harvard.edu). We strongly recommend the use of this HelpDesk as opposed to contacting individual staff members, as it is routinely monitored and not affected by the schedules of individuals.

A.2 *CDO* Staff

- Dr. Harvey Tananbaum, Director
- Dr. Belinda Wilkes, Assistant Director
- Dr. Andrea Prestwich
- Dr. Paul Green
- Dr. Antonella Fruscione
- Ms. Tara Gokas
- Mr. Evan Tingle
- Ms. Katherine Wyman

Appendix B

Acronym List

This list is a superset of acronyms and abbreviations used in this document.

ACA Aspect Camera Assembly

ACACAL ACA Calibration Data

ACIS Advanced CCD Imaging Spectrometer

ACIS-I ACIS Imaging array

ACIS-S ACIS Spectroscopic array

ADC Analog-Digital Conversion

ADU Analog to Digital Unit

AGASC AXAF Guide and Aspect Star Catalog

AO Announcement of Opportunity

ARD Analysis Reference Data

ARF Ancillary Response Function

ARM Alignment Reference Mirror

ASC AXAF Science Center

ASCA also known as Asuka, Astro-D - Japanese X-ray satellite

ASCDS ASC Data Analysis System

ASCII American National Standard Code for Information Exchange

ASVT Avionics and Software Validation and Test (facility)

ASPQUAL Aspect Solution Quality Indicators

AXAF Advanced X-Ray Astrophysics Facility

BI Back-illuminated

CALDB Calibration Data Base

CAP Command Action Procedure (used to communicate with spacecraft)

CC Continuous Clocking

CCD Charge Coupled Device

CCDM Communication, Command, and Data Management

CDO *CXC* Director's Office

CDR Central Data Recorder (also Critical Design Review)

CfP Call for Proposals

CGCD Crossed Grid Charge Detector

CHaRT *Chandra* Ray Tracer

ChaSeR Chandra Search and Retrieval

CIAO Chandra Interactive Analysis of Observations

CoI Co-Investigator

COLDEN Calculate Neutral Hydrogen Column Density

CR Cosmic Ray

CSS Coarse Sun Sensor

CTE Charge Transfer Efficiency

CTI Charge Transfer Inefficiency

CXC Chandra X-ray Center

CXCDS Chandra X-ray Center Data Systems

CXO Chandra X-ray Observatory

DBE Double Bit Error

DEA Detector Electronics Assembly

DDT Director's Discretionary Time

Dec Declination

DOT Detailed Operations Timeline

DSN Deep Space Network

DSS Digital Sky Survey

EA Effective Area

E/PO Education and Public Outreach

EC Ecliptic Coordinates

ECS External Calibration Source

EDT Eastern Daylight Time

EPHIN Electron Proton Helium Instrument

ESA Earth Sensor Assembly

ESC Engineering Support Center

FAQ Frequently Asked Questions

FCM Flux Contamination Monitor

FEF FITS Embedded Function (used to generate RMF for detectors)

FI Focal Plane Instrumentation (Front-Illuminated)

FITS Flexible Image Transport System

FLA Fiducial Light Assemblies

FOT Flight Operations Team

FOV Field of View

FPSI Focal Plane Scientific Instruments

FPX Focal Plane X

FPY Focal Plane Y

FSS Fine Sun Sensor

FTA Fiducial Transfer Assembly

FTS Fiducial Transfer System

FUV Far-UV

FWHM Full Width Half Maximum

GESS Grating Element Support Structure

GMST Greenwich Mean Sidereal Time

GMT Greenwich Mean Time

GO General Observer

GSFC Goddard Space Flight Center

GST Greenwich Sidereal Time

GTO Guaranteed Time Observer

GUI Graphical User Interface

HDOS Hughes-Danbury Optical System

HEASARC High Energy Astrophysics Science Archive Research Center

HEG High Energy Grating

HESF High Energy Suppression Filter

HESS HETG Support Structure

HETG High Energy Transmission Grating

HETGS HETG Spectrometer

HPD Half Power Diameter

HQ Headquarters

HRC High Resolution Camera

HRI High Resolution Imager

HRMA High Resolution Mirror Assembly

HST Hubble Space Telescope

IAU International Astronomical Union

ICD Interface Control Document

IDR Intermediate Data Record

IDS Interdisciplinary Scientist

IPI Instrument Principal Investigator

IPS Integral Propulsion System

IRAF Image Reduction and Analysis Facility

IRU Inertial Reference Unit

ISIS Interactive Spectral Interpretation System

IUE International Ultraviolet Explorer

IUS Inertial Upper Stage

JD Julian Day

JPL Jet Propulsion Laboratory

KSC Kennedy Spaceflight Center

LESF Low-energy Suppression Filter

LETG Low Energy Transmission Grating

LETGS LETG Spectrometer

LGA Low Gain Antenna

LRF Line Response Function

LSF Line Spread Function

LTS Long Term Schedule

MARX Model of AXAF Response to X-rays

MCP Micro Channel Plate

MEG Medium Energy Grating

MIT Massachusetts Institute of Technology

MJD Modified Julian Date

MPE Max-Planck-Institut für Extraterrestrische Physik

MSFC Marshall Space Flight Center

MTA Monitoring and Trends Analysis

MUPS Momentum Unloading Propulsion System

NASA National Aeronautics and Space Administration

NASCOM NASA Communication system

NDC NRT Data Capture

NGST Northrop-Grumman Space Technology

NISN NASA Integrated Services Network

NMM Normal Maneuver Mode

NOAO National Optical Astronomy Observatory

NPM Normal Pointing Mode

NRA NASA Research Announcement

NRAO National Radio Astronomy Observatory

NRT Near-Real Time (telemetry data)

OAC Orbital Activation and Checkout

OBA Optical Bench Assembly

OBC On-Board Computer

OBF Optical Blocking Filter

OBSCAT Observing Catalog

OBSVIS Observation Visualizer

OCC Operations Control Center

ODB Optical Data Base

OFLS Off-line System

ONLS On-line System

OR Observation Request

OS Operating System

PCAD Pointing Control and Attitude Determination

PDF Portable Document Format

PDR Preliminary Design Review

PH Pulse Height

PHA Pulse Height Amplifier (or Amplitude)

PI Principal Investigator

PIMMS Portable Interactive Multi-Mission Software

PRoVis Pitch, Roll and Visibility tool

PSF Point Spread Function

PSMC Power Supply and Mechanism Controller (for ACIS)

PSPC Position Sensitive Proportional Counter

QE Quantum Efficiency

RA Right Ascension

RCS Reaction Control System

RCTU Remote Command and Telemetry Unit

RfO Requests for Observations

RMF Redistribution Matrix Function

RMS Root Mean Squared

ROSAT Roentgen Satellite

RPS Remote Proposal Submission

RRC Retroreflector Collimator

RWA Reaction Wheel Assembly

SADA Solar Array Drive Assembly

SAO Smithsonian Astrophysical Observatory

SI Science Instrument

SIM Scientific Instrument Module

SMF Software Maintenance Facility

SNR Supernova Remnant

SOHO Solar and Heliospheric Observatory

SOP Standard Operating Procedure

SOT Science Operations Team

SSR Solid-State Recorder

STS Short Term Schedule

STScI Space Telescope Science Institute

TAI International Atomic Time

TBD To Be Determined

TBR To Be Reviewed

TE Timed Exposure

TIM Technical Interchange Meeting

TOO Target of Opportunity

TS Telescope System, or Telescope Scientist

UT Universal Time

UTC Universal Time Coordinated

UV Ultraviolet

UVIS UV Ion Shield

VCDU Virtual Channel Data Unit

VETA Validation Engineering Test Article (mirror)

WGACAT White-Giommi-Angelini Catalog (ROSAT)

XMM X-ray Multi-Mirror Mission

XRCF X-ray Calibration Facility

XSPEC X-ray Spectral fitting package

XTE X-ray Timing Explorer

XUV Extreme Ultraviolet